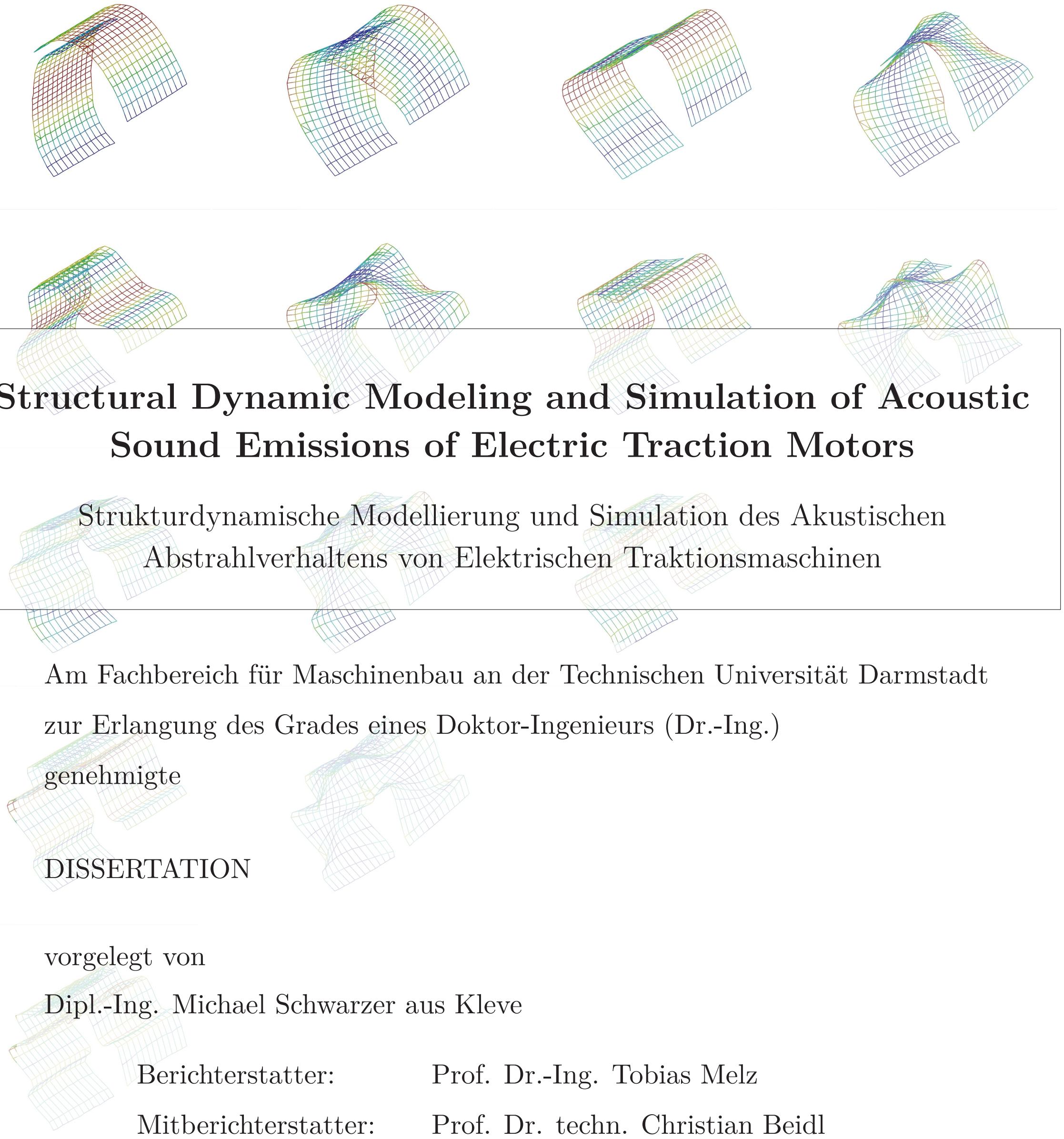

Structural Dynamic Modeling and Simulation of Acoustic Sound Emissions of Electric Traction Motors

Strukturdynamische Modellierung und Simulation des Akustischen Abstrahlverhaltens von Elektrischen Traktionsmaschinen

Am Fachbereich für Maschinenbau an der Technischen Universität Darmstadt
zur Erlangung des Grades eines Doktor-Ingenieurs (Dr.-Ing.)
genehmigte

DISSERTATION

vorgelegt von
Dipl.-Ing. Michael Schwarzer aus Kleve

Berichterstatter:	Prof. Dr.-Ing. Tobias Melz
Mitberichterstatter:	Prof. Dr. techn. Christian Beidl

Tag der Einreichung: 25.10.2016
Tag der mündlichen Prüfung: 20.12.2016
Darmstadt 2017
D17

Danksagung

Die vorliegende Arbeit entstand im Rahmen meiner Tätigkeit im Bereich der Entwicklung elektrischer Antriebsmaschinen bei der BMW Group in München.

Ich bedanke mich bei Professor Melz für die Übernahme der Betreuung meiner Arbeit, insbesondere für das entgegengebrachte Vertrauen hinsichtlich der eigenständigen Ausgestaltung der Forschungsinhalte.

Bei Professor Beidl bedanke ich mich für die Übernahme des Koreferats und dem damit verbundenen Interesse an meiner Arbeit.

Ich bedanke mich bei Professor Bein für die operative Betreuung meiner Arbeit. Ich habe Professor Bein als einen besonders vertauensvollen und geduldigen Förderer des eigenständigen wissenschaftlichen Arbeitens empfunden.

Besonderer Dank gilt Dr. Endre Barti für seine unermüdliche fachliche und überfachliche Betreuung meiner Arbeit bei der BMW Group. Unsere tiefgehenden, inhaltlichen Diskussionen haben den Kern der Arbeit massiv geprägt.

Ebenso danke ich Max Zinner, Maximilian Müller, Clemens Zimmerling und Vlad Somesan, welche mit Ihren Studienabschlussarbeiten signifikant zum Gelingen der Arbeit beigetragen haben.

Insgesamt danke ich dem Bereich der „Entwicklung elektrischer Antriebsmaschinen“ sowie allen Schnittstellenpartnern bei der BMW Group für die durchgängige Unterstützung meiner Forschungsbemühungen. Besonders erwähnen möchte ich dabei Julian Blum, Dr. Arthur Hülsmann, Quentin Duquesne, Robert Heyer, Martin Kohnke, Andreas Heymann, Dr. Yvonne Küssel, Dr. Thomas Bonin, Dr. Christian Guist, Dr. Jörg Merwerth, Gunter Schröter sowie Dr. Stephan Zügner und Dr. Georg Steinhoff, denen ich über ihr fachliches Engagement hinaus auch wertvolle überfachlichen Impulse zu verdanken habe.

Für die gute interdisziplinäre Arbeitsatmosphäre bei der BMW Group danke ich Dr. Thin Nguyen-Xuan, Dr. Andreas Huber sowie Daniel Loos. Weiterhin danke ich Frank Eckstein für das Vertrauen den fachlichen Themenkomplex „Akusik von Elektrischen Maschinen“ innerhalb einer wissenschaftlichen Arbeit tiefgreifend beleuchten zu lassen.

Weiterhin danke ich Lothar Baumgärtel für die Revision der englischen Sprache innerhalb meiner Ausführungen.

Zuletzt gilt mein besonderer Dank meiner Familie, ohne deren Unterstützung und Geborgenheit ich diese Aufgabe vermutlich nicht hätte meistern können. Vielen Dank, dass Ihr immer für mich da seid und mich so nehmt wie ich bin, mit allen meinen Lastern und

Unzulänglichkeiten.

Mein ganz besonderer Dank gilt meiner Freundin Miriam Weigel für ihre bedingungslose Unterstützung bei der Fertigstellung der Arbeit. Ohne Deine durchgängige Rücksichtnahme wäre die Arbeit vermutlich nie abgeschlossen worden.

München, 22. April 2017

Michael Schwarzer

Deutsche Kurzfassung

Strukturdynamische Modellierung und Simulation des Akustischen Abstrahlverhaltens von Elektrischen Traktionsmaschinen

Das Geräuschverhalten elektrifizierter Antriebe ist eines der wesentlichen Komfortkriterien der Elektromobilität. Aufgrund seiner drehzahlsynchronen, teils hochfrequenten Schallemissionen kommt dem Elektromotor hier eine zentrale Bedeutung zu. Quelle der Schallemissionen sind elektromagnetische Kräfte, welche die Zähne des E-Maschinenstators sowohl in radialer als auch in tangentialer Richtung anregen. Gepaart mit dem strukturdynamischen Übertragungsverhalten des Systems wird so das akustische Verhalten des Elektromotors determiniert.

Besonders vor dem Hintergrund zunehmender Leichtbau- und Bauraumanforderungen in mobilen Anwendungen, ist die frühzeitige Berücksichtigung der strukturdynamischen Eigenschaften elektrischer Maschinen im Auslegungsprozess von zentraler Bedeutung. Ein wichtiges Werkzeug stellt dabei die Simulation dar, mit deren Hilfe die Auslegung elektrischer Maschinen bereits in frühen Projektphasen begleitet und weitreichende Konzeptentscheidungen differenziert bewertet werden können. Dabei ist es notwendig, dass das zugrundeliegende Simulationsmodell die zur Konzeptentscheidung notwendigen Effekte abbildet, gleichzeitig jedoch praktikabel und rechnerisch handhabbar bleibt. Diesem Konflikt stellt sich die vorliegende Dissertation.

Das akustische Verhalten elektrischer Maschinen ist wesentlich von dem mechanischen Verhalten des Stators abhängig. Zur Vermeidung axialer Wirbelstromverluste besteht der Stator in seinem Kern aus einem Paket von Einzelstahlblechen. Durch die Statornuten verlaufen Bündel von Kupferdrähten, welche zur mechanischen Fixierung mit einem Tränkharz imprägniert werden. Die mikroskopische Abbildung dieser heterogenen Statorstruktur innerhalb dynamischer Simulationen ist aufwendig und rechenintensiv. Deshalb werden in strukturdynamischen Simulationen elektrischer Maschinen in der Regel sogenannte homogenisierte Ersatzmaterialien verwendet. Diese bilden das effektive direktionale Steifigkeits- und Dämpfungsverhaltens der zugrundeliegenden heterogenen Strukturen in einem transversal isotropen oder othotropen Ersatzmaterial ab. Klassischerweise werden die Steifigkeits- und Dämpfungskennwerte der homogenene Ersatzmaterialien aus experimentellen Untersuchungen an entsprechenden Bauteilen gewonnen. Diese Verfahren sind meist recht zeitintensiv, kostspielig und setzen vor allem voraus, dass bereits erste Bauteile für entsprechende Untersuchungen verfügbar sind. In der vorliegenden Arbeit werden unterschiedliche, so genannte Homogenisierungsmethoden untersucht, die die Identifizierung homogener Ersatzmaterialien für Komponenten elektrischer Maschinen auf Basis mikromechanischer Modelle erlauben. Dabei werden klassische numerische Ansätze unterschiedlichen analytischen Ansätzen gegenübergestellt und hinsichtlich ihrer Prognosegüte bewertet. Die so entwickelten Modellierungsmethoden werden anhand unterschiedlicher experimenteller Modalanalysen an Subkomponenten einer exemplarischen Statorstruktur sukzessiv validiert und anschließend in einer akustischen Simulationen des Gesamtantriebsverbunds verwendet. Mithilfe der in der Dissertation entwickelten Modellierungsansätze zur Abbildung des strukturdynamischen Ver-

haltens elektrischer Maschinen auf Basis mikromechanischer Modelle kann die Akustik elektrischer Antriebe bereits in frühen Projektphasen zuverlässig bewertet werden.

Nichtsdestotrotz bleibt die Simulation der oft breitbandigen Geräuschemission elektrischer Antriebe und somit auch die Bewertung ausgewählter E-Maschinendesigns rechenintensiv. Zur effizienteren Berechnung des strukturdynamischen Verhaltens elektrischer Maschinen ist die Verwendung von Modellreduktionsmethoden vorteilhaft. Diese basieren in der Regel auf mathematischen Algorithmen, welche die gezielte Reduktion von Modellfreiheitsgraden bewirken. In der Dissertation werden ausgewählte Modellreduktionsmethoden vorgestellt und hinsichtlich ihrer Anwendbarkeit im Bereich der strukturdynamischen Simulation von elektrischen Maschinen bewertet. Zahlreiche Publikationen propagieren die Verwendung der Modalen Superposition als geeignete Modellreduktionsmethode. In der Dissertation wird nachgewiesen, dass die Dynamik elektrischer Motoren durch die Modale Superposition, aufgrund der sehr komplexen elektromagnetischen Lastfälle, nur mithilfe aufwendiger Korrekturmaßnahmen abbildbar ist. Demgegenüber konnte eine besonders effiziente Reduktion des Systems durch die Verwendung sogenannter KRYLOV-Unterräumen erreicht werden. Die Rechenzeit ausgewählter Betriebspunkte der betrachteten elektrischen Maschine konnte dabei auf weniger als 10% der ursprünglichen Rechenzeit gesenkt werden.

Insgesamt wird in der Dissertation ein durchgängiger Prozess entwickelt, welcher neben der zuverlässigen Prognose der Schallemission elektrischer Maschinen auch die rechenzeiteffiziente Optimierung ausgewählter Strukturparameter zur Verbesserung des gesamtakustischen Verhaltens ermöglicht. Insbesondere durch den generischen Ansatz zur Beschreibung des strukturdynamischen Gesamtverhaltens der elektrischen Maschine auf Basis komplexer, mikrostruktureller Modelle und der damit verbundenen Robustheit der Modellierungsmethode hebt sich die Arbeit von anderen Forschungsarbeiten ab.

English Summary

Structural Dynamic Modeling and Simulation of Acoustic Sound Emissions of Electric Traction Motors

The acoustic behavior of electric drive systems is one of the main comfort criteria of electromobility. Due to its high-pitched sound emissions, the electric motor plays an important role. The source of these noise emissions are electromagnetic forces that tangentially and radially act on the electric machine's stator teeth. The corresponding noise is then determined by the vibrational behavior of the electric machine given by the structural transfer function.

The early phase consideration of the vibrational behavior of electric machine structures becomes even more relevant if one takes into account the strong requirements towards lightweight design and spatial restrictions inside vehicle applications. One of the most important tools inside the early stage development is the structural dynamic simulation. Structural simulations can be used to evaluate the effect of mechanical design parameters towards the acoustic behavior of the electric motor. However, in order to be able to sustainably evaluate these effects, it is important that the underlying simulation model sufficiently represents all relevant design parameters and so their influence on the vibrational behavior of the overall structure. At the same time, the structural model needs to remain practical and numerically solvable in a reasonable amount of time. This conflict is dealt with in this dissertation.

The acoustic behavior of electric machines is strongly coupled to the vibrational behavior of the electric machine stator. In order to avoid eddy current losses, the stator iron core consists of a stack of laminated steel sheets. The stator slots are filled with copper windings which are typically fixated by an impregnation resin. The microscopic representation of the heterogeneous stator structure is elaborate and requires a large computational effort. Therefore, so-called homogenized substitutional materials are typically employed in structural dynamical simulations of electric motors. The homogenized materials intend to represent the effective stiffness and damping properties of the underlying heterogeneous structure by a transversely isotropic or orthotropic substitutional material. Typically, the corresponding effective stiffness and damping properties of the homogeneous material are reversely obtained from experimental investigations on the particular structure. However, this approach is very time-consuming, expensive and above all, presumes physical prototypes that can be tested. In this thesis, different so-called homogenization techniques will be investigated that allow the identification of homogenized material properties based micromechanical models of the underlying heterogeneous structure. Therefore, classic numerical approaches will be compared to various analytic approaches and validated, based on the different experimental analyses on an exemplary stator structure. The resulting modeling approaches of the stator' structural components will subsequently be employed in a comprehensive acoustic simulation of an entire electric drive train.

However, the simulation and optimization of the mostly broadband acoustic behavior of electric motors remains time-consuming. In order to efficiently predict the acoustic behavior of electric machines the use of model order reduction methods can be advantageous. Model order reduction methods typically involve mathematical algorithms that yield the effective reduction of the model's degrees-of-freedom. In this thesis, different model order reduction

techniques will be applied and evaluated regarding their usability in the area of vibrational simulations of electric machines. One of the most frequently used model order reduction techniques is the mode superposition method. In this thesis, it will be shown that, due to the complex electromagnetic load cases that occur inside the electric machine, the vibrational behavior of the structure can only sufficiently be represented by the mode superposition using elaborate and time-consuming correction algorithms. In contrast, a particularly efficient model order reduction could be achieved by using so-called KRYLOV-subspaces. By employing the KRYLOV-subspace method the solution time for particular operation points of the electric machine could be reduced to less than 10% of the original solution time.

The integrated modeling procedure, presented in this thesis, yields the sustainable and efficient representation of the vibrational behavior of electric machines. It allows the early phase evaluation and optimization of the acoustic behavior of different electric machine designs. This thesis differs from similar research so far that a generic approach was used to make the representation of the global dynamic behavior of the electric machine possible. The process includes micromechanical models which add a unique robustness and sustainability to the approach.

Table of Contents

List of Figures

List of Tables

1. Introduction

1.1. Motivation

Acoustic vehicles are everything but naturally silent.

How do electric cars sound? And how should electric cars sound like? The interior and exterior sound profile of conventional cars is one of the most crucial criteria that determines the car's individual character. It determines emotions that are connected to the car. But what are the expectations to the sound of an electric car? Recently, THE ATLANTIC reported about the dream of silent cities coupled with the continuous growth of electromobility in large urban areas [1]. THE WALL STREET JOURNAL foresees electric cars to stop the „National Nightmare“ caused by noise emitted by conventional cars [2]. Others see a big danger in electric cars being noiseless. Already in 2009 THE NEW YORK TIMES and THE WASHINGTON POST entitled „The Silence of Hybrids Causes Some Alarm“ and „The Deadly Silence of the Electric Car“ [3, 4]. Apparently, electric cars are expected to be absolutely noiseless. However, the expectation of a zero noise emission of electric cars puts the automobile industry under big pressure. Because electric vehicles are everything but naturally silent.

The natural sound character of an electric car is majorly determined by the sound of the electric traction machine that drives the car. The investigation of noise emitted by electric motors is a well known topic. Already in 1949 JORDAN published design guidelines that yield the noise reduction of squirrel cage electric motors [5]. In the following years many researchers like GIERAS, TIMAR or YANG (just to name a few) have continuously extended these investigations for all kinds of electric machine technologies [6–8].

However, facing the fast development of electromobility and the corresponding requirements of car manufacturers regarding light weight design and dynamic speed and torque spectra, the acoustic behavior of modern electric motors is becoming more relevant than ever before. In conventional cars powered by an internal combustion engine the noise emissions emitted by the drive train could well be masked by the wind and rolling noise. However, the frequencies that are excited by the electromagnetic forces inside electric motors are much higher and cause narrowband tonal noise emission. Inside the vehicle interior the audible high-pitched sound which is emitted by the electric motor leads to an unpleasant acoustic atmosphere and significant comfort losses.

What role the electric machine's structure plays.

In order to develop electric cars that satisfy the customer's expectations, the sound of the electric drive train needs to be continuously considered and evaluated throughout the entire product development process. However, the acoustic character of an electric car is often fully assessable only in later design phases when large design changes are typically no longer possible. In order to early gain information about the acoustic behavior of a newly developed electric car, simulations can be helpful.

In Figure 1.1 the conversion process of electric energy into sound energy is illustrated. It contains three almost independent domains, the electromagnetic system, the mechanical system, and the acoustic environment. Assuming an exemplary electric traction machine with a given electromagnetic configuration that satisfies the machine requirements regarding torque, power and efficiency and a given acoustic environment which is characterized by the circumferential car body, the acoustics of the electric machine is exclusively determined by the vibrational behavior of the electric machine structure. The sound power Π that is caused by the electromagnetic force excitation f can be calculated using the basic equation of machine-acoustics which is defined as

$$\Pi(\omega) = \rho_a \cdot c_a \cdot \sigma_A(\omega) \cdot A \cdot h_t^2(\omega) \cdot f^2(\omega) \tag{1.1}$$

with ρ_a and c_a as the density and sound velocity of air, respectively, $\sigma_A(\omega)$ as the frequency-dependent acoustic radiation loss factor, A as the sound emitting machine surface, and h_t as the structural transfer admittance [9].

The frequency-dependent structural transfer admittance h_t which quantifies the relation between the exciting load and the effective surface velocity depends on the structural properties of the machine including stiffness, mass and damping. Thus, presuming linearity and a specific electromagnetic load inside an electric machine, the structural transfer admittance acts as a simple linear transfer function that determines the surface vibration and hence the acoustic behavior of the machine.

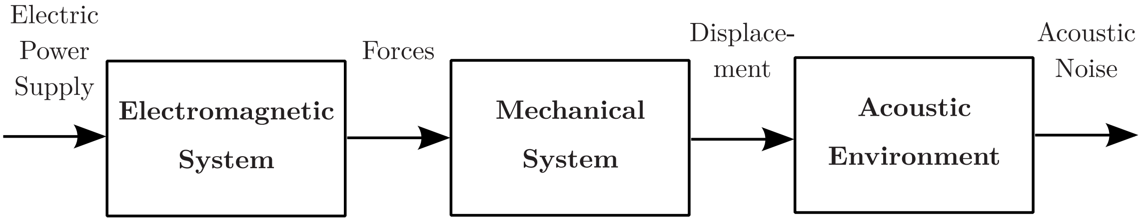

Figure 1.1.: Conversion process of electric into acoustic energy in electric motors [6].

The electric machine's stator as the crucial component.

The vibrational behavior of electric motors is strongly coupled to the vibrational behavior of the stator. It significantly contributes to the overall stiffness and mass of the machine and thus determines the dynamic response of the system towards electromagnetic force loads. The stator iron core is usually made of silicon steel sheets which are axially laminated in order to reduce eddy current losses. Inside the stator slots, copper windings coils that carry the electric current are located. Due to the heterogeneous structure of the stator, the prediction of the structural transfer function of the electric motor is difficult. In most scientific works that deal with the numerical investigation of the acoustic behavior of electric motors, the stator structure is significantly simplified and the corresponding material data is obtained from model updating algorithms or based on experience. Thus, if geometrical parameters like the yoke thickness, production parameters like the normal lamination prestress, machine requirements like the minimum operation temperature, or material parameters like the damping properties of the impregnation resin change, the material properties obtained from model updating lead to erroneous simulation results. Hence, the effect of any design change on the overall acoustic behavior of the electric machine can not reliably be evaluated. However, design engineers need reliable simulation results in order to generate optimal solutions.

In order to satisfy these requirements, generic and transferable modeling approaches need to be established. These approaches need to be capable of representing the effect of all relevant design changes towards the acoustic behavior of the electric motor. At the same time, the simulation process needs to be efficient in order to quickly compare different machine configurations at various operation points. This conflict is dealt with in this thesis.

1.2. Scope and Goals of this Thesis

Structural simulation - A trade-off between accuracy and computational effort

Multiple scientific works have investigated ways and methods that yield the acceleration of the computation time of structural simulations of electric machines [10–31]. However, most measures reducing the simulation time are achieved by major simplifications that automatically cause a loss of accuracy and significance. Thus, the effect of numerous design parameters like the slot fill ratios or the axial prestress of the laminated steel stacks are numerically not evaluable but were found to influence the vibrational and thus the acoustic behavior of the electric motors.

In order to appropriately consider the heterogeneous structure of electric machines inside numerical simulations, homogenized homogenization can be applied. Homogenization yield the representation of the mechanical behavior of a heterogeneous composite material by a substitutive homogeneous material with the same effective stiffness and damping behavior. Using homogenized models of the composite materials, the effect of microscopic design changes inside the composites on the overall vibrational behavior of the system can efficiently be evaluated. The use of homogenized, transversely isotropic or orthotropic materials for the representation of the structural dynamic behavior of electric machine components is standard procedure. It has successfully been applied in multiple investigations [20, 32–37]. However, in most applications the effective properties of the homogenized material are iteratively obtained by an automatic correlation process based on the results of an experimental modal analysis [21, 38]. Multiple investigations focus on the identification of the transversely isotropic material properties of the stator iron core while the copper windings are fully neglected [39–46]. However, it can be shown that the copper windings, especially the end windings, significantly influence the mass, stiffness and damping of the structure and thus need to be considered [21, 32, 47–55].

How to obtain effective material properties when no prototypes are around.

In this thesis, an integrated approach is presented that allows the quantification of effective material properties from the properties of the underlying constituent materials based on micromechanical models. In contrast to other scientific works, the developed approaches yield a fully generic and parameterizable method which can easily be adapted to different electric motor configurations and thus is capable of numerically representing the effect of any possible design change. The presented approach allows the consideration of viscoelasticity and stator segmentation effects which both can fundamentally influence the dynamic behavior of the structure as will be shown in this thesis. Based on a generic non-linear stress-strain contact formulation, that was developed in this research work, a micromechanical model of the stator iron core can be formulated. This allows the reliable quantification of effective material properties of laminated steel even for resin-impregnated laminated steel. Most scientific works that involve the numerical prediction of electric machine acoustics consider the damping of the structure in an integral sense e.g. by using global damping ratios which are mostly empirically quantified [6, 36, 56]. However, in order to reliably predict absolute acoustic values, damping needs to be treated as a local field variable inside the system. Therefore, in this thesis, the homogenization techniques that are usually applied to provide effective stiffness values are extended to the representation of damping in order to quantify the effective directional damping properties of the composite materials.

How to accelerate the acoustic simulation process.

Even though the structural model based on homogenized materials can numerically be solved very efficiently by modern solvers, the number of operation points that need to be considered to entirely evaluate the acoustic behavior of the electric motor can be considerably large. Thus, the overall computational effort can be significant. In order to efficiently calculate the broadband sound emission of electric motors at different operation points the use of model order reduction methods can be advantageous. Model order reduction techniques yield the mathematical reduction of the original system of ordinary differential equations which represents the dynamic behavior of the structure without truncating relevant effects. They can be separated into physical, generalized, and hybrid techniques.

One of the most frequently applied generalized model order reduction techniques is the mode superposition method. It is used and proposed in multiple scientific works that deal with the vibrational behavior of electric motors [26, 33, 57–63]. However, it was shown that the applicability of the mode superposition is naturally limited to systems with spatially simple load cases. In this thesis, it will be shown that due to the spatially complex load cases that occur in electric machines the mode superposition as it is traditionally applied can cause significant errors predicting the vibrational and thus acoustic behavior of the machine structure [64, 65]. Even the use of correction algorithms like the modal truncation augmentation method does not necessarily lead to a reduced error. In contrast, the KRYLOV subspace method, a further generalized model order reduction technique, will be found to provide good accuracy while significantly reducing the computational effort.

Physical model order reduction techniques neglect the degrees of freedom that do not contribute to the overall force response of the structure. The component-mode-synthesis (CMS) is a popular hybrid model order reduction that combines both, the reduction of physical degrees of freedom (DOF) as well as the transformation of physical coordinates into generalized coordinates. In this thesis the applicability of the CMS for the reduction of peripheral components will be investigated. These components, like the gear box or the rotor of the electric motor, do not necessarily contribute to the acoustic emission but need to be considered in order to correctly represent the system stiffness and damping.

Benefits and potentials of micromechanically-based simulation approaches.

Based on the straightforward generic modeling process of the electric machine components as well as the application of efficient simulation techniques, this thesis contributes to the evaluation of the acoustic behavior of electric motors in early project phases. It introduces strategies of how to efficiently but robustly predict the structural response of electric machines to an electromagnetic force excitation. Based on micromechanical models, the effect of each individual structural parameter on the global acoustic behavior of the electric machine can be evaluated. The application of appropriate model order reduction techniques provides a significant reduction of the overall computational effort by a moderate decrease of accuracy. The proposed simulation procedure thus allows the fast evaluation and optimization of specific design parameters regarding the acoustic behavior of the machine. It thus could for example be applied to determine the mechanical properties of an acoustically optimized impregnation resin.

1.3. Method and Structure

Premises.

The numerical investigations presented in this thesis are all based on the finite element method (FEM). The noise emitted by the system is mostly caused by small oscillation magnitudes at the structural surface. Thus, a numerically linear system behavior was assumed throughout this thesis which allows LAPLACE transformation and the solution inside the frequency domain.

The basic structure and assembly of an electric motor will be introduced in Section 2.1.1. The majority of investigation in this research work was performed on an exemplary internal permanent magnet machine (IPM) for mobile applications at BMW Group. However, most methods and findings presented in this thesis are generally transferable to any other electric motor.

The fundamentals of the acoustic phenomena in electric motors are dealt with in Section 2.1. It is well documented in literature that the stator path, meaning the acoustic emissions caused by the electromagnetic forces that act on the stator, is dominant over the rotor path. Thus, in this thesis, the stator path will be focused on.

Homogenization Techniques.

The general structure of stator cores of electric machines will be explained in Section 2.1.1. It consists of an axially laminated silicon steel core, axially oriented copper windings which are redirected at both ends of the stator representing the so-called end windings and a variety of different insulation materials. In order to numerically evaluate the influence of each constituent on the acoustic behavior of the system, homogenization techniques were employed in this research work. Section 2.5 is about different numerical and analytical homogenization techniques for both, laminated and fiber-reinforced systems. An advanced approach, the so-called method of cells (MOC), which is based on the analytic solution of a discrete micromechanical model, will be described in Section 2.5.3. It intends to satisfy both, the increased accuracy of a numerical approach and the reduced computational effort of an analytical approach. Unlike other analytical approaches, the presented MOC is adjustable to the representation of orthotropic effective properties which e.g. occur at segmented stator yokes. In order to gain detailed information about the micro-structural topology of inhomogeneous components e.g. the segmentation gap, different microscopic analyses of various cross sections were performed. In Chapter 3 the introduced homogenization approaches will be evaluated regarding accuracy and computational effort.

Viscoelasticity.

Thermosetting-materials commonly show viscoelastic behavior which results in frequency and temperature-dependent stiffness and damping properties. Thermosetting materials like the impregnation resin have been found to lead to frequency- and temperature-dependent stiffness and damping properties of the entire structure. The basic theory of viscoelastic materials will briefly be described in Section 2.4. In order to evaluate the effect of the impregnation resin on the overall structure, the viscoelastic properties were identified performing Dynamical-Mechanical-Analyses (DMA). In this research work, The DMA testings were performed using a commercially available GABO test apparatus. The corresponding master curves were generated using the software EPLEXOR. A corresponding modeling approach that is commonly used to represent viscoelastic behavior based on a Prony series will be introduced and validated in Section 3.1. Based on this approach, the viscoelastic character of the impregnation resin can be considered inside the homogenized material models. The effect of the resin on the overall structural behavior, especially the temperature- and frequency-dependent stiffness and damping properties, will be analyzed and evaluated in Chapter 4.

Validation.

The validation of the developed modeling approaches will be described in Chapter 4. Most of the validation in this research work was based on the correlation of an experimental and numerical modal analysis including the eigenfrequencies, mode shapes as well as the modal damping ratios. All modal analyses for the validation of the different modeling approaches were performed under free-free boundary conditions using common elastic strings and rubber bands for the support of the specimens. The test structures were excited by employing different electromagnetic shakers and a harmonic chirp signal with a step size of 5 Hz. The deflection of the specimen structure was measured using the one-dimensional Polytec PSV-400 laser scanning vibrometer (1D-LSV) which only quantifies the out of plane deflection parallel to the laser beam. The eigenfrequencies and corresponding mode shapes were identified by using the software Siemens LMS Test.Lab. The correlation between the numerically and experimentally mode shapes were supported by the software Siemens LMS Virtual.Lab.

Model Order Reduction.

The application of model order reduction techniques will be discussed in Chapter 5. The fundamentals of each model order reduction will briefly be introduced in Section 2.3. In Section 5.1, the component mode synthesis (CMS) will be employed for the reduction of ambient structural parts like the gear box. The most frequented model order reduction technique is the mode superposition method which will be discussed in Section 5.2. Two different types of mode superposition, namely the ordinary modal truncation method (OMTM) and the modal truncation augmentation method (MTAM) will be employed on the structure of an exemplary electric machine. In Section 5.3 a more advanced alternative model order reduction technique that is based on the use of Krylov subspaces will be applied and evaluated.

An overall discussion of the results and findings of this research work will be given in Chapter 6.

Additional Information.

All numerically applied material modeling methods, contact modeling methods, numerical homogenization techniques, modal analyses and model reduction techniques are implemented and commercially available in Ansys version 16.2. All applied analytical methods were implemented in Matlab. Due to confidential reasons, the viscoelastic material data of neither impregnation resin will be published in this thesis. Furthermore, no absolute values are given throughout the thesis. All stiffness and damping values are referred reference values which were held constant throughout the investigations and thus allow a relative interpretation of the results. However, the presented approaches are consistently provided in this thesis and can easily be adapted to any electric machine structure.

2. Fundamentals

2.1. Acoustics in Electric Motors

All electrified drive trains contain one or more electric motors that convert the electric energy provided e.g. by a battery or fuel cell into mechanical energy for the drive train. The choice of machine technology that is employed for the particular use case is mainly based on the set of performance requirements like durability, efficiency, speed-torque characteristics or power density but also maintenance effort, fully automated producibility and of course the manufacturing costs [66]. Today, the most commonly used technologies for traction motors in electric drive trains are induction and synchronous motors which can be divided into non-excited and and externally excited synchronous machines depending on the generation of the rotor magnetic field [67]. A special form of non-excited synchronous motors is the interior permanent magnet motor (IPM) which is applied for most of the analyses in this thesis. Nevertheless, the majority of investigations and findings of this thesis are transferable to any type of electric traction machine.

2.1.1. Electric Machines

All electric machines consist of a rotating part, the rotor, and a stationary part, the stator, which are separated by a small air gap. The common configuration of synchronous machines in electric drive trains contains an internal rotor that directly transmits the developed torque to the drive unit and an external stator that surrounds the rotating part and is fixated inside a machine housing. The driving torque is generated by electromagnetic forces that tangentially act on both components, the rotor as well as the stator of the electric motor.[68]

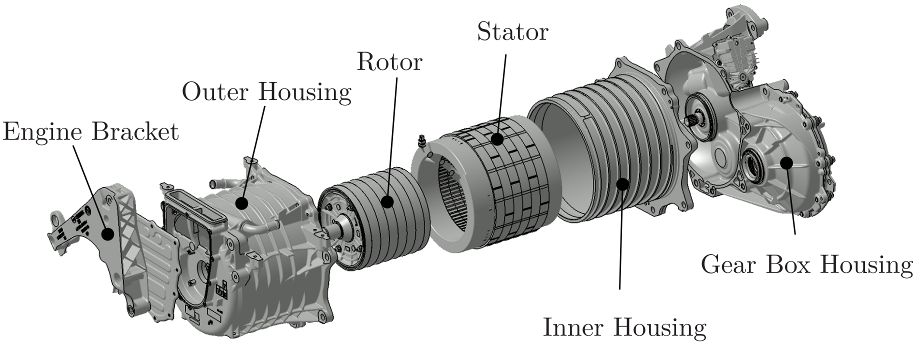

Figure 2.1.: Schematic view of the BMW i3 electric drive unit.

2.1.1.1. Electromagnetic Force Waves

This thesis focuses on the accurate prediction of the structural transfer admittance (see Equation 1.1). Considering the mechanic system (see Figure 1.1) the electromagnetic forces that work inside the structure can simply be considered as an input parameter. Nevertheless, the spatial distribution of the electromagnetic forces significantly influence the structural response of the motor. Therefore, a brief introduction into the basic principles of electromagnetic forces in synchronous machines will be given in this section. The theoretical background of electromagnetic forces in electric motors is extensively discussed and reviewed in multiple scientific works for example by Gieras or Timár et al. [7, 68]. The following explanations are inspired by Gieras.

The magnetic force vector field $\underline{f}$ that arises in electric machines can be obtained from the Maxwell stress tensor

$$\underline{f} = \int \left[\frac{1}{\mu_0} \underline{b} \left(\underline{b} \cdot \underline{n} \right) - \frac{1}{2\mu_0} \underline{b}^2 \cdot \underline{n} \right] dA \tag{2.1}$$

with μ_0 as the magnetic permeability of vacuum, b as the local magnetic flux density, and n as the local normal unit vector to the corresponding surface area A. The Maxwell stress tensor determines the relation between the actual force $\underline{f}$ that excites the structure and the magnetic flux $\underline{b}$. The force vector field is commonly calculated by means of numerical methods, commonly the FEM. In order to reduce the computational effort the axial flux inside the machine is neglected and only radial and tangential components are considered. Thus, the force densities can be determined based on a two-dimensional model.

Performing a Fourier transform the magnetic forces along the the circumference of the rotor can be decomposed into a series of harmonics sine- and cosine-waves that oscillate with an angular frequency ω

$$F(x,t) = \sum_{r=1}^{\infty} \left(\left(A_r \cdot \sin\left(\omega t\right) + B_r \cdot \cos\left(\omega t\right) \right) \right) \cdot \left(C_r \cdot \sin\left(r \frac{2\pi x}{x_a} \right) + D_r \cdot \cos\left(r \frac{2\pi x}{x_a} \right) \right) \tag{2.2}$$

with A_r, B_r, C_r, and D_r as generic magnitude variables of the waves that correspond to the particular circumferential spatial order r. This equation can be rewritten as

$$\begin{aligned} F(x,t) = \sum_{r=1}^{\infty} \Bigg(& F_{r,fw,im} \cdot \cos\left(\omega t + r \frac{2\pi x}{x_a} \right) + F_{r,bw,im} \cdot \cos\left(\omega t - r \frac{2\pi x}{x_a} \right) + \\ & F_{r,fw,re} \cdot \sin\left(\omega t + r \frac{2\pi x}{x_a} \right) + F_{r,bw,re} \cdot \sin\left(\omega t - r \frac{2\pi x}{x_a} \right) \Bigg) \end{aligned} \tag{2.3}$$

Thus, two groups of independently rotating spatial force waves result, the first one rotating in the same direction as the fundamental stator magnetic field (forward-rotating waves) and the second one rotating in the opposite direction (backward-rotating waves) [6].

In Equation 2.3 x_a denotes the arc length after which rotational symmetry occurs. In ideal cases of synchronous machines, if for example perfect coaxiality of rotor and stator is assumed and no fractional slot winding occurs, x_a is equal to the pole arc length.

$$x_a = \frac{2\pi r}{2p} \tag{2.4}$$

Thus, for those cases the minimum force wave harmonic, the so-called fundamental space harmonic, equals the number of poles. The fundamental space harmonic as well as its higher harmonics are all oscillating forces with a mean value of zero. These force waves do not contribute to the torque development but lead to an oscillating excitation of the stator causing noise emissions. In synchronous machines the frequency of each force wave is proportional to the rotational speed of the rotor. Thus, the force harmonics are also referred to as engine orders and are numerated by the factor to which the excitation frequency is faster than the rotational speed of the rotor e.g. the 72^{nd} engine order (EO).

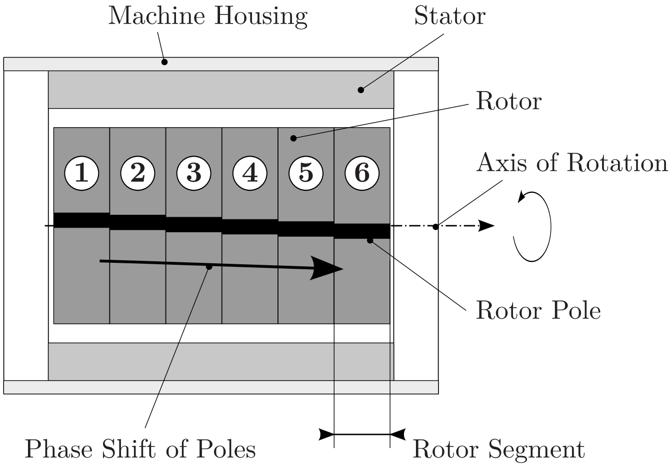

Figure 2.2.: Side view of electric machine including rotor with stepwise twisted, stator and housing.

Skewing In order to reduce the torque ripple that may result from tangential higher force harmonics, skewing or shifting of permanent magnets can be applied [69]. Both measures yield the phase shifting of the force waves over the axis of the machine so that at any instant of time the torque ripple that occurs inside a particular segment of the rotor is equaled out by the torque ripple inside a different segment. Skewing can be applied to stator slots as well as to the rotor even though this would involve the continuous skewing of magnets. An easier way to modulate the rotor is to shift the permanent magnets (see Figure 2.2). In shifted rotor configurations discrete rotor segments are axially arranged and stepwise twisted in order to achieve a similar effect as skewing.[6]

The mechanical design of permanent magnet synchronous machines is very individual. Nevertheless, some general design principles are recurrent. The following section provides an overview of some mechanic design standards. However, it is inspired by the particular electric motor that will be investigated later in this thesis. A good overview of some general design standards, in particular of different insulation techniques and materials, can be found in [70]. Some practical remarks on electric motors that are particularly used in electric drives can be found in [71].

2.1.1.2. Stator Structure

The stator is one of the two so-called active components inside electric machines.

Its core consists of laminated steel sheets, mostly made of silicon steel, that are usually less than 1 mm thick. Figure 2.3 shows the cross section of an exemplary stator iron core. It consists of teeth and a yoke. The circumferential part of the iron core, the yoke, can either be continuous or segmented. A segmentation of the yoke can be advantageous regarding the industrial production of the stator e.g. during the press cutting process or the assembly process of stators with concentrated windings. Each single steel sheet is insulated by a thin coating in order to avoid axial flux between the sheets. The laminated steel sheets are held

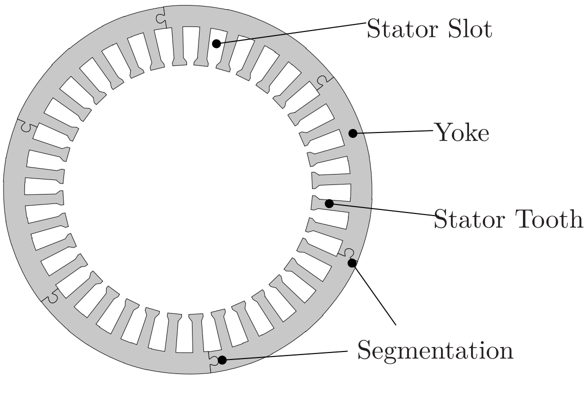

Figure 2.3.: Schematic cross section of stator iron core.

together using rivets, bolts, or edge welding. The so-called stacking factor denotes the relative volumetric amount of silicon steel inside the laminated stack. In order to avoid motion between the sheets and to increase the stacking factor the stack is exposed to a normal pressure.

The slots of the stator iron core are filled with windings. Since the windings carry electric current they are mostly made of copper, sometimes of aluminum [70]. There are three basic types of stator winding structures [70]:

- Random-wound stators
- Form-wound stators using multiturn coils
- Form-wound stators using ROEBEL bars

In most applications random-wound stators are used. Their windings consist of round wires that are individually insulated by a thin coating. Typically many small wires are used in order to avoid parasitic effects like the skin effect or eddy current losses inside the windings. The active windings that are located inside the stator slots are connected to the so-called end windings on both sides of the stator core. Usually the end windings are just a circular conglomerate of coils that were redirected between two slots. Each winding coil needs to be electrically separated from the grounded stator iron core. This is provided by a so-called ground insulation or slot cell. Currently all larger original equipment manufacturers (OEM) are using various types of mica papers to maintain the ground insulation [70]. If two phase coils are located along each other, e.g. if more than one phase is located inside one slot, the phases need to be electrically insulated by a phase separator. This can also be provided by mica papers. In addition to the ground and phase insulation, the windings are impregnated using a thermosetting polymer resin. The resin fixates the windings in place and maintains the heat removal from the windings. Furthermore, it mechanically supports the end windings. In most impregnation processes the entire structure is simply dipped into a tank of liquid resin. Thus, all parts of the stator are exposed to the resin. The thermosetting process of the resin is usually activated by heat, catalysts, hardeners or radiation.[70]

2.1.1.3. Rotating Parts

The second active component inside an electric machine is the rotor. The iron core of the rotor is also laminated. Depending on the technology that is used to generate a magnetic field that interacts with the rotating stator magnetic field, synchronous electric motors can be divided into different groups. Permanent magnet machines contain permanent magnets that consist of a special magnetized material, usually a mixture of common and rare-earth metals. The permanent magnets can either be buried in the rotor core or located at the surface. Synchronous machines contain axially aligned windings that are fed with a direct current in order to generate a magnetic field. The current can either be provided by slip rings or contactless via an induction coil. A centrally located shaft transfers the developed torque to the attached driven shaft of the car. The rotational degree of freedom of the rotor is provided with bearings. Both, the laminations as well as the bearings are mostly press-fitted onto the shaft. Analogue to the stator, the laminated steel sheets are held together using rivets, bolts or edge welding.

2.1.1.4. Housing and Peripheral Components

Both, rotor and stator are surrounded by a housing structure. If weight is of interest the housing is made of aluminum, otherwise of steel. A major function of the housing structure is to support the stator and rotor and reliably maintain coaxiality. Since the air gap between the rotor and stator is typically very small in comparison to the overall dimensions of the machine, a sufficient static and dynamic housing stiffness is a central requirement. The stator as well as the outer bearing rings of the rotor are usually press-fitted into the housing enabling a frictional transmission of the torque. Due to a variety of different energy dissipation mechanisms inside the machine, cooling is necessary. In case of a liquid cooling the housing contains small pipes in which the cooling medium circulates. If air cooling is applied, the heat is conducted to the outer surface of the machine where it is absorbed by the surrounding air. Often cooling fins are attached to the housing surface in order to increase the radiating area.[68]

In most automotive applications the traction machine is directly attached to the gear box that converts the torque and rotational speed. Sometimes both entities, the gear box and the electric motor, share a mutual housing. The entire drive unit of electric machine and gear box is mechanically attached to the car body, thus providing a proper support.

2.1.2. Vibration Characteristics of Electric Motors

2.1.2.1. Free Vibration Analysis of Cylindrical Structures

The dynamic response of electric motors towards electromagnetic forces waves is determined by the vibrational behavior of the electric machine stator. Based on its iron core and copper windings, the stator substantially contributes to the overall stiffness and weight of the machine. Since the stator is basically a cylindrical structure, the dynamic behavior is often referred to the dynamic behavior of a plain cylinder. The generic modal behavior of plain cylindrical structures is schematically illustrated in Figure 2.4. It shows the first 6 circumferential mode shapes ($r = 0 \ldots 5$) that radially oscillate. The radial modal deflection field $u(x,t)$ can mathematically be expressed as

$$u(x,t) = u_{re,r_i,\omega_i}\cos(r_i\varphi + \omega_i t) + u_{im,r_i,\omega_i}\sin(r_i\varphi + \omega_i t) \tag{2.5}$$

denoting generic standing waves with the spatial order r and the magnitudes u_{re,r_i,ω_i} and u_{im,r_i,ω_i} [8].

The decomposition of the modal behavior of stator cores is extensively analyzed in [49].

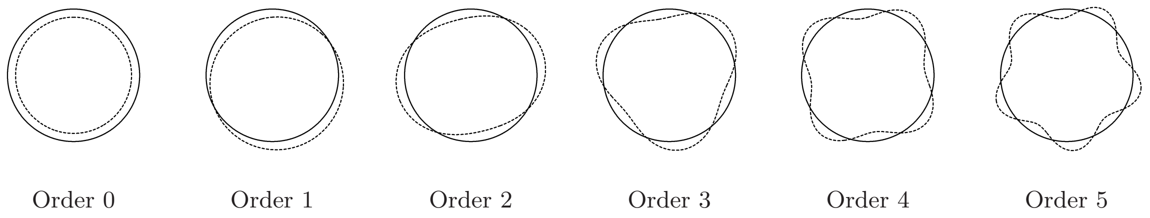

Figure 2.4.: Generic circumferential mode shapes of cylindrical structure [8].

Aside from the circumferential modal behavior, the oscillation of the stator along its axis can be phase-shifted. The resulting axial deflection field is independent from the circumferential mode shapes and hence determines a second dimension of the spatial mode shapes of cylindrical structures. The axial deflection shapes are illustrated in Figure 2.5.

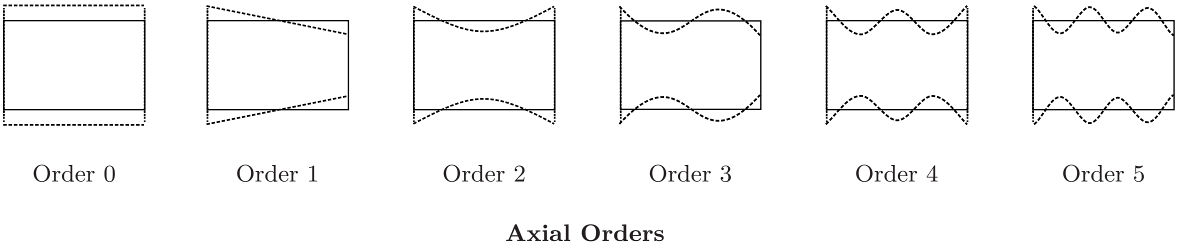

Figure 2.5.: Generic axial mode shapes of cylindrical structure [8].

The axially shifted mode shapes particularly become relevant if the electromagnetic forces acting on the stator are phase shifted over the axis of the machine e.g. in skewed machines. In the following, the mode shapes of the stator are denoted with two digits where the first one refers to the circumferential and the second one to the axial spatial order, e.g. mode shape 2.1 for the second circumferential and the first axial spatial order.

2.1.2.2. Forced Vibration Characteristics of Electric Motors

In Section 2.1.1.1 the forward and backwards-rotating force waves were introduced. These force waves act on the stator as well as the rotor. Due to the high radial stiffness of the rotor, the local distribution of circumferential forces that act on the rotor is negligible. Since the vectorial integral of each radial force wave around the circumference of the rotor is equal to zero, the total radial excitation of the rotor is also zero. Thus, most literature studies that investigate the acoustic behavior of electric machines focus on the stator vibrational transfer path [6, 29, 72–74]. Nevertheless, there are acoustical phenomena that are connected to the dynamics of the rotor e.g. in case of significant torsional vibrations, unbalances or eccentricity [6, 36, 75–82]. Based on the assumption of perfectly symmetric electromagnetic excitations this thesis focuses on the stator vibrational transfer path. In multiple publications, acoustic investigations are reduced to only considering the radial forces acting on the stator [29–31, 33, 60, 83–88]. However, further publications have proved that the consideration of tangential forces leads to an increased accuracy regarding the prediction of noise emission [89–91]. In this thesis both, the radial as well as the tangential force excitations will be taken into account. Based on the assumption of a negligible axial flux, the majority of electromagnetic FEM simulations are two-dimensional, which leads to a significantly reduced computational effort. Thus, axial forces will be neglected in this thesis. If skewing or shifting of permanent magnets (see Section 2.1.1.1) is applied the axial variation of the electromagnetic field can be represented by discrete axial segments with individual force wave fields [92] which will be employed in this thesis.

In Section 2.1.1, the structure of a common slotted stator of a synchronous machine was introduced. Its laminated iron core consists of a circumferential yoke and radially oriented teeth. In contrast to the yoke, the resistance of the stator teeth towards bending in tangential direction is very high. Thus, the previously introduced circumferential spatial order modal vibrations of the stator are only provided by the bending of the compliable part of the yoke between the teeth. This only applies for the tangential bending of the structure, not for the axial. Thus, the stator teeth can, in terms of tangential bending, be treated as almost rigid and the radial force field can be integrated to a resultant radial force vector for each single tooth. Since the stator forces mainly act on the tips of the stator teeth, all tangential parts of forces have coincident lines of action and hence can also be integrated to a resultant tangential force if the tangential compression of the tooth tip is neglected.[93]

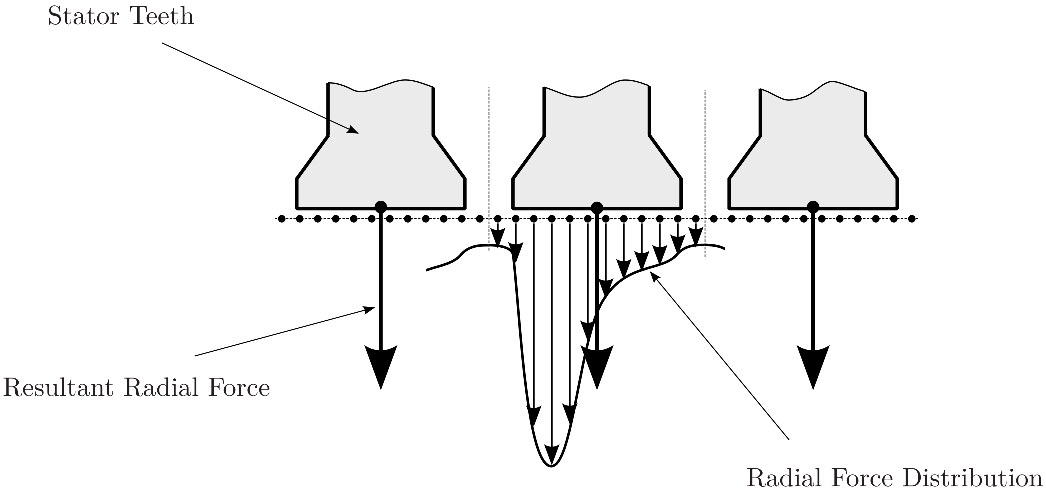

Figure 2.6.: Resultant radial force vector.

Considering the previously derived relations, the number of force vectors that act on one axial segment of the stator is equal to the number of stator teeth. Taking into account Nyquist's criteria, the maximum number of harmonic waves that can uniquely be decomposed by a certain number n of discrete points is $n/2$. Hence, the maximum circumferential force harmonic that can be represented by the number of teeth s is $s/2$. This leads to the phenomenon that higher harmonic spatial force waves excite lower order circumferential structural mode shapes. A deeper explanation of this effect can be found in Section 5.2.2.

2.1.2.3. Equivalent Radiated Power

In Figure 1.1, the conversion process of electric energy to acoustic energy was illustrated. The time-space-decomposition of the electromagnetic force excitation was discussed in Section 2.1.1.1. This thesis focuses on the mechanical system. It yields the accurate prediction of the displacement field of the electric motor as a response to distinct electromagnetic excitation.

However, the representation of the real system in a numerical model is always connected to assumptions and simplifications. Hence, the simulated displacement field will never exactly match the displacements that can be measured on the real structure. Thus, it is necessary to focus on the correct modeling of the displacements that are acoustically relevant.

The sound emissions inside the car that can directly be traced back to the force excitation within the electric motor can be separated into two parts [7]:

1. **Air-borne sound**, that is emitted at the surface of the electric machine
2. **Structure-borne sound**, that is mechanically conducted through the connection of the electric motor to the car body.

Both transfer paths are relevant for the acoustic behavior of the electric car, whereas the higher the frequency of the excitation the more dominant the air borne transfer path gets [94].

In order to predict the sound pressure field, numerical approaches can be applied. Most popular techniques are the boundary element method (BEM) and the finite element method (FEM) which becomes more and more powerful due to modern computational resources. Nevertheless, numerical predictions are still very time-consuming and elaborate due to complex material behavior.

A more convenient way to predict the sound emission of electric machines is to apply analytical techniques. Multiple researchers have investigated the relation between the radiated sound power at the machine surface Π_0 and the sound power at a particular distance to the machine Π, the so-called sound radiation efficiency σ

$$\sigma(\omega) = \frac{\Pi}{\Pi_0}. \tag{2.6}$$

These investigations are mostly based on the assumption of a cylindrical sound source [5, 6, 8, 56, 95–99]. However, all different techniques, numerical and analytical, are based on an accurate prediction of the displacement field at the machine surface.

An integrated value that considers the surface displacement field is the equivalent radiated power (ERP) Π. The ERP is the integrated sound power that is emitted by the structure surface A

$$\Pi = \sigma \rho_a c_a \int_A v_{eff}^2 dA. \tag{2.7}$$

where ρ_a and c_a are the density and the sound velocity of air, respectively, and v_{eff} is the root-mean-square of the normal surface velocity [9]. In this thesis the ERP with a unit radiation efficiency $\sigma(\omega) = 1$ will be used in order to evaluate structural model accuracy in terms of acoustically relevant displacements.

2.2. General Structural Dynamics

The linear dynamic behavior of complex continuous systems can be described by a set of differential equations. The dynamic analysis of these systems requires the solution by numerical procedures. Therefore, the set of differential equations of the continuous system needs to be substituted by a set of numerically solvable, algebraic equations that describe the linear dynamic behavior of a discrete system, a finite element model.[100]

2.2.1. Forced Vibration Analysis

The general equilibrium equation of a damped linear dynamic problem is given as

$$\underline{K} \cdot \underline{x}(t) + \underline{C} \cdot \underline{\dot{x}}(t) + \underline{M} \cdot \underline{\ddot{x}}(t) = \underline{f}(t). \tag{2.8}$$

in which the mass matrix $\underline{M}$, the damping matrix $\underline{C}$, and the stiffness matrix $\underline{K}$ denote the three system matrices while $\underline{f}(t)$ represents the excitation force load. In many engineering cases the input is not a single load vector $\underline{f}(t)$ itself but a set of different load vectors which can be given as a vector $\underline{u}(t)$ that contains the coefficients for a linear combination of a number of load vectors which are stored in the load vector matrix $\underline{\mathrm{F}}$

$$\underline{K} \cdot \underline{x}(t) + \underline{C} \cdot \underline{\dot{x}}(t) + \underline{M} \cdot \underline{\ddot{x}}(t) = \underline{F} \cdot \underline{u}(t) \tag{2.9}$$

$$\underline{F} = \left[\underline{f}_1,\ \underline{f}_2,\ \underline{f}_3, \dots,\ \underline{f}_k \right], \quad \text{with} \quad \underline{F} \in \Re^{n \times k}. \tag{2.10}$$

The system is called undamped if damping is neglected

$$\underline{K} \cdot \underline{x}(t) + \underline{M} \cdot \underline{\ddot{x}}(t) = \underline{F} \cdot \underline{u}(t). \tag{2.11}$$

The explicit formulation of the undamped system is given as

$$\underline{\ddot{x}}(t) = \underline{A} \cdot \underline{x}(t) + \underline{B} \cdot \underline{u}(t) \tag{2.12}$$

with $\underline{A} = -\underline{M}^{-1} \cdot \underline{K}$ denoting the system matrix and $\underline{B} = -\underline{M}^{-1} \cdot \underline{F}$ the scattering matrix of the explicit system. In order to investigate the harmonic response of the system Equation 2.12 is transformed into the frequency domain by LAPLACE transform

$$\omega^2 \cdot \underline{x}(\omega) = -\underline{A} \cdot \underline{x}(\omega) - \underline{B} \cdot \underline{u}(\omega) \tag{2.13}$$

where ω denotes the angular frequency of the system response [101]. The transfer function of the system $G(s)$ with $s = -\omega^2$ thus is given as

$$G(s) = \frac{u(s)}{x(s)} = (s \cdot \underline{I} - \underline{A})^{-1} \cdot \underline{B}. \tag{2.14}$$

The explicit formulation of the general equilibrium equation and its system matrices $\underline{A}$ and $\underline{B}$ are fundamental for the derivation of KRYLOV subspaces.

2.2.2. Free Vibration Analysis

In most dynamic problems the eigenfrequencies of the system are of interest. In order to quantify the system eigenfrequencies the undamped equilibrium equation under free vibration conditions

$$\underline{K} \cdot \underline{x}(t) + \underline{M} \cdot \underline{\ddot{x}}(t) = 0 \tag{2.15}$$

is solved using

$$\underline{x}(t) = \underline{x} \cdot e^{i\omega t} \tag{2.16}$$

which leads to the generalized eigenvalue problem

$$\underline{K}\underline{\phi}_i = {\omega_i}^2 \underline{M}\underline{\phi}_i. \tag{2.17}$$

The combinations of each eigen angular frequency ω_i and the corresponding eigenvector $\underline{\phi}_i$ is called eigenpair. In general, a system with n degrees-of-freedom (DOF) has n different solutions and hence n eigenpairs.

Using

$$\underline{\Phi} = \left[\underline{\phi}_1,\ \underline{\phi}_2,\ \underline{\phi}_3, \ldots,\ \underline{\phi}_n\right] \tag{2.18}$$

and

$$\underline{\Omega}^2 = \begin{pmatrix} \omega_1^2 & & \\ & \ddots & \\ & & \omega_n^2 \end{pmatrix};\ 0 \leq \omega_1^2 \leq \omega 2^2 \cdots \leq \omega_n^2 \tag{2.19}$$

Equation 2.17 can be expressed as

$$\underline{K} \cdot \underline{\Phi} = \underline{M} \cdot \underline{\Phi} \cdot \underline{\Omega}^2 \tag{2.20}$$

where $\underline{\Phi}$ denotes the modal subspace which will later be used in the mode superposition method. Since the norm of each eigenvector is scalable, it can be adapted to the mass matrix values in order to form the identity matrix $\underline{I}$

$$\underline{\Phi}^T \underline{M} \underline{\Phi} = \underline{I}. \tag{2.21}$$

This formulation is called the mass normalized formulation. Using the mass normalized formulation, the stiffness matrix can be transformed into a diagonal matrix which can be of use regarding the efficiency of the numerical solution

$$\underline{\Phi}^T \underline{K} \underline{\Phi} = \underline{\Omega}^2. \tag{2.22}$$

2.2.3. Damping

In contrast to Equation 2.11, real structures are always damped which means that mechanical energy is irreversibly converted into other forms of energy. Multiple effects can cause the irreversible energy loss in structures like microscopic friction processes inside materials, slip effects between two constituents of a composite material but also the energy loss of a system due to sound emission.

The most common modeling approaches for the representation of structural damping are viscous and hysteretic damping. The following derivations of different damping models are based on [102] and [103].

2.2.3.1. Viscous Damping

The functionality of multiple engineering applications is based on viscous damping like e.g. shock absorbers. The assumption of viscous damping leads to a very simple damping model in which the damping force $F_{c,v}$ is proportional to the velocity $\dot{x}$

$$F_{c,v} = c \cdot \dot{x}. \tag{2.23}$$

Damping Ratio Often the particularly measured damping value of a structure is referred to the so-called critical damping value c_c which defines the fastest way of the system back to equilibrium without overshooting based on viscous damping characteristics. The so-called damping ratio ξ is defined as

$$\xi = \frac{c}{c_c} \tag{2.24}$$

where c is the actual damping value of the structure.[102]

Proportional Damping Often the damping matrix $\underline{C}$ of the system is assumed to be proportional which means that it can be expressed as a linear combination of the mass matrix $\underline{M}$ and the stiffness matrix $\underline{K}$

$$\underline{C} = \alpha \underline{M} + \beta \underline{K} \tag{2.25}$$

where α and β are the so-called Rayleigh coefficients.

Modal Damping Ratio Assuming proportional damping the damping matrix can be transformed into the modal subspace by

$$\underline{\phi}_i^T \cdot \underline{C} \cdot \underline{\phi}_j = 2\omega_i \xi_i \delta_{ij};\ \delta_{ij} = \begin{cases} 1 & \text{if } i = j \\ 0 & \text{if } i \neq j \end{cases} \tag{2.26}$$

where ξ_i is the so-called modal damping ratio [100]. It corresponds to the previously introduced damping ratio which was given in Equation 2.24. The modal damping ratio that corresponds to a particular eigenpair can be identified from experimental modal analyses and hence is a frequently used value for the validation of a numerical model.

2.2.3.2. Hysteretic Damping

In contrast to the viscous damping, the damping force using a hysteretic damping model is not assumed to be frequency dependent but constant. The hysteretic damping force can thus be obtained from the corresponding viscous damping force by diving it by the angular frequency ω

$$F_{c,h} = \frac{F_{c,v}}{\omega} = \frac{c}{\omega} \cdot \dot{x}. \tag{2.27}$$

The hysteretic damping model hence is closer to the observations that were made on the investigations on the actual damping behavior of solid materials and structures [102]. The loss factor η, as a value for the hysteretic damping, will be introduced later in Section 2.4.

2.3. Model Order Reduction Techniques

From a computational perspective solving Equation 2.8 is very expensive since the system state vector $x(t)$ usually is very large in size. A practical way to decrease the computational effort is to reduce the degrees of freedom (DOF) of the system by substituting the system state vector $x(t)$ by a linear combination of a set of vectors that are contained in a transformation matrix X.

$$\underline{x}(t) = \underline{X} \cdot \underline{z}(t), \quad \text{with } \underline{X} \in \Re^{n \times p}. \tag{2.28}$$

Then the damped system of ordinary differential equations (ODE) 2.8 can be transformed into

$$\underline{\hat{M}} \cdot \underline{\ddot{z}}(t) + \underline{\hat{C}} \cdot \underline{\dot{z}}(t) + \underline{\hat{K}} \cdot \underline{z}(t) = \underline{\hat{f}}(t) \tag{2.29}$$

in which $\underline{\hat{M}} = \underline{X}^T \cdot \underline{M} \cdot \underline{X}$, $\underline{\hat{C}} = \underline{X}^T \cdot \underline{C} \cdot \underline{X}$, $\underline{\hat{K}} = \underline{X}^T \cdot \underline{K} \cdot \underline{X}$, $\underline{\hat{f}}(t) = \underline{X}^T \cdot \underline{f}(t)$, and $z(t)$ is the low-order system state vector in the generalized coordinate system [104]. Many model order reduction techniques follow that scheme using the so-called coordinate transformation matrix or projection matrix $\underline{X} \in \Re^{n \times p}$ in order to reduce the DOFs of the system from n to p with $p \ll n$. These model order reduction techniques are called generalized coordinate reduction techniques [104]. The transformation can also be effective in computational ways if the new system matrices $\underline{\hat{M}}$, $\underline{\hat{C}}$, $\underline{\hat{K}}$ have a better structure than the original matrices $\underline{M}$, $\underline{C}$, and $\underline{K}$ [100].

The error that is generated by the order reduction can be expressed as the difference between the state vector $\underline{x(t)}$ of the full order system and the state vector $\underline{x}_p(t) = \underline{X} \cdot \underline{z}(t)$ expanded from the reduced system [100]

$$\varepsilon(t) = \frac{\|\underline{x}(t) - \underline{X} \cdot \underline{z}(t)\|_2}{\|\underline{x}(t)\|_2}. \tag{2.30}$$

Without having to solve the direct integration system the error can be approximated by

$$\varepsilon(t) = \frac{\|\underline{F}(t) - (\underline{M} \cdot \underline{X} \cdot \ddot{\underline{z}} + \underline{C} \cdot \underline{X} \cdot \dot{\underline{z}}(t) + \underline{K} \cdot \underline{X} \cdot \underline{z}(t))\|_2}{\|\underline{F}(t)\|_2}. \tag{2.31}$$

2.3.1. Mode Superposition Method

The mode superposition method is probably the most frequently used model order reduction technique in dynamic analyses. Its basic principle is to transform the dynamic equilibrium equation into a more effectively solvable form by building the transformation Matrix $\underline{X}$ based on the eigenmode shape vectors $\underline{\phi_i}$ of the full order system [100]

$$\underline{X} = \left[\underline{\phi_1}, \ldots, \ \underline{\phi_n}\right]. \tag{2.32}$$

If proportional damping is assumed (see Section 2.2.3.1), the transformation into the modal coordinate system forms reduced system matrices that are diagonal so that mode superposition can be interpreted as substituting the response of the coupled multi-DOF-system by a linear combination of the responses of each individual mode

$$\underline{x}(\omega) = \sum_{i=1}^{n} \underline{\phi}_i \frac{\underline{\phi}_i^T \cdot \underline{F}}{\omega_i^2 + 2i\xi_i\omega_i\omega - \omega^2} \tag{2.33}$$

in which ω_j is the eigen angular frequency and ξ_j the modal damping ratio of the particular eigenmode [105]. Hence, the participation of a particular eigenmode to the overall frequency response is determined by the eigen angular frequency ω_j, the degree to which the load vector matrix $\underline{F}$ excites the eigenmode shapes vector ϕ_j, and the degree of which the eigenmode shapes vector $\underline{\phi_j}$ influences the desired response vector coordinate x_i.

The most time-consuming operation in performing the mode superposition is the acquisition of the eigenpairs of the system. The computational effort to perform the modal analysis is mainly determined by the number of DOFs of the full order system which becomes even more relevant if damping is considered. In most practical cases using the mode superposition method, the so-called modal truncation method is applied.[105]

2.3.1.1. Modal Truncation

In Figure 2.7, the dynamic response factor of a single-mass-oscillator is exemplarily mentioned. It can be divided into the under-critical area in which the angular excitation frequency ω is much lower than the angular resonance frequency ω_0, the resonance area in which the angular excitation frequency is close to the angular resonance frequency and the over-critical area in which the angular excitation frequency is much higher than the angular resonance frequency. In the under-critical area, the dynamic response factor is close to unity which represents a static response while for the over critical area decoupling takes place, meaning the dynamic response factor is approaching zero. Thus, assuming the dynamic excitation to be within a certain frequency range, eigenfrequencies that are far out of that range at most show static response.

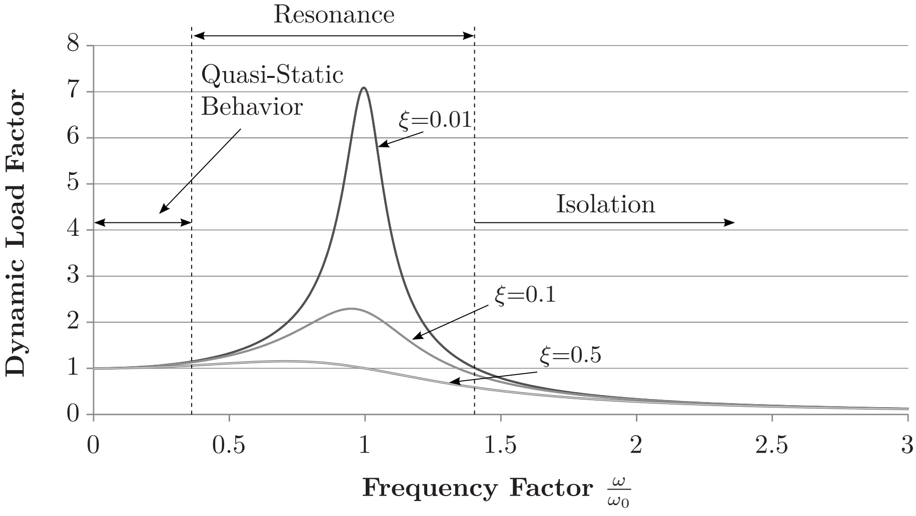

Figure 2.7.: The dynamic response factor of a single-mass-oscillator as a function of the angular excitation frequency ω.

Truncating those eigenfrequencies, the full system order n is reduced to a small number of considered eigenfrequencies p with $p \ll n$ which lie inside a certain frequency range. This method is referred to as the mode displacement method. The modal coordinate transformation matrix $\underline{X}$ is given as

$$\underline{X} = \left[\underline{\phi}_1, \ldots, \underline{\phi}_p\right] \subseteq \underline{\Phi};\ p \leq n. \tag{2.34}$$

As given for a load vector matrix in Equation 2.9 a particular dynamic load vector $\underline{f}(t)$ can also be separated into two parts where $\underline{f}$ is the invariant spatial part and $u(t)$ is the time varying portion

$$\underline{f}(t) = \underline{f} \cdot u(t). \tag{2.35}$$

Performing the standard modal displacement method the retained eigenfrequencies are exclusively selected based on the time varying portion $u(t)$ neglecting the spatial representation of the load vector by the selected eigenfrequencies. For complex load cases this negligence of the spatial representation can cause significant errors.[64] In the following section the modal truncation augmentation methods will be introduced. It intends to minimize the error caused by an insufficient spatial representation of the load case. The derivations are mainly taken from [65].

2.3.1.2. Modal Truncation Augmentation Method

The residual load case that results from an insufficient spatial representation of the load case within the modal subspace is given as

$$\underline{f}_r = \underline{f}_0 - \underline{f}_s. \tag{2.36}$$

where $\underline{f}_s$ is the part of the load case that is contained in the modal subspace and given by

$$\underline{f}_s = \underline{M} \cdot \underline{\Phi} \cdot (\underline{\Phi}^T \cdot \underline{f}_0). \tag{2.37}$$

The quasi-static response of the system to the residual force vector $\underline{f}_r$ yields a state vector $\underline{x}_r$

$$\underline{f}_r = \underline{K} \cdot \underline{x}_r. \tag{2.38}$$

Assuming the static displacement vector $\underline{x}_r$ to be a pseudo eigenvector of the system the stiffness and mass matrix can be transformed into these pseudo modal coordinate system using

$$\underline{\tilde{M}} = \underline{x}_r^T \cdot \underline{M} \cdot \underline{x}_r \tag{2.39}$$

and

$$\underline{\tilde{K}} = \underline{x}_r^T \cdot \underline{K} \cdot \underline{x}_r. \tag{2.40}$$

The Rayleigh-Ritz frequencies as well as the mass normalized pseudo eigenvector ϕ_r can be derived by solving the reduced eigenvalue problem

$$\underline{\tilde{K}} \underline{\phi}_r = \underline{\tilde{M}} \underline{\phi}_r \omega_r^2. \tag{2.41}$$

with ω_r as the pseudo-eigen-angular-frequency that corresponds to the pseudo-eigenvector $\underline{\phi}_r$. This procedure needs to be executed for each of the k spatial load vectors. All pseudo eigenvectors can be added to the retained modal subspace forming the new transformation matrix $\underline{X}_r$ by

$$\underline{X}_{mt} = \left[\underline{\phi}_1, \dots, \ \underline{\phi}_p, \ \underline{\phi}_{r,1}, \dots, \ \underline{\phi}_{r,k} \right]. \tag{2.42}$$

The order of the reduced system is then $p + k$.

2.3.2. Krylov Subspace Method

In the following section the use of Krylov subspaces as a model order reduction technique is introduced. A good overview of the basic principle and different algorithms that provide an orthonormal basis for the Krylov subspace is given in [106]. The use of Krylov subspaces for the model reduction in electric motors was already addressed in [107]. Nevertheless, this section provides a brief introduction into the main principle of Krylov subspaces in model reduction and an insight into one particular process that yields the generation of Krylov subspaces, namely the Arnoldi process [108]. The more detailed discussion can be found in [106].

2.3.2.1. Krylov subspaces

Krylov subspaces are basically all subspaces that satisfy the following

$$\underline{K}_k^r = span \left\{ \underline{v}, \underline{A} \cdot \underline{v}, \ \dots, \ \underline{A}^{k-1} \cdot \underline{v} \right\}, \quad \text{with} \ \ \underline{A} \in \Re^n \times \Re^n \ \ \text{and} \ \ \underline{v} \in \Re^n \times \Re^1. \tag{2.43}$$

with $\underline{K}_k^r$ as the Krylov subspace, $\underline{A}$ as a system matrix of the size $n \times n$ and $\underline{v}$ as a vector with the size $n \times 1$, where n denotes the number of DOFs of the system. Krylov subspaces were first introduced in 1931 by Alexei Krylov [109]. Today Krylov subspaces are mainly used for iterative solution methods [110] or the solution of large systems of linear equations [111]. Here, Krylov subspaces are used as the basic principle of a generalized coordinate model order reduction.

2.3.2.2. The Arnoldi Algorithm

As with increasing number of vectors within the Krylov subspace the vectors get almost linear dependent due to power iteration, an orthogonalization algorithm like the Arnoldi process needs to be applied. The Arnoldi process is one of different algorithms that generate an orthonormal basis $X \in \Re^n \times \Re^p$ for a given Krylov subspace. The main advantage of the Arnoldi algorithm over alternative approaches like the Lanczos algorithm is the stability of the process. The Arnoldi algorithm also works for $\underline{V} = [\underline{v}_1,\ \underline{v}_2,\ \underline{v}_3, \ldots,\ \underline{v}_k]$ with $\underline{V} \in \Re^{n \times k}$ and is then called block-Arnoldi.[106]

2.3.2.3. Padé and Padé-Type approximants

In Equation 2.14 the general transfer function of an undamped explicit system $H(s)$ was introduced. For a single-input-single-output system the general form of the transfer function in state space can be expressed as a rational function of the state space variable s

$$H(s) = \frac{a(s - z_1) \ldots (s - z_{n-1})}{(s - p_1) \ldots (s - p_n)} \tag{2.44}$$

where p_i are the poles and z_i the zeros of the transfer function. Like any rational function the general transfer function can be displayed by a Taylor series of s around an expansion point s_0

$$H(s) = \sum_{i=0}^{\infty} m_i (s - s_0)^i. \tag{2.45}$$

The coefficients of the polynomial m_i are called moments. The idea of Padé [112] and Padé-Type approximants [113] is to find a reduced order system of which the transfer function matches the first q moments of the transfer function of the full order system and therefore not exactly displays the transfer function for all different $s \in \Re$ but gives a good approximation of $H(s)$ around the expansion point s_0. Padé approximants match the maximum number of moments, $q = 2 \cdot k$, while Padé-type approximants match the first $q < 2 \cdot k$ moments. The projection matrix $\underline{X}$ that is the outcome of the Arnoldi process for the right Krylov subspace based on the system matrix $\underline{A}$ and the scattering matrix $\underline{B}$ of the explicit ODE (see Equation 2.12)

$$K_k^r \left\{ (A - s_0 I)^{-1}, (A - s_0 I)^{-1} \cdot B \right\} \tag{2.46}$$

produces a reduced system according to Equation 2.29 that matches the first k moments of the transfer function and therefore provides a Padé-type approximant

$$\hat{m_i} = m_i \quad \text{for} \quad i = 1,\ \ldots,\ k. \tag{2.47}$$

The use of Krylov subspaces hence assures the representation of the full system transfer in a certain frequency range by a system of lower order. Eid et al. showed that this also applies if proportional damping is added to the undamped system considerations [114].

2.3.2.4. The Principle of Multiple Expansion Points

The choice of the number of Krylov vectors as well as the choice of the expansion point can significantly influence the quality of the reduced order model in terms of accuracy at a particular frequency range. A procedure that yields the automatic identification of an optimal single expansion point is discussed in [115]. Alternatively, advanced procedures propose the use of multiple expansion points [116–119]. Bonin et al. introduce an adaptive method in which both parameters, namely the number of Krylov vectors per expansion point and the expansion frequency, are iteratively varied for multiple expansion points in order to optimally reduce the full system in terms of numerical reduction effort and numerical solution effort [120].

2.3.3. Component Mode Synthesis

The component mode synthesis (CMS) is a hybrid model order reduction technique since the reduced order model contains some physical and some generalized coordinates [104]. It yields the substitution of one or more parts of the structure by a reduced order model. In the following section, the main idea of the CMS will briefly be introduced. Even though more advanced types have been developed over the years, the introduction will be given based on the so-called fixed-interface method which still is the most frequently used form of CMS. A more detailed discussion and an overview of the various types of CMS can be found in [121].

The first step of the component mode synthesis is to define so-called master DOFs, mostly boundary DOFs, that remain as physical coordinates. All truncated physical DOFs are called slave DOFs.[1] The state vector $\underline{\mathrm{x}}$ can be divided into master and slave DOFs

$$\underline{x} = \begin{pmatrix} \underline{x}_m \\ \underline{x}_s \end{pmatrix}. \tag{2.48}$$

The fixed-interface CMS is mostly referred to as the Craig-Bampton method. Its basic principle is to extend the Guyan transformation matrix (see [122]) by a set of p normal modes that represent the dynamic behavior of the reduced structure

$$\underline{x} = \begin{pmatrix} \underline{x}_m \\ \underline{x}_s \end{pmatrix} = \begin{pmatrix} \underline{I}_m^{m\times m} & \underline{0}^{m\times p} \\ \underline{\Phi}_c^{s\times m} & \underline{\Phi}_n^{s\times p} \end{pmatrix} \cdot \begin{pmatrix} \underline{x}_m \\ \underline{z}_s \end{pmatrix} = \underline{X} \cdot \underline{z} \tag{2.49}$$

where $\underline{\Phi}_c^{s\times m}$ is the matrix of so-called constraint modes.

$$\underline{\Phi}_s^{s\times m} = \underline{K}_{ss}^{-1}\underline{K}_{ms} \tag{2.50}$$

Physically each constraint mode represents a static deflection of the structure due to a unity displacement of one boundary DOF while all other boundary DOFs are fixed and internal DOFs are free [104]. $\underline{\Phi}_n^{s\times p}$ is the retained modal subspace

$$\underline{\Phi}_n^{s\times p} = \left[\underline{\phi}_1,\ \underline{\phi}_2,\ \underline{\phi}_3, \ldots,\ \underline{\phi}_p\right] \tag{2.51}$$

with $\underline{\phi}_1 \ldots \underline{\phi}_p$ as the normalized eigenvectors of the component under fixed boundary conditions $\underline{x}_m = 0$. The reduced system is often referred to as a superelement. The order of the superelement is $m + p$. It can simply be used in usual FEM analyses coupling the master DOFs and thus the superelement to an ordinary finite element structure. Today, various types of CMS methods have been established using free-interface normal modes as well as so-called attachment modes. However, the fixed-interface-method based on fixed-interface modes plus interface constraint modes is numerically preferable and hence the most frequently used CMS method [121].

---

[1] Subscripts m and s refer to master and slave DOFs, respectively

2.4. Viscoelasticity

2.4.1. Linear Viscoelastic Material Properties

Typically polymers show a viscoelastic behavior. In this section, a brief overview of the basic principles of viscoelasticity, particularly linear viscoelasticity, will be given. Linear viscoelastic materials are characterized by a time-dependent but fully reversible reaction towards an imposed mechanical load [123]. The following relations are based on the assumption of a linear viscoelastic material behavior. A deeper insight and more detailed information about viscoelasticity can be found in [124] and [125]. A rather mathematical discussion can be found in [126]. The following explanations are mainly inspired by [124].

2.4.1.1. The Complex Modulus

In contrast to elastic materials which show a temperature- and time-independent linear stress-strain-relation given by HOOKE's law, the static response of linear viscoelastic materials is characterized by a time-dependent stiffness or compliance behavior that results in a relaxation or creep effect, respectively.

The uniaxial stress-strain relation of a viscoelastic material then is given as

$$\sigma(t) = \varepsilon_0 \cdot E(t) \tag{2.52}$$

where ε_0 is the internal strain at the time $t = 0$ and $E(t)$ the time-variant relaxation modulus.

If a dynamic strain $\varepsilon(t)$ is imposed, with

$$\varepsilon(t) = \varepsilon_0 \cdot e^{i\omega t} \tag{2.53}$$

as a complex load, the stress response of the material will be complex as well

$$\sigma(t) = \sigma^* \cdot e^{i\omega t} \tag{2.54}$$

with

$$\sigma^* = \varepsilon_0 \cdot E^*(i\omega) \tag{2.55}$$

and hence

$$\sigma(t) = \varepsilon_0 \cdot E^*(i\omega) \cdot e^{i\omega t} = \varepsilon(t) \cdot E^*(i\omega). \tag{2.56}$$

E^* is defined as the complex modulus with the real and imaginary part which are referred to as the storage modulus $E'(\omega)$ and the loss modulus $E''(\omega)$, respectively

$$E^*(i\omega) = E'(\omega) + i \cdot E''(\omega). \tag{2.57}$$

It was first introduced by HASHIN [127].

2.4.1.2. The Loss Factor

The tangent of the phase angle between the loss modulus and the storage modulus is a measure for the hysteretic inherent damping of the material. It is often referred to as the loss factor η

$$\eta = tan(\delta) = \frac{E''(\omega)}{E'(\omega)}. \tag{2.58}$$

The loss factor equals half of the damping ratio, $\eta = \xi/2$.[103]

2.4.2. Viscoelastic Material Model

2.4.2.1. General Time- and Temperature Dependency

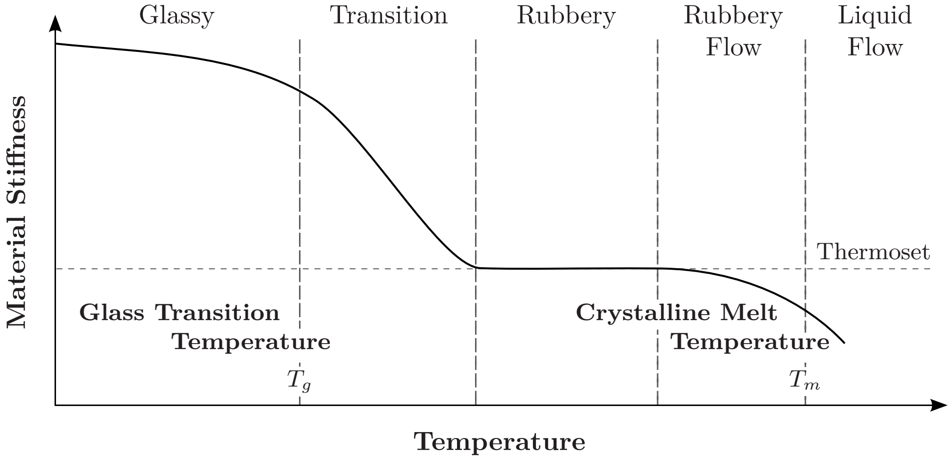

Figure 2.8.: Characteristic temperature-dependent stiffness behavior of polymer materials [124].

In Figure 2.8, the general temperature-dependent stiffness behavior of polymer materials is schematically illustrated. The temperature T_g is the so-called glass transition temperature. It denotes the temperature in which the molecular structure of the polymer changes and the maximum loss factor occurs. In stable engineering applications, only the glassy, the transition and the rubbery area are of interest while the rubbery flow as well as the liquid flow areas are to be avoided.

2.4.2.2. Prony Series

In order to represent the viscoelastic behavior of materials in structural simulations advanced material models need to be applied. The most frequented model that represents the previously introduced basic time- and temperature-dependency of polymers is the generalized MAXWELL model that is mathematically expressed by a PRONY series.

In Figure 2.9, the generalized MAXWELL model is schematically illustrated. It is a parallel connection of multiple individual MAXWELL elements. The storage modulus E' is then given as

$$E'(\omega) = E_\infty + \sum_j E_j \cdot \frac{(\omega\tau_j)^2}{1 + (\omega\tau_j)^2} \tag{2.59}$$

and the loss modulus E'' as

$$E''(\omega) = \sum_j E_j \cdot \frac{\omega\tau_j}{1 + (\omega\tau_j)^2} \tag{2.60}$$

where τ_j is the relaxation time and E_j the characteristic stiffness of each individual element.

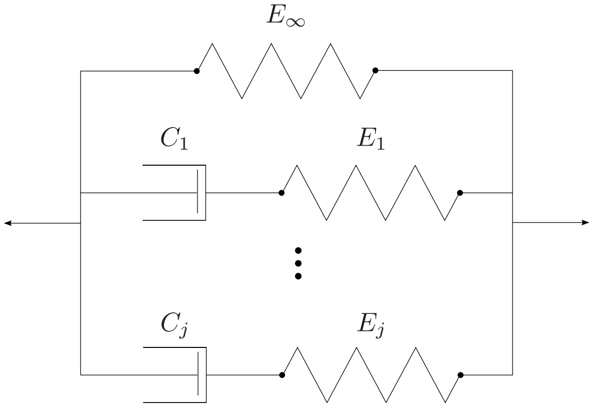

Figure 2.9.: Generalized MAXWELL model [124].

The characteristic curves for both, the storage and the loss modulus, are exemplarily given in Figure 2.10 for the simplest case of a generalized MAXWELL model with only one MAXWELL element connected in parallel to the spring, the so-called 3-parameter-model.

The storage modulus increases in a sigmoid shaped curve over the frequency starting from E_0. The loss modulus starts at zero, increases up to a distinct maximum at $\omega \cdot \tau = 1$ and then slowly declines.

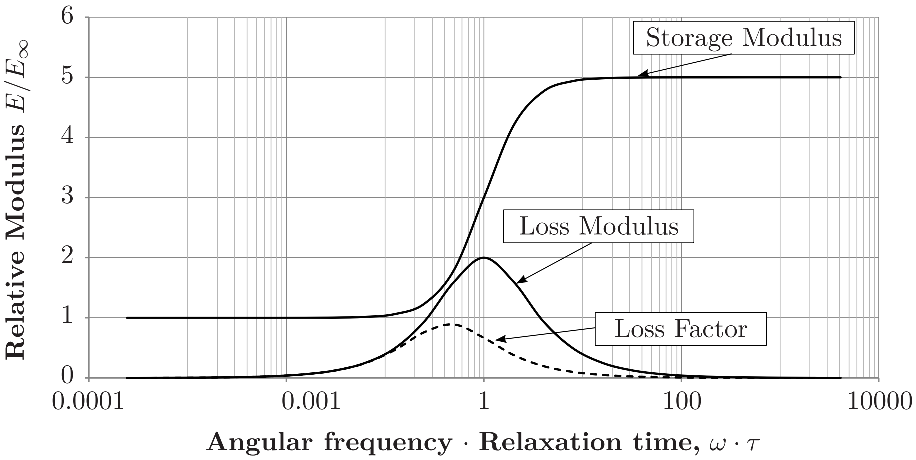

Figure 2.10.: Storage and loss modulus as well as loss factor as a function of the frequency for a 3-parameter model.

2.4.2.3. Time-Temperature Superposition

Due to their material-inherent characteristic structure, most polymers show an equal mechanical behavior with time and temperature. This phenomenon is called the time-temperature-superposition principle (TTSP). Polymers that behave this way are called thermorheologically simple [124].

The relation between the time and temperature domain can be expressed by the so-called shift factor α_T with

$$E(t, T) = E(t \cdot \alpha_T(T), T_0). \tag{2.61}$$

where T_0 is a reference temperature.

2.4.2.4. Williams-Landel-Ferry Function

Due to the standard measurement procedure of viscoelastic material properties (see Section 2.4.3), shift factors are typically only quantifiable at discrete measurement points. In order to obtain the shift factors between those discrete samples Williams, Landel and Ferry invented the following relation [128]

$$\log_{10}(\alpha_T) = \frac{-C_1(T-T_0)}{C_2+(T-T_0)} \tag{2.62}$$

with the two constants C_1 and C_2 based on the empirical investigation of different polymers. In the following, this relation will be referred to as the Williams-Landel-Ferry (WLF) function.

2.4.3. Identification of Viscoelastic Material Properties

In order to quantify the characteristic material properties of viscoelastic polymers numerous standard test applications exist. Multiple scientific papers have been published on various measurement procedures and applications. Most of them are listed and reviewed in [129] and to some extent in [125, 130]. The most frequently applied standard measurement technique is the the Dynamic-Mechanical-Analysis (DMA). It is extensively discussed in [131]. All measurement data of viscoelastic materials in this thesis are obtained by the DMA. A detailed introduction into the measurement procedure of the DMA as well as the subsequent identification of the time- and temperature-dependent material properties can be found in the Appendix of this thesis (see Appendix C.1.2).

The Poisson Ratio In the previous section, the basic principle of the time- and temperature-dependency of the compliance and stiffness of viscoelastic materials was introduced. For isotropic materials two independent material properties, for example the Young's and the shear modulus uniquely determine the total compliance or stiffness behavior. All further elastic constants like the Poisson ratio can be inferred from these two. However, for viscoelastic materials even small inaccuracies during the measurement especially inside the glass transition area can lead to significant errors or even unphysical stiffness properties of the material. The need of an accurate determination of the viscoelastic Poisson ratio as a crucial quality criteria has been addressed in various scientific publications [132–134]. The easiest way to avoid computational instability is the assumption of a constant Poisson ratio inside finite element simulations [132]. However, this simplification naturally leads to a decreased accuracy and a lack of significance [135]. Some more advanced but still computationally stable methods aim at the analytical description of the time and temperature-dependency of an elastic Poisson ratio. A general ansatz proposes the expression of the Poisson ratio by a Prony series which can be assigned to the basic principle of viscoelasticity. It was successfully employed and reviewed in multiple publications [132, 136–140]. However, the identification of the corresponding Prony parameters is elaborated and does not necessarily provide an optimal approximation of the measurement data (see Appendix C.2). A more convenient ansatz was proposed by Göhler expressing the complex Poisson ratio $\nu^*(\omega)$ by sigmoid function based on four independent parameters

$$\nu^*(\omega) = \nu_\infty + \frac{\nu_0 - \nu_\infty}{1 + exp\left(10 \cdot \frac{log_{10}(\omega)-b}{m}\right)}. \tag{2.63}$$

including the two independent variables b and m as well as ν_0 and ν_∞ which denote the rubbery and glassy Poisson ratio, respectively [141]. However, Göhler's ansatz is based on the assumption of a purely real Poisson ratio which is only valid for low loss materials [142].

2.5. Homogenization Techniques

In Section 2.1.1, the components of electric motors were introduced. The components were illustrated in Figure 2.1. Particularly the rotor and stator consist of a very heterogeneous composite structure. The detailed discretization of these heterogeneous structures inside structural dynamic simulation models is complicated and involves a significant computational effort. In order to avoid this effort, homogenization can be applied. Homogenization yields the identification of a set of material properties that effectively represent the mechanical behavior of the underlying heterogeneous composite structure in a homogeneous material. Over the time numerous procedures were developed that all aim at the efficient quantification of homogeneous effective stiffness and damping properties of composite materials. The different procedures are divided into numerical and analytical techniques. In the following, a brief explanation of the main principle of homogenization will be given. Furthermore, some standard numerical and analytical homogenization techniques will be introduced. The derivations are mainly inspired by [143–146]

2.5.1. Representative Volume Element

One of the most frequently used concepts of homogenization techniques is the introduction of a so-called representative volume element (RVE). A RVE is a small volume element that sufficiently represents the macroscopic mechanical behavior of a corresponding large composite structure in terms of stiffness, damping, and mass distribution. Since the RVE is much smaller than the underlying composite structure it is advantageous in a computational sense. Most homogenization approaches are based on micromechanical models of the corresponding RVE.

The identification of an RVE in complex structures can be elaborate and time consuming. Critical remarks on the limitations of RVEs in practical applications due to an insufficient representation of the underlying structure e.g. in case statistical homogeneity can be found in [147, 148]. However, in this thesis periodicity of the composite structure will be assumed which means that the composite consists of a periodic formation of recurrent elements, the so-called unit cells (or repeating unit cells (RUC)) [143]. A RUC is the smallest possible unit from which the total structure can be synthesized based on symmetry and periodicity. Thus, the representative unit is directly given by the RUC [147]. The following introduction into the basic principles of RVEs are inspired by [149].

In 1963 Hill postulated that a homogeneous material represents the macroscopic behavior of a composite if and only if the total strain energy of the substitutive homogeneous material U^0 due to an imposed load is equivalent to the total strain energy of the heterogeneous composite U due to the same displacement [150].

$$U \overset{!}{=} U^0. \tag{2.64}$$

The total strain energy that is stored in a structure can be calculated from the average stress and average strain

$$U_{ij} = \frac{1}{2}\int_V \sigma_{ij}\varepsilon_{ij} dV = \frac{1}{2}\overline{\sigma}_{ij}\overline{\varepsilon}_{ij}V \tag{2.65}$$

with the averaged stress tensor

$$\overline{\sigma}_{ij} = \frac{1}{V}\int_V \sigma_{ij} dV \tag{2.66}$$

and averaged strain tensor

$$\overline{\varepsilon}_{ij} = \frac{1}{V}\int_V \varepsilon_{ij} dV \tag{2.67}$$

The application of homogeneous boundary conditions on the surface of a homogeneous body, meaning

$$u_i(A) = \varepsilon^0_{ij} x_j \tag{2.68}$$

with $u_i(A)$ as the surface displacements and ε^0_{ij} as the strain in the substitutive homogeneous material, implies a homogeneous field inside the structure. For homogeneous materials the average stress and strain then simply equate the local stress and strain of the homogeneous field, respectively

$$\varepsilon^0_{ij} = \overline{\varepsilon}_{ij} \tag{2.69}$$

$$\sigma^0_{ij} = \overline{\sigma}_{ij}. \tag{2.70}$$

Using the Gauss theorem the averaged strain $\overline{\varepsilon}_{ij}$ can be expressed as a surface integral of the boundary surface

$$\overline{\varepsilon}_{ij} = \frac{1}{V}\int_V \varepsilon_{ij} dV = \frac{1}{2V}\int_S (u_i n_j + u_j n_i) dS \tag{2.71}$$

with u_i as the ith component of the displacement and n_j as the jth component of the unit normal vector to A. Hence, the average strain can be calculated from the displacement information at the boundaries. A more detailed explanation of the theoretic background can be found in [149].

Applying homogeneous stress σ^0_{ij} or strain ε^0_{ij} boundary conditions to the heterogeneous RVE yields the computation of the strain or stress field inside the RVE, respectively, and allows the calculation of the average strain $\overline{\varepsilon}_{ij}$ or stress $\overline{\sigma}_{ij}$ in order to retrieve the effective stiffness matrix K_{ijkl} of the composite from

$$\overline{\sigma}_{ij} = K_{ijkl}\overline{\varepsilon}_{kl} \tag{2.72}$$

A good overview of the mathematical principles of RVEs as well as the derivation of the relation between the average values is given in [151]. In order to retrieve effective mechanical properties of the composite material the RVE is exposed to external displacements on its surface A. The purpose of proper boundary conditions is to maintain symmetry and periodicity conditions. The correct application of homogeneous boundary conditions is important for the validity of the numerical procedure aiming the determination of effective properties. The importance of proper boundary conditions is extensively discussed in [152]. A detailed description of the numerical solution procedure of an exemplary RVE with periodic boundary conditions as it was used throughout this research work will be given in appendix of this thesis.

2.5.1.1. Fiber-Reinforced Structures

An unidirectional fiber-reinforced composite material typically consists of a fibers which are unidirectionally oriented and surrounded by a matrix material. The actual distribution of the fibers inside the matrix material is quite random. Nevertheless, for homogenization purposes it can be advantageous to assume a periodic distribution of the fibers throughout the composite.

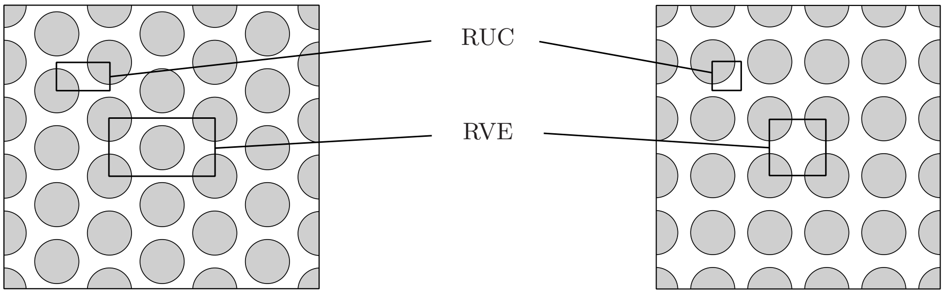

(a) Hexagonal

(b) Quadratic

Figure 2.11.: Exemplary illustration of a representative volume element (RVE) and a repeating unit cell (RUC) of hexagonal and quadratic packing pattern of uniaxially fiber-reinforced structures [153].

The general case of the effective material behavior of fiber-reinforced composite materials is orthotropic. Orthotropy is characterized by three independent perpendicular symmetry planes within the structure and hence a linear-elastic stress-strain relation that is determined by nine independent elastic constants [154]:

$$\begin{pmatrix} \varepsilon_{xx} \\ \varepsilon_{yy} \\ \varepsilon_{zz} \\ 2\varepsilon_{yz} \\ 2\varepsilon_{zx} \\ 2\varepsilon_{xy} \end{pmatrix} = \begin{pmatrix} \frac{1}{E_x} & -\frac{\nu_{yx}}{E_y} & -\frac{\nu_{zx}}{E_z} & 0 & 0 & 0 \\ -\frac{\nu_{xy}}{E_x} & \frac{1}{E_y} & -\frac{\nu_{zy}}{E_z} & 0 & 0 & 0 \\ -\frac{\nu_{xz}}{E_x} & -\frac{\nu_{yz}}{E_y} & \frac{1}{E_z} & 0 & 0 & 0 \\ 0 & 0 & 0 & \frac{1}{G_{yz}} & 0 & 0 \\ 0 & 0 & 0 & 0 & \frac{1}{G_{zx}} & 0 \\ 0 & 0 & 0 & 0 & 0 & \frac{1}{G_{xy}} \end{pmatrix} \begin{pmatrix} \sigma_{xx} \\ \sigma_{yy} \\ \sigma_{zz} \\ \sigma_{yz} \\ \sigma_{zx} \\ \sigma_{xy} \end{pmatrix} . \tag{2.73}$$

In most practical cases of unidirectional fiber-reinforced composite materials, the two symmetry planes which are perpendicular to the direction of fiber are assumed to be isotropic which is called transverse isotropy. Thus, the elastic behavior is determined by only five independent material properties

$$\begin{pmatrix} \varepsilon_{xx} \\ \varepsilon_{yy} \\ \varepsilon_{zz} \\ 2\varepsilon_{yz} \\ 2\varepsilon_{zx} \\ 2\varepsilon_{xy} \end{pmatrix} = \begin{pmatrix} \frac{1}{E_x} & -\frac{\nu_{xy}}{E_x} & -\frac{\nu_{zx}}{E_z} & 0 & 0 & 0 \\ -\frac{\nu_{xy}}{E_x} & \frac{1}{E_x} & -\frac{\nu_{zx}}{E_z} & 0 & 0 & 0 \\ -\frac{\nu_{xz}}{E_x} & -\frac{\nu_{xz}}{E_x} & \frac{1}{E_z} & 0 & 0 & 0 \\ 0 & 0 & 0 & \frac{1}{G_{zx}} & 0 & 0 \\ 0 & 0 & 0 & 0 & \frac{1}{G_{zx}} & 0 \\ 0 & 0 & 0 & 0 & 0 & \frac{2(1+\nu_{xy})}{E_x} \end{pmatrix} \begin{pmatrix} \sigma_{xx} \\ \sigma_{yy} \\ \sigma_{zz} \\ \sigma_{yz} \\ \sigma_{zx} \\ \sigma_{xy} \end{pmatrix} . \tag{2.74}$$

where the z-direction is the direction of fiber. Common distribution schemes are the quadratic array, which is also referred to as square array, and the hexagonal array [149]. Both types of fiber distributions are schematically given in Figure 2.11. The RUC corresponds the

the smallest entity of which the structure can be synthesized based on symmetry and periodicity. In contrast, the smallest entity of which the structure can be synthesized exclusively based on periodicity is referred to as a RVE. Both RVEs, the quadratic and hexagonal, will be employed later in a this thesis.

2.5.1.2. Laminated Structures

As opposed to the fiber-reinforced composites, the general case of the effective mechanical behavior of laminated structures is transversely isotropic presuming planar isotropy within the single layers. Hence, the effective stiffness is determined by five independent elastic constants as illustrated in Equation 2.74. An exemplary RVE with periodic boundary conditions as well as a RUC of the structure are given in Figure 2.12.

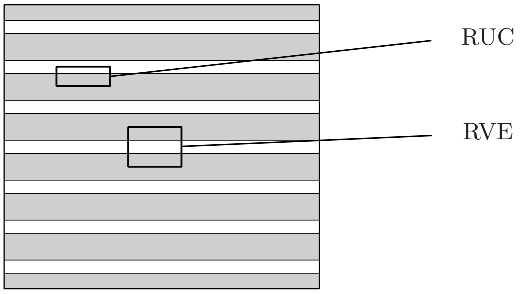

Figure 2.12.: Representative volume element (RVE) and repetitive unit cell (RUC) of laminated structures.

2.5.2. Analytical Homogenization Techniques

In contrast to the numerical solution of the representative volume element, different analytical methods exist that yield the efficient identification of the effective properties of a heterogeneous structure. Each of the methods takes into account the elastic constants of each individual constituent as well as the filling factor χ which is defined as

$$\chi = \frac{V_f}{V} = \frac{V_f}{V_m + V_f} \tag{2.75}$$

with V_f and V_m as the total volume of the fiber and matrix, respectively, and V as the total volume of the composite. In the following, some of the most frequented analytical approaches will be introduced using the notation of the transversely isotropic compliance matrix in Equation 2.74 where the z-direction is the direction of fiber.

2.5.2.1. Method of Voigt and Reuss

The method of Voigt, the so-called rule of mixtures, as well as the Reuss estimate, the inverse rule of mixtures, are based on a phenomenological investigation of the effective behavior of composites. The five independent properties can be calculated by the following relations

$$E_x = \frac{1}{\frac{\chi}{E_f} + \frac{1-\chi}{E_m}} \tag{2.76}$$

$$E_z = \chi \cdot E_f + (1 - \chi) \cdot E_m \tag{2.77}$$

$$\nu_{zx} = \chi \cdot \nu_f + (1-\chi) \cdot \nu_m \tag{2.78}$$

$$\nu_{xy} = 1 - \nu_{zx} - \frac{E_x}{3K} \tag{2.79}$$

$$G_{xy} = \frac{1}{\frac{\chi}{G_f} + \frac{1-\chi}{G_m}} \tag{2.80}$$

where K is the compression modulus of the composite and given as

$$K = \frac{1}{\frac{\chi}{K_f} + \frac{1-\chi}{K_m}} \tag{2.81}$$

with

$$K_{f,m} = \frac{E_{f,m}}{3(1-2\nu_{f,m})}. \tag{2.82}$$

2.5.2.2. Method of Halpin-Tsai

Based on multiple investigations, the rule of mixture was empirically extended in order to give a better estimation of the transverse YOUNG's modulus E_x as well as the longitudinal shear modulus G_{xy} [155–160]. The method is called the HALPIN-TSAI method. The axial YOUNG's modulus as well as the longitudinal POISSON ratios are taken over from the rule of mixtures.

$$E_x = E_m \cdot \frac{1+\zeta\eta_E\chi}{1-\eta_E\chi} \tag{2.83}$$

$$G_{xy} = G_m \cdot \frac{1+\zeta\eta_G\chi}{1-\eta_G\chi} \tag{2.84}$$

with

$$\eta_E = \frac{E_f/E_m - 1}{E_f/E_m - \zeta} \tag{2.85}$$

$$\eta_G = \frac{G_f/G_m - 1}{G_f/G_m - \zeta}. \tag{2.86}$$

ζ is a parameter that can be empirically obtained from measurements. Reasonable estimates for the value of ζ for practical materials are 1 in case of the calculation of G_{xy} and 2 for the calculation of E_x [146].

2.5.2.3. Method of Chamis

One of the most frequently used micromechanical model is the CHAMIS model. Analogue to the HALPIN-TSAI model, the CHAMIS model uses the relations of the rule of mixture for the axial YOUNG's modulus as well as the longitudinal POISSON ratio. CHAMIS assumes that the shear moduli in all three planes are the same provided that the fiber material itself is isotropic

$$E_x = \frac{1}{\frac{\sqrt{\chi}}{E_f} + \frac{1-\sqrt{\chi}}{E_m}} \tag{2.87}$$

$$G_{xy} = G_{xz} = \frac{1}{\frac{\sqrt{\chi}}{G_f} + \frac{1-\sqrt{\chi}}{G_m}}. \tag{2.88}$$

2.5.3. Method of Cells

In the previous sections, the numerical RVEs as well as different analytical homogenization techniques were introduced. The so-called method of cells (MOC) was developed in order to combine the advantages of both, the accuracy of numerical approaches and the computational efficiency of analytical approaches. It is based on the analytical solution of a system of equations that arises from a discrete micromechanical model. It thus represents a quasi-analytical technique. Postma first applied the method of cells on laminated structures investigating the wave propagation in stratified media [161]. Aboudi modified Postma's model for the use in fiber-reinforced structures [162]. In order to apply the MOC for a random composite material a RVE with periodic boundary conditions has to be identified. The RVE of the composite then needs to be divided into individual areas of homogeneous material, the so-called-subcells. Figure 2.15 shows the generic geometry of a RVE as it is used inside the MOC. The micromechanical model is typically divided by vertical and horizontal planes forming subcells of the dimensions d_α, h_β and l_γ. The coordinates of each subcell in the three spatial directions x_1, x_2, and x_3 are given by means of the coefficients α, β, and γ, respectively, as exemplarily illustrated for the subcell with the coordinates $\alpha = 1$, $\beta = 2$, $\gamma = 2$ in Figure 2.13).

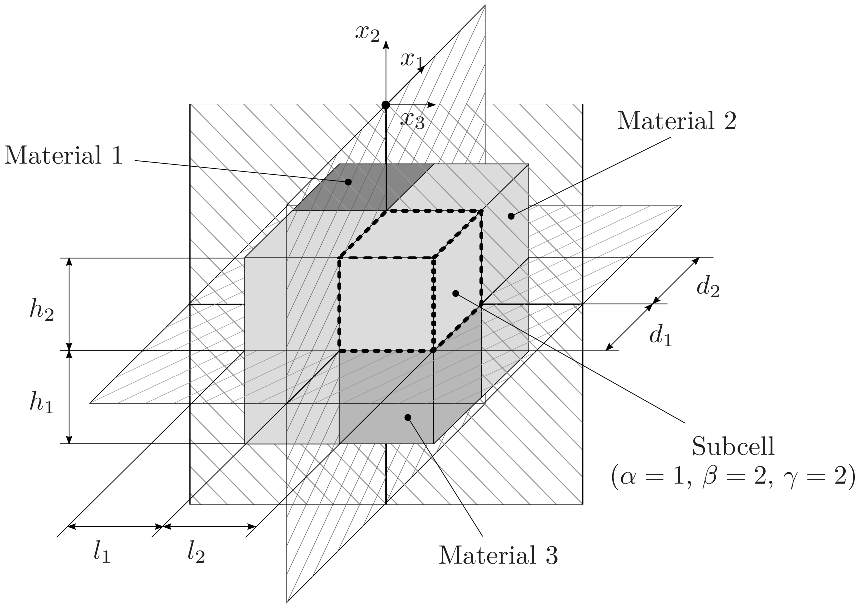

Figure 2.13.: Generic micromechanical model as it is used inside the MOC.

In the following the basic principles of the MOC as it was developed for a RVE with periodic boundary conditions will be briefly introduced. The denotations are mainly inspired by [151]. More detailed explanation of the underlying assumptions can be found in [151].

Analogue to the RVE procedure, all entries of the effective stiffness matrix inside the MOC can be obtained from Equation 2.72 where the average values $\overline{\varepsilon}_{ij}$ and $\overline{\sigma}_{ij}$ are given as the sum of the average strains and stresses of all subcells, respectively, weighted by their volume fraction

$$\bar{\varepsilon}_{ij} = \frac{1}{dhl} \sum_{\alpha,\beta,\gamma=1}^{k} d_\alpha h_\beta l_\gamma \bar{\varepsilon}_{ij}^{(\alpha,\beta,\gamma)} \tag{2.89}$$

$$\bar{\sigma}_{ij} = \frac{1}{dhl} \sum_{\alpha,\beta,\gamma=1}^{k} d_\alpha h_\beta l_\gamma \bar{\sigma}_{ij}^{(\alpha,\beta,\gamma)} \tag{2.90}$$

with k as the number of subcells in each corresponding direction. The displacement field in each subcell is obtained from a first order Taylor-expansion providing

$$u_i^{(\alpha,\beta,\gamma)} = w_i^{(\alpha,\beta,\gamma)} + \xi_i^{(\alpha,\beta,\gamma)} \bar{x}_1^{(\alpha)} + \phi_i^{(\alpha,\beta,\gamma)} \bar{x}_2^{(\beta)} + \psi_i^{(\alpha,\beta,\gamma)} \bar{x}_3^{(\gamma)} \tag{2.91}$$

with $w_i^{(\alpha,\beta,\gamma)}$ as the displacement of the center of each subcell, and $\xi_i^{(\alpha,\beta,\gamma)}$, $\phi_i^{(\alpha,\beta,\gamma)}$, and $\psi_i^{(\alpha,\beta,\gamma)}$ as so-called microvariables, which dentote the first order coefficients of the Taylor-expansion and thus characterize the linear distortion field of each individual subcell.

The assumption of periodic boundary conditions and thus

$$\frac{\partial w_i^{(\alpha,\beta,\gamma)}}{\partial x_j} = \frac{\partial w_i}{\partial x_j} \tag{2.92}$$

yields the average strain and stress of each subcell to be identical to the local strain and stress field of each subcell, respectively

$$\bar{\varepsilon}_{ij}^{(\alpha,\beta,\gamma)} = \varepsilon_{ij}^{(\alpha,\beta,\gamma)}, \quad \text{and} \quad \bar{\sigma}_{ij}^{(\alpha,\beta,\gamma)} = \sigma_{ij}^{(\alpha,\beta,\gamma)}. \tag{2.93}$$

Employing the generic strain-displacement relation

$$\varepsilon_{ij}^{(\alpha,\beta,\gamma)} = \frac{1}{2}\left[\partial_j u_i^{(\alpha,\beta,\gamma)} + \partial_i u_j^{(\alpha,\beta,\gamma)}\right], \tag{2.94}$$

with $\partial_1 = \partial/\partial\bar{x}_1^{(\alpha)}$, $\partial_2 = \partial/\partial\bar{x}_2^{(\beta)}$, and $\partial_3 = \partial/\partial\bar{x}_3^{(\gamma)}$, the strain-displacement relation of each subcell can be written as

$$\begin{aligned}
\varepsilon_{11}^{(\alpha,\beta,\gamma)} &= \xi_1^{(\alpha,\beta,\gamma)} && (2.95)\\
\varepsilon_{22}^{(\alpha,\beta,\gamma)} &= \phi_2^{(\alpha,\beta,\gamma)} && (2.96)\\
\varepsilon_{33}^{(\alpha,\beta,\gamma)} &= \psi_3^{(\alpha,\beta,\gamma)} && (2.97)\\
2\varepsilon_{12}^{(\alpha,\beta,\gamma)} &= \xi_2^{(\alpha,\beta,\gamma)} + \phi_1^{(\alpha,\beta,\gamma)} && (2.98)\\
2\varepsilon_{13}^{(\alpha,\beta,\gamma)} &= \xi_3^{(\alpha,\beta,\gamma)} + \psi_1^{(\alpha,\beta,\gamma)} && (2.99)\\
2\varepsilon_{23}^{(\alpha,\beta,\gamma)} &= \phi_3^{(\alpha,\beta,\gamma)} + \psi_2^{(\alpha,\beta,\gamma)}. && (2.100)
\end{aligned}$$

The subcell strains are coupled to the subcell stresses by the constitutive equations of each subcell in normal direction

$$\begin{pmatrix} \sigma_{11}^{(\alpha,\ \beta,\ \gamma)} \\ \sigma_{22}^{(\alpha,\ \beta,\ \gamma)} \\ \sigma_{33}^{(\alpha,\ \beta,\ \gamma)} \end{pmatrix} = \begin{pmatrix} K_{11}^{(\alpha,\ \beta,\ \gamma)} & K_{12}^{(\alpha,\ \beta,\ \gamma)} & K_{13}^{(\alpha,\ \beta,\ \gamma)} \\ K_{21}^{(\alpha,\ \beta,\ \gamma)} & K_{22}^{(\alpha,\ \beta,\ \gamma)} & K_{23}^{(\alpha,\ \beta,\ \gamma)} \\ K_{31}^{(\alpha,\ \beta,\ \gamma)} & K_{32}^{(\alpha,\ \beta,\ \gamma)} & K_{33}^{(\alpha,\ \beta,\ \gamma)} \end{pmatrix} \begin{pmatrix} \varepsilon_{11}^{(\alpha,\ \beta,\ \gamma)} \\ \varepsilon_{22}^{(\alpha,\ \beta,\ \gamma)} \\ \varepsilon_{33}^{(\alpha,\ \beta,\ \gamma)} \end{pmatrix} \tag{2.101}$$

and in shear direction

$$\begin{pmatrix}\sigma_{23}^{(\alpha,\ \beta,\ \gamma)}\\ \sigma_{31}^{(\alpha,\ \beta,\ \gamma)}\\ \sigma_{12}^{(\alpha,\ \beta,\ \gamma)}\end{pmatrix}=\begin{pmatrix}K_{44}^{(\alpha,\ \beta,\ \gamma)} & 0 & 0\\ 0 & K_{55}^{(\alpha,\ \beta,\ \gamma)} & 0\\ 0 & 0 & K_{66}^{(\alpha,\ \beta,\ \gamma)}\end{pmatrix}\begin{pmatrix}2\varepsilon_{23}^{(\alpha,\ \beta,\ \gamma)}\\ 2\varepsilon_{31}^{(\alpha,\ \beta,\ \gamma)}\\ 2\varepsilon_{12}^{(\alpha,\ \beta,\ \gamma)}\end{pmatrix}. \tag{2.102}$$

The stiffness matrix entries can be deduced from the elastic constants of each subcell material.

In order to solve for the subcell microvariables the continuity conditions, namely the continuity of displacements and the continuity of tractions, at the interfaces inside the RVE as well as at the RVE boundaries have to be considered.

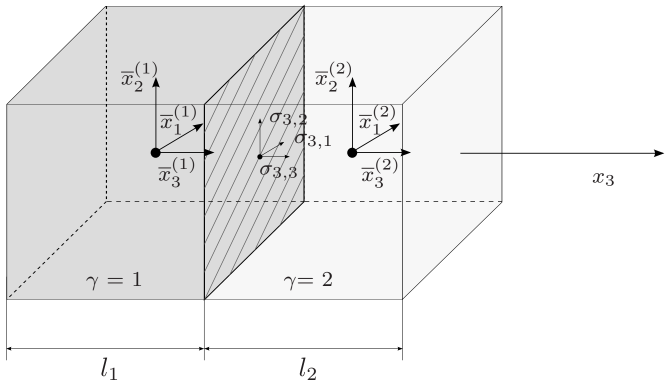

Figure 2.14.: Exemplary illustration of continuity conditions at the interfaces inside a RVE.

In Figure 2.14 an exemplary interface between two subcells is given.

The continuity of displacements is applied in an average sense yielding:

$$\int_d\int_h\left(u_i^{(\gamma=1)}\Big|_{\overline{x}^{(1)}{}_3=\frac{l_1}{2}}-u_i^{(\gamma=2)}\Big|_{\overline{x}^{(2)}{}_3=\frac{-l_2}{2}}\right)d\overline{x}_2 d\overline{x}_1=0 \tag{2.103}$$

The continuity of tractions provides

$$\sigma_{3j}^{(\gamma=1)}=\sigma_{3j}^{(\gamma=2)} \tag{2.104}$$

Employing the continuity conditions on all interfaces and boundaries provides a sufficient number of equations to solve for the microvariables and obtain the effective composite stiffness matrix.

In Figure 2.15, two basic micromechanical models that will be used in this thesis are illustrated. One model is based on two subcells and goes back to Postma's investigations (see [161]) and the other one is based on four subcells and goes back to Aboudi [162].

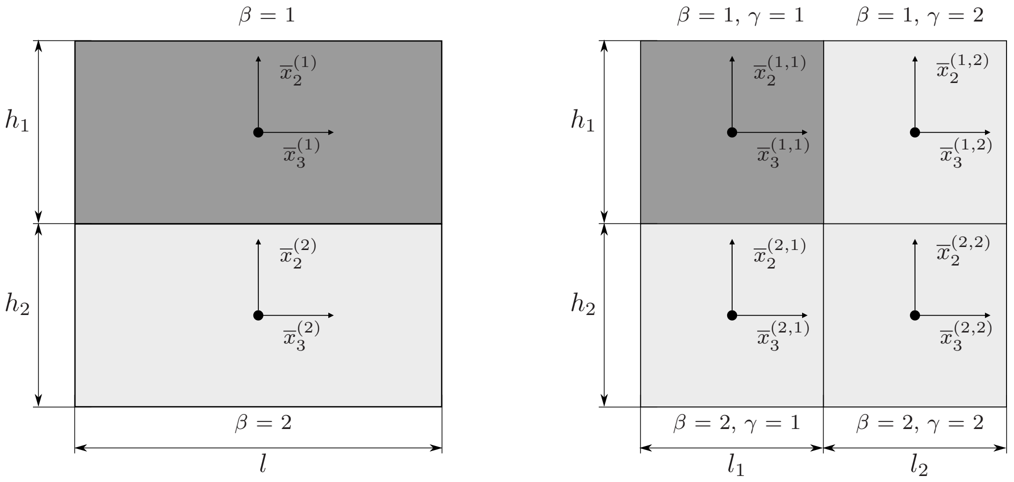

(a) MOC with two subcells [161]   (b) MOC with four subcells [151]

Figure 2.15.: Method of cells (MOC) for laminated and fiber-reinforced structures.

A detailed description of the singles steps that are necessary to generate the set algebraic equations for the effective elastic constants of the composite material will be given in the appendix of this thesis (see Appendix A).

2.5.4. Effective Damping Properties

The structural vibrational behavior of composite materials is not only characterized by the directional stiffness behavior of the medium but also by the directional damping properties.

SUN ET AL. distinguished four different damping mechanisms in fiber-reinforced composite materials [163]:

- viscoelastic behavior of matrix and/or fibers,
- thermoelastic damping due to cyclic heat flow,
- COULOMB friction due to slip in unbounded regions of the fiber-matrix interface, and
- dissipation caused by microscopic or macroscopic damage in the composite.

In the following two frequently used approaches that yield the quantification of effective directional damping properties of composite structures, namely UNGAR's strain energy method and HASHIN's concept of complex moduli, the so-called correspondence principle, will be introduced. Both methods are based on the directional combination of the material-inherent damping of the single material phases. Hence, both approaches neglect further damping effects like frictional damping. Nevertheless, both methods are extensively used for the determination of the directional effective damping properties of composite materials. A deeper explanation of the theoretic background is given in [154]. A detailed review of different methods that yield the quantification of effective directional damping properties of composite structures is given in [164–166].

2.5.4.1. Strain Energy Method

The basic idea behind the strain energy method which was first introduced by Ungar and Kerwin is that the effective composite damping can be expressed as a combination of the material-inherent damping of all constituents by the following relation

$$\eta = \frac{\sum_{p=1}^{n} \eta^p U^p}{\sum_{k=1}^{n} U^p} \tag{2.105}$$

where η^p is the loss factor of the pth phase and U^p the strain energy that is stored in the corresponding phase. The strain energy that is stored within the phases can be expressed as

$$U^p = \frac{1}{2} \int_{V^p} \sigma_{ij} \varepsilon_{ij} dV \tag{2.106}$$

and thus numerically be obtained. The directional loss factors η_{11}, η_{33}, η_{12}, and η_{13} of a transverse isotropic material as well as the two additional loss factors η_{22} and η_{23} of an orthotropic system can be obtained by applying appropriate directional boundary conditions and loads to the numerical model. A good overview of appropriate boundary conditions and loads can be found in [165]. The strain energy method was successfully used in multiple applications [167–171]. Its adaption to the use inside the MOC is presented in [172]. In this thesis the strain energy method will be used in combination with the discrete RVE in order to quantify directional damping properties. A detailed description of the numerical solution of Equation 2.106 will as well be presented in the appendix of this thesis (see Appendix B.3).

2.5.4.2. Correspondence Principle

The constitutive relation between the stress and strain of a composite material was given in Equation 2.72. Assuming the stress and strain to be oscillating, time-dependent values, as expressed by Equations 2.54 and 2.53, respectively, the stiffness matrix becomes complex

$$\sigma^*_{ij}(\omega) = K^*_{ijkl} \varepsilon^*_{kl}(\omega) \tag{2.107}$$

The basic idea of the correspondence principle is to replace the isotropic elastic moduli of the composite's constituents by complex moduli. Hence, in performing an analytical or numerical homogenization, the real problem is replaced by a complex problem which goes back to Alfrey's so-called correspondence principle [124]. Thus, the effective elastic moduli M^*_{ij} of the composite material are as complex as the effective stiffness matrix with $M^*ii = \Re(M_{ij}) + i \cdot \Im(M_{ij})$ [127]. Analogue to the expression of the isotropic loss factor of viscoelatic materials 2.58, the directional loss factor η_{ij} can be expressed as

$$\eta_{ii} = \frac{\Im(E_{ii})}{\Re(E_{ii})} \quad \text{and} \quad \eta_{ij} = \frac{\Im(G_{ij})}{\Re(G_{ij})} \tag{2.108}$$

The nature of complex elastic moduli was introduced in Section 2.4. The correspondence principle was successfully applied in various publications for different analytical homogenization approaches, providing good accordance to experimental results [163, 173–176]. The correspondence principle will later be employed in this thesis in order to obtain direction damping properties from analytical homogenization techniques. A detailed description of the application of the correspondence principle inside the MOC will be given in the appendix of this thesis (see Appendix A.2).

3. Structural Dynamic Modeling Approaches

3.1. Impregnation Resin

During their mounting process random-wound stators are exposed to an impregnation resin (see also Section 2.1.1.2). Thermosetting materials like impregnation resins typically behave viscoelastic. The basic principles of viscoelasticity including the time- and temperature-dependent mechanical behavior were introduced in Section 2.4. In Section 2.1.1.2, the resin's main functions like e.g. heat conduction of ohmic losses were listed. In order to achieve its functionality inside the copper windings the impregnation resin has to be brought to a state of low viscosity yielding an optimal expansion between the copper wires. However, due to the impregnation process which typically involves the dipping of the full stator structure into a basin of resin, the entire stator is exposed to the resin material. Figure 3.1 shows two micrographs that exemplarily show the microscopic composition of a stator iron core after the impregnation process.

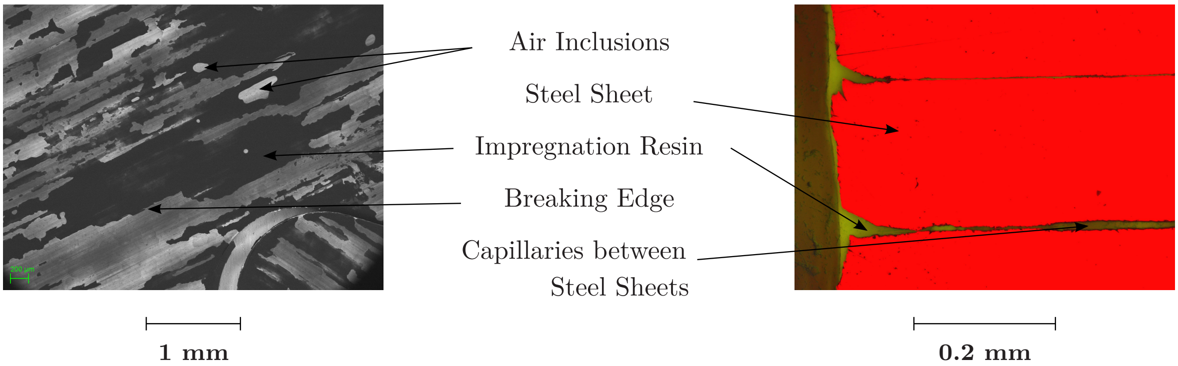

Figure 3.1.: Micrograph of the surface of a single steel sheet extracted from an impregnated laminated stator (left) and cross-section of stator laminations (right).

The left micrograph shows the surface of a single steel sheet as it occurs in the laminated stator iron core. Apparently, the capillary action and the low-viscosity of the resin are sufficient for the resin to penetrate not only the capillaries between the copper windings but also the air gaps between the steel sheets. Except for small air inclusions, the resin entirely covers the surface of the steel sheets. The areas of air inclusions can be separated from areas where the resin was dismantled during the disassembly by examining the edges of the resin surfaces. Air inclusions show a naturally soft gradient as exemplarily pointed out in the left micrograph of Figure 3.1 whereas the dismantled areas show rough breaking edges. In the right micrograph a cross-section of the stator lamination is illustrated. It shows the intrusion of the resin into two neighboring contact gaps. Apparently, all capillaries are homogeneously filled with resin. The same findings could be made on different cross-sections of the stator. Thus, it can be postulated that the impregnation resin not only influences the mechanical behavior of the copper windings but also has an effect on the stiffness and damping behavior of the stator iron core. In order to investigate the basic vibrational behavior of stator structures the viscoelastic behavior of the impregnation resin needs to be analyzed. In the following the frequency- and temperature-dependent behavior of two different impregnation resins, referred to as Resin 1 and Resin 2, will be investigated. Both impregnation resins will be used in subsequent analyses in this thesis.

3.1.1. Identification of Viscoelastic Resin Properties

In order to characterize the structural dynamic behavior of a viscoelastic material, its time- and temperature-dependent mechanical properties need to be quantified performing a Dynamic-Mechanical-Analysis (DMA). The basic principle of DMA testing was introduced in Section 2.4.3. A detailed description of the DMA measurement procedure as well as the procedure of extracting so-called master curves from multiple individual measurements at different temperatures will be given in the appendix of this thesis (see Appendix C.1). Master curves are curves that characterize the stiffness and damping of viscoelastic materials as a function of the frequency or temperature using the so-called time-temperature superposition principle (see Section 2.4.2.3). Figure 3.2 shows the setup of the tension DMA testing of a bar specimen of Resin 1. The specimen is fixated between two clamping jaws. The whole measurement setup is located inside a climate chamber in order to perform DMA testings at different temperatures (see Appendix C.1). Both DMA types, the tensional and the torsional DMA, were performed on both resin types, Resin 1 and Resin 2, using bar specimens with a rectangular cross section as specified in Appendix C.1. The tensional DMA yields the complex Young's modulus, the torsional DMA the shear modulus.

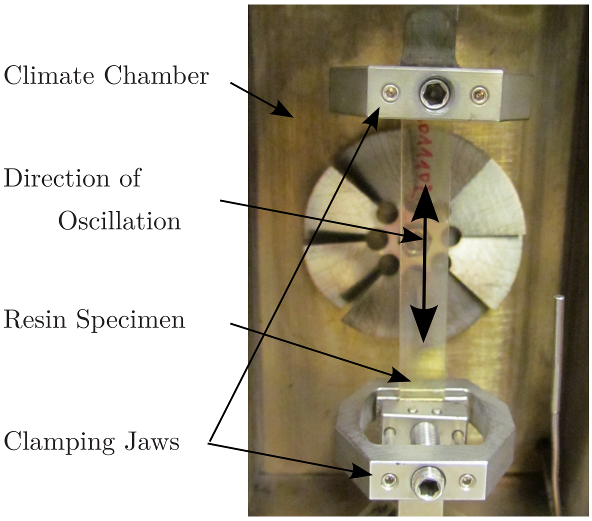

Figure 3.2.: Setup of dynamic mechanical analysis of a viscoelastic impregnation resin specimen.

In Figure 3.3(a), the master curves of both moduli, the Young's and the shear modulus, are given as a function of the frequency for both resin types. The master curves correspond to the temperature $T_0 = 0\,^{\circ}\mathrm{C}$. Figure 3.3(b) shows the corresponding loss factors. The distinct peaks of both loss factor functions indicate the glass transition areas of the two materials. While the data of the loss factor is normalized with respect to the peak loss factor values of either resin type, the stiffness data is normalized with respect to the stiffness obtained from a quasi-static tensile tests[1] of either material at $T = 23\,^{\circ}\mathrm{C}$. At low frequencies both resin types show values lower than 20% of the quasi-static Young's modulus. However, with an increasing frequency the stiffness properties of both materials increase which matches the viscoelastic material theory introduced in Section 2.4.2.2. For Resin 1, the stiffness parameters could only be measured down to a temperature of 0 °C which is why the maximum frequency of the curves is limited to 10 Hz at

---

[1] The tensile test was performed following the international standard procedure EN ISO 527-1 [177].

0 °C. At lower temperatures the minimum implemented strain of the DMA testing application was beyond the tensile strength of the material.

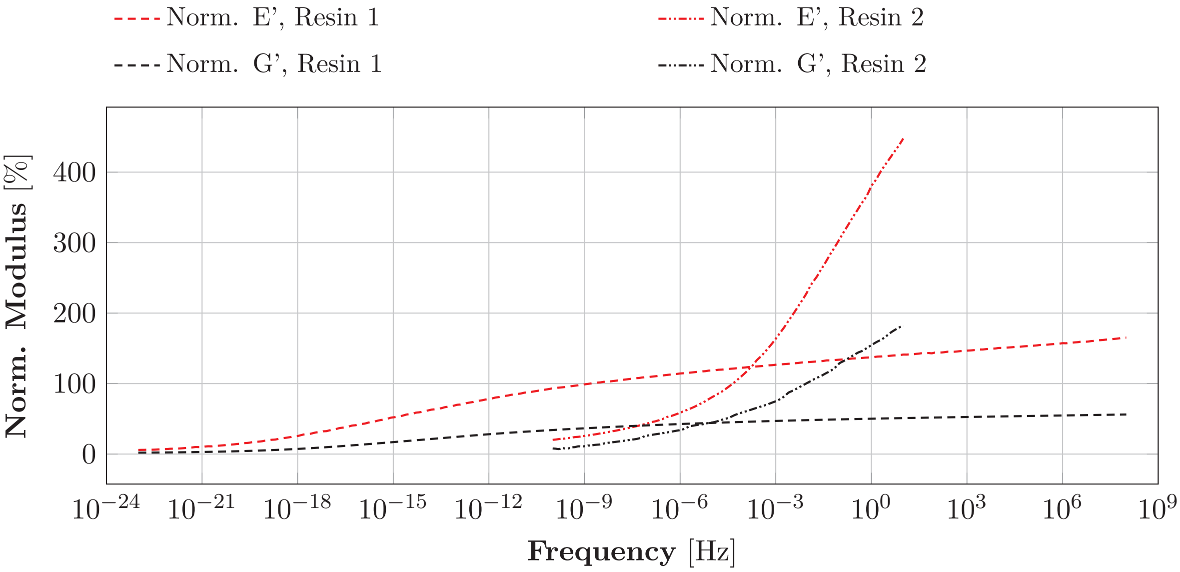

(a) Storage Young's and shear modulus.

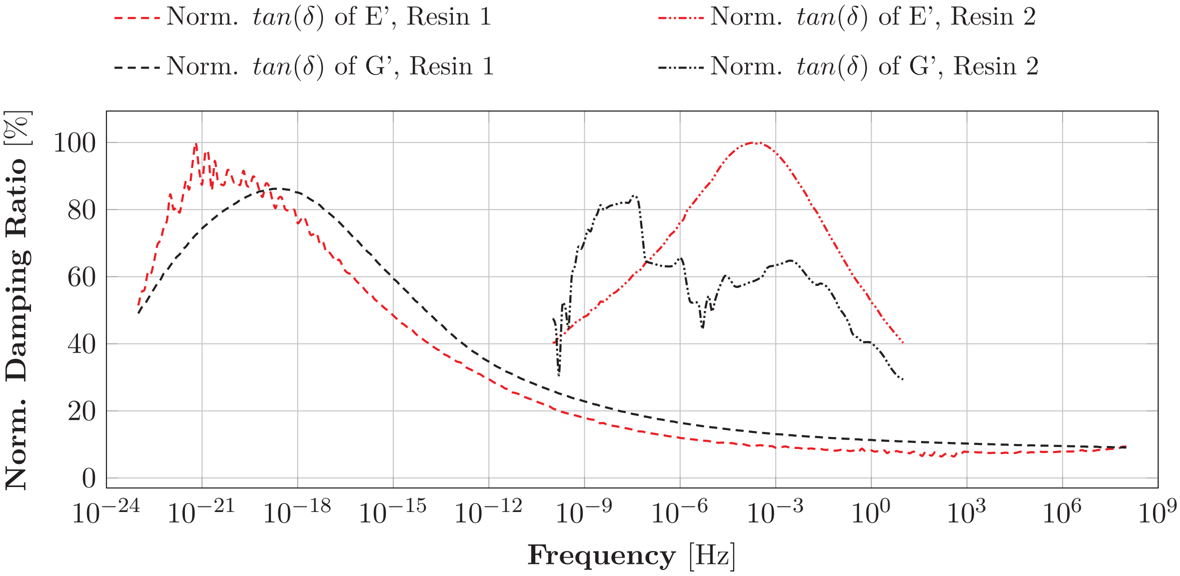

(b) Loss factors $tan(\delta)$.

Figure 3.3.: Normalized storage Young's and shear moduli, E' and G', respectively, as well as the corresponding loss factors $tan(\delta)$ of two different impregnation resins at $T_0 = 0$°C.

Since both resin types are assumed to behave isotropically, the constitutive stress-strain relation of each material can uniquely be expressed by two independent elastic constants e.g. by the shear modulus and the Young's modulus. The complex Poisson ratio ν^* can then simply be calculated from the two elastic constants following

$$\nu^*(\omega) = \frac{E^*}{2G^*} - 1. \tag{3.1}$$

However, the quantification of the Poisson ratio from the complex shear and Young's modulus is very sensitive towards errors of the DMA (see Section 2.4.3). At the same time numerical simulations are very sensitive towards an erroneous Poisson ratio. In order to avoid numerical instabilities, Göhler proposed an analytical procedure which deduces a synthetic, numerically stable Poisson ratio from the Poisson ratio that was derived from the Young's and shear moduli [141]. Göhler's procedure is based on the assumption that the Poisson ratio is purely real which is tolerable for low loss materials [142] and that the frequency-dependent storage Poisson ratio can be expressed by a sigmoid curve. (see Appendix C.3). In Figure 3.4 the two analytical Poisson ratios of the two resin types are given as a function of the frequency for $T = 0\,°\mathrm{C}$. For stability reasons, all further investigations will be based on the synthetically derived Poisson ratios.

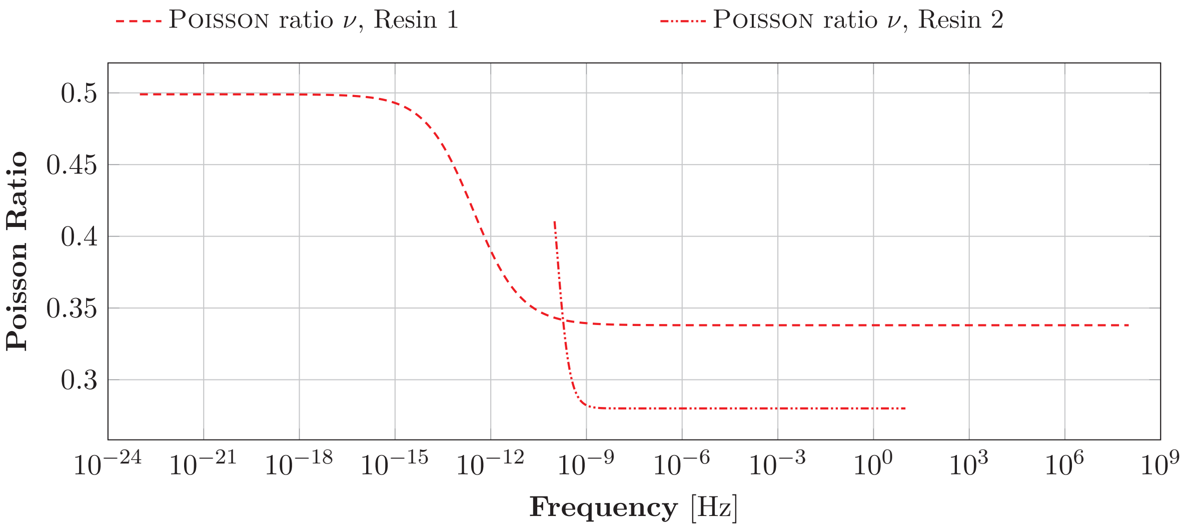

Figure 3.4.: Analytical curve of Poisson ratios of Resin 1 and Resin 2 based on sigmoid ansatz at $T_0 = 0°\mathrm{C}$.

A detailed explanation of Göhler's assumptions and the derivation of the two analytical Poisson ratio curves can be found in the appendix of this thesis.

3.1.2. Prony Series

In order to conveniently apply the measured frequency-dependent stiffness and damping characteristics of viscoelastic materials in subsequent investigations it is advantageous to analytically express the master curves as a function of the frequency. Assuming the material behavior to be represented by a generalized Maxwell model as given in Figure 2.9, the complex moduli of the resins can be expressed by a Prony series following Equation 2.59 and 2.60 (see Section 2.4.2.2). Each of the single elements inside the Prony series depends on two independent parameters, namely the relaxation time τ_j and the characteristic stiffness E_j. The two Prony parameters of each Prony element are typically quantified based on an automatic curve fitting routine. In this thesis the lsqnonlin function which is an integrated Matlab function was used for the automatic identification of the Prony parameters E_j and τ_j of Resin 1 and Resin 2. The lsqnonlin function is frequently used for curve fitting problems with nonlinear regression. It is based on the least-squares method. A detailed description of the exact optimization routine yielding the Prony parameters for Resin 1 and Resin 2 is given in Appendix C.2. In Figure 3.5 the Prony series of the storage Young's modulus and the corresponding loss factor are compared to the measurement data for both resins.

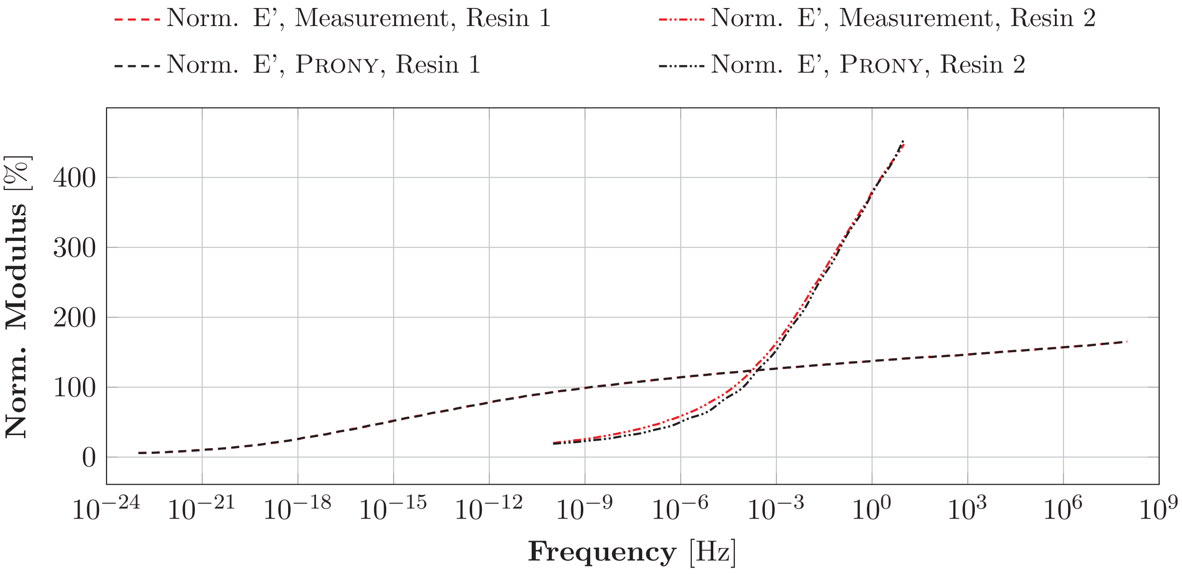

(a) Young's modulus.

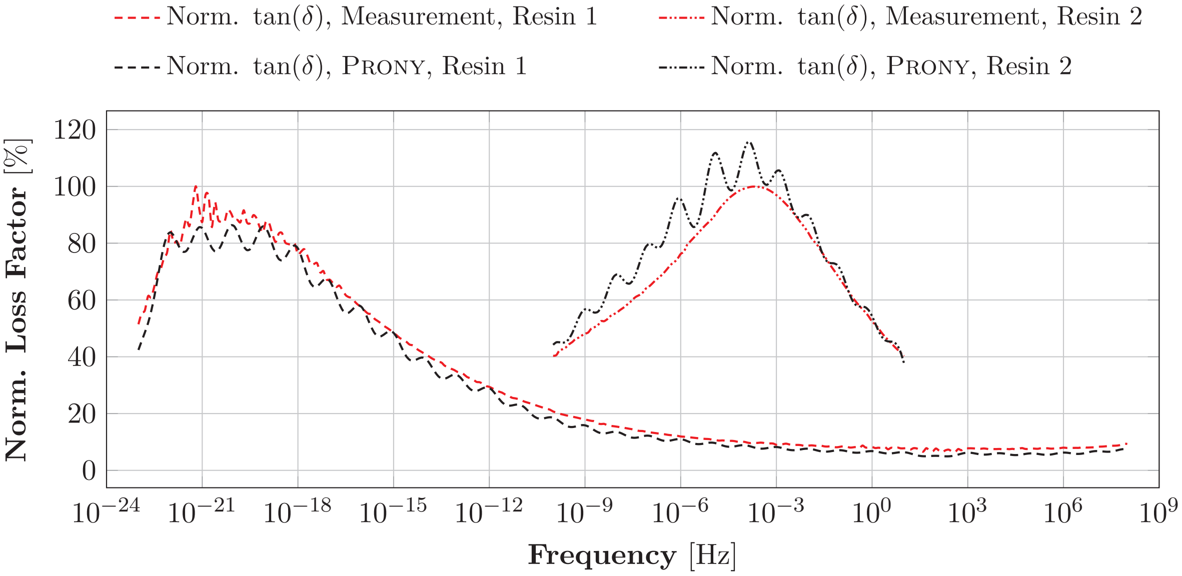

(b) Loss factor.

Figure 3.5.: Comparison between the measured and analytically approximated normalized Young's storage modulus and loss factor of Resin 1 and Resin 2 at $T_0 = 0$°C.

3.1.3. Time-Temperature Superposition

In Figure 3.5, the storage Young's modulus and the loss factor were given as a function of the frequency. These frequncy-dependent stiffness and damping characteristics are only valid for a particular temperature $T = T_0$. In order to be able to describe the mechanical behavior of viscoelastic materials at temperatures other than $T = T_0$, the so called time-temperature-superposition principle (TTSP) can be employed. The basic idea of the TTSP was introduced in Section 2.4.2.3. Du to their material-inherent characteristic structure viscoelastic materials mechanically behave equally at with time and temperature. Mathematically, the relation between the time and the temperature can be expressed by means of so-called shift factors (see Equation 2.61). The generation of master curves from the measurement data of the DMA automatically provides discrete shift factors for specific temperature steps. However, in order to extend the TTSP for temperatures other than the discrete temperature steps from the DMA an analytic function for the shift factors needs be generated. In Section 2.4.2.4 the so-called Williams-Landel-Ferry (WLF) function was introduced. It yields the analytic description of the shift factors by two independent parameters C_1 and C_2 as given in Equation 2.62. Based on the experimental data points, C_1 and C_2 can be quantified for both resin types by curve fitting with the ansatz from Equation 2.62 yielding $C_1 = 231.7\%$ and $C_2 = 102.2$℃ for Resin 1 and $C_1 = 602.1\%$ and $C_2 = 360.1$℃ for Resin 2. In Figure 3.6 the normalized discrete shift factors are compared to the WLF functions of Resin 1 and 2. For Resin 2 the WLF function provides a good approximation of the discrete shift factors. For Resin 1 the WLF function shows good accordance for higher temperatures but diverges from the discrete shift factors at temperatures below T_0.

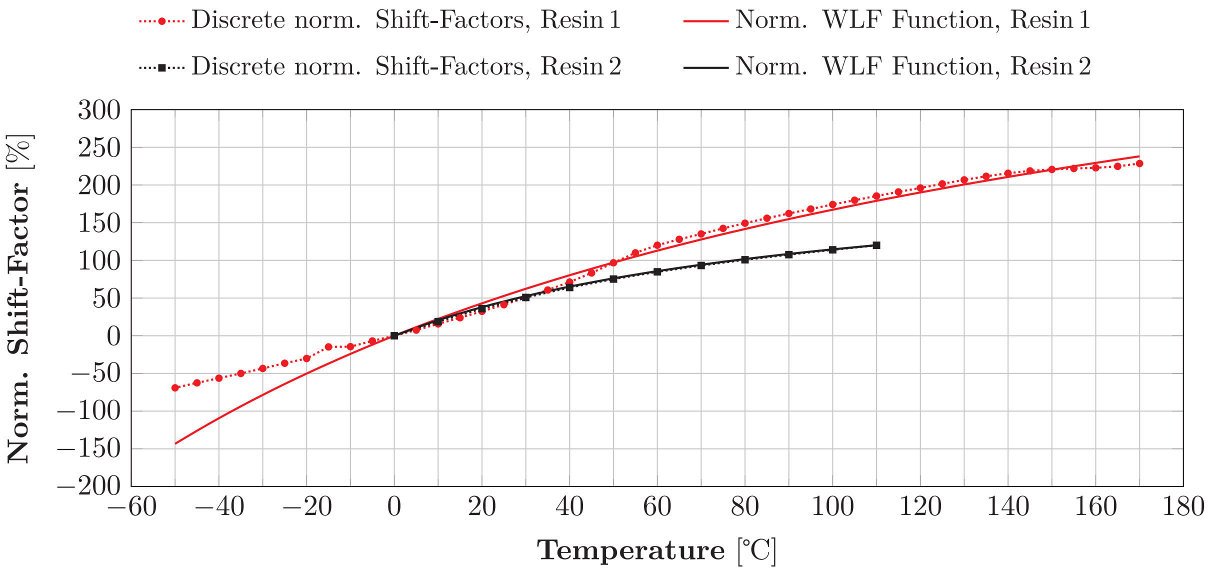

Figure 3.6.: Comparison between the discrete normalized shift factors and the normalized WLF-Function for two different viscoelastic impregnation resins.

3.1.4. Validation of Viscoelastic Modeling Approach

In the previous section an analytical representation of the frequency- and temperature-dependent stiffness and damping characteristics of two impregnation resins was developed using a synthetic Poisson ratio based on a sigmoid ansatz function, a Prony series for the frequency- and temperature-dependent storage and loss moduli and the WLF-function in order to represent the time-temperature relation. Thus, the analytical representation was connected to numerous assumptions which now need to be validated. Therefore, a bar test specimen of Resin 2 as it was used for the DMA testings was elastically mounted and dynamically excited by a mechanical load. The test configuration is schematically illustrated in Figure 3.7. The mechanical load was imposed by an electromagnetic shaker. The shaker rod was mounted to one end of the structure while the structural response was measured at the other end of the specimen using a 1D-LSV.

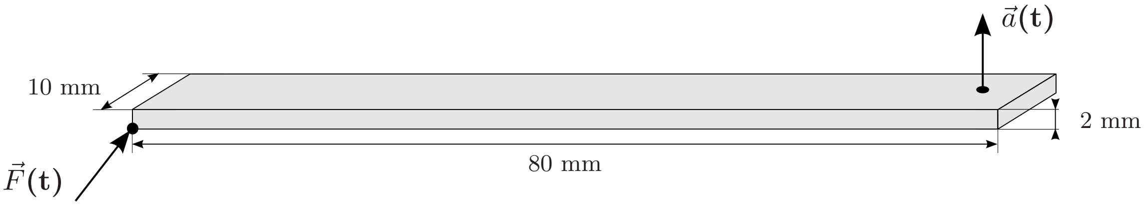

Figure 3.7.: Dynamic testing of a bar viscoelastic specimen.

In Figure 3.8 the dynamic load factor of the resin specimen is given as a function of the frequency. The curve involves three distinct resonance areas in a frequency range from 50 Hz to 4000 Hz. In order to validate the viscoelastic material model of Resin 2 the dynamic load factor was numerically obtained from two different models. The first model is based on an isotropic elastic frequency-independent material characterization which involves the YOUNG'S modulus, POISSON ratio and loss factor of the resin as it was extracted from quasi-static tensile tests at $T = 23\,^{\circ}\mathrm{C}$. The second model is based on an isotropic, viscoelastic material model taking into account the frequency and temperature-dependent material properties of the resin. The results show, that the dynamic behavior which is predicted by the viscoelastic material model is in good accordance with the measurements. In contrast, the error caused by the non-viscoelastic material model is significant regarding both, the prediction of the resonance frequencies as well as the prediction of the corresponding resonance damping.

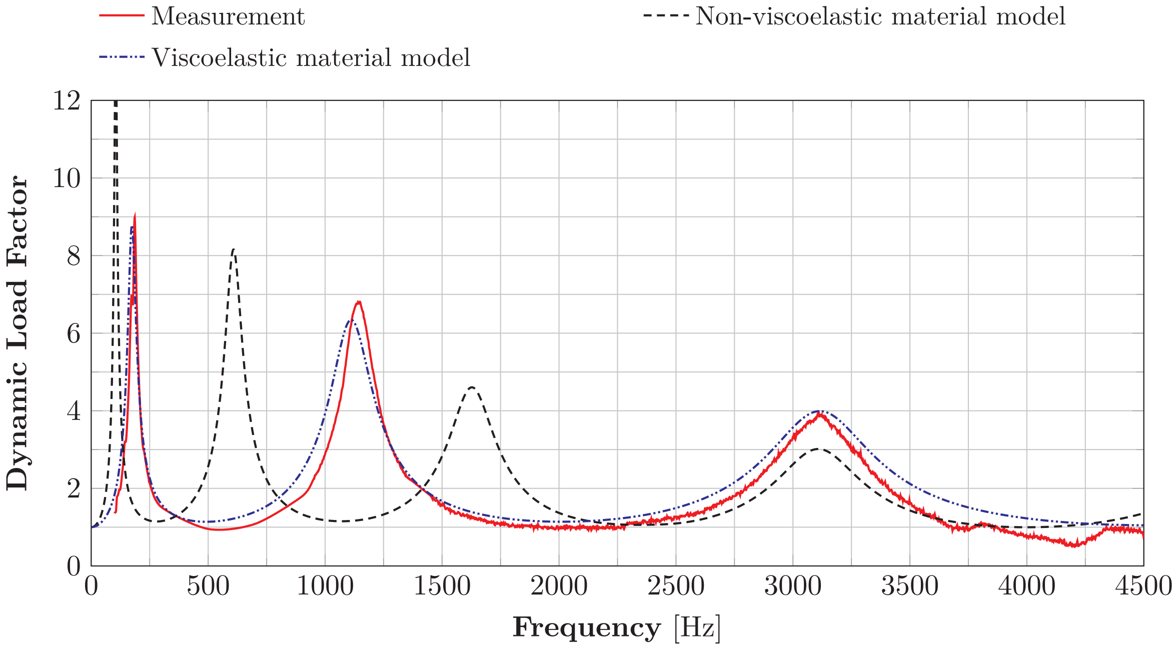

Figure 3.8.: Comparison of experimentally and numerically obtained dynamic load factor of a resin specimen using a non-viscoelastic and a viscoelastic material model.

3.2. Copper Windings

In Section 2.1.1, the general structure and function of copper windings in random-wound stators was introduced. Copper windings consist of a bundle of copper wires which are uniaxially arranged inside the stator slots and typically surrounded by an impregnation resin.

Figure 3.9(b) shows a cross-section which was extracted from an exemplary stator core (see Figure 3.9(a)). The copper wires are randomly distributed inside the stator slots.

(a) Part of stator and location of the cross-section

(b) View on cross-section $S2$

Figure 3.9.: Cross-section through copper windings of an exemplary stator segment.

In order to be able to characterize the mechanical behavior and thus the influence of copper windings on the acoustics an electric motor, the directional stiffness and damping properties of copper windings need to be investigated. In Section 2.5 different numerical and analytical homogenization techniques were introduced. Homogenization yields the quantification of homogeneous material properties that represent the effective mechanical properties of a composite material. In the following section, different homogenization techniques that are commonly used for fiber-reinforced composites will be applied to copper windings in order to quantify effective stiffness and damping properties that can efficiently be employed in subsequent structural simulations.

3.2.1. Numerical Homogenization

In Section 2.5.1 the basic principle of a representative volume element (RVE) was introduced. The RVE is a discrete micromechanical model which can be numerically solved in order to quantify effective stiffness and damping properties of a composite material.

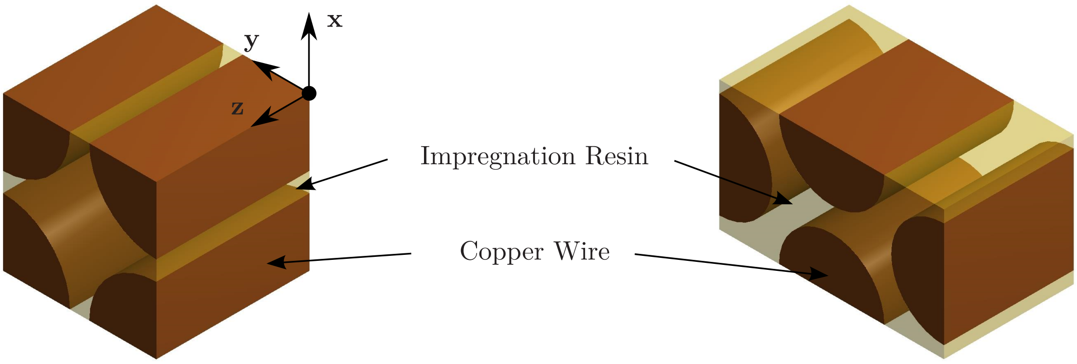

(a) Quadratic pattern

(a) Hexagonal pattern

Figure 3.10.: Schematic view of hexagonal and quadratic RVE of copper windings.

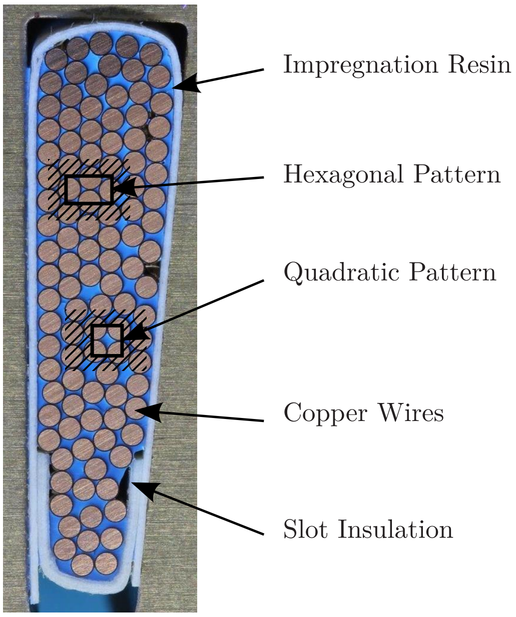

Figure 3.11.: Exemplary cross-section of copper windings that contains both characteristic wire packing patterns, the hexagonal and quadratic.

Figure 3.9 shows a close-up cross-section of copper windings as to be found in the stator slots of an electric machine. The distribution of the copper wires inside the windings follows no specific pattern but is rather stochastic. However, two generic packing patterns for fiber-reinforced structures that were introduced in Section 2.5.1.1, namely the quadratic and the hexagonal packing pattern, can be found within the cross-section (see Figure 3.11). The RVEs with periodic boundary conditions for both patterns are schematically illustrated in Figure 3.10. Both RVEs provide transversely isotropic material properties (see Section 2.5.1). However, the actual packing of the copper windings illustrated in Figure 3.9 differs from the two generic packing patterns. Thus, the influence of the actual wire distribution inside the copper windings on the effective stiffness and damping properties of the homogenized material model needs to be analyzed.

Thus, in order to investigate the influence of the wire distribution on the mechanical properties of the winding structure four different copper winding specimens were produced. Therefore Resin 1 from Section 3.1 was employed. In Figure 3.12, the cross-sections of the four specimens are illustrated. The impregnation process of the winding specimens was adapted to the impregnation process of the corresponding electric motor. The axial length of the specimens was between 79.5 mm and 80.5 mm. The outer dimensions of the cross-sections are around 4.5 mm and 19.5 mm for the height and width, respectively. Assuming an inner diameter of a copper wire of 1.07 mm filling factors around 63% are achieved inside the specimens. All cross-sections show a slightly different wire distribution.

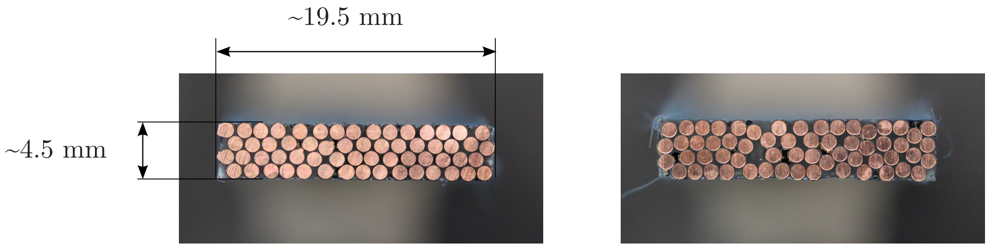

(a) Specimen 1

(b) Specimen 2

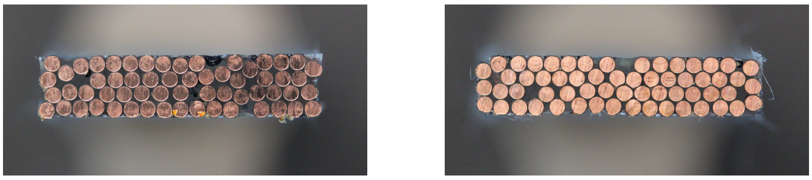

(c) Specimen 3

(d) Specimen 4

Figure 3.12.: Cross-section of copper winding specimens.

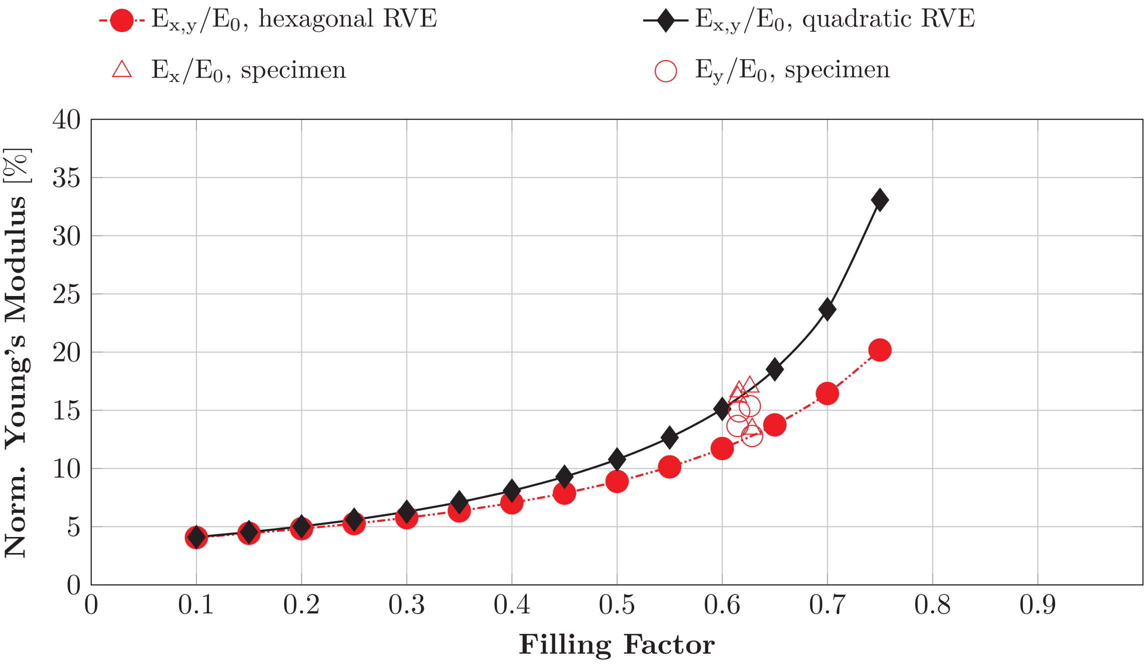

(a) Young's modulus

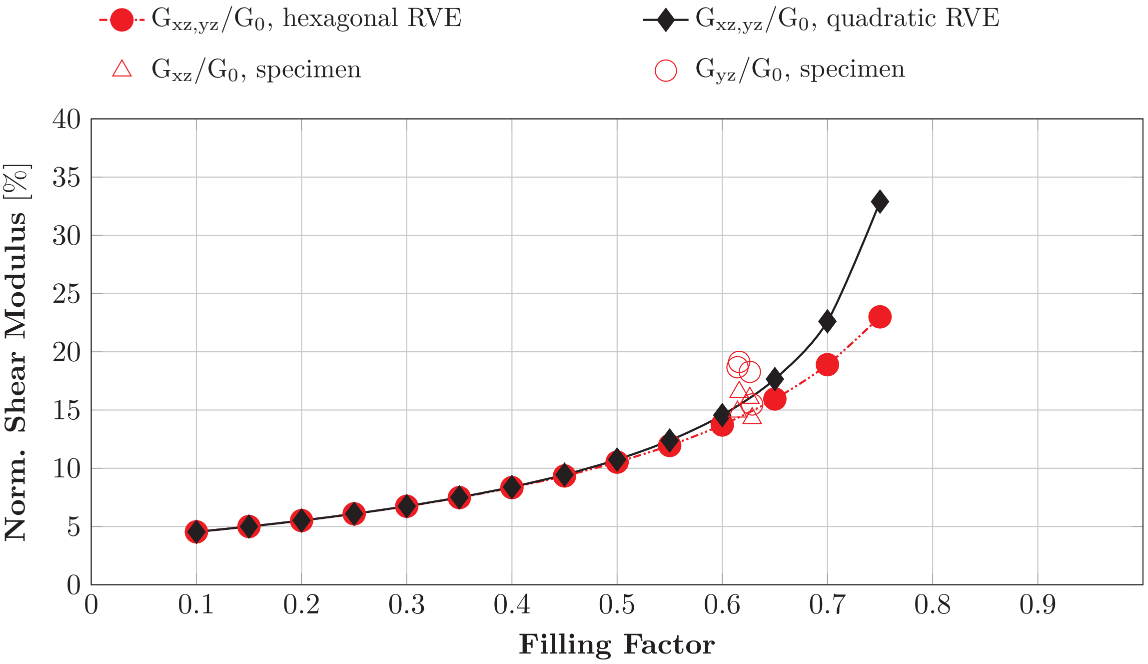

(b) Shear modulus

Figure 3.13.: Comparison between the numerically obtained normalized Young's and shear moduli as a function of the filling factor for the hexagonal and quadratic packing pattern as well as the four different copper winding specimens.

Figure 3.14 shows the numerical models of the four winding specimens. The directional stiffness and damping properties that correspond to the different wire distribution schemes of the specimens can be obtained following the procedure of the numerical RVE (see Section 2.5.1).

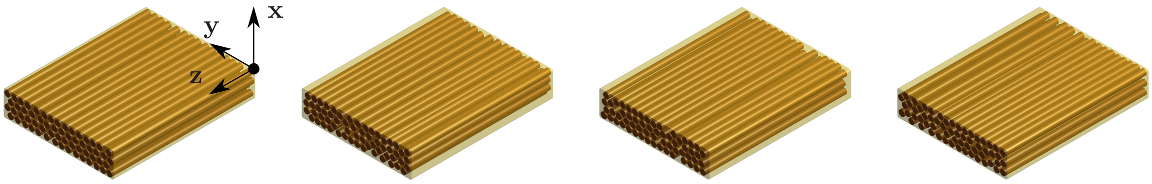

(a) Specimen 1 (b) Specimen 2 (c) Specimen 3 (d) Specimen 4

Figure 3.14.: Schematic view of RVEs of copper windings specimens.

3.2.1.1. Stiffness Properties

The effect of the packing pattern on the stiffness properties of copper windings is illustrated in Figure 3.13. Two different moduli, namely the YOUNG's modulus perpendicular to the direction of fiber $E_{x,y}$ and the shear modulus in transverse direction $G_{xz,yz}$, are given as a function of the filling factor. Both values are normalized with respect to the corresponding stiffness values of pure copper E_0 and G_0. The stiffness properties of either packing pattern at different filling factors were extracted from the solution of the numerical RVEs given in Figure 3.10 varying the diameter and thus the volume fraction of the copper wires. At the same time, the material properties of both constituents, the copper wires and the matrix material, were held constant at appropriate stiffness values. A detailed description of the solution process of the numerical RVE can be found in Appendix B. The curves show, that the quadratic packing pattern provides larger stiffness values than the hexagonal packing pattern for both moduli. The difference between the two packing patterns increases with an increasing filling factor. Both curves of generic packing patterns are compared to the effective stiffness properties of the winding specimens that were extracted from the numerical models given in Figure 3.14 and correspond to a filling factor of about 63%. It can be found that, for all specimen models, the YOUNG's modulus in x-direction slightly diverges from the YOUNG's modulus in y-direction. The same applies for the corresponding transverse shear moduli. Thus, the actual stiffness behavior of the specimens is not transversely isotropic but orthotropic. However, the elastic constants that are quantified based on the two generic wire distributions provide good approximates of the actual effective stiffness behavior despite the underlying assumption of a transversely isotropic mechanical behavior of the copper windings.

3.2.1.2. Damping Properties

Analogue to the effective directional stiffness properties, the effective directional damping properties of copper windings can be obtained from homogenization techniques. In Section 2.5.4.1, the strain energy method was introduced. It is based on the idea that each directional damping values of a composite material can be calculated from the individual material damping ratios weighted by the fraction to which the particular constituent contributes to the overall strain energy of a deformed structure. For each homogeneous load case that corresponds to a particular directional damping value, the strain energy contribution factors of all constituents can directly be extracted from the numerical solution of the RVE as shown in Appendix B.3. In Figure 3.15, two of the effective directional damping ratios are given as a function of the filling factor for both, the quadratic volume element as well as the hexagonal one. Both values are again normalized with respect to conventional loss factor values of copper η_0. The damping ratios of both constituent, the copper wire material and the matrix material, were assumed to be constant at appropriate damping values.

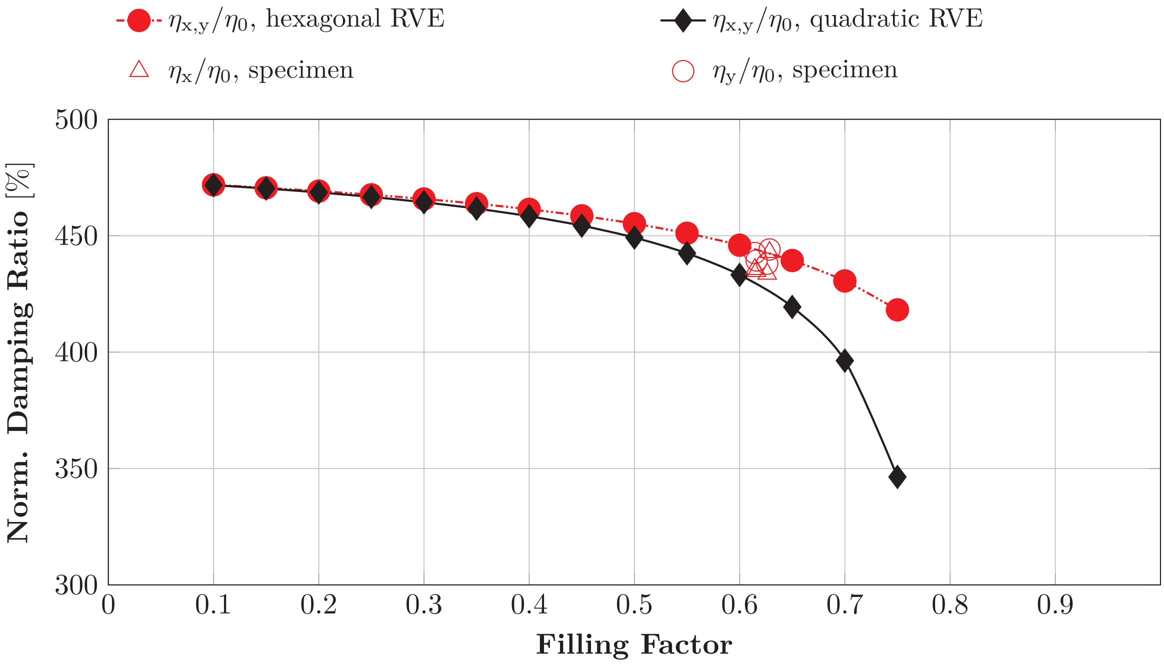

(a) Tensional damping ratio

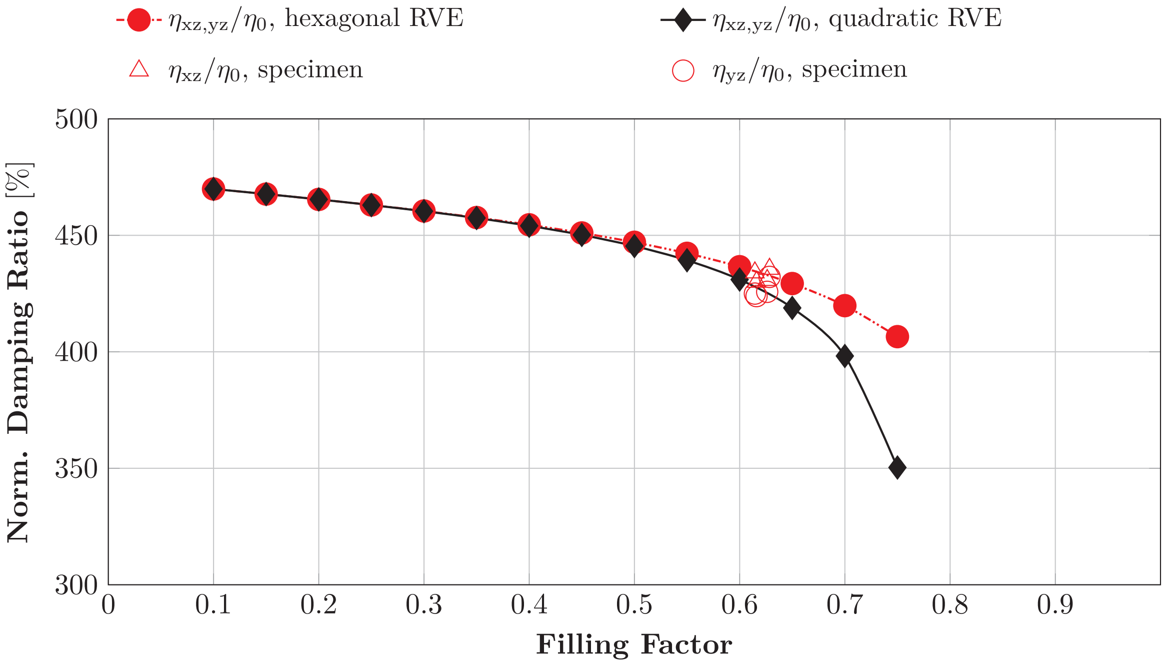

(b) Shear damping ratio

Figure 3.15.: Comparison of the numerically obtained normalized tensional and torsional damping ratios as a function of the filling factor between the hexagonal and quadratic packing pattern as well as the four different copper winding specimens.

The results are again compared to the distinct damping properties that correspond to the winding specimens shown in Figure 3.12 and were numerically obtained from the specimen models given in Figure 3.14. Again, the damping values of the copper winding specimens in x-direction slightly diverge from the damping values in y-direction. The same applies for the transverse damping properties. Thus, analogue to the stiffness properties the damping properties of the winding specimens are not transversely isotropic but orthotropic. However, the difference between the two directions is small and thus negligible. The influence of the filling factor on the damping ratio increases with an increasing filling factor. The larger the copper volume fraction, the lower the damping ratio of the composite. The hexagonal RVE provides larger damping values than the quadratic RVE. However, the difference between the two generic wire distribution models is small. All given damping values that arise from the RVEs of the actual winding specimens are close to the damping values obtained from the two generic RVEs

3.2.2. Analytical Homogenization

3.2.2.1. Stiffness Properties

In Section 2.5.2, different analytical homogenization techniques were introduced. Analytical homogenization techniques provide an efficient way to quantify homogeneous directional stiffness and damping properties of heterogeneous composite materials. Most of the approaches yield properties for fiber-reinforced composites, typically assuming a transversely isotropic behavior. In this section, the different analytical methods that were introduced in Section 2.5.2 as well as the method of cells (MOC) (see Section 2.5.3) will be evaluated regarding their applicability for the structure of copper windings. All relations for the quantification of the directional elastic constants given in Section 2.5.2 and 2.5.3 can be solved presuming the material properties of the constituents as well as the filling factor to be known. A detailed description of an exemplary solution process of the MOC can be found in the appendix of this thesis (see Appendix A). For the structure of copper windings a MOC based on four subcells will be employed as proposed by Aboudi [151] and illustrated in Figure 2.15(b) with $h_1 = l_1$ and $h_2 = l_2$.

In Figure 3.16, the two previously introduced stiffness values $E_{x,y}$ and $G_{xz,yz}$ that were obtained from the two generic RVEs (see Figure 3.10) are given as a function of the filling factor. Furthermore, the distinct stiffness properties that correspond to the four winding specimens (see Figure 3.12) are illustrated. The numerically obtained values are compared to the stiffness values that arise from different analytical approaches, namely the Voigt-Reuss method, the Chamis method, the Halpin-Tsai method, as well as Aboudi's MOC based on four subcells. The stiffness properties of both constituent, the copper wires and the matrix material, were held constant at appropriate values for all investigations. Except for the Voigt-Reuss method, all advanced analytical approaches provide stiffness parameters that are close to the RVE values and the quantities of the four winding specimens.

3.2.2.2. Damping Properties

In order to obtain effective directional damping properties from analytical homogenization techniques, the so-called correspondence principle can be applied (see Section 2.5.4.2). The basic idea of the correspondence principle involves the assumption that the stiffness and damping behavior of both constituents, the fiber as well as the matrix material, can be expressed by means of a complex stiffness matrix (see Section 2.4.1.1). The directional damping properties can then be obtained from the ratio of the corresponding loss to the corresponding storage part of the complex stiffness matrix using Equation 2.108.

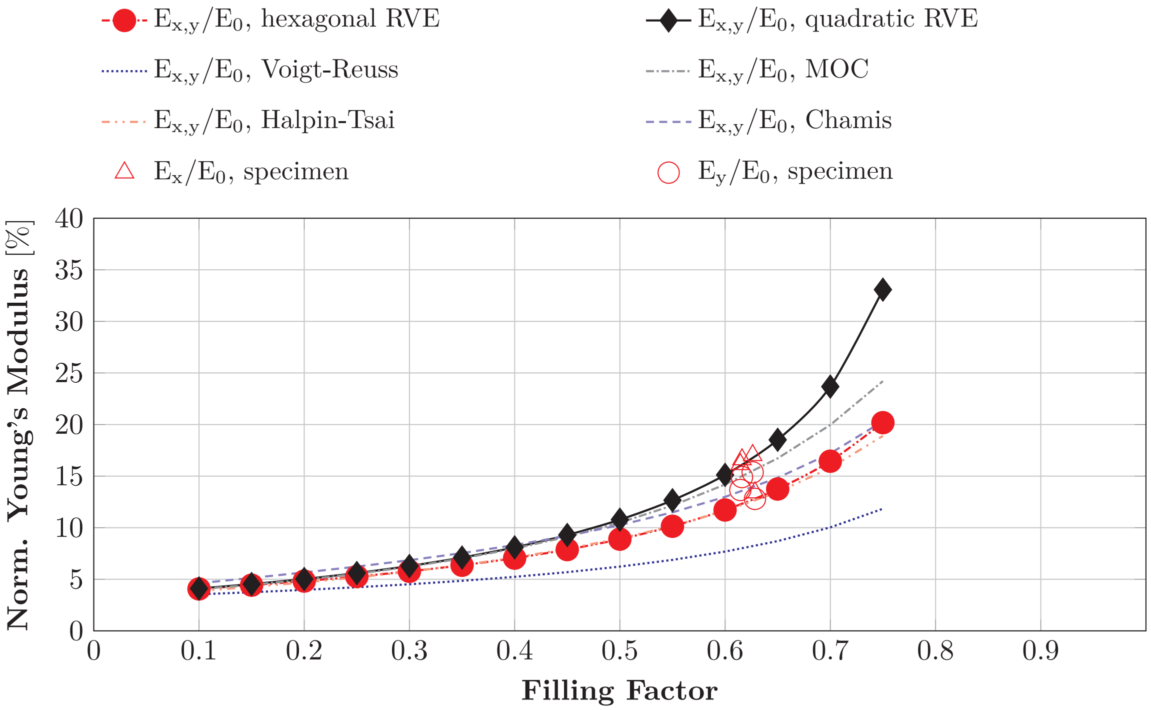

(a) Young's modulus

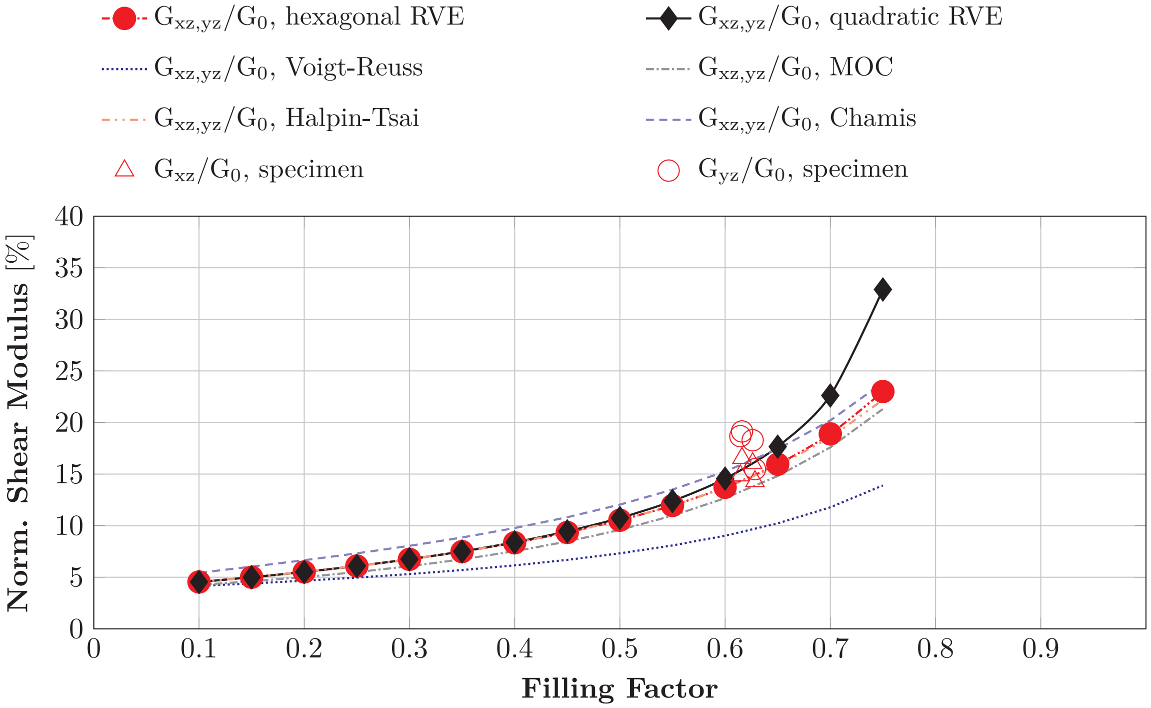

(b) Shear modulus

Figure 3.16.: Comparison of the numerically obtained normalized Young's and shear moduli as a function of the filling factor between the hexagonal and quadratic packing pattern, the four different copper winding specimens as well as four different analytical methods.

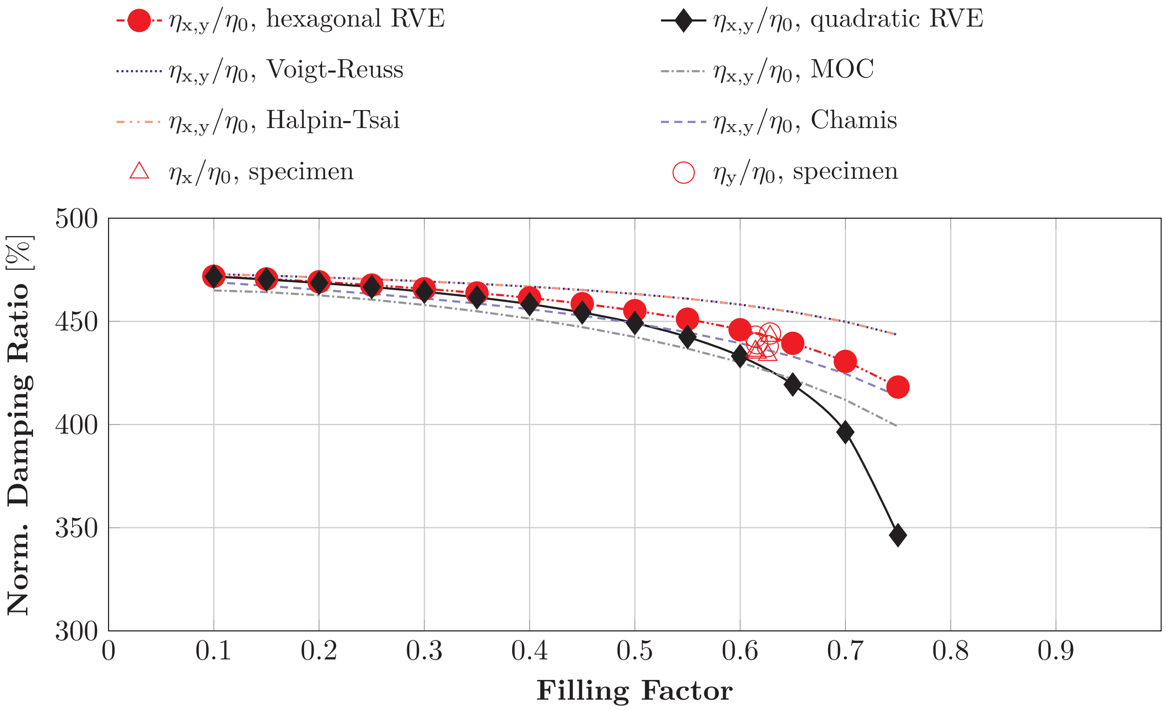

(a) Tensional damping ratio

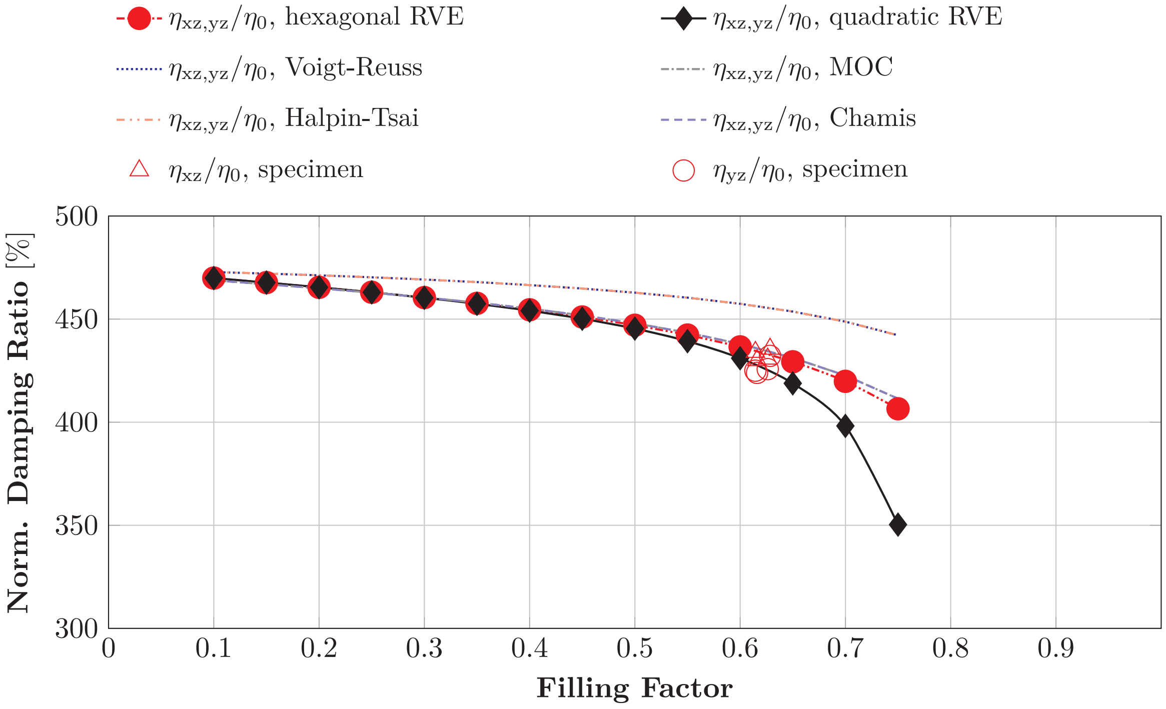

(b) Shear damping ratio

Figure 3.17.: Comparison of the numerically obtained normalized tensional and torsional damping ratios as a function of the filling factor between the hexagonal and quadratic packing pattern, the four different copper winding specimens as well as four different analytical methods.

Detailed information about the use of the correspondence principle attached to analytical homogenization techniques can be found in Appendix A.2. In Figure 3.17 two independent directional damping properties are given as a function of the filling factor for all four analytical homogenization approaches as well as the numerical RVEs from Section 3.2.1. Except for the the Halpin-Tsai method and the Voigt-Reuss method the accordance between the analytical and numerical approaches is good. Both, the Halpin-Tsai method as well as the Voigt-Reuss method, provide damping ratios which are slightly above the values provided by the other methods.

3.2.3. Validation of Modeling Approach for Copper Windings

In Section 3.1 the viscoelastic character of the impregnation resin was introduced. It was shown that the consideration of the temperature- and frequency-dependent behavior of the resin is necessary in order to sufficiently represent the stiffness and damping of the material and thus provide accurate simulation results (see Figure 3.8).

In the previous section, different homogenization techniques were evaluated regarding their applicability for copper winding structures as to be found in electric machines. It was shown that the orthotropic stiffness and damping values that arise from the actual distribution of the wires inside the stator slots can well be approximated by the transversely isotropic mechanical properties obtained from numerical RVEs with a periodic fiber distribution pattern, like the quadratic or hexagonal packing pattern (see Figure 3.10). Furthermore, it was shown that advanced analytical approaches, like the Chamis method or the method of cells, efficiently provide good approximates of the numerically obtained effective stiffness and damping properties of impregnated copper windings.

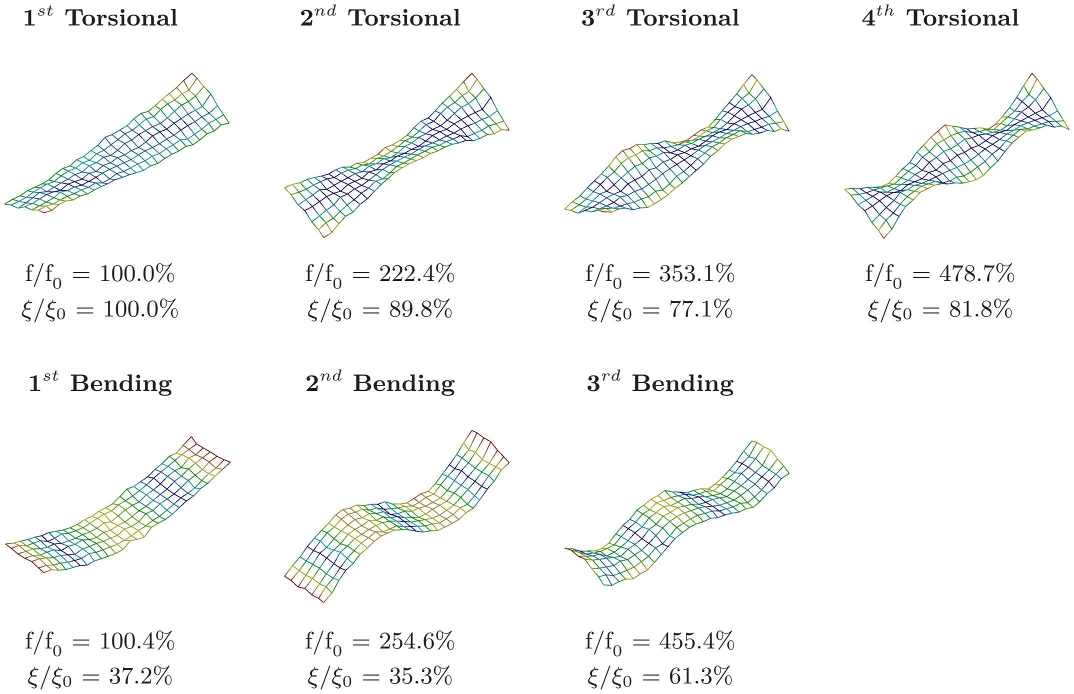

Figure 3.18.: Schematic view of mode shapes, mean eigenfrequencies and mean modal damping factors of experimental modal analysis of copper windings specimens at $T = 23°\mathrm{C}$.

However, all above homogenization techniques involve fundamental assumptions like the ideal connection between wires and matrix material or the negligibility of the wire coating.

Thus, in order to further evaluate the different modeling techniques regarding their capability of an accurate representation of the dynamic behavior of copper windings the general modeling technique needs to be validated. Therefore, an experimental modal analysis was performed on each of the four windings specimens that were given in Figure 3.12.

3.2.3.1. Experimental Modal Analysis of a Copper Winding Specimen

The dynamic excitation of the four specimens was provided by a small piezo element that was attached to one end of the specimen. The system was supported by a soft bedding layer that minimized the influence of the environment and hence provided almost free boundary conditions. The ambient temperature was held constant at 23℃. The dynamic behavior of the specimens was measured in a frequency range from 100 Hz to 15 kHz using a 1D-LSV. Three bending and four torsional modes were uniquely identified inside the given frequency range. The experimentally obtained mode shapes, the corresponding average eigenfrequencies as well as the average modal damping ratios are given in Figure 3.18. Both values, the eigenfrequencies as well as the modal damping ratios, are normalized with respect to the corresponding values of the first torsional mode.

3.2.3.2. Stiffness Properties

In order to validate the general modeling technique as well as the above introduced numerical and analytical homogenization techniques, five different numerical modal analyses were performed.

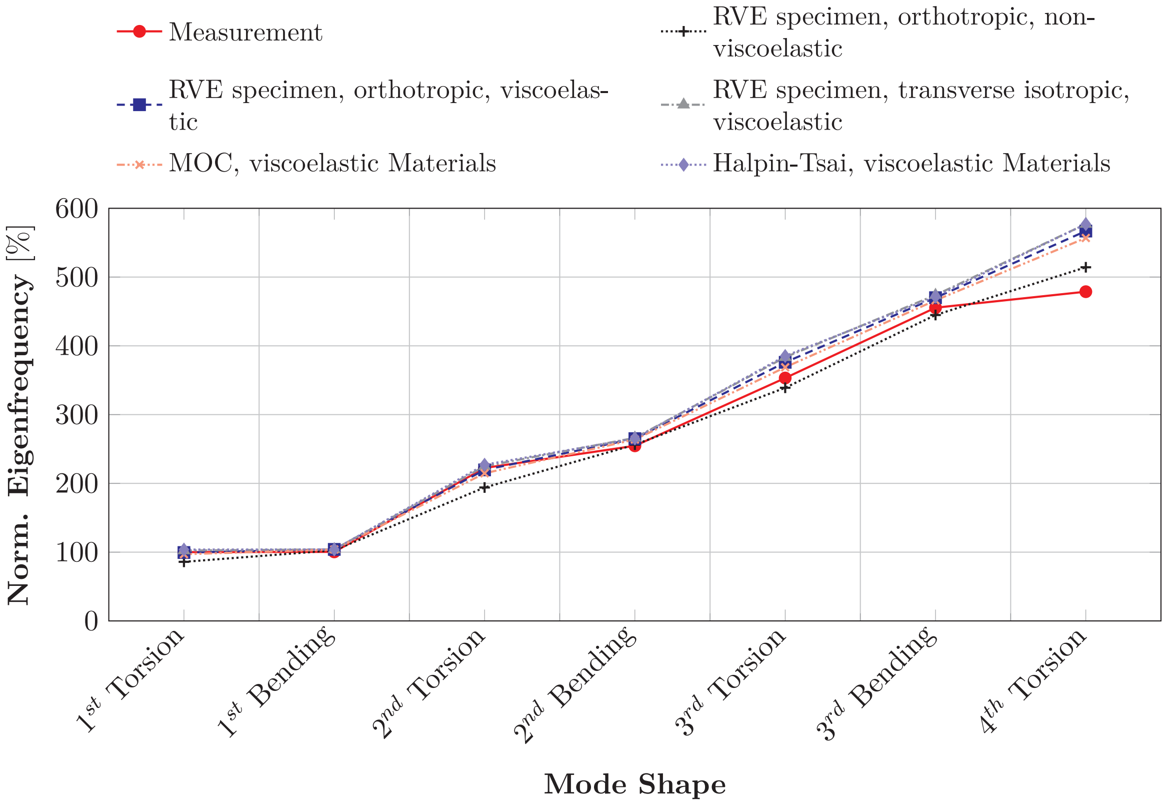

Figure 3.19.: Comparison of experimental and numerical normalized eigenfrequencies of the copper windings specimens for different modeling approaches.

In Figure 3.19 the corresponding eigenfrequencies of the different numerical modal analyses are compared to the experimentally obtained average eigenfrequencies of the winding specimens. Three of the five simulation models are based on the effective stiffness properties that arise from the winding models given in Figure 3.14. However, two of the three model consider the material to behave orthotropic while the other one assumes transversely isotropy. The orthotropic material properties are obtained from the average directional properties of all four specimens. The same applies for the transversely isotropic model assuming the transverse directions, x and y, to be equal. The numerically homogenized models are compared to the MOC based on four subcells and the Halpin-Tsai model. Four of the five models consider viscoelasticity meaning the frequency dependent stiffness and damping characteristics of the matrix material Resin 1 (see Section 3.1.1). The non-viscoelastic model neglects the frequency-dependency by assuming the resin to constantly show quasi-static material properties.

The curves in Figure 3.19 show, that all different models provide eigenfrequencies which are in good accordance with the measured eigenfrequencies. As given in Figure 3.18 three of the seven eigenmode shapes were found to be bending modes. The corresponding eigenfrequencies are significantly influenced by the effective Young's modulus in fiber direction E_z. This particular elastic constant is known to be analytically well predictable and is strongly influenced by the Young's modulus of copper. Thus, all homogenization techniques show good results predicting the eigenfrequencies of the pure bending modes. However, the torsional modes are dominantly influenced by shear effects. Thus, the influence of the resin is noticeable. Consequently, the modeling approach neglecting the viscoelastic behavior leads to increased errors predicting the eigenfrequencies of all torsional mode shapes.

3.2.3.3. Damping Properties

A frequently used approach that is employed to validate modal damping ratios is the strain energy method which was introduced in Section 2.5.4.1. The total strain energy of each of the identified mode shapes can be decomposed into its directional strain energy fractions. It was found that a particular modal damping ratio can be composed from the directional damping ratios the same way the total strain energy of the corresponding mode can be composed from the directional strains energies (see Section 2.5.4.1).

In Figure 3.20, the decomposition of the total strain energy of each mode shape given in Figure 3.18 into its directional strain energy fractions is illustrated. The diagram shows that the damping of the bending modes significantly depends on the damping ratio in fiber direction while the damping of the torsional modes is mainly influenced by the shear damping ratios even though the dependency decreases for higher mode orders. In Figure 3.21, the modal damping ratios of the experimental modal analysis are compared to the synthetically composed modal damping ratios that were derived from the above models. The bending modes are much less damped than the torsional mode shapes. The consideration of viscoelasticity significantly influences the model accuracy. Using the quasi-static damping ratio of the impregnation resin, the damping of the copper windings is significantly overestimated for all different mode shapes. In contrast, all analytical and numerical approaches considering the frequency-dependent damping of the matrix material show good accordance with the measured data. The actual wire distribution of the winding specimens and hence the orthotropic material behavior of the copper windings seems to be negligible. Hence, transverse isotropy can be assumed.

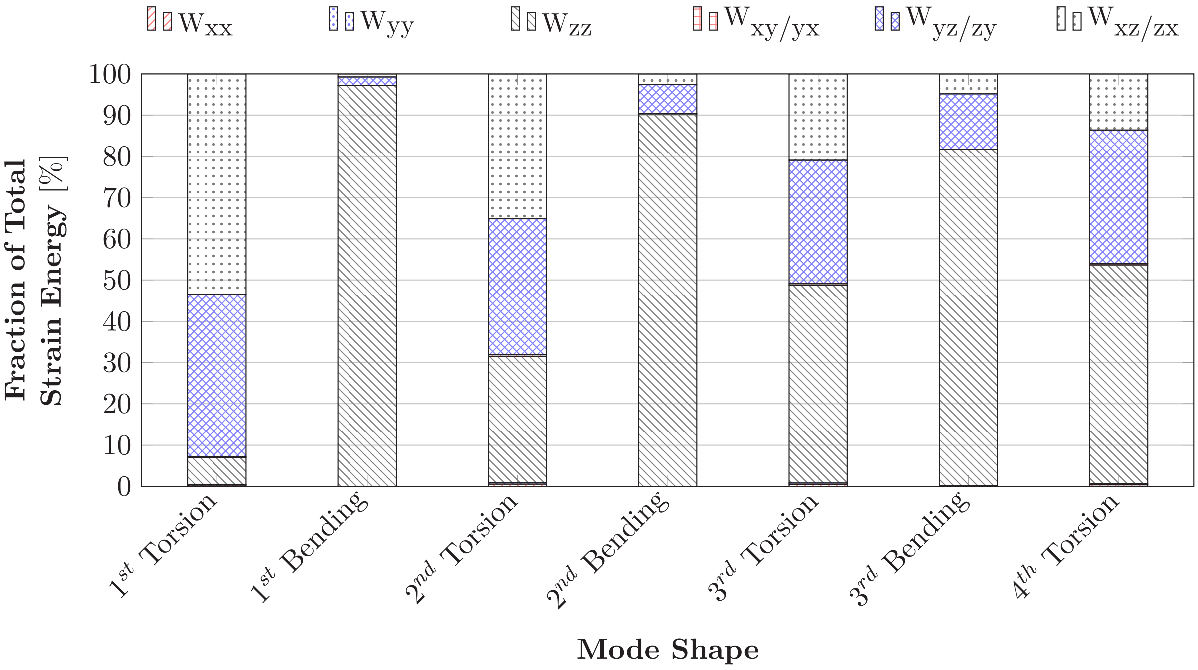

Figure 3.20.: Overview of the directional strain energy fractions for the different mode shapes.

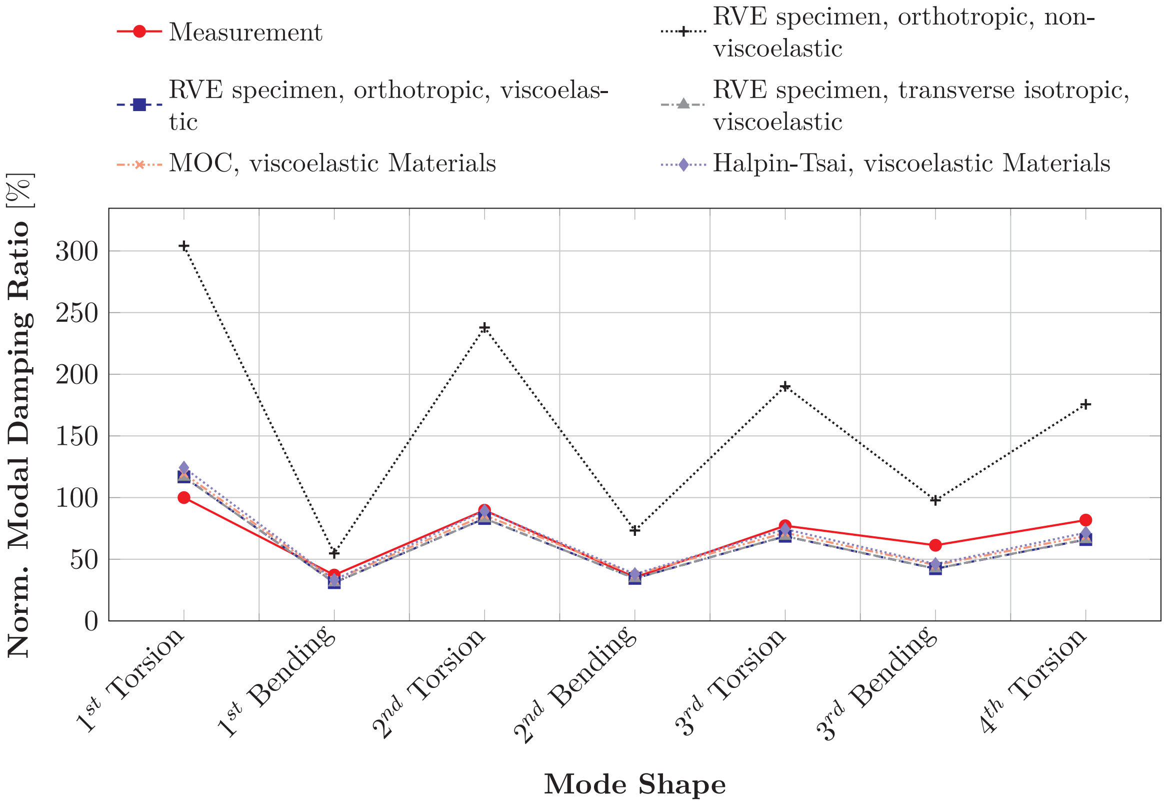

Figure 3.21.: Comparison of the experimentally and numerically obtained normalized modal damping ratios of copper windings for different modeling approaches.

3.2.3.4. Evaluation of the Modeling Approaches

Based on the previous observations and findings general recommendations on the modeling of copper windings can be made:

- The actual effective behavior of the windings is orthotropic. Nevertheless, the error caused by the assumption of transverse isotropy is negligible. Thus, in all following investigations a transversely isotropic effective mechanical behavior of the copper windings will be presumed.
- The consideration of viscoelasticity is mandatory for the accurate representation of the impregnation resin. However, the influence of viscoelasticity on the total composite stiffness, especially in fiber direction, could not uniquely be proven due to disadvantageous mode shapes of the experimental modal analysis. Nevertheless, the effect of viscoelasticity on the damping behavior was found to be significant.
- Advanced analytic homogenization techniques like the MOC showed good accordance with the more detailed numerical homogenization techniques and hence are preferable due to the significant reduction of computational and model preparation efforts.
- The effective damping values were well approximated by the homogenization techniques. Nevertheless, only one of the many damping effects in fiber-reinforced structures, namely the material-inherent damping, was considered. Damping of fiber-reinforced composites much depends on the quality and continuity of the matrix material. In order to generate reliable predictions for the damping of copper windings as they are applied in electric motors, further investigations on the microscopic structure need to be made.

3.3. Laminated Steel

In Section 2.1.1, the basic mechanical structure of electric motors was introduced. In order to reduce eddy current losses, the stator iron core does not consist of monolithic steel but is assembled by multiple single steel sheets that form a laminated steel package. The mechanical properties of the laminated steel package differ from the mechanical properties of a monolithic material. Thus, attention has to be laid on an appropriate modeling of the laminated steel package. In order to reduce the model complexity, the laminated steel is typically treated as a homogeneous material[2]. The corresponding material properties aim at the sufficient representation of the effective stiffness and damping behavior of the underlying heterogeneous structure. The quantification of homogeneous material properties is elaborate since the contact topology between the steel sheets is statistical and the normal and tangential stiffness properties of the contact areas were found to be strongly nonlinear [179]. Öztürk and Bahadir has even identified an influence of magnetostriction on the contact topology and hence on the overall mechanical behavior of the laminations [180]. In most practical applications the effective material properties are reversely quantified based on an experimental modal analysis of the corresponding stator iron core [21, 38]. However, the characteristic eigenmode shapes that occur in cylindrical structures do not allow an entire identification of the transversely isotropic stiffness characteristics of the laminated steel stack. Singhal

---

[2] Except for very specific applications like the combination of rigid annular disks and torsional springs in order represent the reduced torsional stiffness of a rotor laminated iron core [178]

et al. and Ede et al. extracted material data based on experimental investigations on a laminated rotor core which shows more advantageous eigenmode shape and allows the quantification of the overall effective stiffness matrix of the laminated steel package [181, 182]. Garvey used a prismatic laminated specimen to experimentally investigate the dynamic behavior of laminated steel [183, 184]. Employing a special test application Garvey was able to measure the influence of the clamping pressure on the directional stiffness and loss factor of a laminated steel stack. Garvey's investigations found the insulation varnish which covers the steel sheets to have a significant influence on both, the effective stiffness and the effective damping properties. Giet et al. used a similar test configuration in which the laminations were held together by a varnish that hardens at high temperatures [185]. Giet et al. performed an experimental modal analysis as well as a static tension test on each specimen. The elastic moduli which were extracted from the static tests were found to be much lower than the dynamic ones. Tang et al. identified the effective stiffness properties of a laminated steel stack using ultrasonic waves [186]. However, the stiffness values obtained from the ultrasonic data were much higher than the properties derived from other methods. Millithaler et al. analyzed the derivation of effective stiffness properties from analytical homogenization methods [187]. Millithaler et al. assumed the layer between the steel sheets to be equivalent to the thin insulation varnish layer that covers the steel sheets and hence provided a continuous heterogeneous composite structure. However, multiple investigations on the contact topology of laminated steel packages have found the contact area to be strongly heterogeneous and thus significantly more compliant than the underlying contact materials which refutes Millithaler et al.'s assumptions. Wang et al.'s investigations on the quantification of homogeneous material properties of sandwich structures that consist of two thick annular plates separated by a thin viscoelastic layer also involve the use of homogenization techniques [188]. In order to provide directional damping properties, Wang employed complex moduli for the constituents following the correspondence principle (see Section 2.5.4.2). Wang et al. found the damping properties of the composite structure to be significantly influenced by the frequency-dependent damping properties of the viscoelastic layer.

For production and vibrational reasons, the laminated steel stack is subjected to a normal prestress (see Section 2.1.1.2). Multiple scientific works have investigated the influence of the normal prestress on the dynamic behavior of the structure. Wang and Williams analyzed the influence of the clamping pressure and number of steel sheets on the eigenfrequencies of laminated structures and found a significant correlation [189]. They furthermore pointed out the strong correlation between the damping of laminated structures and the clamping pressure as well as the number of steel sheets [190]. Millithaler et al. carried out homogeneous stiffness properties for a prestressed laminated steel stack based on analytical homogenization techniques and a continuous contact layer model [191]. However, Walker et al. showed that the actual contact stiffness between two steel sheets varies depending on the prestressing that is locally preserved within the structure and hence yields a more complex model [192]. Cepon et al. and Pirnat et al. tried to quantify homogenized material properties for a prestress laminated steel stack based on a linear contact model between the steel sheets [193, 194]. However, no further remarks on the type of contact model are given. The contact parameters that determined the directional stiffness and damping of the contact area were obtained from experimental modal analyses neglecting frequency dependency. The character of the nonlinear force-deflection relation of the sheet contacts and hence the contact stiffness was extensively investigated by Luchscheider et al.. Combining different contact models Luchscheider et al. developed a method that provided values for the normal and tangential contact stiffness for a coated and uncoated steel sheet configurations based on an exponential ansatz that took into account the contact roughness of the metal sheet surface [195, 196]. In later publications Luchscheider et al. investigated the use of the developed contact model in numerical homogenization methods [197, 198]. However, the method presumes the measurement of the surface roughness which is highly elaborate and significantly varies depending on the stacking configuration [199].

Despite the variety of different research works on the topic of effective material properties of laminated steel, no consistent procedure exists that efficiently allows the quantification of directional stiffness and damping values of laminated steel from the material properties of the underlying constituents and the consideration of further circumferential parameters like the normal prestress. Clearly, the crucial parameter in developing a suitable and transferable homogenization procedure is the definition of the non-linear stress-strain-relation of the sheet contacts. In the following section two different analytical expressions will be developed that yield the directional stiffness values of impregnated and non-impregnated laminated steel based on the normal prestress that the laminated steel package is subjected to. The expression will be based on the investigation of the dynamic behavior of a prismatic laminated steel specimen as it is shown in Figure 3.22.

3.3.1. Prismatic Laminated Steel Sheet Specimen

In order to investigate the influence of the normal stress on the dynamical behavior of laminated steel, a generic laminated steel specimen was developed. The specimen was designed to allow the convenient variation of the normal prestress and deduce the prestress' effect on the lamination stiffness by measuring the system eigenfrequencies.

3.3.1.1. Geometry and Configuration

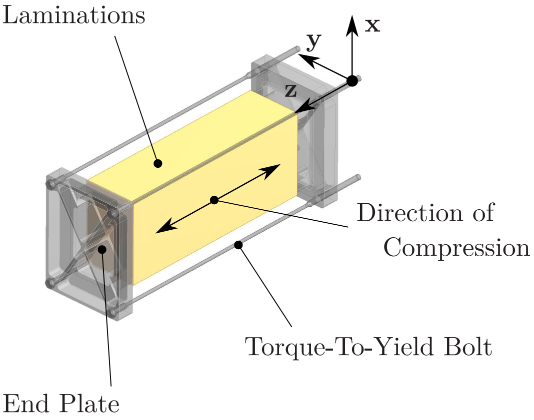

Figure 3.22.: Isometric view of laminated specimen structure.

In Figure 3.22, the geometry of the laminated steel specimen is shown. It consist of a prismatic laminated steel core, two end plates at each side of the laminated steel and four torque-to-yield bolts which are periodically arranged around the laminations. The dimensions of the specimen are given in Figure 3.23. The cross section of the laminated steel was chosen to be rectangular in order to avoid rotational symmetry and thus double eigenvalues and to form plane surfaces whose dynamics can conveniently be measured by a 1D-LSV. The dimensions of the rectangular cross section given in Figure 3.23 are sufficiently large in order to minimize the influence of edge effects. The two end plates are designed to be identical. Both are symmetric with respect to the x and y-axis and made of aluminum to avoid a significant mass influence. The four torque-to-yield bolts are periodically arranged at the outer corners of the end plates in order to impose a homogeneous axial stress field inside the laminated steel package. By tightening the screws, the prestress can be varied between 1 MPa and 6 MPa. The current prestress value can be deduced from the overall screw lengthening. The prismatic laminated steel core can consist of different electric steel sheet types regarding the material, coating or the steel sheet thickness. The entire system can be exposed to an impregnation process.

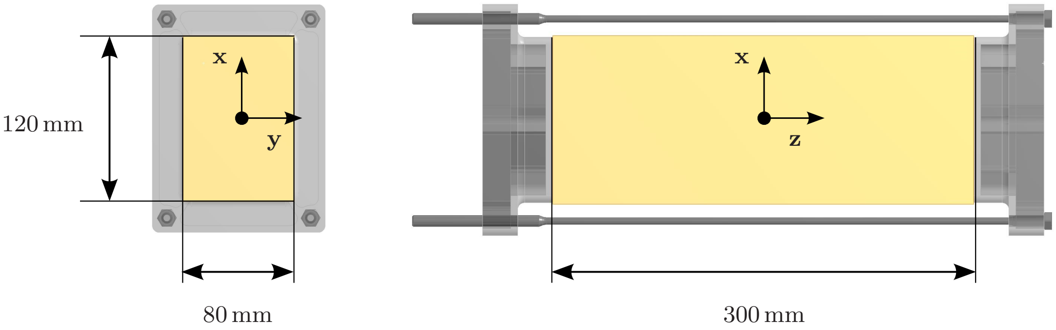

(a) Top view (b) Side View

Figure 3.23.: Geometry and measures of generic laminated specimen.

3.3.1.2. Free Vibration Analysis

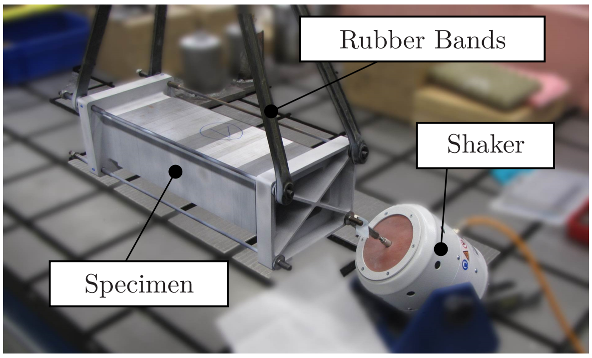

Figure 3.24.: Setup of modal analysis of laminated specimen.

In Figure 3.24, the measurement setup of the experimental modal analyses is illustrated. The specimens were elastically mounted by rubber bands providing almost free boundary conditions. The excitation of the structure was diagonally imposed by an electromagnetic shaker at one vertex of the front plate. All modal analyses were performed in a frequency range from 100 Hz to 3 kHz. Two different lamination configurations were tested. The first was made of 0.2 mm thick silicon steel sheets, the second one of 0.3 mm. Table 3.1 gives an overview of the different specimen configuration that were investigated for each of the steel sheet thicknesses.

In Figure 3.25 the basic mode shapes of the prismatic specimen are illustrated. All specimen configurations showed the same basic mode shapes. However, the corresponding eigenfrequencies diverged based on the stiffness properties of the particular specimen configuration. Each mode shape corresponds to one particular directional stiffness value which determines the eigenfrequency. For the bending an compression modes the stiffness value is the YOUNG's modulus E_z in stack direction and for the torsional mode shapes it is the shear modulus $G_{xz,yz}$. Thus, the elastic constants that correspond to a particular eigenmode shape can uniquely be identified based on the mode shape and the eigenfrequency. During the experimental modal analysis only one of the two different lateral surfaces of the prismatic specimen was measured using a 1D-LSV. Thus, based on the measurement technique of a 1D-LSV which can only measure out-of-plane oscillations, the first and second bending mode around the x-axis could only be identified based on the oscillation of the two end plates (see Figure 3.25). Due to the numerous mode shapes of the specimen that show a similar oscillation of the end plates, the two previously mentioned mode shapes could not uniquely be identified during the analysis of the measurement data and hence will be neglected in the following investigations.

Table 3.1.: Overview of the different specimen configurations that were analyzed.

	Experiment 1	Experiment 2	Experiment 3
Specimen	**Reproducibility Measurement**	**Prestress Dependency**	**Impregnation Dependency**
1	3.6 MPa, non-impregnated	1.6 MPa, non-impregnated	1.6 MPa, impregnated
2	3.6 MPa, non-impregnated	2.6 MPa, non-impregnated	2.6 MPa, impregnated
3	3.6 MPa, non-impregnated	5.7 MPa, non-impregnated	5.7 MPa, impregnated

In order to validate the reproducibility of the dynamic behavior of the laminated steel specimens an experimental modal analysis was performed on all three given specimens of both kinds of sheet thicknesses. Therefore, all specimens were subjected to a normal stress of 3.6 MPa. The corresponding mode shapes and measured eigenfrequencies of the reproducibility measurements are listed in the appendix of this thesis (see Section D). Due to low reproducibility, the 0.3 mm-stack was not further investigated inside this research work.

1st Bending, x **1st Bending, y** **1st Torsional** **Compression**

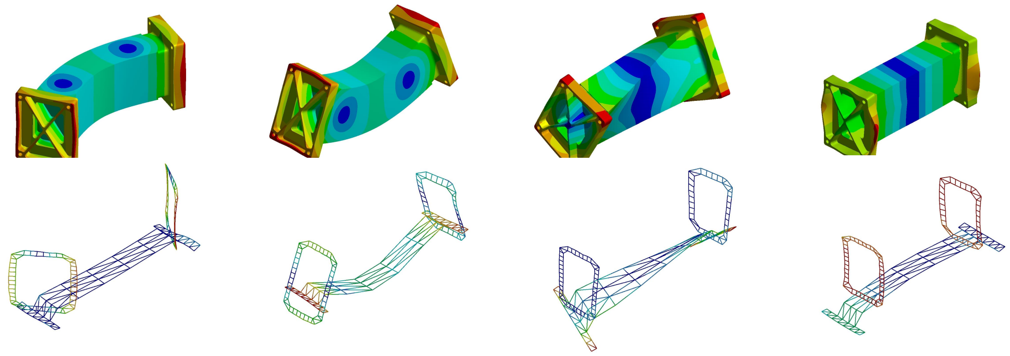

2nd Bending, x **2nd Bending, y** **2nd Torsional**

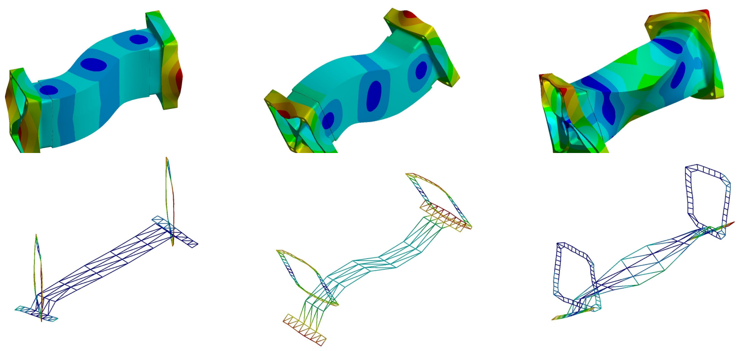

Figure 3.25.: Mode shapes of the generic laminated steel package specimen.

3.3.2. Analysis of Non-Impregnated Laminated Steel

In Table 3.1, the different specimen configurations were listed. In order to investigate the influence of the prestress on the dynamic behavior of the laminations, the three different specimens that correspond to the steel sheet thickness of 0.2 mm were set to the three different prestress values, namely 1.6 MPa, 2.6 MPa, and 5.7 MPa. In a subsequent experimental modal analysis the eigenfrequency values of the three specimens were measured using a 1D-LSV. All generic mode shapes given in Figure 3.25 could uniquely be assigned to a particular eigenfrequency.

Since the eigenfrequency that corresponds to a particular mode shape is determined by only one directional stiffness value of the laminated steel stack the corresponding directional stiffness value could be identified using model updating. Therefore, a structural dynamic simulation model of the specimen configuration including the end plates and the torque-to-yield bolts was set up. Presuming the material properties of the end plates and the torque-to-yield bolts to remain constant over all measurements, the particular directional stiffness value of the laminated steel core was quantified by minimizing the difference between the numerical and experimental eigenfrequency of each mode shape. For each specimen three frequency-dependent values of the YOUNG's modulus E_z in stack direction were obtained from the two bending modes and the compression mode while two frequency-dependent values of the shear modulus $G_{xz,yz}$ in transverse direction were extracted from the two torsional mode shapes (see Figure 3.25). Thus, from the measurements the frequency- and prestress-dependency of the two directional stiffness values could be evaluated. In Figure 3.26, the YOUNG's modulus E_z in stack direction as well as the shear modulus $G_{xz,yz}$ are given as a function of the frequency and the prestress. Both values are normalized with respect to the corresponding isotropic values of silicon steel E_0 and G_0. The eigenfrequency values are again normalized with respect to the first measured eigenfrequency of the system f_0. The eigenfrequency values of the first measurement at a prestress of 3.6 MPa were considered in an average sense. The results show that the prestress significantly influences the stiffness behavior of the structure. In contrast, the the excitation frequency only has a minor effect on the elastic constants.

Assuming a linear dependency in both dimensions, namely the frequency-dimension and the prestress-dimension, the relation between the prestress, the frequency, the directional stiffness values can be approximated by a plane as illustrated in Figure 3.26.

The plane equation as well as the coefficient of determination B are given as

$$\frac{E_z}{E_0} = 0.4349\ \frac{\%}{\mathrm{MPa}} \cdot p_{pre} + 0.0045 \cdot \frac{f}{f_0} + 0.4188\ \%, \quad B^2 = 0.9768 \tag{3.2}$$

$$\frac{G_{xz,yz}}{G_0} = 0.3403\ \frac{\%}{\mathrm{MPa}} \cdot p_{pre} + 0.0096 \cdot \frac{f}{f_0} + 1.6957\ \%, \quad B^2 = 0.9731 \tag{3.3}$$

3.3.3. Analysis of Impregnated Laminated Steel

It was shown, that exposing a laminated stator structure to an impregnation process, the cavities inside the contact gap between the steel sheets are penetrated by the impregnation resin (see Figure 3.1). Thermosetting impregnation resins typically behave viscoelastic. The frequency- and temperature-dependent stiffness and damping behavior of viscoelastic materials was introduced in Section 2.4. Various scientific works have pointed out the effect of a viscoelastic layer on the general mechanical properties of laminated composites [200–210]. CHEN ET AL. investigated the influence of a viscoelastic layer on the general effective damping properties of laminated steel sheets [211]. CHEN ET AL. found the overall damping of the composite to follow the frequency dependent damping properties of the viscoelastic layer. Similar observations were made by El Mahi et al. and Wang et al. [171, 188].

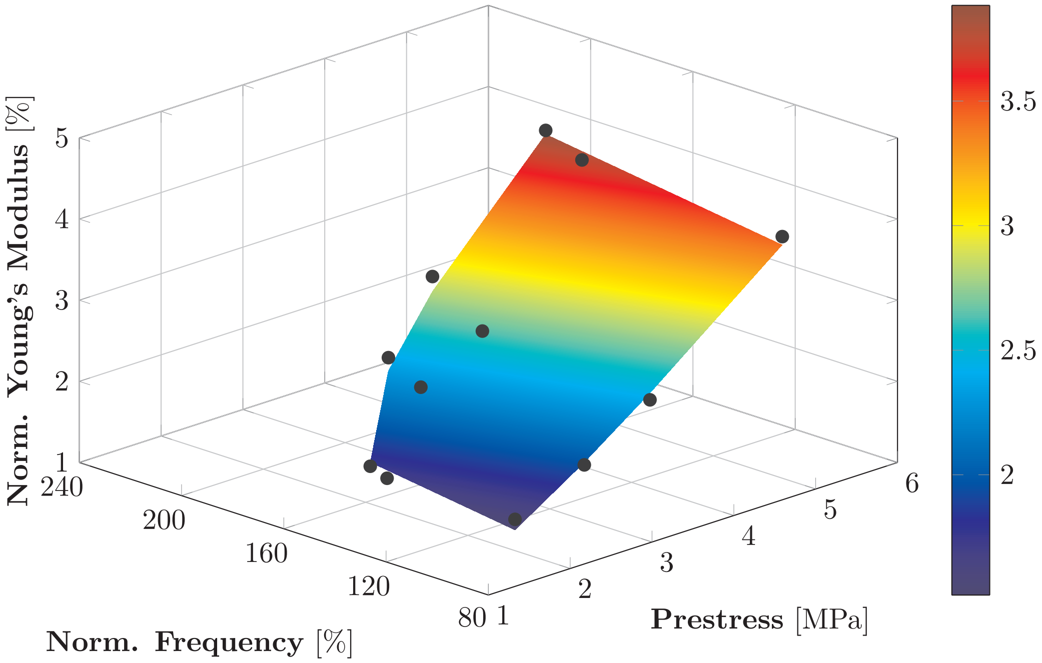

(a) Linear interpolation of normalized Young's modulus

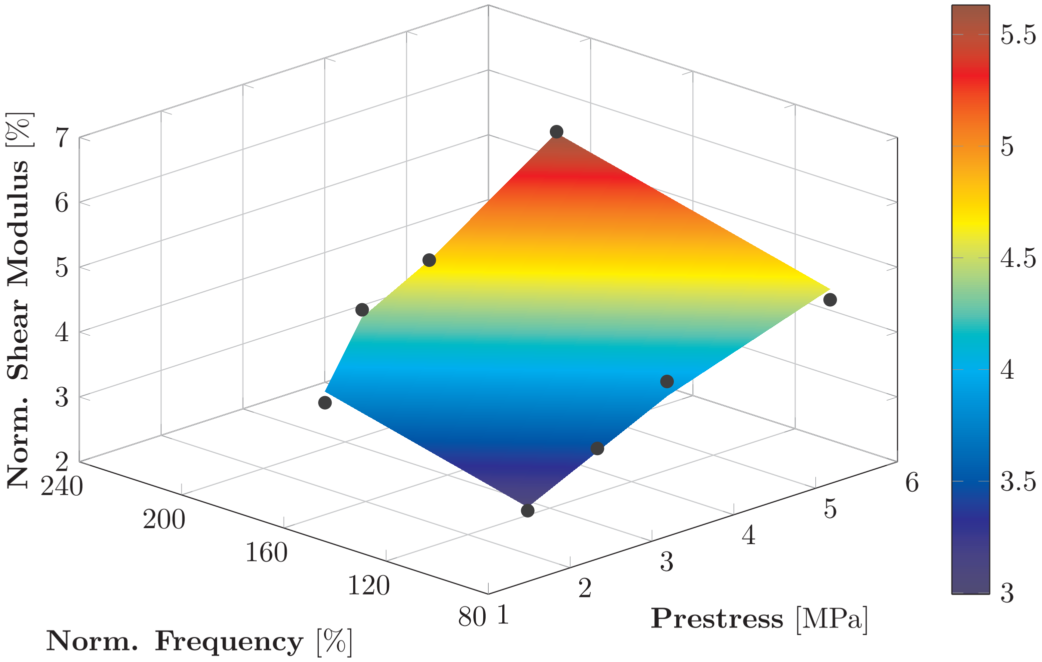

(b) Linear interpolation of normalized shear modulus

Figure 3.26.: Linear interpolated normalized Young's and shear moduli of non-impregnated laminated steel stack as a function of the normal prestress and the normalized frequency

In order to investigate the influence of the impregnation resin on the mechanical properties of the three prismatic laminated steel specimens that were introduced in Section 3.3.1 were exposed to an impregnation process as it is commonly employed for series electric machine stators. Therefore, Resin 2 which was introduced and characterized in Section 3.1 was utilized. In order to further investigate the prestress dependency which is assumed to influence the contact topology between the steel sheets, the three specimens were set to different prestress conditions before being exposed to the impregnation resin. Figure 3.27 shows an exemplary specimen after the impregnation process. Subsequently to the impregnation, an experimental modal analysis was performed, analogue to the modal analysis described in Section 3.3.1.2 for the non-impregnated specimen. Again, the eigenfrequencies were assigned to the generic mode shapes that were illustrated in Figure 3.25. After the modal analysis was performed, the intrusion of the impregnation resin into the lamination was analyzed. In the left part of Figure 3.28 a micrograph of an exemplary disassembled electrical steel sheet taken from the laminated steel specimen is shown.

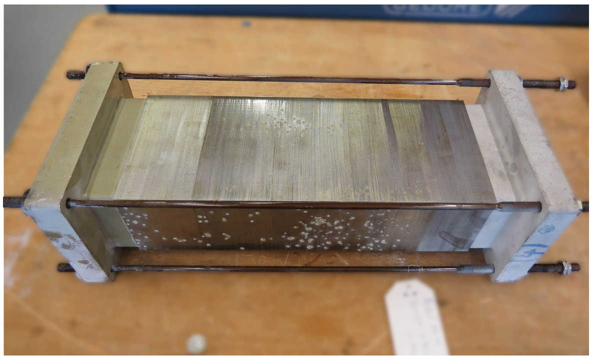

Figure 3.27.: Laminated specimen after the impregnation process.

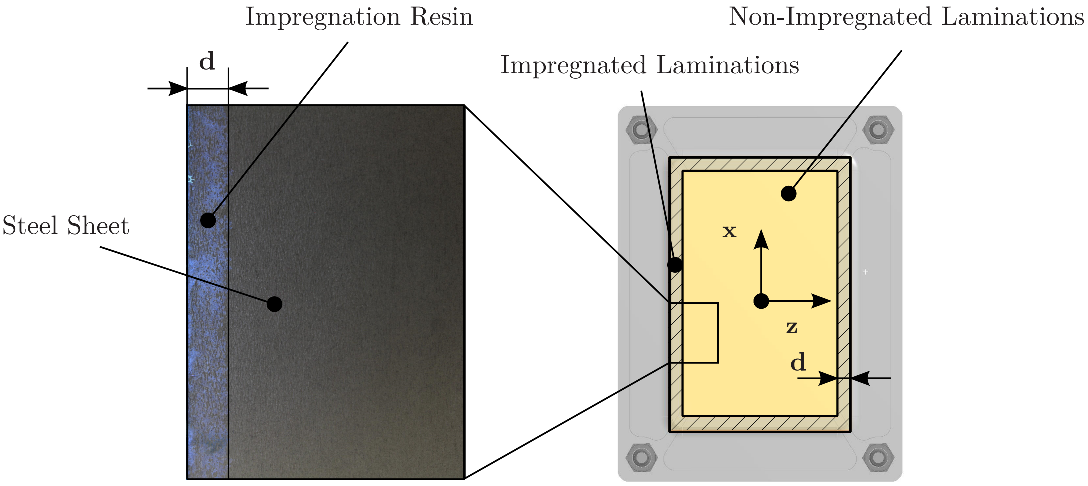

(a) Micrograph of impregnated area

(b) Top view of laminated

Figure 3.28.: Micrograph of impregnated laminated specimen (left) and modeling of the impregnated laminated specimen using two different homogeneous materials.

By using ultraviolet light, the impregnation resin that covers the sheet surface can be visualized. The micrographs show that the impregnation resin does not fully penetrate the contact cavities of the laminations but only covers the boundary areas. It was found that the penetration depth of the resin into the gap was almost constant around the whole circumference of the steel sheets. This observation was confirmed by further probes that were randomly taken from the stack at different locations. All sheets showed similar impregnation profiles. Thus, the total effective stiffness behavior of the laminated stack was influenced by two independent areas, the impregnated outer boundary area and the non-impregnated inner area.

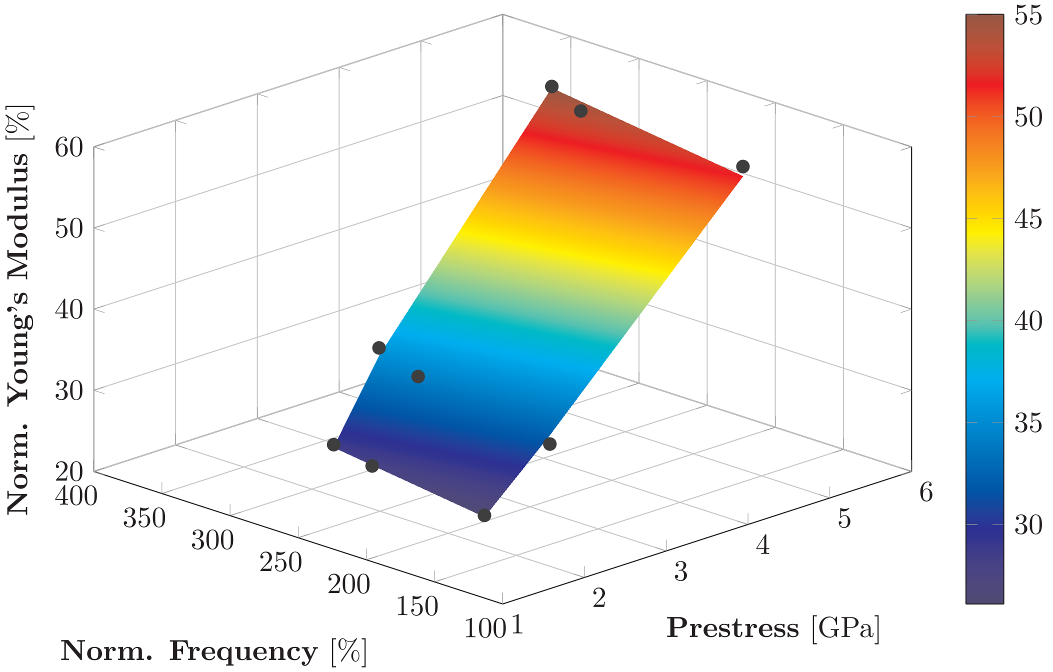

(a) Linear interpolation of normalized Young's modulus

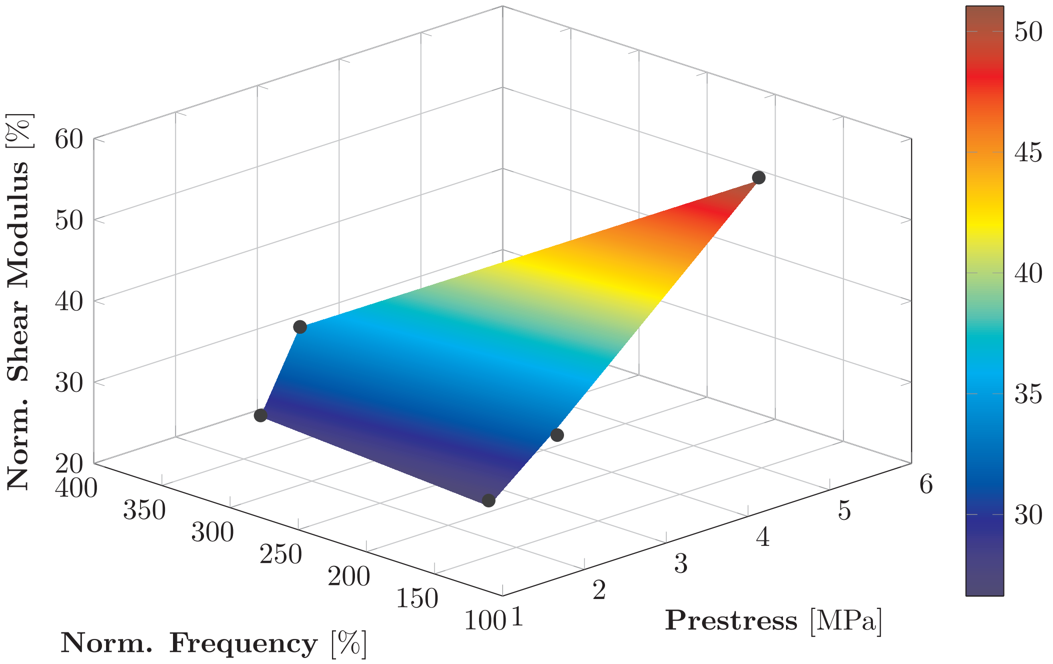

(b) Linear interpolation of normalized shear modulus

Figure 3.29.: Linear interpolated normalized Young's and shear moduli of impregnated laminated steel stack as a function of the normal prestress and the normalized frequency

Consequently, the simulation model of the laminated specimen needed to be adapted to the findings. Therefore, two different homogenized materials, the non-impregnated inner material and the impregnated outer material were considered. The corresponding simulation model is schematically illustrated on the right side of Figure 3.28. Employing Equation 3.2 and 3.3 which allows the quantification of the directional stiffness values of the non-laminated part of the model, the properties of the impregnated outer material were identified again based on model updating. It was found that the eigenfrequencies of the structure are much more sensitive towards the outer impregnated material properties than towards the inner non-impregnated material. Hence, the two plane equations for the inner material, Equation 3.2 and 3.3, could be assumed to not cause any significant errors.

The results of the modal analysis and the subsequently derived stiffness parameters of the impregnated laminations are illustrated in Figure 3.29. The values are normalized with respect to the corresponding moduli of silicon steel and the first eigenfrequency of the non-impregnated specimen (see Section 3.3.2). Again, the correlation between the prestress and the elastic moduli is significant while the frequency-dependency of the elastic moduli is rather moderate. As for the non-impregnated laminations, the overall gradient seems to follow a linear dependency in either direction. Thus, assuming linear dependency of both parameters, the frequency and the prestress, a plane equation can be obtained from curve fitting. The plane is also shown in Figure 3.29.

The corresponding plan equation as well as the coefficient of determination B are given in Equations 3.4 and 3.5. Again the accordance with the measured data is good which is indicated by the coefficient of determination close to one

$$\frac{E_z}{E_0} = 5.9109 \ \frac{\%}{\mathrm{MPa}} \cdot p_{pre} + 0.0230 \cdot \frac{f}{f_0} + 13.2171\ \%, \quad B^2 = 0.9952 \tag{3.4}$$

$$\frac{G_{xz,yz}}{G_0} = 5.7467 \ \frac{\%}{\mathrm{MPa}} \cdot p_{pre} + 0.0113 \frac{f}{f_0} + 15.7726\ \%, \quad B^2 = 0.9960. \tag{3.5}$$

Based on the analytic descriptions that were introduced in this chapter the YOUNG's modulus E_z in stack direction and the shear modulus $G_{xz,yz}$ can be quantified. However, in order to fully describe the transversely isotropic material behavior of the laminated steel stack three more elastic constants as well as the damping behavior of the composite need to be known. Therefore, a more advanced analytical approach that is based on the previously developed results from the experimental modal analysis will be introduced in the following section.

3.3.4. Effective Material Properties of Impregnated Laminated Steel

3.3.4.1. Homogenization Methods for Impregnated Laminations

Figure 3.30(a) schematically showed the microscopic structure of the contact topology between two steel sheets inside the laminations. The inhomogeneous cavities between the steel sheets were filled with impregnation resin as schematically illustrated in Figure 3.30(a). Assuming the gap to have a constant thickness and the impregnation resin to be homogeneously distributed inside the gap, the impregnated laminated steel package can very well be seen as a laminated structure consisting of two constituents, the silicon metal and the impregnation resin, which are periodically arranged. The corresponding representative volume element is schematically illustrated in Figure 3.30(b). Assuming the the thickness of each layer to be known the effective mechanical properties of the impregnated laminations can be derived from the mechanical properties of the underlying constituents, e.g. by utilizing one of the different homogenization techniques for laminated structures that were introduced in Section 2.5.

In Figure 3.30(c) and 3.30(d), two micromechanical models are shown. The left one corresponds to the discrete RVE which was introduced in Section 2.5.1 the right model corresponds to the method of cell based on two subcells as introduced in Section 2.5.1. Both models are capable of providing homogeneous stiffness and damping properties of laminated structures. However, regarding the thickness of the resin layer compared to the thickness of the steel sheets, an appropriate representation of the resin layer inside the micromechanical model is numerically elaborate. Therefore, the discretization of the RVE needs to be chose sufficiently small. In contrast, the number of subcells inside the MOC is fixed to two. Furthermore, the solution of the constitutive equations using the MOC is based on several assumptions which might cause significant errors regarding the quantification of suitable effective material properties for the impregnated laminated steel. In order to evaluate the applicability of the MOC for the representation of impregnated laminated steel, the elastic properties obtained from the MOC were compared to the numerically obtained effective properties from the detailed RVE model. A detailed description of the solution of the MOC with two subcells will be given in the appendix of this thesis (see Appendix A). The numerical solution procedure of the RVE will also be discussed in the appendix of this thesis (see Appendix B).

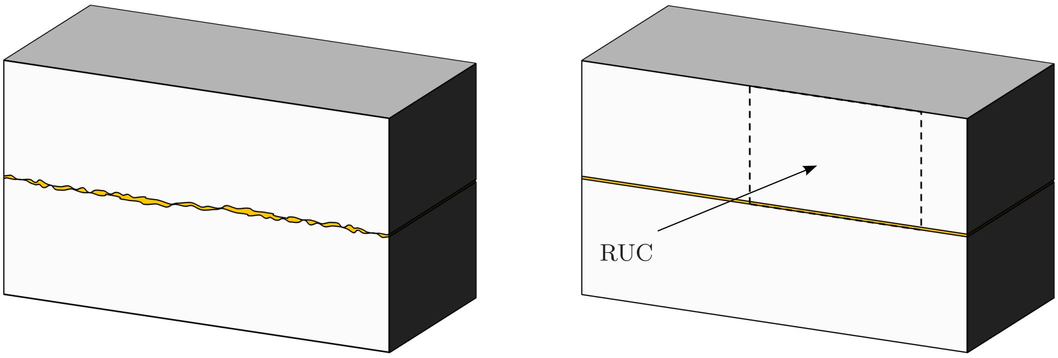

(a) Schematic gap geometry between two steel sheets

(b) Idealized gap geometry

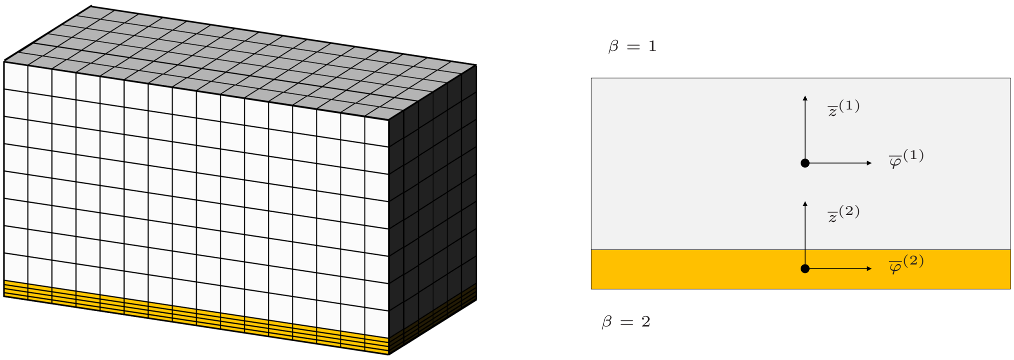

(c) Unit cell of laminations

(d) MOC of laminations

Figure 3.30.: Simplified models of the laminated steel.

Figure 3.31 shows the homogenized YOUNG's modulus E_z in stack direction as well as the shear modulus $G_{xz,yz}$ for both models given as a function of the resin layer thickness. The thickness of each single steel sheet as well as the material properties of the constituents were held constant at appropriate values throughout the study. The MOC shows very good accordance with the numerical RVE for all relevant elastic constants. It can thus be utilized to generate homogenized stiffness properties for the impregnated laminated steel. Hence, the following investigations involving the homogenization of impregnated laminated steel will be based on the MOC.

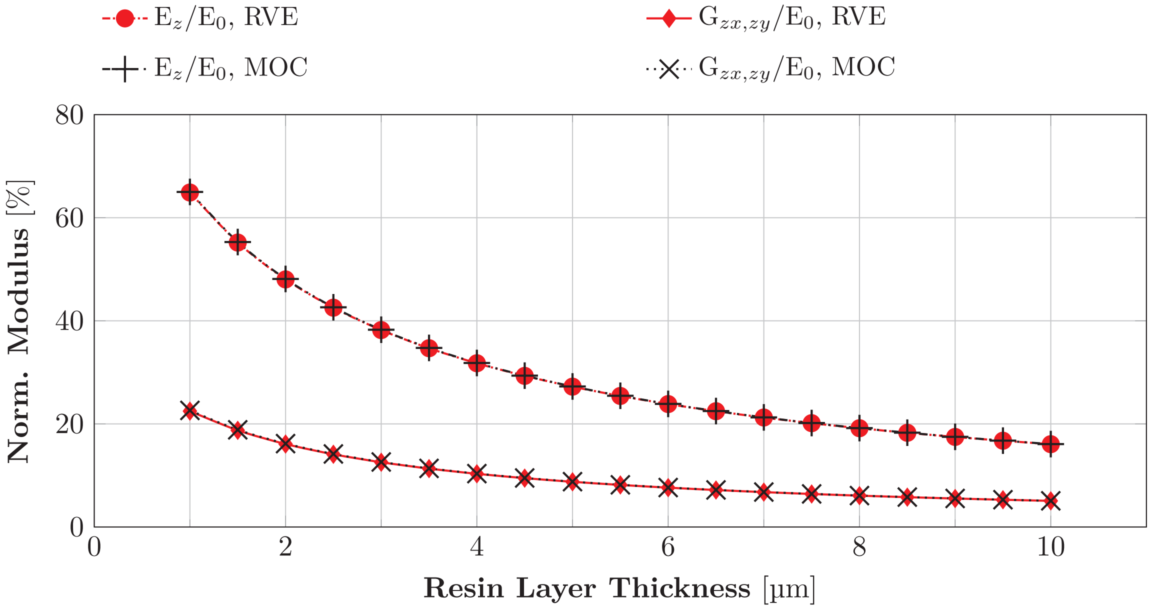

Figure 3.31.: Normalized Young's and shear moduli as a function of the resin layer thickness for the RVE and the method of cells (MOC).

3.3.4.2. Prestress Dependency of Stacking Factor

The surface of any structure is naturally not perfectly even but shows roughness. Thus, the contact topology of surfaces is typically characterized by areas of actual contact and areas of no physical contact. Subjecting a surface contact between two metal bodies to normal stress, the surface profile deforms [192, 210, 212, 213]. Consequently, the area of actual physical contact between the sheets increases which affects the normal and tangential stiffness of the contact itself. This was as well indicated by the significant influence of the prestress on the elastic properties of the non-impregnated laminated steel. Due to the successive deformation of the local contact texture by employing a normal stress the capillaries inside the contact area decrease and less resin is able to remain inside the impregnated laminated steel.

Assuming the laminated steel specimens to have a microscopic structure that is similar to the schematically illustrated structure in Figure 3.30(b), and assuming the material properties of each single steel sheets as well as the impregnation resin to be known, the two previously identified homogenized elastic constants of the impregnated laminated specimen can uniquely be assigned to a particular resin layer width which corresponds to a stacking factor. The relation between the stacking factor, the frequency, and the two elastic moduli is shown in Figure 3.32. The Young's modulus E_z in stack direction as well as the shear modulus $G_{xz,yz}$ obtained from the MOC as given in Figure 3.30(d) using the analytical expression of the frequency- and temperature-dependent material properties of Resin 2 by the Prony series as shown in Figure 3.5. The material properties of the silicon steel were obtained from tensile tests and supposed to be constant over the frequency. The discrete measurement points shown in Figure 3.32 correspond to the measured eigenfrequencies from the previously discussed impregnated laminations (see Section 3.3.3).

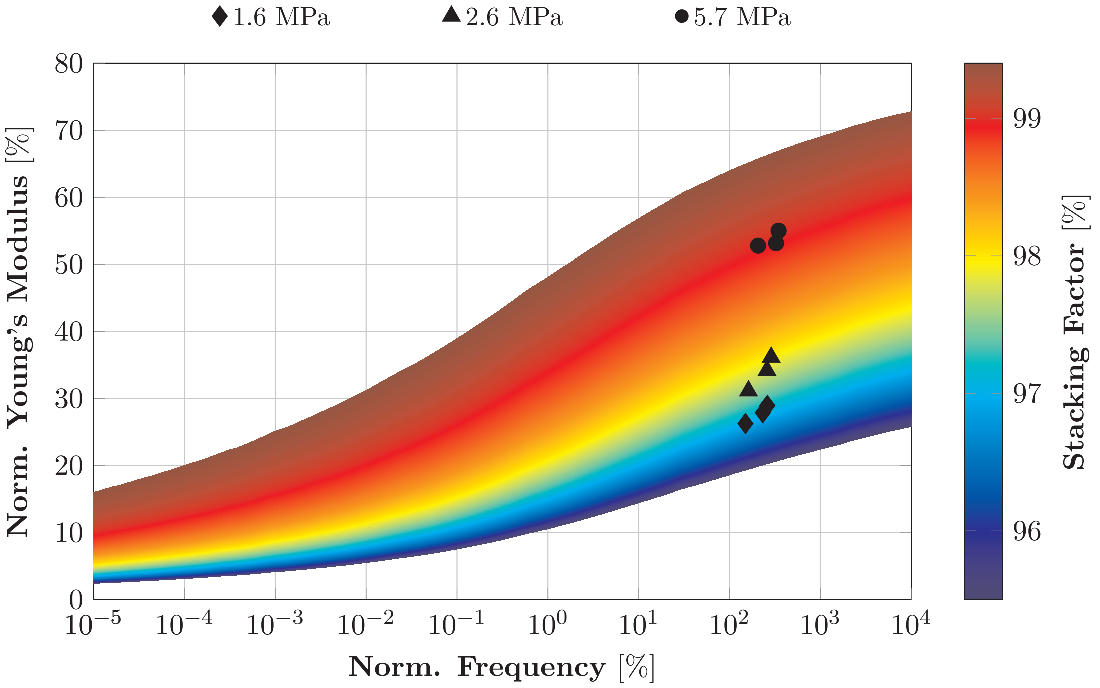

(a) Normalized Young's Modulus

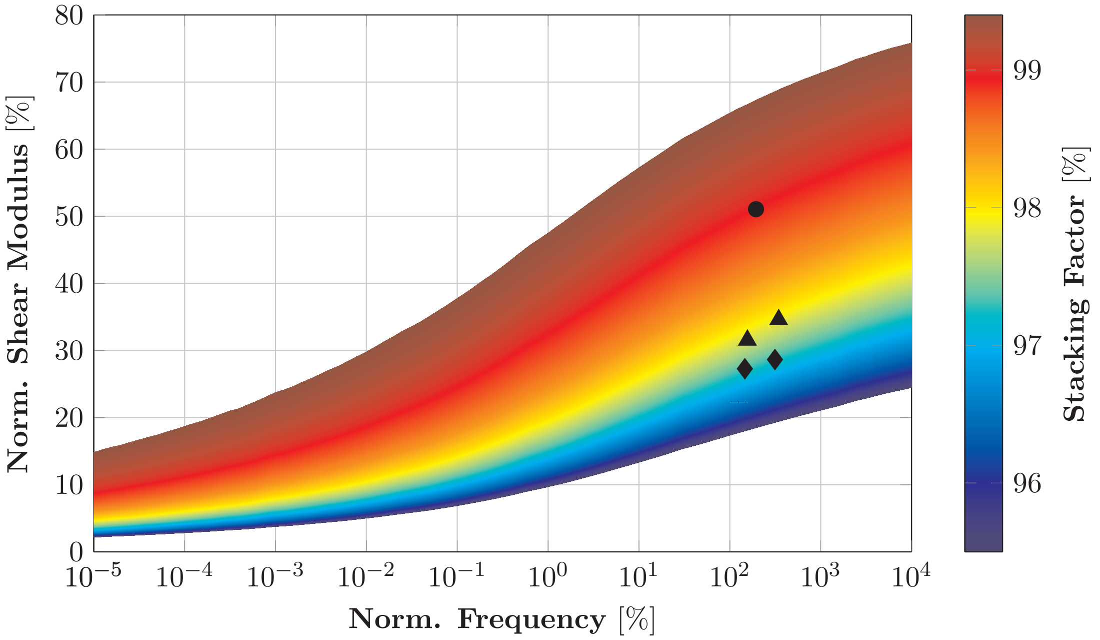

(b) Normalized Shear Modulus

Figure 3.32.: Normalized Young's and shear moduli of impregnated laminated steel package based on the MOC shown as a function of the normalized frequency and stacking factor.

The measured eigenmodes that are related to different prestress conditions can all be assigned to particular stacking factors. This applies for the normal stiffness as well as for the shear stiffness. The diagrams show that the data points that correspond to one particular prestress all lead to similar values of the stacking factor. In Figure 3.33, the distinct stacking factors that were derived from Figure 3.32 are plotted as a function of the normal prestress for all three specimens and eigenfrequencies. The variation between the different filling factors is small which supports the proposition that the impregnation resin within the gap shows a viscoelastic behavior and that the whole heterogeneous structure can be approximated by a periodic formation of recurrent layers with a homogeneous thickness (see Figure 3.30(b)).

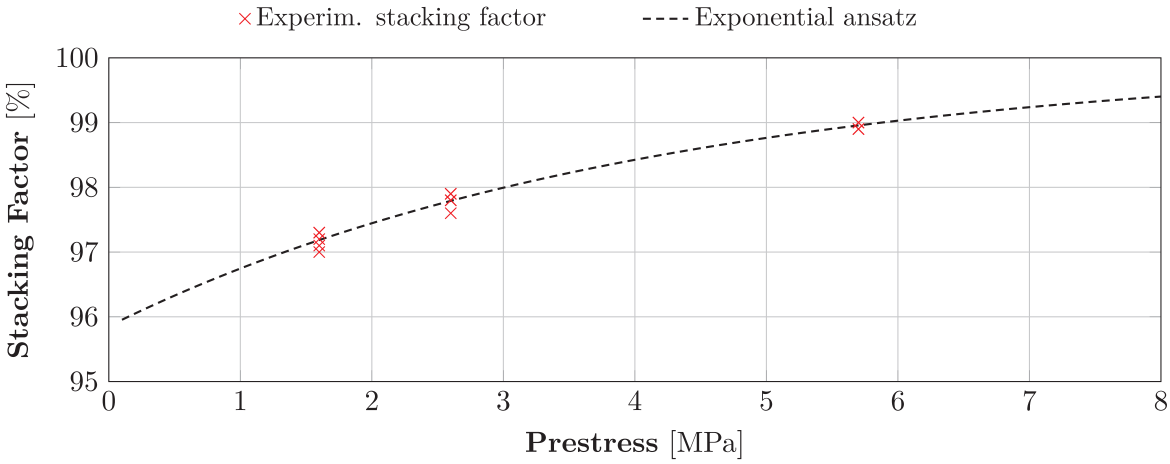

Figure 3.33.: Normalized stacking factor of laminated steel as a function of the normal prestress.

Investigations of the contact mechanics of rough surface contacts show a degressive normal force-deflection behavior of the contact structure. Due to the successive deformation of the rough contact surfaces, the real contact area increases with an increasing normal compression force [214]. Thus, the corresponding stacking factor has a declining gradient and asymptotically approaches unity. Berry postulates an exponential ansatz for the stress-strain-relation of laminated stack [215].

The exponential function that satisfies the boundary conditions and gives an optimal approximation of the given samples is shown in Equation 3.6 and plotted in Figure 3.33.

$$\chi = 105.3\% - A\, e^{-\frac{p_{pre}}{B}}, \quad \text{with} \quad A = 4.3621\% \quad \text{and} \quad B = 4.1338 \text{ MPa} \tag{3.6}$$

with χ as the stacking factor and p_{pre} the normal prestress. The relation is independent of the type of resin which is used during an impregnation process.

3.3.4.3. Viscoelastic Homogenized Material Properties

Assuming the micromechanical model in Figure 3.30(b) to represent the effective behavior of the impregnated laminated steel stack and applying the previously developed analytical function in Equation 3.6 that gives the relation between the stacking factor and the normal prestress, the transverse isotropic stiffness matrix as well as the homogenized damping matrix of any laminated steel configuration can be quantified based on homogenization techniques.

In Figure 3.34, the Young's modulus E_z in stack direction as well as the shear modulus $G_{xz,yz}$ that correspond to the analytical relation between the normal prestress and the stacking factor are shown as surface plots. The homogenized elastic constants were derived from the analytical MOC based on the material properties of the silicon steel sheet and the viscoelastic properties of Resin 2 from Section 3.1. The analytically derived surface plots are compared to the discrete measured data points obtained from the experimental modal analyses.

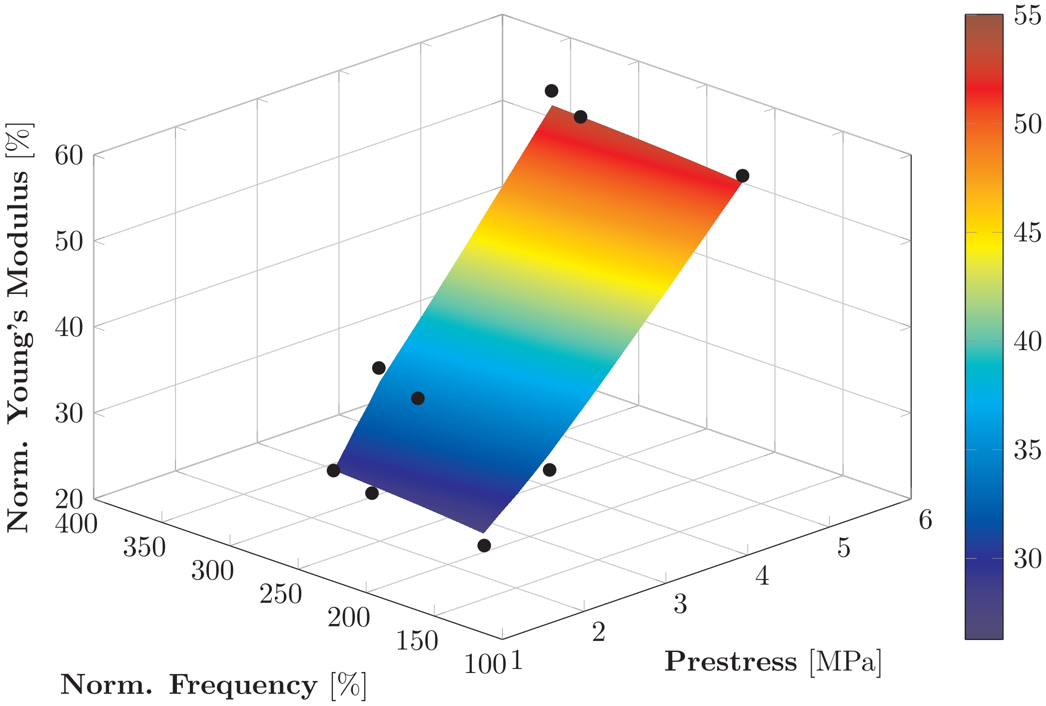

(a) Normalized YOUNG'S Modulus

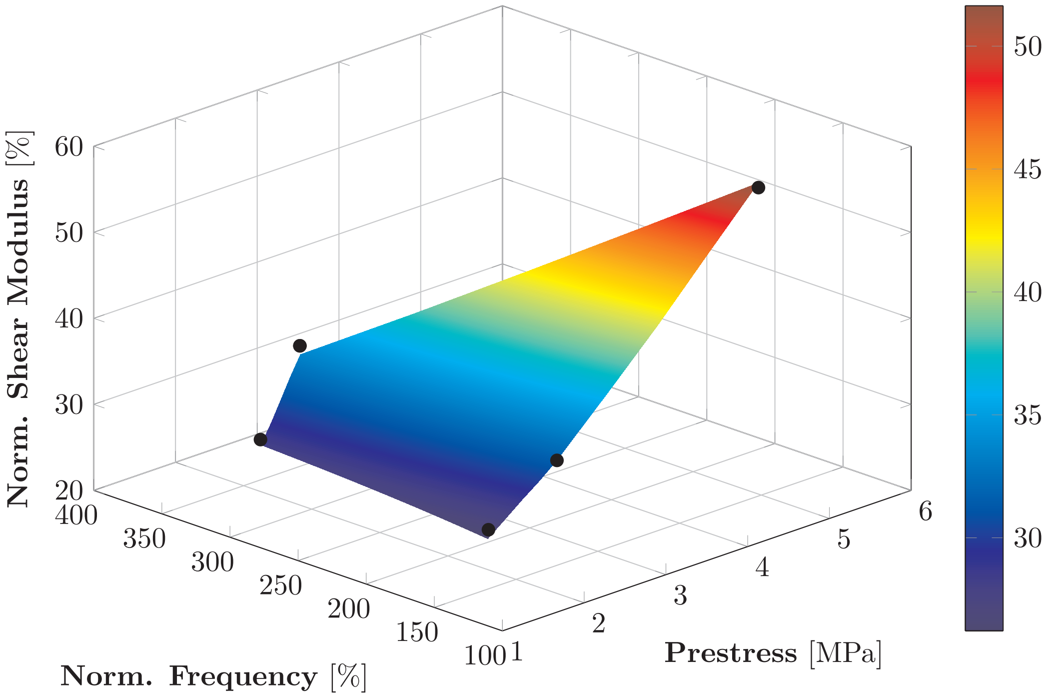

(b) Normalized Shear Modulus

Figure 3.34.: Normalized YOUNG'S and shear moduli of impregnated laminated steel package based on an analytical relation between the normal prestress and the stacking factor as a function of the normal prestress and the normalized frequency.

Table 3.2.: Comparison between measured, analytically, and numerically derived normalized YOUNG'S modulus E_z of an impregnated laminated steel stack with a single sheet thickness of 0.2 mm using the plane equation and the MOC.

	Pres. [MPa]	f/f_0 [%]	$E_{z,exp}/E_0$ [%]	$E_{z,lin}/E_0$ [%]	Error [%]	$E_{z,MOC}/E_0$ [%]	Error [%]
1^{st} Bend. Mode	1.6	149.4	26.3	26.1	0.56	27.7	5.36
	2.6	161.4	31.1	32.3	3.69	33.0	5.83
	5.7	205.7	52.8	51.6	2.20	51.9	1.70
2^{nd} Bend. Mode	1.6	231.8	27.9	28.0	0.40	28.8	3.15
	2.6	258.0	34.2	34.5	0.88	34.2	0.05
	5.7	324.7	53.2	54.4	2.29	53.1	0.03
Comp. Mode	1.6	260.0	29.0	28.7	1.05	29.0	0.29
	2.6	286.7	36.2	35.2	2.77	34.5	4.67
	5.7	346.0	55.0	54.9	0.30	53.3	3.17

Table 3.3.: Comparison between measured, analytically, and numerically derived normalized shear modulus $G_{xz,yz}$ of an impregnated laminated steel stack with a single sheet thickness of 0.2 mm using the plane equation and the MOC.

	Pres. [MPa]	f/f_0 [%]	$G_{z,exp}/G_0$ [%]	$G_{z,lin}/G_0$ [%]	Error [%]	$G_{z,MOC}/G_0$ [%]	Error [%]
1^{st} Tors. Mode	1.6	146.3	27.3	26.6	2.54	26.3	3.91
	2.6	156.0	31.5	32.5	2.99	31.6	0.21
	5.7	194.1	51.0	50.7	0.49	51.7	1.40
2^{nd} Tors. Mode	1.6	313.6	28.6	28.5	0.30	27.4	4.34
	2.6	344.7	34.5	34.6	0.25	32.9	4.70
	–	–	–	–	–	–	–

In Table 3.2 and Table 3.3, the effective stiffness properties derived from the two different analytical approaches, namely the best-fit plane (see Equations 3.4 and 3.5) and the previously developed micromechanical model, are listed and compared to the elastic constants data obtained from the experimental modal analyses. The error of the viscoelastic MOC is larger then the error of the regression plane. However, the ansatz based on the MOC is more generic. It provides a full set of effective elastic constant as well as directional damping properties. It can furthermore be assigned to different types of impregnation resins which enables the engineer to evaluate the effect of different resin types on the overall dynamic behavior of the laminations and thus the electric machine.

4. Validation of Electric Machine Modeling

The analysis and simulation of the structural dynamic behavior of electric machine stators has been addressed in multiple publications. In order to provide fast structural simulations, e.g. for an optimization of the electromagnetic design of the machine, different analytical methods that predict the natural frequencies and mode shapes of the stator were developed. Most approaches are based on thin shell assumptions. Verma et al. introduced an analytical approach based on the three-dimensional elasticity theory [216, 217] which was extended by the energy-method in order to satisfy the junction boundary conditions [218]. In [219] and [220], Verma et al. introduced a further approach that aimed the analytical calculation of axial spatial order eigenfrequencies of cylindrical structures as illustrated in Figure 2.5. In further investigations, these analytical approaches were extended to more complex stator configurations [11–16]. Analytical approaches are extensively used for the fast prediction of the stator vibrational behavior, especially in case of optimization of the electromagnetic excitation [18, 19, 27–31]. However, all analytical approaches are limited to a small range of standard stator structures. If the effect of the micromechanical structure of the stator on its vibrational behavior is of interest, the use of analytical methods is insufficient for modern stator applications [61]. Thus, more detailed numerical methods like the FEM, involving advanced structural models and material formulations need to be applied. In the previous chapter, different modeling methods that yield the effective simulation of the dynamic behavior of electric machine components especially components that correspond to the stator, were introduced. In this chapter, these approaches will be validated based on a stator structure employed in current electric traction motor configurations.

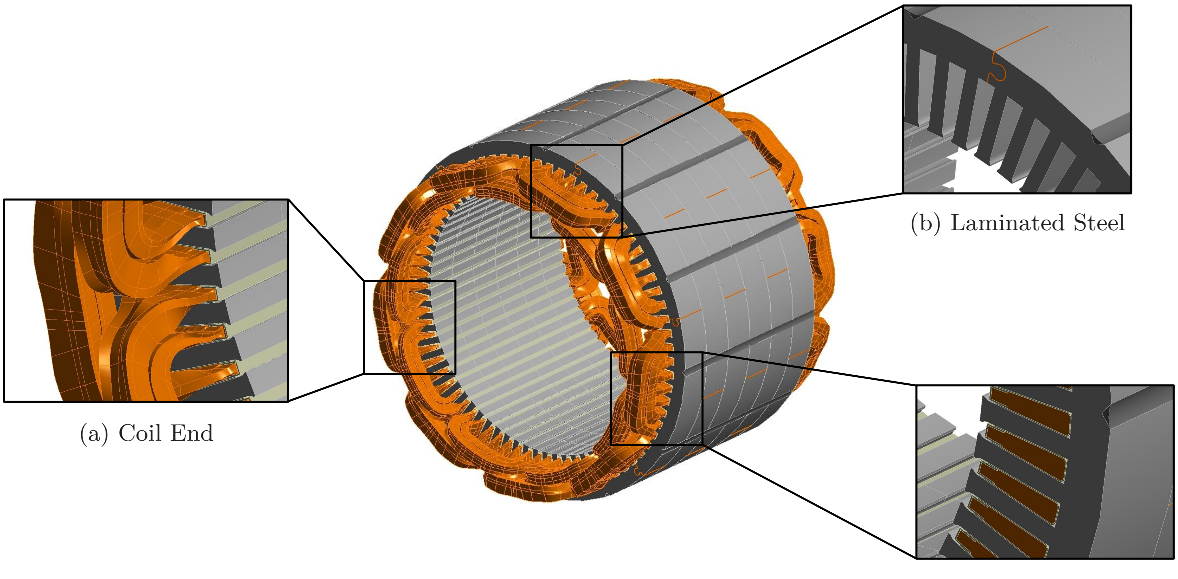

(a) Coil End

(b) Laminated Steel

(c) Active Windings

Figure 4.1.: Overview of stator as it appears in current electric traction motor configurations.

The stator structure is illustrated in Figure 4.1. It consists of a laminated iron core which is held together by eight welding beads that are periodically distributed around the outer circumference. The stator slots are filled with copper windings that are impregnated using the viscoelastic impregnation Resin 2 from Section 3.1. On both ends of the slots, the wires are redirected into one of the neighboring slots defining the end windings.

In order to reliably validate the stator modeling approach, the stator structure was successively assembled and analyzed in three consecutive steps. In the first step, only the pure impregnated stator iron core was investigated providing the validation of the modeling approach of impregnated laminations. In the second step, the active impregnated copper windings that are typically located inside the stator slots were added to the impregnated laminated iron core. The third step involved the analysis of the full stator structure including the end windings.

Finally, the fully validated stator model was considered in a comprehensive acoustic simulation of the entire electric drive unit as it is operated inside an electric vehicle (see Section 4.4).

4.1. Segmented Impregnated Laminated Stator Core

The basic structure and function of stator iron cores was introduced in Section 2.1.1.2. Stator iron cores consist of multiple silicon steel sheets which are held together using rivets, bolts, or edge welding. In multiple publications which involve the characterization of the vibrational behavior of stator cores, the laminated structure is simply considered as an isotropic material with the elastic properties of the underlying steel sheet material [28, 46, 53, 60, 79, 87, 221]. In other investigations, homogenized orthotropic material properties were employed for the stator structure which are typically reversely quantified, based on experimental data [20, 32–37]. Long et al. derived the corresponding density of the homogenized material from the stacking factor multiplied by the density of the silicon steel material [32]. Roivainen separated the material inside the stator into an impregnated and non-impregnated configuration for which two individual orthotropic materials needed to be generated [222]. The corresponding elastic constants were reversely obtained from experimental modal analyses using model updating. Yim et al. employed an analytical relation between the shear and Young's moduli of the laminated steel in order to quantify transversely isotropic elastic properties [58]. However, the applied relations are practical but physically unfounded. Schwarzer et al. showed that the orthotropic homogenized material properties of a segmented impregnated stator iron core can be obtained from the method of cells which was introduced in Section 2.5.3 [223]. The corresponding dynamic simulation results were in good accordance with vibrational measurements of an exemplary stator iron core. A similar approach was applied by Millithaler et al. who employed analytical homogenization methods [224]. However, Millithaler et al.'s approach neglects the normal and tangential compliance of the steel sheet contacts and thus provides material properties which significantly overestimate the shear stiffness of the stator iron core. Regarding the consideration of damping inside stator structures, multiple different approaches can be found in literature. While Le Besnerais, Durantay et al. and Neves et al. obtained modal damping ratios from experimental investigations, Sakamoto et al. assumed a constant damping ratio of 1% over the whole frequency range [26, 36, 57, 225]. In contrast, Giet and Gieras et al. assumed the modal damping ratio to follow a linear frequency-dependent function [6, 56]. Schwarzer et al. used the method of cells in order to deduce directional damping properties of a segmented impregnated stator iron core [223]. The corresponding numerically obtained modal damping ratios were in good accordance with experimental results.

In the following section, the validation of the different structural modeling approaches of the impregnated laminated steel which were developed in Section 3.3.4 will be described. Therefore, an experimental modal analysis was performed on the stator core given in Figure 4.2. Based on the deviation of the experimentally and numerically identified eigenfrequencies and modal damping ratios the applicability of the different modeling approaches regarding the use in structural dynamic simulations of electric motors will be evaluated.

4.1.1. Structure of Laminated Stator Core

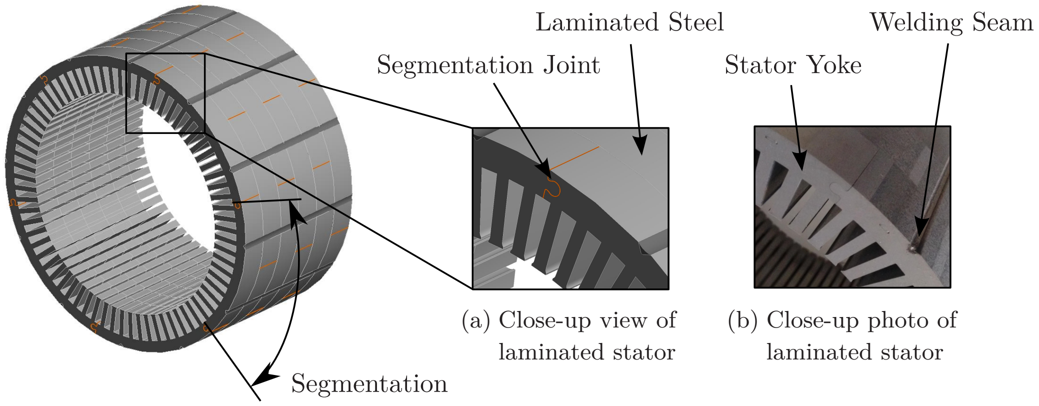

(a) Close-up view of laminated stator

(b) Close-up photo of laminated stator

Figure 4.2.: Isometric view of the stator iron core and detailed view of the yoke segmentation.

In Figure 4.2, the examined stator iron core schematically is illustrated. 72 stator teeth are distributed around the circumference of the stator. The stator yoke is tangentially divided into six segments around the circumference. In axial direction the stator is also separated into six segments.The axial segments are stepwise turned by half a tangential segmentation angle and then pressed together by a normal stress of approximately 4 MPa (see Figure 4.2). Eight axial welding beads that fix the lamination are periodically distributed around the circumference of the stator. In order to generate a distinct state of continuous material close to the stator configuration inside the electric motor, the laminated steel stack was impregnated before the experimental modal analysis using Resin 2 which was introduced and characterized in Section 3.1. The impregnation process was adapted to the impregnation process that is typically used in the series production of the corresponding stator core. In order to employ the homogenized material models that were introduced in Section 3.3.4 information about the contact gap width between the steel sheets and thus the thickness of the resin layer had to be obtained (see Section 3.3.4.2). Since the actual prestress conditions inside the stator laminations after the welding process were unknown, the stacking factor of the laminated steel package and thus the fraction of resin inside the laminations could not be quantified based on Equation 3.6 but had to be obtained from measurements on the actual stator iron core structure. Therefore, the volume of the enclosure of the stator as well as the mass were measured. Based on the material densities of laminated steel and Resin 2 and assuming all gaps within the stator to be homogeneously filled with resin (see Figure 3.1) yielding the stator to only consist of two constituents, namely the laminated steel sheets and the resin, the total stacking factor of the stator was found to be 98.1%.

4.1.2. Effective Material Properties

In the previous sections the structure of the stator as well as its generic dynamic behavior were introduced (see Figure 4.2). Each steel sheet layer of the stator is divided into six independent segments that are periodically distributed around the circumference of the stator yoke. The vibrational behavior of stator structures was introduced in Section 2.1.2.1. The characteristic eigenmode shapes of stators predominantly involve radial oscillation and thus bending of the stator yoke (see Figure 2.4). Consequently, the corresponding eigenfrequencies are mainly determined by the circumferential yoke stiffness. However, the circumferential stiffness of the stator structure given in Figure 4.2 can assumed to be significantly influenced by the segmentation. Thus, the effect of the stator segmentation on the circumferential stiffness of the stator yoke needs to be investigated.

In Figure 4.3(a) the segmentation of the stator yoke is schematically illustrated. Since the six independent circumferential segments are periodically distributed around the circumference of the stator yoke, the yoke could very well be seen as a periodical structure of six recurrent elements. The circumferential mechanical properties of the stator yoke could thus be obtained from homogenization techniques as introduced in Section 2.5.

Assuming the actual segmentation topology given in Figure 4.3(a) to be mechanically well represented by the substitutional radially oriented topology given in Figure 4.3(b) the RVE given in Figure 4.3(c) arises. In z-direction, the micromechanical model follows the scheme of the laminated structure, in y-direction, it represents the segmentation and in x-direction, it equals the radial scheme of the stator. The RVE can either be solved by means of numerical methods as illustrated in Figure 4.3(c) or by utilizing the MOC based on four subcells as it was introduced in Section 2.5.3 and is given in Figure 4.3(d).

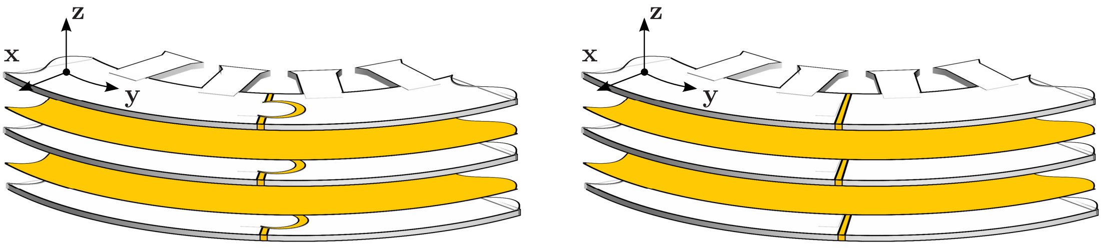

(a) Segmented geometry

(b) Substitutional model of segmentation

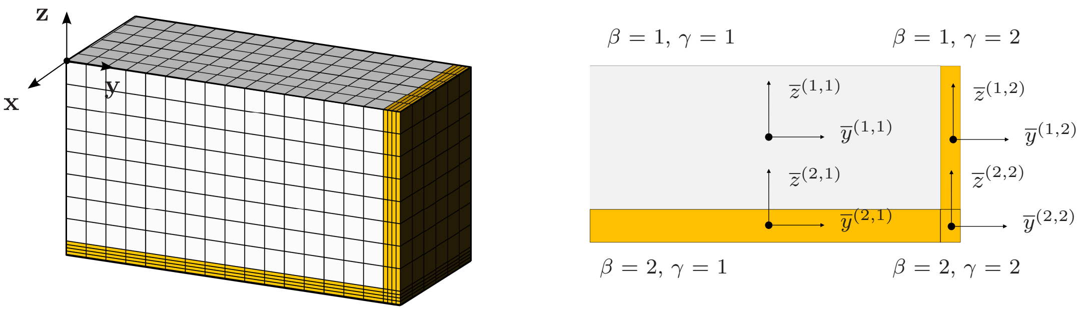

(c) Unit cell of segmented stator

(d) Aboudi model of segmented stator

Figure 4.3.: Homogenization steps of the segmented stator structure.

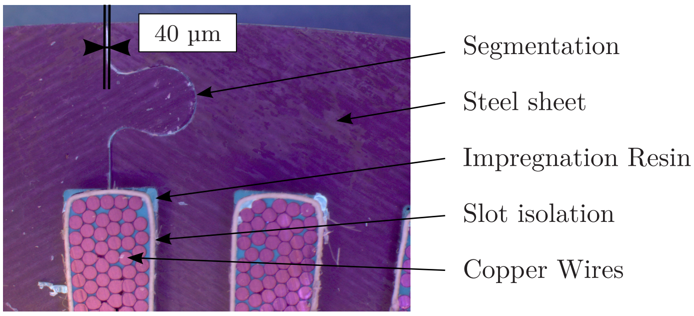

Figure 4.4.: Cross-section of segmented stator yoke.

In order to obtain suitable effective material properties for the segmented stator iron core, the thickness of the segmentation gap between two yoke segments needs to be quantified. Figure 4.4 shows a micrograph of the segmentation gap. An empirical study on multiple micrographs found the gap width and thus the thickness of the resin layer inside the segmentation gap to be 40 µm. In Figure 4.3(c) and 4.3(d), two micromechanical models are shown. The left one corresponds to the discrete numerical RVE which was introduced in Section 2.5.1 the right model corresponds to the method of cell based on two subcells as introduced in Section 2.5.1. By comparing the effective stiffness properties that arise from the method of cells (MOC) to the effective stiffness properties obtained from the numerical RVE (see Figure 3.31), it was shown that the MOC can very well be used for the quantification of effective material properties of impregnated laminated steel, even for very small resin layers inside the laminated steel stack (see Section 3.3.4).

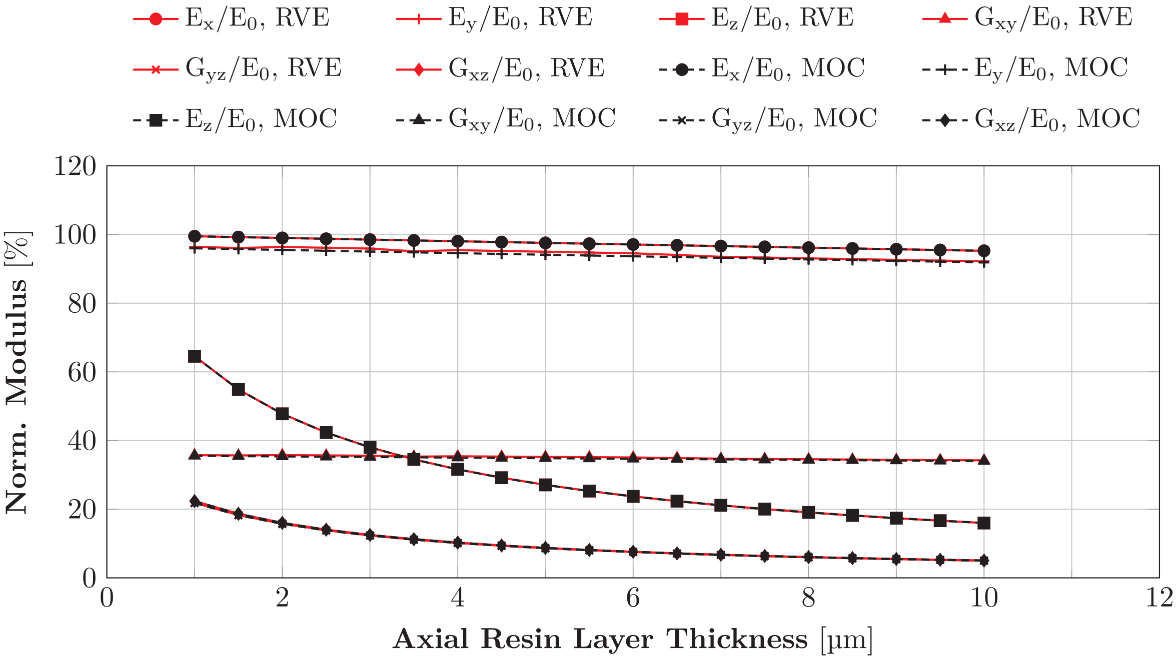

Figure 4.5.: Comparison of the normalized stiffness properties of the homogenized impregnated laminated stator iron core using the 4-cell MOC and the numerical representative volume element (RVE) based on a segmentation gap thickness of 40 µm.

However, including the segmentation into the RVE yields a more complex micromechanical model. In order to evaluate the applicability of the MOC for the representation of segmented impregnated laminated stator iron cores the orthotropic elastic properties extracted from the MOC were compared to the numerically obtained orthotropic properties from the detailed RVE model. The solution procedure of the MOC based on four subcells is analogue to the procedure for the MOC based on four subcells which is exemplarily given in the appendix of this thesis (see Appendix A). The numerical solution procedure of the RVE will also be discussed in the appendix of this thesis (see Appendix B). In Figure 4.5, the six different directional stiffness properties of the orthotropic stator iron core are given for both models as a function of the axial resin layer thickness between the steel sheets. The material properties of both constituents, the silicon steel sheets and the impregnation resin, were held constant at appropriate values throughout the study. The thicknesses of each single steel sheet was set to 0.2 mm while the the thickness of the resin inside the segmentation gap was set to 40 μm. The MOC shows very good accordance with the numerical RVE for all elastic constants an different axial resin layer thicknesses. It will thus be utilized throughout the following investigations regarding the validation of the general modeling approach for impregnated laminated stator iron cores.

4.1.3. Free Vibration Analysis

In order to validate the stator modeling approach based on the micromechanical model given in Figure 4.3(d) an experimental model analysis was performed. Figure 4.6 shows the measurement setup. The structure was diagonally excited by an electromagnetic shaker in a frequency range from 200 Hz up to 5500 Hz. Two surface areas on the outer cylinder jacket were independently measured using a 1D-LSV. The independent measurements were subsequently merged in order to get an extended overview of the circumferential modal behavior. In Figure 4.7, the results of the experimental modal analysis, namely the eigenfrequencies as well as the corresponding eigenmode shapes and modal damping ratios, are shown. In total 19 different eigenfrequencies were identified. In Section 2.1.2.1 the classification of stator eigenmode shapes using two independent digits was introduced. The first digit refers to the circumferential and the second one to the axial spatial order. Thus, in the left column of Figure 4.7 all eigenmodes with the axial spatial order zero are listed. The right column corresponds to the eigenmodes with the axial spatial order equal to one. The different rows denote the circumferential spatial order starting from zero to nine.

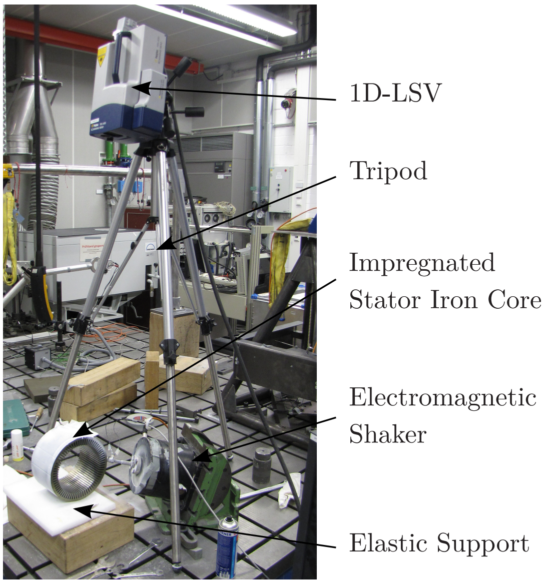

Figure 4.6.: Setup of experimental modal analysis of impregnated stator iron core.

4.1.4. Validation of the Modeling Approach

4.1.4.1. Stiffness Properties

Based on the results of the experimental modal analysis from Section 4.1.3, different modeling approaches for the impregnated laminated stator steel package can be evaluated by comparing the numerically and experimentally obtained eigenfrequencies. In Figure 4.8, the results are given separately for the modes with the axial spatial order zero and one, respectively. Five different numerical models were employed.

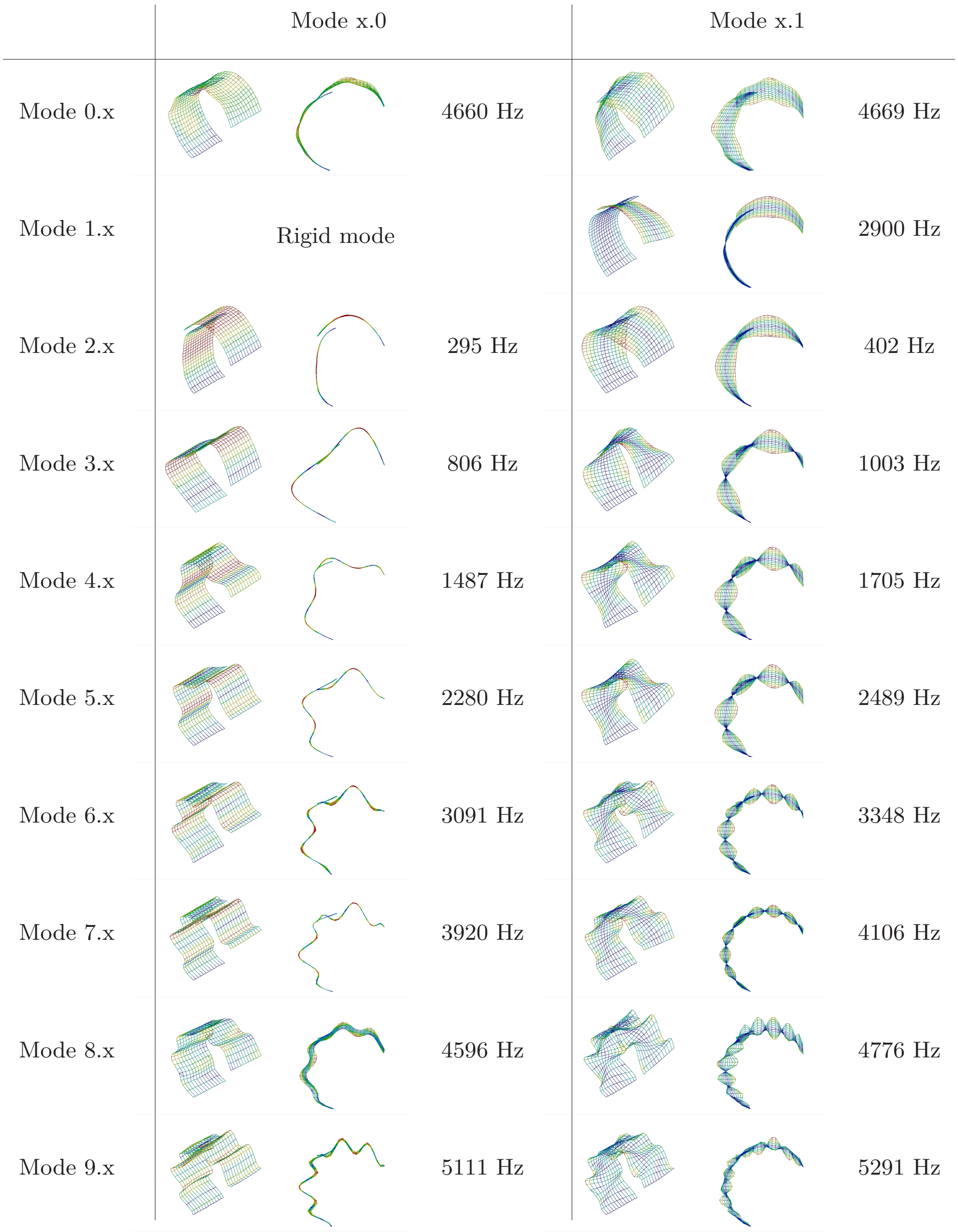

Figure 4.7.: Measured eigenfrequencies and corresponding mode shapes of impregnated laminated stator iron core.

Four of the five models consider the effective properties of the stator iron core to be influenced by the laminations in axial direction while the model „Steel“ is based on the assumption of an isotropic stiffness and damping behavior of the iron core based on the material properties of the corresponding silicon steel. In three models the frequency-dependent material properties of Resin 2 that were characterized in Section 3.1.1 were considered yielding frequency-dependent effective stiffness properties of the laminated steel. The other models neglected the frequency-dependent viscoelastic properties of the resin by assuming constant quasi-static properties of the resin as obtained from tensile tests (see Section 3.1.1). In order to evaluate the effect of viscoelasticity on the overall dynamic behavior of the structure, two models were implemented based on the 4-cell MOC as illustrated in Figure 4.3(d).

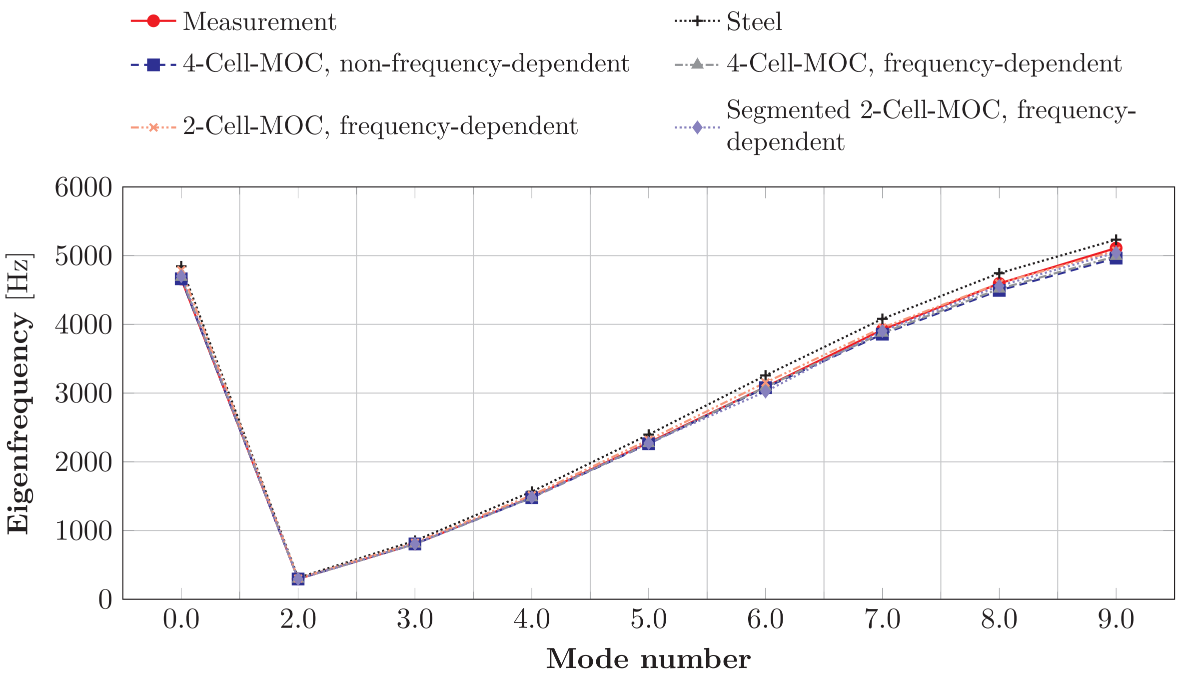

(a) x.0-modes.

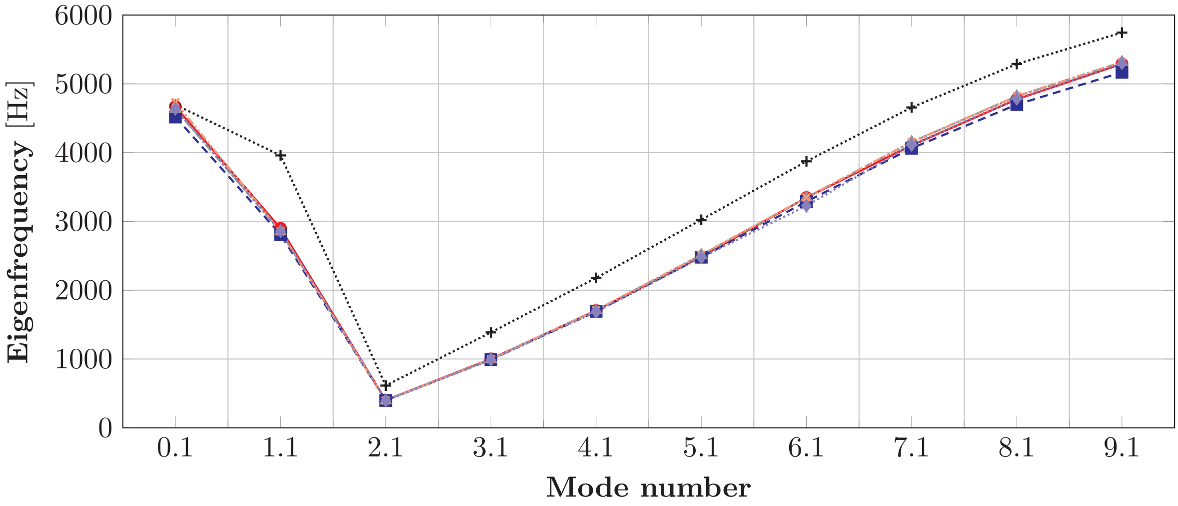

(b) x.1-modes.

Figure 4.8.: Comparison of the eigenfrequencies for different modeling approaches of the stator iron core.

One of the two models considered the frequency-dependency of the resin while the other model neglected this effect. The influence of the segmentation was investigated by comparing the 2-cell MOC as shown in Figure 3.30(d) in which the tangential properties of the yoke equal the radial ones to the 4-cell orthotropic MOC which was illustrated in Figure 4.3(d). Furthermore, a detailed model in which the actual segmentation configuration was microscopically discretized was investigated in order to validate the simplification of the segmentation gap as shown in Figure 4.3(a) and 4.3(b).

The investigations show that the mode shapes with the spatial order zero are well represented by all models. The eigenfrequencies obtained from the solid steel stator as well as the stator model based on the 2-cell MOC model are slightly too high which indicates that the circumferential YOUNG's modulus is overestimated by the two modeling approaches. Apparently the segmentation of the stator leads to a reduced tangential stiffness of the stator iron core which was not represented inside these two models. However, the error caused by the neglect of the tangential segmentation is low. For the mode shapes with the spatial order equal to one the monolithic steel stator model leads to large errors while all four other simulation models provide good results. Apparently, the consideration of the laminations seems to be crucial to match higher axial spatial order eigenmode shapes. The consideration of the frequency-dependent stiffness characteristics of the lamination seem to be rather insignificant to the eigenfrequencies of the given stator iron core.

4.1.4.2. Damping Properties

In order to further validate the different modeling approaches, not only the stiffness of the different models but also the damping needs to be considered. In Section 2.5.4.1 the identification of modal damping ratios from the strain energies of the single eigenmode shapes was introduced. This procedure was already successfully applied in Section 3.2.1.2 for the structure of copper windings. Assuming the mode shapes that correspond to the different simulation models to be perfectly equivalent regarding their distribution of strain energies inside the different materials, namely stator steel package and welding beads, the strain energy distribution needs to be evaluated only once. The only exception regarding the distribution of strain energy is the segmented model that contains a detailed discretized resin layer model inside the segmentation gaps. Both different strain energy distributions are given in Figure 4.9 and 4.10. In Figure 4.11 the corresponding absolute modal damping ratios that arise from the different models introduced in Section 4.1.4.1 are compared to the measured modal damping ratios.

The damping ratios of the mode shapes with the axial spatial order zero are much lower than the damping ratios that correspond to the mode shapes with the axial spatial order one. Apparently, the modal damping ratios that correspond to the mode shapes with the axial spatial order zero are significantly influenced by the damping characteristics of the silicon steel which is low compared to the damping of the impregnation resin.

However, the consideration of the tangential segmentation of the stator iron core seems to be relevant in order to match the measured modal damping ratios that correspond to the x.0-mode-shapes. Both simulation models that neglect the segmentation effect predict much lower modal damping ratios. In contrast to the x.0-mode-shapes, the modal damping ratios of the mode shape with the axial spatial order one show an increased influence of the resin which is indicated by much higher damping values. In case of the non-frequency-dependent simulation model, the damping ratio of the resin layer corresponds to the relaxation behavior obtained from quasi-static tests. All simulation models that consider the laminated character of the stator iron core to influence its mechanical properties and are thus orthotropic or transversely isotropic, show good accordance with the measurements. However, the neglect of viscoelasticity leads to an overestimation of the total modal damping ratio. The simulation model considering the stator iron core to behave isotropic leads to a significant underestimation of the modal damping ratios. This equals other researchers findings who have shown that assuming the stator iron core to behave isotropically, causes significant errors regarding the system's natural frequencies as well as the damping properties [189, 226, 227].

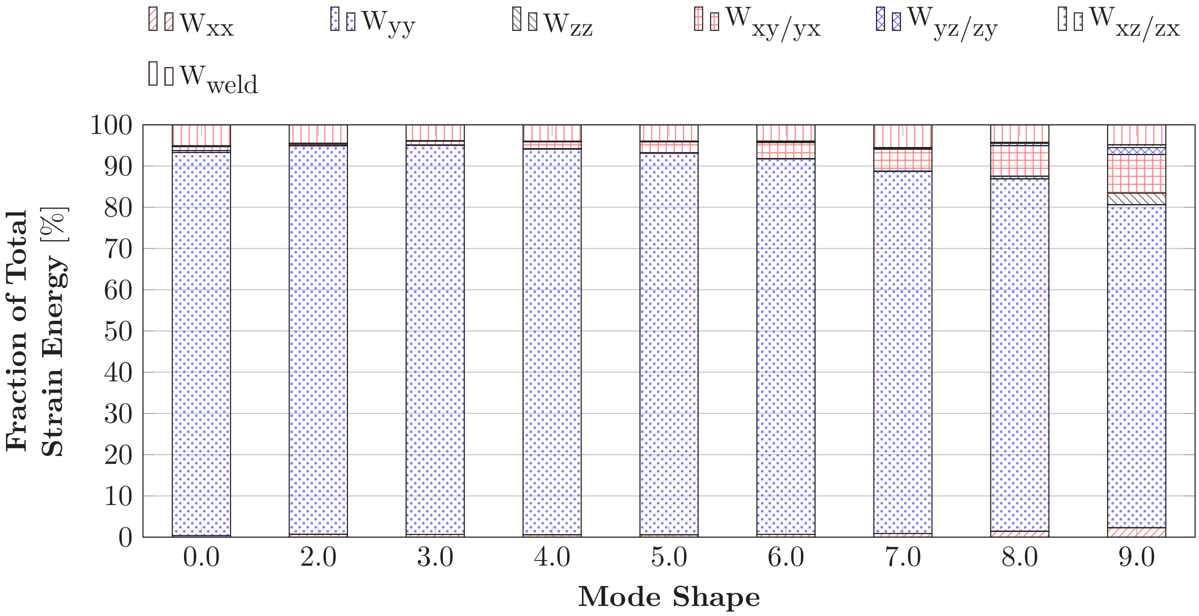

(a) x.0-modes.

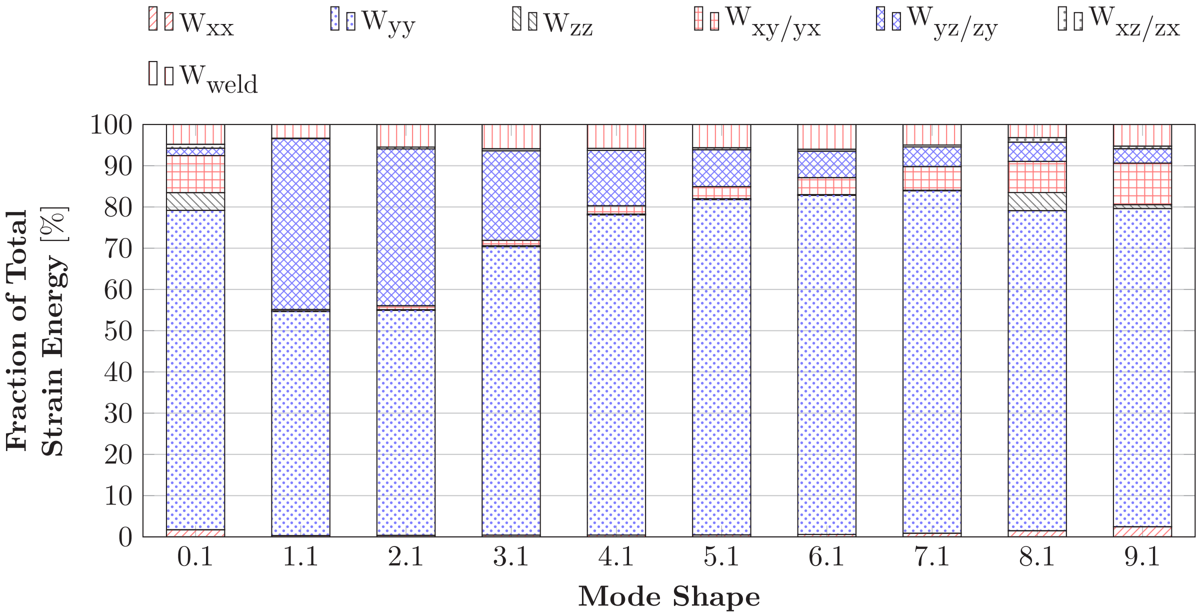

(b) x.1-modes.

Figure 4.9.: Overview of the directional strain energy fraction for the different mode shapes using the 4-cell-MOC model and the structure of an unsegmented stator.

The results presented in this chapter confirm the insufficiency of the monolithic silicon steel model regarding the accurate representation of higher axial spatial order eigenmode shapes for both dynamic properties, the stiffness as well as the damping ratio. In contrast, considering the laminated structure by transversely isotropic or orthotropic effective material properties provides good accordance with the measurements. The consideration of the segmentation only moderately influences the eigenfrequencies but has a more significant effect on the modal damping ratios, especially for the x.0-mode shapes. ABOUDI's MOC provides a sufficient alternative to the detailed but numerically expensive segmentation model. The consideration of viscoelasticity shows a rather moderate influence on the accurate prediction of the structure eigenfrequencies but leads to a much better estimation of the modal damping ratios in case of the x.1-mode-shapes.

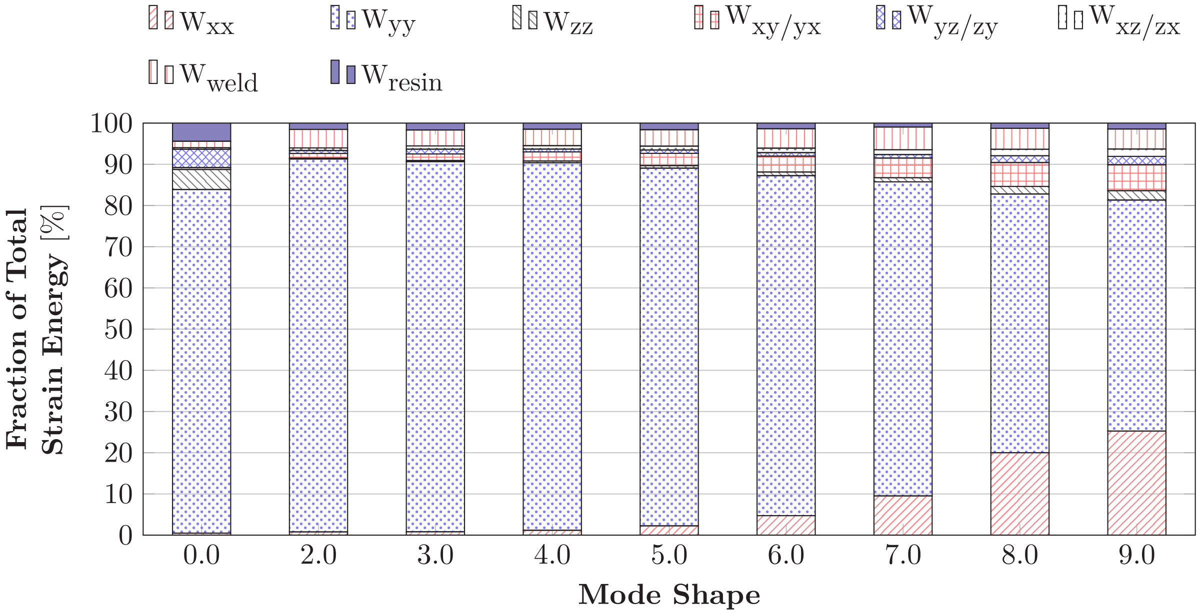

(a) x.0-modes.

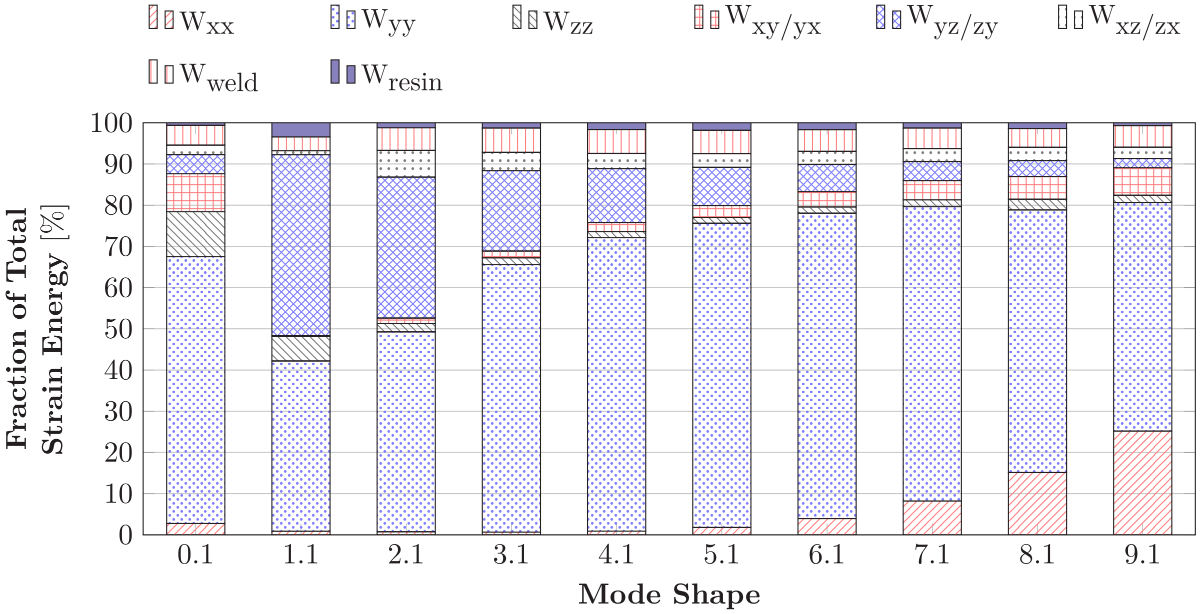

(b) x.1-modes.

Figure 4.10.: Overview of the directional strain energy fraction for the different mode shapes using the 4-cell-MOC model and the structure of a segmented stator.

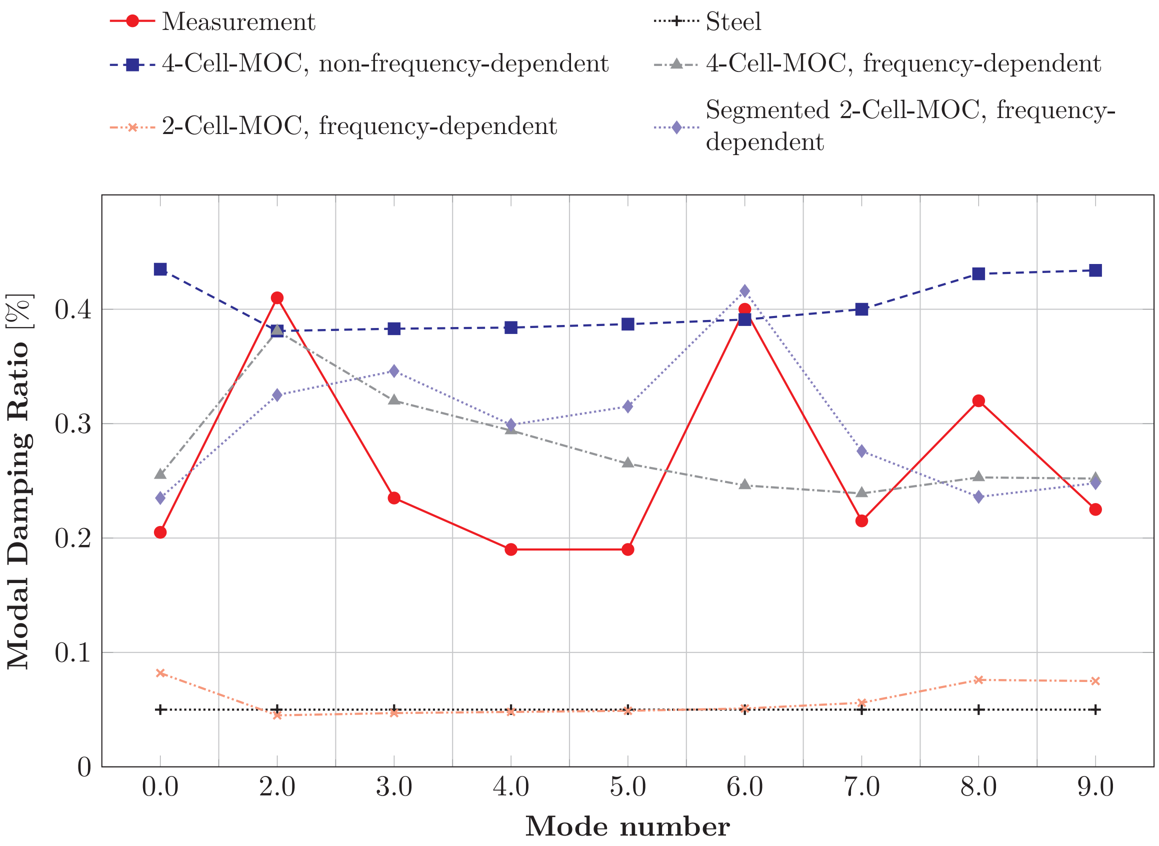

(a) Damping ratio x.0-modes.

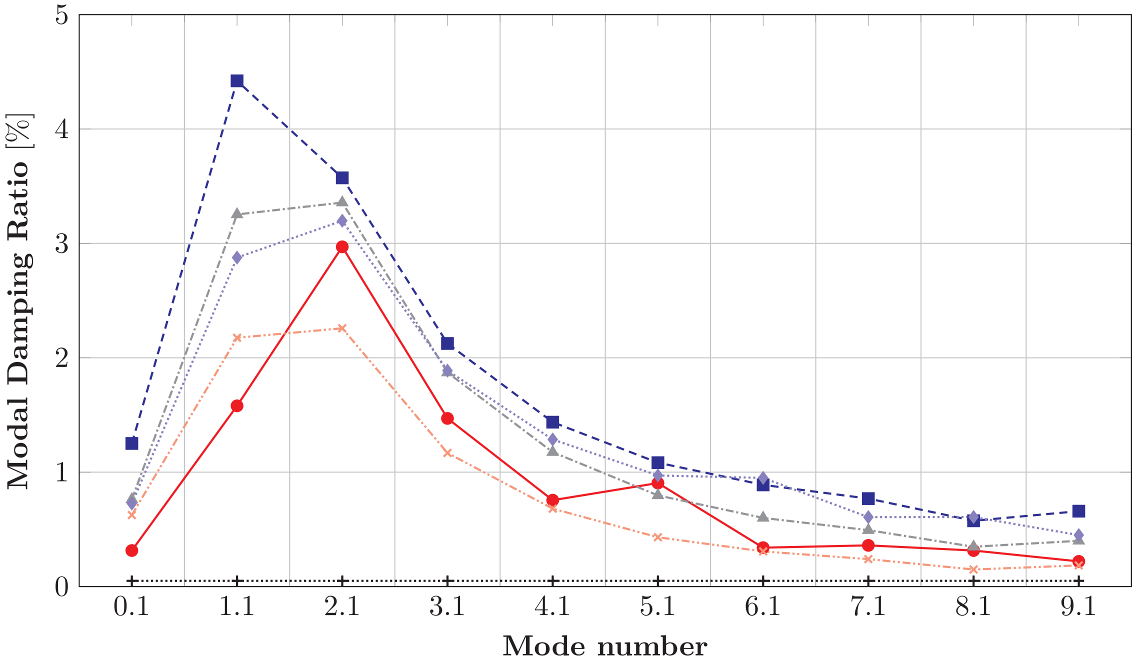

(b) Damping ratio x.1-modes.

Figure 4.11.: Comparison of the modal damping ratios for different modeling approaches of the stator iron core.

4.2. Stator Core with Copper Windings

4.2.1. Structure of the Stator Core with Copper Windings

The influence of copper windings on the structural dynamic behavior of the stator was investigated in multiple scientific works. Cai et al., Giet and Hameyer, Ishikawa, Verma and Girgis, Watanabe et al., and Weilharter et al. experimentally analyzed the natural frequencies of laminated stator cores with and without copper windings, finding a significant deviation of the eigenfrequencies as well as the modal damping ratios between the two different configurations [21, 47–51]. Fengge et al., Nitzsche, and Wang and Lai performed numerical comparisons of stator structures with and without copper windings, again leading to a considerable deviation of the eigenfrequencies [52–54]. Singal et al. experimentally found the copper windings to significantly increase the total damping of the stator structure [55]. Long compared measured eigenfrequencies of a stator to simulated eigenfrequencies, continuously varying the tangential stiffness of the copper windings [32]. The influence of the copper winding stiffness on the eigenfrequencies was found to be significant. In a numerical study, Long compared an advanced modeling approach using homogenized transversely isotropic stiffness properties for the copper windings to other less advanced approaches neglecting either the stiffness or both, the mass and the stiffness, finding significant deviations regarding the system eigenfrequencies [32]. Thus, the influence of the copper windings on the stiffness as well as the damping behavior of the stator core has been verified in multiple independent investigations. Long pointed out the need of advanced modeling approaches that involve the assumption of transversely isotropic material properties for the copper windings in order to retrieve accurate and reliable simulation results. However, the derivation of the corresponding transversely isotropic stiffness and damping properties from the mechanical properties of the underlying constituent materials has not been addressed in any of the literature.

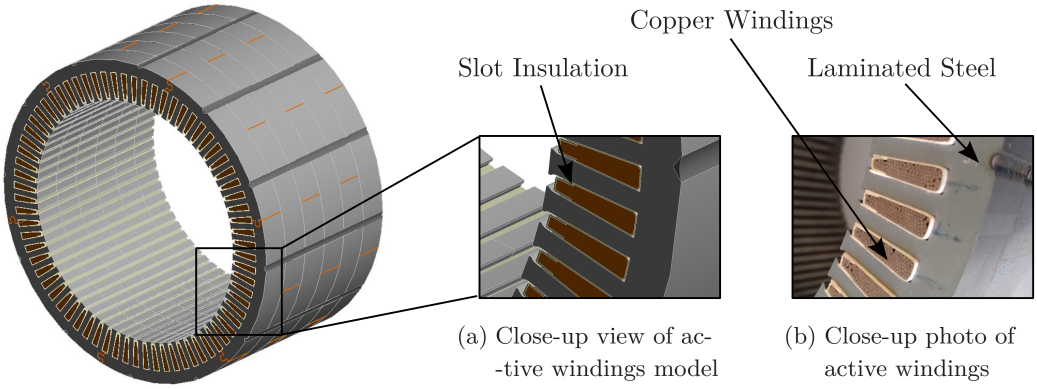

(a) Close-up view of active windings model

(b) Close-up photo of active windings

Figure 4.12.: Isometric view of the stator iron core including the slot filling and detailed view of the copper windings inside the stator slots.

In Figure 4.12 the structure of a stator including copper windings is shown. The laminated stator is identical to the previously investigated stator core of Section 4.1. The uniaxial copper wires that transverse along the axis of the stator are surrounded by the thermosetting impregnation resin, Resin 2 from Section 3.1. In Figure 3.11 a cross section of the copper windings inside the stator slots was shown. The volume fraction of the wires inside the slot was found to be about 48%. Between the copper windings and the laminated steel, a thin slot insulation layer made from mica paper is located (see Section 2.1.1). Nitzsche has found the slot insulation to be significantly compliant compared to the current carrying slot filling and thus to influence the overall tangential stiffness of the structure [53]. In order to evaluate the influence of the copper windings as well as the thin slot insulation layer on the vibrational behavior of the stator an experimental modal analysis was performed on the stator structure shown in Figure 4.12 at an ambient temperature of $T = 23$°C. Therefore, the end windings were removed from a full stator structure to retrieve a test geometry similar to the one shown in Figure 4.1. In Figure 4.13, the characteristic eigenmode shapes as well as the eigenfrequencies are given.

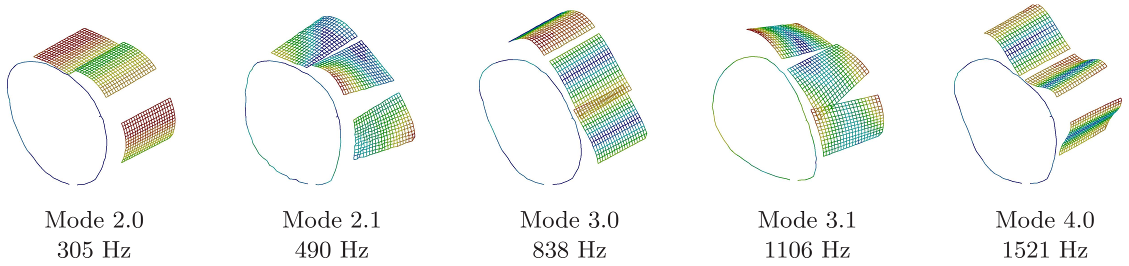

Figure 4.13.: Measured eigenfrequencies and corresponding mode shapes of stator iron core including the slot filling.

4.2.2. Stator Slot Insulation

4.2.2.1. Modeling of Stator Slot Insulation

Due to its significantly compliant character, the thin insulation paper which is located between the laminated stator and the copper windings needs to be considered inside the numerical simulation model. Since the detailed modeling of the thin insulation paper using discrete finite elements would lead to a considerably increased computational effort alternative approaches need to be employed in order to efficiently represent the insulation paper. The paper evenly surrounds the copper windings at a constant thickness of 0.25 mm. The micrograph in Figure 3.11 shows the detailed structure of the entire slot filling. A numerically efficient way to consider the increased compliance of the insulation layer is to adjust the normal and tangential contact stiffness of the Augmented-LAGRANGE contact between the laminated iron core and the copper windings. The basic principle is illustrated in Figure 4.14. The approach is only valid if the POISSON ratio of the paper and thus the contact itself can be neglected which can be assumed for the insulation paper due to air inclusions [228].

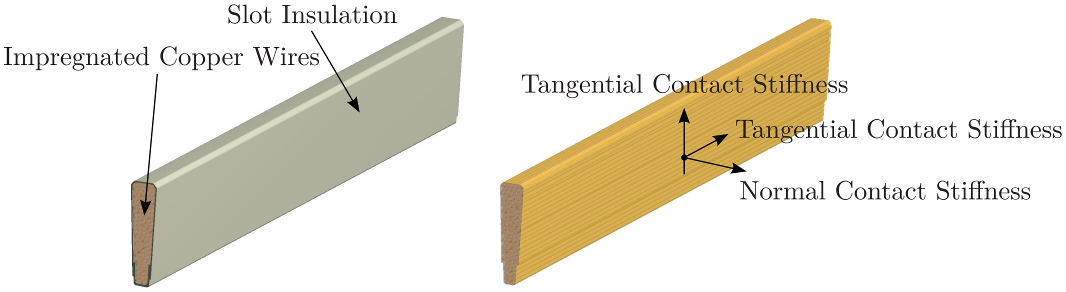

(a) Active copper windings including slot isolation

(b) Active copper windings adapted contact stiffness

Figure 4.14.: Schematic view of copper windings surrounded by the slot insulation paper and the substitutive modeling approach of the slot insulation.

4.2.2.2. Normal and Tangential Contact Stiffness Factors

In Section 3.2, different homogenization techniques yielding effective stiffness and damping properties of copper windings were introduced and validated based on dynamic measurements of generic copper winding specimens. Assuming the dynamic behavior of both, the laminated stator core as well as the copper windings, to be well represented by the effective values that arise from the homogenization approaches from Chapter 3.2 and 4.1, and assuming all input data of the corresponding homogenization techniques, meaning the stacking factor of the laminations, the filling factor of the copper windings as well as the mechanical properties of all constituents to be given, the normal and tangential contact stiffness factors between the copper windings and the stator iron core can be obtained from the results of the experimental modal analysis by means of model updating (see Figure 4.13). Therefore, the normal and tangential contact stiffness factors were subjected to a parameter study yielding optimal values in order to match the experimental eigenfrequencies given in Figure 4.13. However, the simultaneous identification of both values, the normal and tangential contact stiffness factor, based on the given five eigenfrequencies was found to be disadvantageous due to multiple optima. Thus, the two contact stiffness factors were successively identified starting with the normal contact stiffness factor. It was found that the eigenfrequencies of stator mode shapes with an axial order of zero, namely the mode shapes 2.0, 3.0 and 4.0, are predominantly influenced by the normal stiffness of the slot contact. Thus, the normal contact stiffness factor could uniquely be identified for the three identified mode shapes, namely 2.0, 3.0 and 4.0.

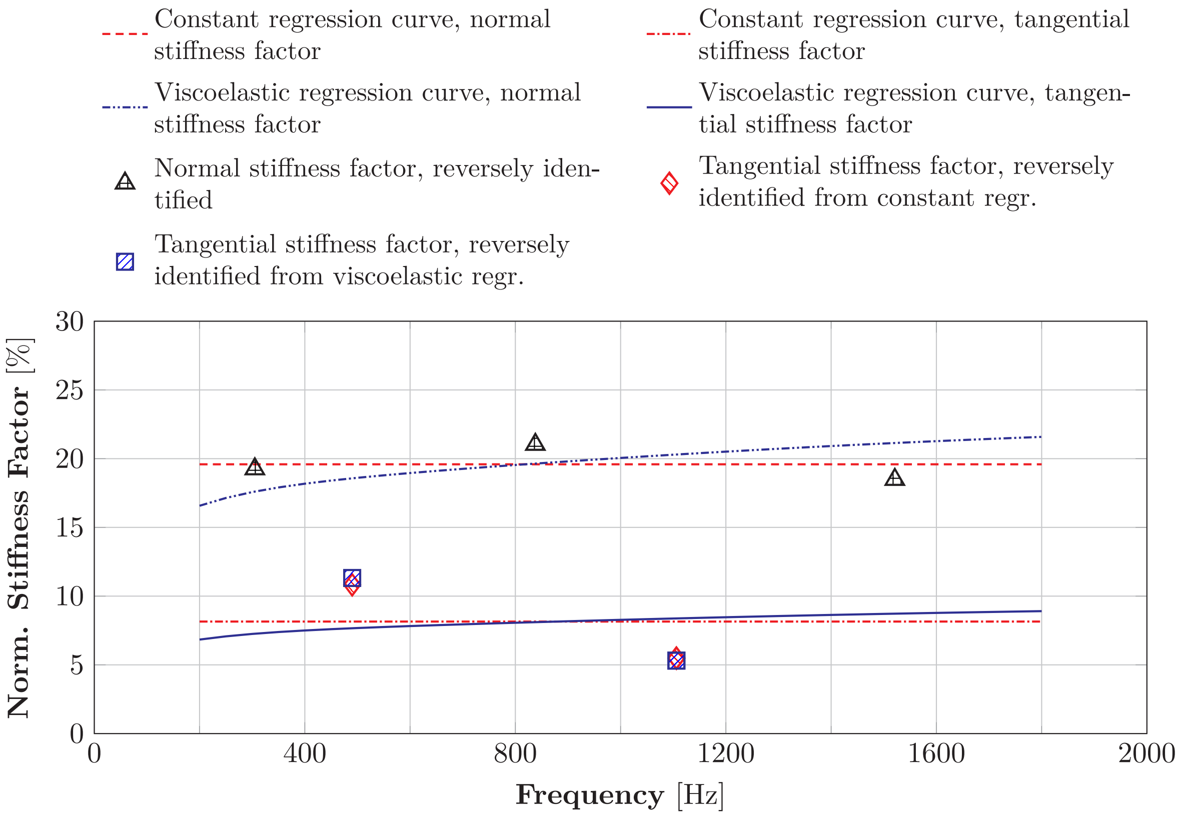

Figure 4.15.: Regression curves of normalized normal and tangential contact stiffness factors of the contact between the stator iron core and the slot filling.

In contrast, eigenfrequencies of stator mode shapes with an axial order higher than zero, like the mode shapes 2.1 and 3.1., are influenced by both, the normal and the tangential contact stiffness. Assuming the normal contact stiffness factor to be frequency-independent, a comprehensive value can be obtained from averaging the three initially derived normal contact stiffness factor of the x.0-mode-shapes. The constant comprehensive value of the normal contact stiffness factor denotes the first regression curve. In the following a second regression curve will be introduced. DURANTAY ET AL. found the slot insulation of impregnated electric machines to show a significantly temperature-dependent stiffness behavior [225]. Assuming the resin to influence the dynamic behavior of insulating mica paper, e.g. by entering the small capillaries of the paper, a viscoelastic and thus temperature-dependent behavior of the insulation paper would arise. Therefore, a second regression curve was developed based on the character of the viscoelastic behavior of Resin 2 which was used throughout this study. The second regression was obtained from scaling the PRONY series of Resin 2 at the temperature $T = 23$°C (see Section 3.1.2) by a constant factor to optimally approximate the three distinct data points of the normal contact stiffness factor. The optimal value of the scaling factor was identified by means of the least-square method. Based on the two different regression curves, the constant and the viscoelastic one, each of the higher axial order mode shapes can assigned to particular values of the normal contact stiffness factor. This allows the unique quantification of the corresponding tangential contact stiffness factor by means of model updating. However, due to the two different regression curves two sets of tangential contact stiffness factors arise. The two regression curves as well as the corresponding normal and tangential contact stiffness factors are illustrated in Figure 4.15.

4.2.3. Validation of the Modeling Approach

Over the time, multiple ways to consider copper windings inside dynamic simulations of electric machine stators have been proposed in literature. In numerous research works the copper windings and thus the influence the dynamic behavior of the stator are entirely neglected [39–46]. This violates all aforementioned findings of a strong correlation between the copper winding properties and the vibrational behavior of stator structures. Others consider the mass of the copper windings either by mass points, density increase of the stator core or by a distributed mass assigned to the slot surface [16, 37, 58, 61, 75, 79, 84, 216, 217, 229–232]. However, in all these investigations the damping and stiffness effect of the windings is neglected. [55] considers the mass and damping influence but neglects the stiffness increase. GARVEY ET AL. and CHANG AND YACAMINI use beams to represent the stiffness of the copper windings but neglect the damping effect [89, 233]. ZHANG ET AL. considers the copper windings as an isotropic continuous structure inside the stator slots [60]. The corresponding elastic material properties are derived iteratively from experimental modal analysis. LONG and LI both consider the copper windings as a homogenized material with transversely isotropic material properties [32, 33]. The corresponding effective stiffness properties are again obtained reversely from experimental modal analyses. A more advanced approach is introduced by BENBOUZID using solid elements to represent the copper windings [234]. The corresponding material properties are obtained from homogenization techniques that take into account the insulation layers within the windings as well as the fiber and matrix structure leading to an excellent correlation between experimental and numerical natural frequencies. However, viscoelasticity and damping are not contained in BENBOUZID's investigations.

In the following, different modeling approaches that aim to the accurate representation of the slot filling will be validated based on the experimentally obtained eigenfrequencies given in Figure 4.13. All modeling approaches were applied to the stator structure that was shown in Figure 4.12. In Figure 4.13 the numerically obtained eigenfrequencies of five different modeling approaches as well as the experimental eigenfrequencies are given. All five given simulation models assume the stiffness properties of both, the copper windings as well as the the laminations of the stator iron core, to be well represented by the homogenized effective stiffness properties obtained from the MOC. The influence of the contact stiffness between the slot filling and the stator iron core was investigated using three different contact topologies, namely a stiff contact, a compliant contact based on the frequency-independent regression curve from Section 4.2.2.2 and a compliant contact based on the viscoelastic and thus frequency-dependent regression curve again from Section 4.2.2.2. Furthermore, the effect of the viscoelasticity on the dynamic behavior of the stator structure was carried out by using two different homogenized material formulations, one considering viscoelasticity and the other neglecting the frequency-dependent behavior of the resin inside the structure. In the last simulation model, the influence of the copper winding stiffness was totally neglected by employing mass points that are located at the center of gravity of each slot and represent the copper winding mass.

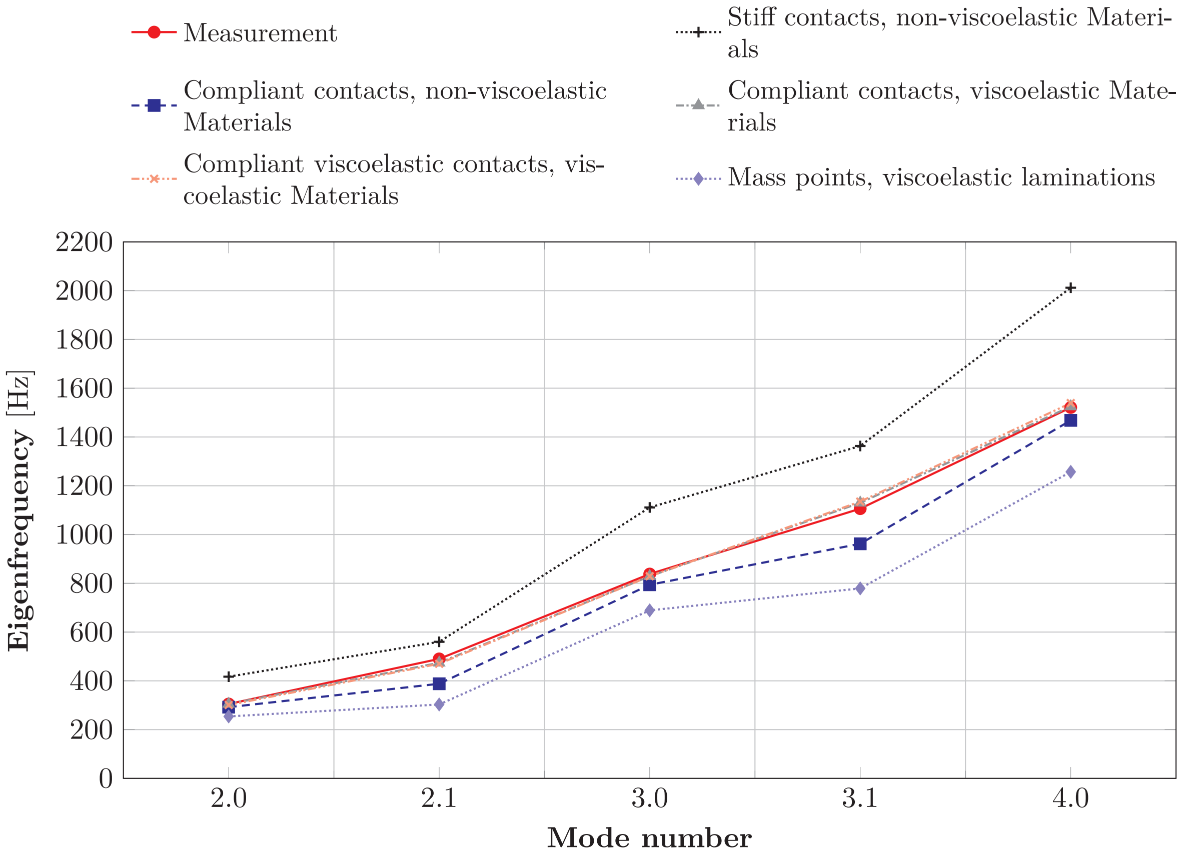

Figure 4.16.: Comparison of eigenfrequencies for different modeling approaches of stator with copper windings.

The results of the numerical modal analyses based on the different simulation models show that the contact stiffness between the slot filling and the stator iron core has a significant effect on the eigenfrequencies of the system. Assuming the slot insulation to have a negligible influence on the dynamic behavior of the stator and thus the contact to behave perfectly stiff leads to considerable errors regarding the eigenfrequencies of the system. In contrast, employing compliant contact formulations produce a good accordance between the numerically and experimentally obtained system eigenfrequencies. The consideration of viscoelasticity inside the dynamic simulation models further increases the model accuracy, especially for higher axial spatial order mode shapes. In contrast, neglecting the frequency- and temperature-dependent stiffness behavior of the impregnation resin causes an underestimation of all system eigenfrequencies. Employing mass points that are located at the center of gravity of each slot winding can be regarded as beneficial in terms of numerical efforts. However, neglecting the copper winding stiffness by using mass points causes significant errors regarding the system eigenfrequencies.

4.2.4. Temperature-Dependent Vibrational Behavior of Stator Structures

In Section 4.1, the influence of the impregnation resin on the dynamic behavior of the stator iron core was investigated. It was shown that the thin resin layer located between two steel sheets needs to be considered inside structural dynamic simulations in order to reliably predict the vibrational behavior of stator iron cores. Furthermore, it was shown that the viscoelastic character of the impregnation resin, meaning the frequency-dependent mechanical properties, significantly affect the comprehensive damping properties stator iron cores as well as copper windings (see Section 4.1.4.2 and 3.2.3.3, respectively). However, the influence of the frequency-dependent resin properties on the eigenfrequencies of the stator was found to be rather insignificant for both investigated structures, the pure impregnated stator iron as well as the stator iron core including copper windings (see Section 4.1 and 4.2, respectively). The consideration of viscoelasticity inside dynamic simulations is elaborate due to the complex measurement technique and hence increases the overall effort of dynamic simulations (see Section 2.4.3).

Figure 4.17.: Test configuration of experimental modal analyses at different frequencies.

In order to further evaluate the effect of the frequency- and temperature-dependent properties of the resin on the stiffness and damping behavior of stator structures a series of experimental modal analyses was performed at different temperatures. The experimental setup is shown in Figure 4.17. Again, the stator end windings were removed from a full stator specimen yielding a geometry similar to the one shown in Figure 3.10. The stator was placed inside an oven supported by elastic springs in order to provide almost free boundary conditions. The excitation was provided by a shaker below the oven that was attached to the structure by a thin rod. The dynamic response of the structure was measured by a 1D-LSV that pointed through the oven window.

In Figure 4.18, the chronology of the experimental study is shown. The eigenfrequencies of the stator were measured in a temperature range from -40°C to 100°C at temperature steps of 20°C. In order to assure a constant temperature within the structure the temperature at each step was held constant for two hours before each measurement. At the end of each step, a modal analysis was performed. Pre-tests have shown that the resin in some cases tends to change its mechanical behavior at temperatures above 100°C due to insufficient hardening. In order to maintain reproducibility, the stator was heated up and held constant at a temperature of 180°C for six hours before the actual study started.

The results of the temperature-dependent modal analyses are given in Figure 4.19. A total of six different eigenmodes were uniquely identified in a preliminary reference measurement at 20°C and tracked over all temperatures steps (see Figure 4.18).

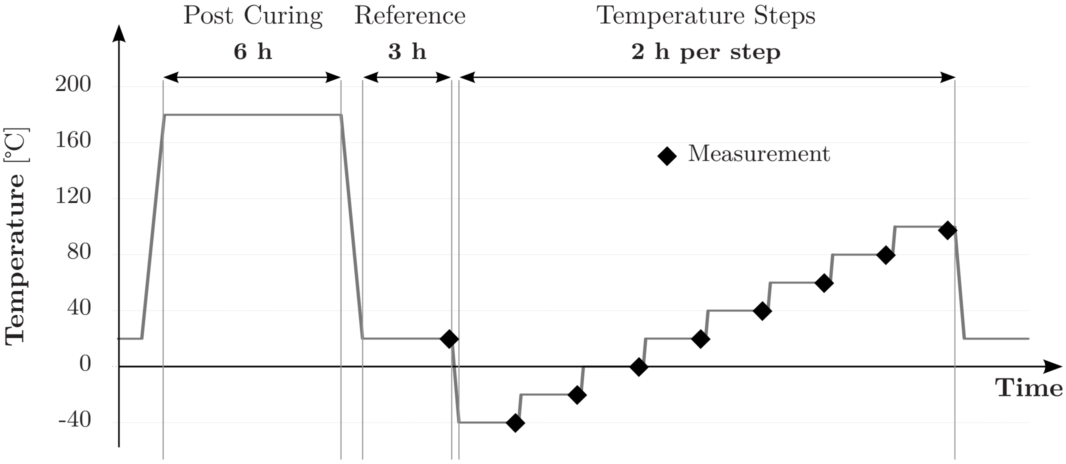

Figure 4.18.: Chronology of measurements of the natural frequencies of a stator at different temperatures.

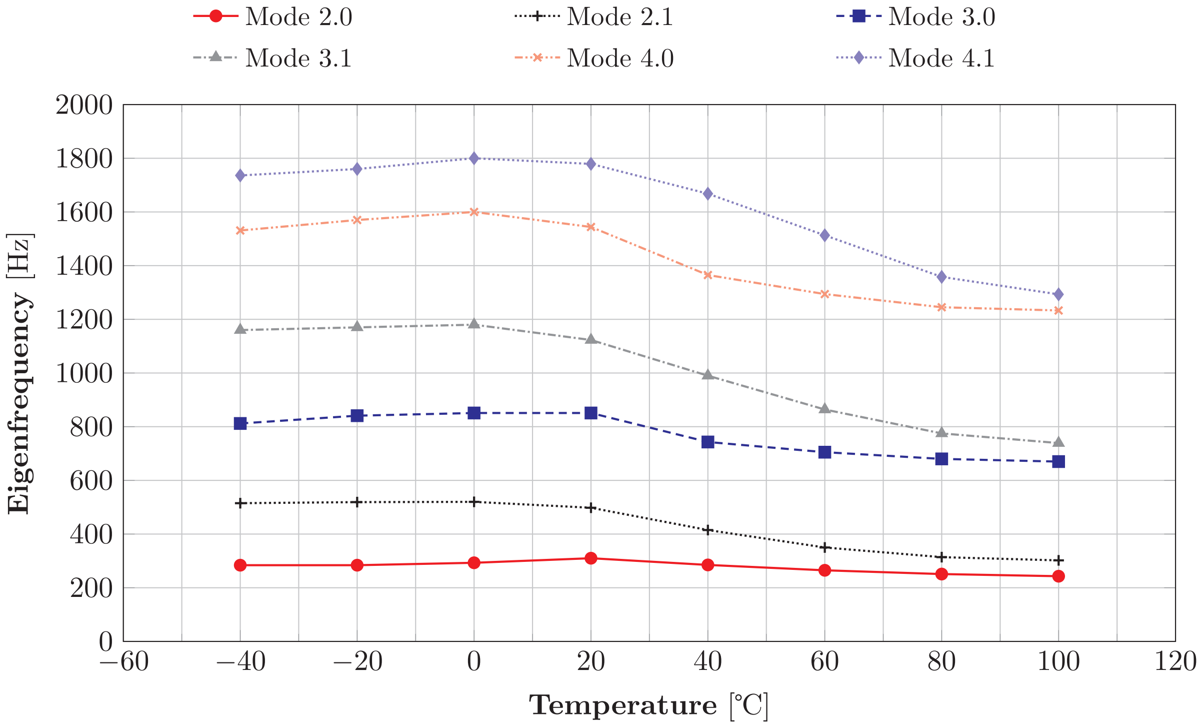

Figure 4.19.: Temperature-dependent eigenfrequencies of stator with copper windings.

4.2.5. Validation of the Temperature-Dependent Modeling Approach

In Figure 4.20, 4.21, and 4.22, the change of eigenfrequency of each mode shape over the temperature is separately compared to numerical eigenfrequencies obtained from different simulation models.

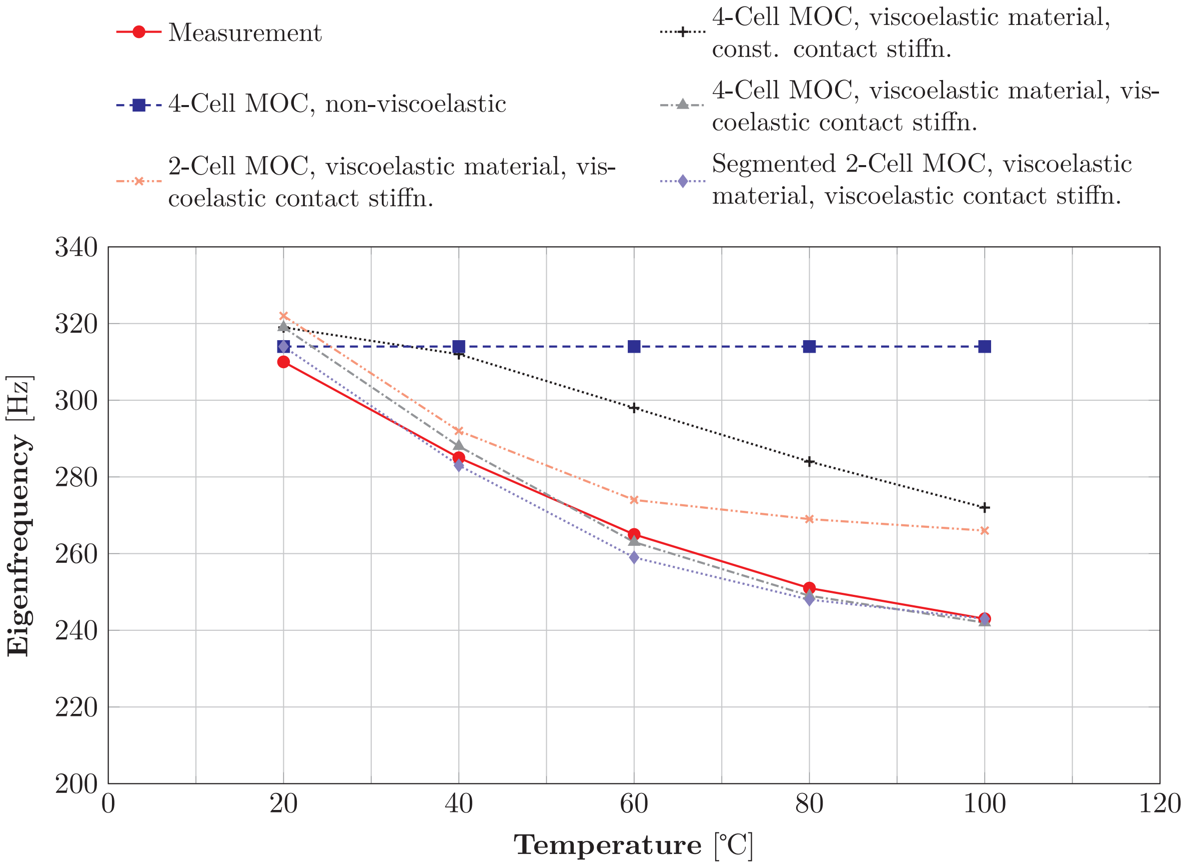

(a) 2.0-mode.

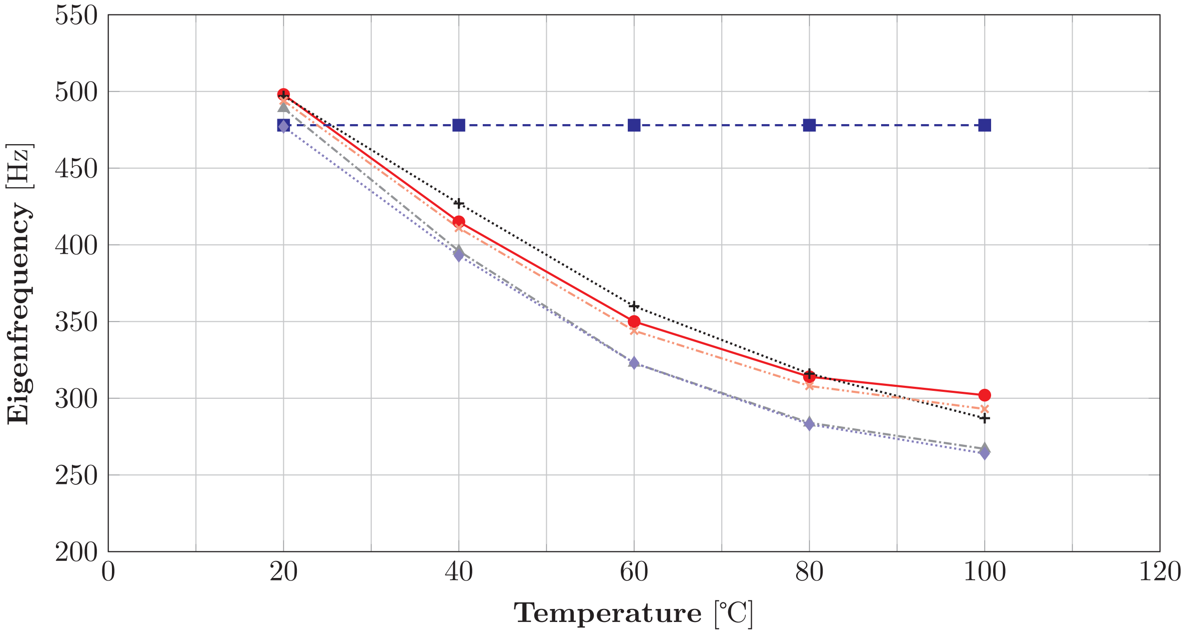

(b) 2.1-mode.

Figure 4.20.: Comparison of temperature-dependent eigenfrequencies (2.0-mode and 2.1-mode) of different modeling approaches for stator with copper windings.

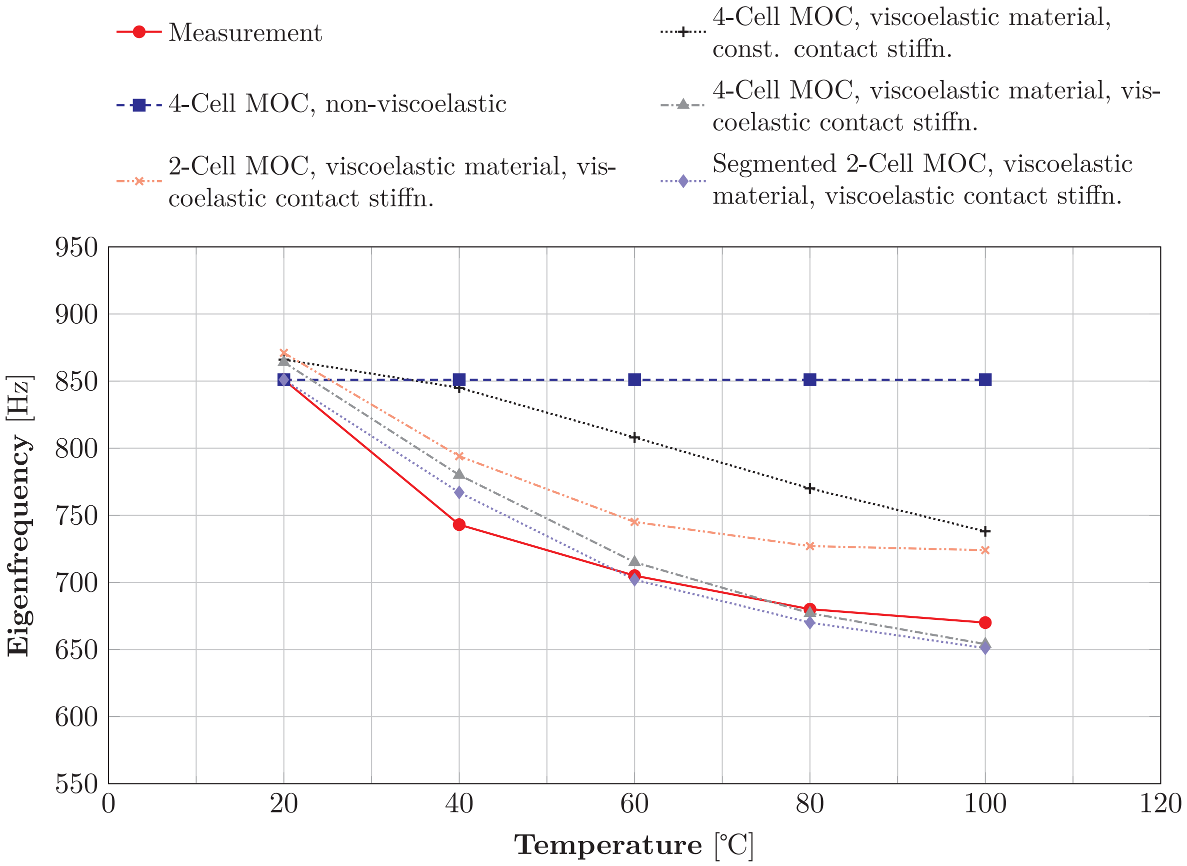

(a) 3.0-mode.

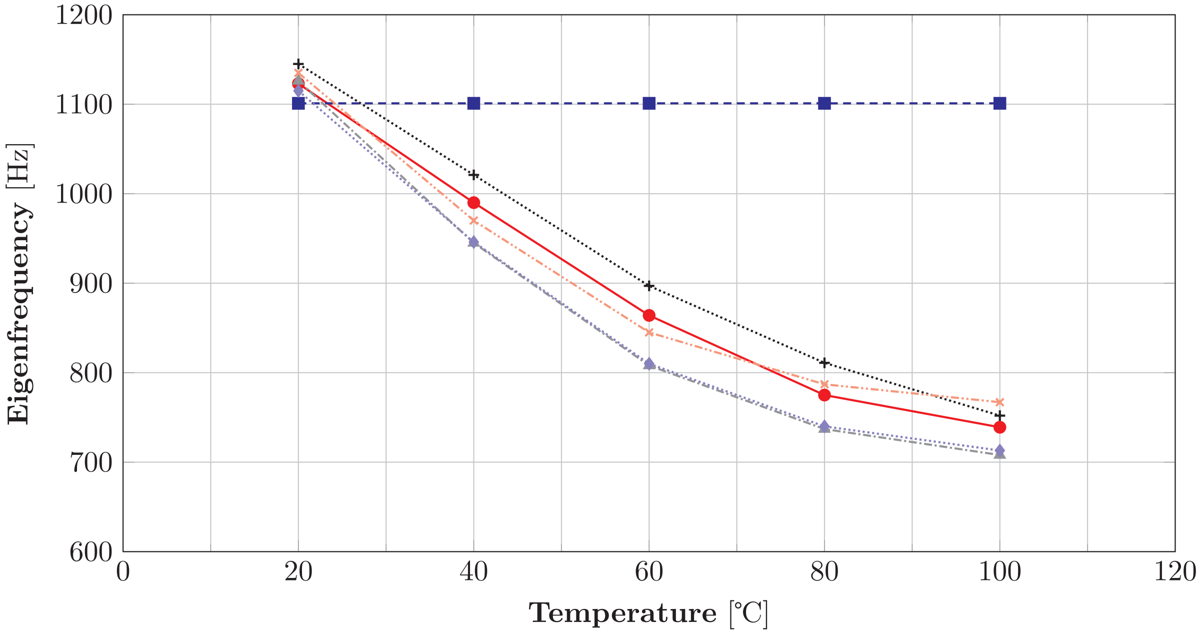

(b) 3.1-mode.

Figure 4.21.: Comparison of temperature-dependent eigenfrequencies (3.0-mode and 3.1-mode) of different modeling approaches for stator with copper windings.

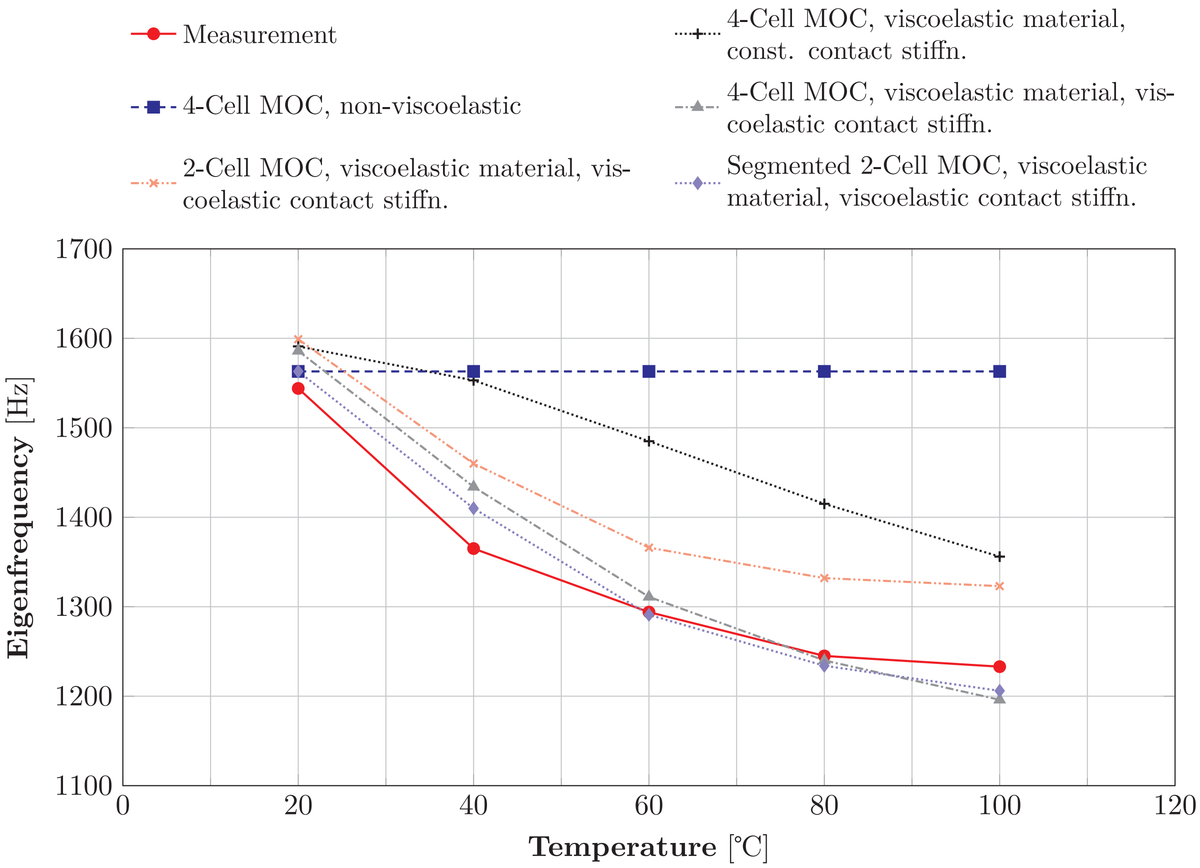

(a) 4.0-mode.

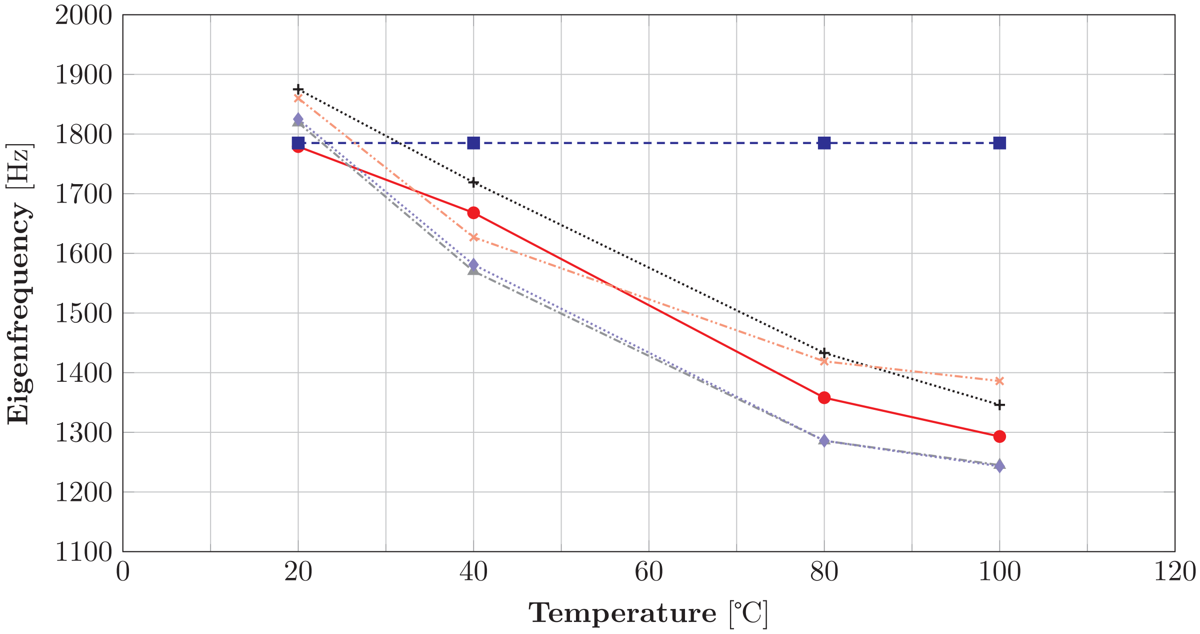

(b) 4.1-mode.

Figure 4.22.: Comparison of temperature-dependent eigenfrequencies (4.0-mode and 4.1-mode) of different modeling approaches for stator with copper windings.

All six eigenfrequencies show a temperature-dependent behavior. Due to the limited measured temperature range of the viscoelastic stiffness and damping properties of Resin 2 (see Section 3.1.1), the results are only given for a temperature range from 20℃ to 100℃. In all different models the effect of the stator laminations was considered employing the advanced MOC based on two and four subcells. In order to evaluate the influence of the temperature-dependent properties of the impregnation resin a non-viscoelastic model was compared to different viscoelastic models. The effective stiffness properties of the non-viscoelastic simulation model correspond to the resin properties of Resin 2 at 23℃ obtained from quasi-static tensile tests while for the viscoelastic models the frequency and temperature-dependent properties of Resin 2 that were introduced in Section 3.1 were employed. The representation of the slot insulation by using a reduced normal and tangential contact stiffness behavior of the slot contact was investigated using two different models. The first model assumed a constant frequency- and temperature-independent formulation of the contact stiffness, the second model assumed a viscoelastic and thus frequency- and temperature-dependent formulation. The tangential stator segmentation was either considered reducing the circumferential stiffness of the stator yoke in an integral sense using the micromechanical 4-cell MOC or by employing a detailed FE-model of the stator segmentation topology including the thin resin layer between two a yoke segments. Both modeling approaches for the stator segmentation were already employed in the temperature-independent investigations of the impregnated stator iron core (see Section 4.1.4). The effect of the segmentation on the vibrational behavior of the stator structure is neglected by employing the 2-cell MOC.

The measurement results show that the eigenfrequencies of the stator structure considerably depend on the temperature of the system. All eigenfrequencies decrease with an increasing temperature. Consequently, assuming a non-viscoelastic behavior of the structure leads to significant errors especially at higher temperatures. Due to the low stiffness of the impregnation resin at higher temperatures, the representation of the stator segmentation inside the structural dynamic model is more relevant for higher temperatures. DURANTAY has found the slot isolation as a combination of epoxy-resin and mica paper to show a significantly temperature-dependent stiffness behavior [225]. These findings can be confirmed by the measurement results. Assuming a viscoelastic temperature-dependent behavior of the slot contact stiffness instead of a constant temperature-independent slot contact stiffness the model accuracy increases significantly.

4.3. Stator Core with End Windings

4.3.1. Structure of the Stator Core with End Windings

In the previous section, a linear dynamic model of the stator including the slot filling was introduced. In order to close the electric circuit, the current-carrying copper wires that are located inside the stator slots are galvanically connected at the front and back end of the stator core, forming the so-called end windings. The end windings can be designed in different ways (see Section 2.1.1). In the present case, the wires are twice redirected, first from an axial to a circumferential and then back into an axial direction as shown in Figure 4.23. The directional stiffness and damping properties of the end windings naturally follow the fiber direction. The presented stator configuration contains two slots per pole and phases. Thus, at the average two phases run parallel within the circumferential part of the end windings. Since the phases in the end windings need to be electrically isolated from one another (see Section 2.1.1), an insulation paper as introduced in Section 4.2.2.1 is located between two different phases. Figure 4.23 schematically shows the structure of the coil end as well as the fiber direction.

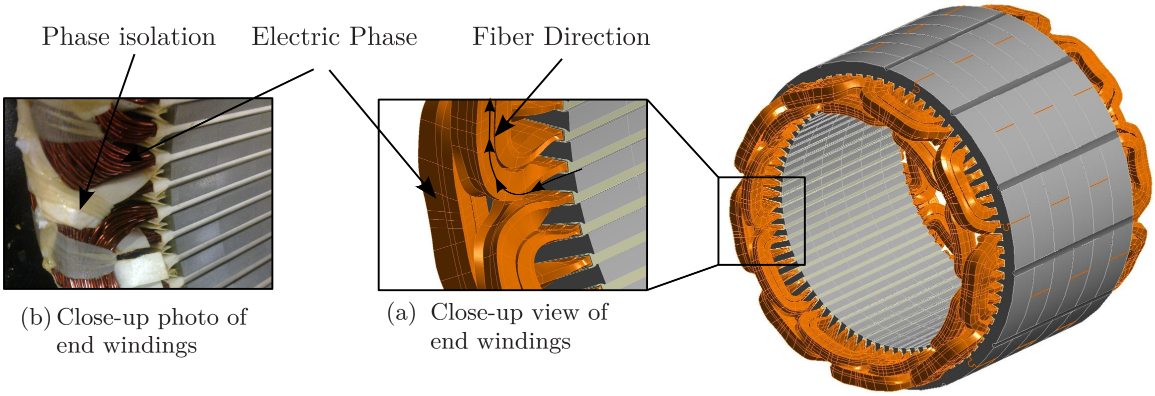

(b) Close-up photo of end windings

(a) Close-up view of end windings

Figure 4.23.: Isometric view of a full stator core including copper windings and end windings.

4.3.2. Validation of the Modeling Approach

Typically, the detailed finite element analysis of the end windings' vibrational behavior intends the analysis of the durability of the end windings whereas in most practical investigations that yield the prediction of the vibrational behavior of an entire stator structure as given in Figure 4.23, the influence of the copper windings including the end windings is typically either reduced to the inertia effect or fully neglected [16, 37, 39–46, 58, 61, 75, 79, 84, 216, 217, 229–232]. Noda et al. and Long et al. have independently identified a significant influence of the end windings on the vibration behavior of the electric machine stator [32, 235]. End windings can be designed in multiple ways (see Section 2.1.1) e.g. by bars, wires or circuit rings. Thus, defining general model guidelines is difficult. Nevertheless, the major geometric shape of end windings remains annular and contains current-conducting parts that are oriented in a circumferential direction. Noda et al. and Lin et al. have numerically investigated the vibrational behavior of end windings using a material model with homogenized orthotropic properties [235, 236]. The stiffness values were reversely quantified based on experimental modal analyses. Noda et al. and Lin et al. independently found the stiffness values of the composite to be much lower than the stiffness of the underlying fiber material. Noda et al. furthermore identified a strong frequency-dependency of the end windings' stiffness. Schlegl et al. numerically investigated the vibrational behavior of stator bar end windings [237–239]. The applied orthotropic material properties in Schlegl et al.'s investigations were obtained from analytical homogenization techniques. Drubel et al. experimentally detected a significant temperature dependency of the circumferential end winding stiffness [240]. Similar findings were carried out by Seske et al. [241].

In order to validate different modeling approaches for the stator including end windings, an experimental modal analysis was performed. In Figure 4.24, the natural frequencies as well as the mode shapes are given. Again, a total of five distinct mode shapes were uniquely identified. Based on the validated modeling approach of the laminated steel stack including copper windings which was described in Section 4.2, different modeling approaches for the end windings can be validated based on the comparison between the numerically and experimentally obtained eigenfrequencies of the full stator structure. The results are given in Figure 4.25. Four different simulation models were employed to investigate the effect of different modeling techniques of stator end windings.

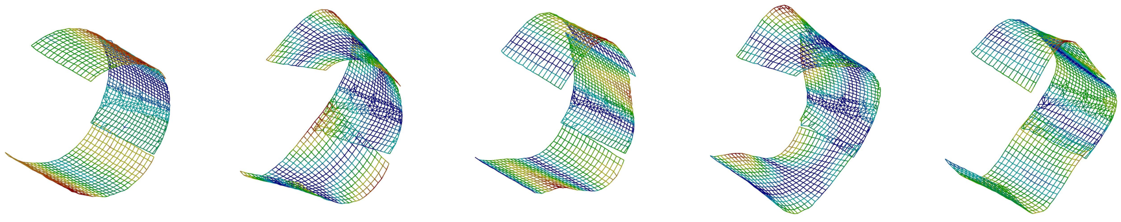

Mode 2.0
282 Hz

Mode 2.1
378 Hz

Mode 3.0
765 Hz

Mode 3.1
870 Hz

Mode 4.0
1381 Hz

Figure 4.24.: eigenmode shapes and natural frequencies of an entire stator including copper windings and end windings.

In order to demonstrate the effect of the varying fiber direction inside the end windings on the total stiffness characteristics of the stator structure, Long et al. proposed an adaptable coordinate system which follows the fiber direction and thus provides appropriate transversely isotropic stiffness and damping properties for both, the copper windings inside the stator slots and the end windings [32]. In the presented simulation models, the orientation of the windings was assumed to be axial inside the active copper windings and tangential inside the end windings. The corresponding transversely isotropic effective material properties were obtained from the MOC that was introduced in Section 3.2.2 and illustrated in Figure 2.15(b).

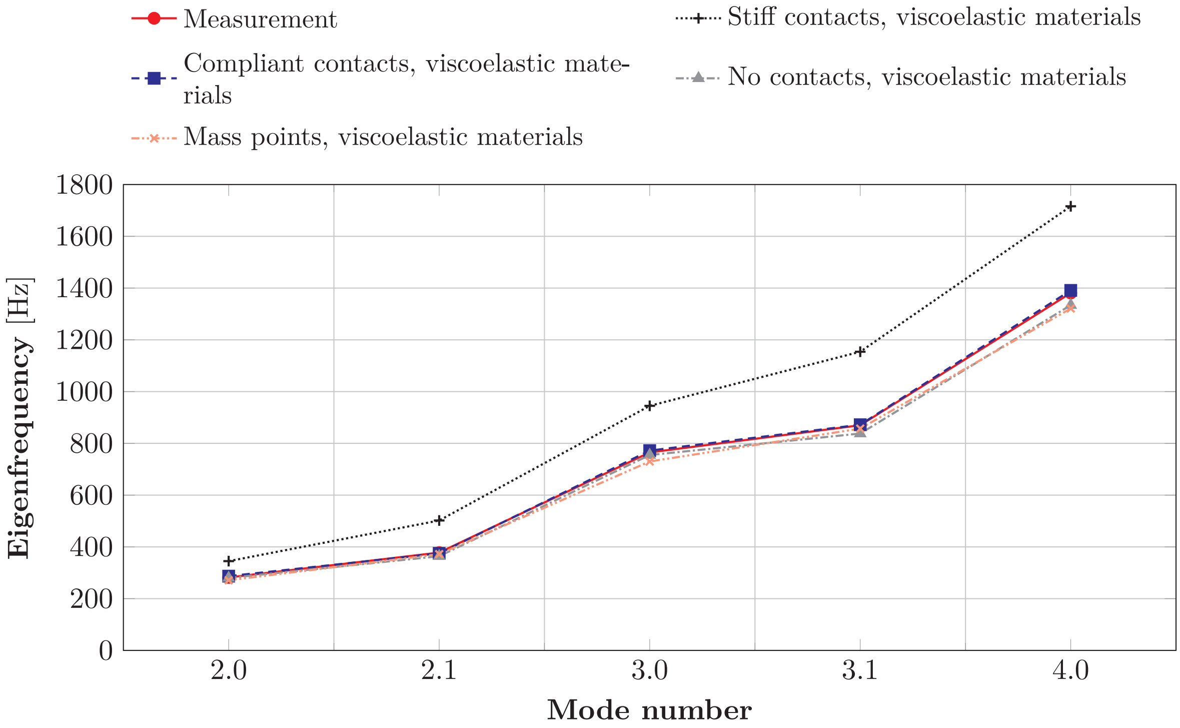

Figure 4.25.: Comparison of experimental and numerical eigenfrequencies of a full stator core for different modeling approaches of end windings.

The effect of the phase insulation that is radially located between two phase coils is represented by either compliant contacts that are based on the reduced contact stiffness formulations from Section 4.2.2 or by stiff contacts which presume no relative displacement between two neighboring phase coils. These two modeling approaches were compared to the modeling which assumes no contact between the phase coils and thus the coils to oscillate independently. The last simulation model is based on the neglect of the end windings' stiffness by using lumped mass points that are connected to the slot filling on both ends of the stator. This method is thus numerically very beneficial. All presented modeling approaches consider viscoelastic material behavior. The results show that the contact stiffness and hence the modeling approach of the phase insulation has a significant influence on the dynamic behavior of the stator. Apparently, the phase insulation inside the end windings causes the different phase coils to oscillate rather individually. Using reduced contact stiffness factors instead of neglecting the interaction between two coils leads to no significant improvement of model accuracy. The end windings as individual mass points that are periodically distributed around the circumference and axially attached to the slot filling provide eigenfrequencies that are in good accordance with the measurement results. Nevertheless, the mass points do not provide a physical model which is able to represent design changes inside the end windings. Based on the previously identified temperature-dependent vibrational behavior of the stator structure without end windings (see Section 4.2.4), it can be presumed that the dynamic behavior of the full stator structure is numerically only reliably predictable by considering the viscoelastic resin properties inside the simulation model (see Section 4.2.5). However, the temperature-dependent stiffness and damping effects of the impregnation resin are not representable by the lumped mass points which can cause errors regarding the prediction of the stator vibration magnitudes and hence the acoustic sound emission of the entire system. In contrast, modeling approaches that consider the end windings as a homogeneous material with transversely isotropic and viscoelastic material properties are capable of representing the temperature-dependent vibrational behavior of the structure and are thus recommendable to use for the dynamic modeling of copper end windings.

4.4. Acoustics of an Electric Motor

4.4.1. Specification of the Acoustic Simulation Model

In the previous sections, different modeling approaches of the full stator core were developed and validated. In Figure 4.26, an entire electric drive system including the electric motor as well as the gear box is shown.

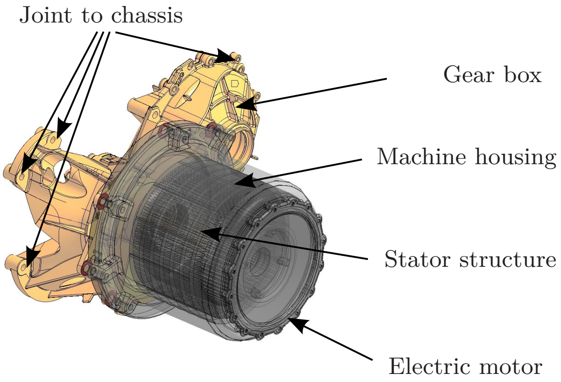

Figure 4.26.: Schematic view of entire electric drive train including electric motor and gear box.

The electric machine stator core of the given electric motor corresponds to the stator core that was investigated in the previous sections. In order to validate the structural dynamic simulation model as a basis for comprehensive acoustic investigations, the entire drive train was operated in an free-field acoustic room. The sound pressure was measured at five different microphone positions at a distance of 1 m from the machine surface. In Figure 4.27, the test configuration including the microphone positions is illustrated. In order to simulate the acoustic sound pressure pressure field of a system subsequently to the structural dynamic simulation of the system different numerical methods can be applied. In this thesis, the finite-element method (FEM) was used. Therefore, the acoustic volume which surrounded the drive train structure was discretized inside a simulation model. In order to maintain a reasonable computational effort, the number of elements inside the acoustic volume was reduced based on the wavelength of the corresponding acoustic sound and the wavelength of the structural deflection. Therefore, the element length of linear acoustic elements in radial direction was set to a sixth of the acoustic wavelength while the element length along the structure was set to an eighth of the structural wavelength [242]. Thus, to high frequencies the total number of elements significantly increased. In order to obtain a numerically solvable system the outer part of the acoustic volume which is at a certain distance of the structure can be truncated. Typically, the distance of the truncated volume corresponds to the acoustic wavelength [243]. Due to short acoustic wavelengths at high frequencies the microphone positions not necessarily need to be represented inside the discretized acoustic volume.

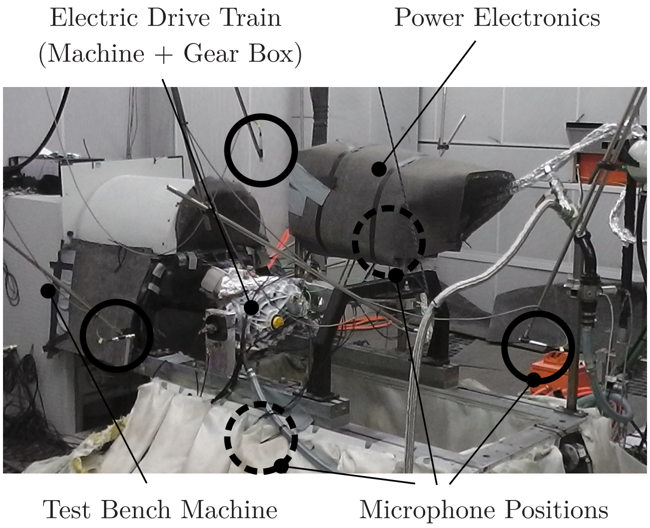

Figure 4.27.: Acoustic measurement configuration of the electric drive train including the electric motor and gear box and mounting devices.

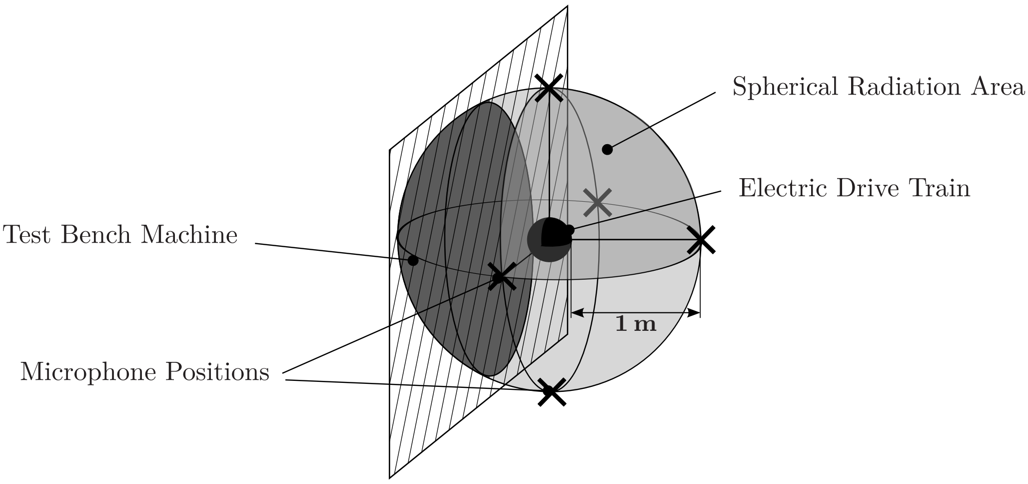

Figure 4.28.: Schematic test configuration including the spherical radiation of the electric machine.

Further remarks on standards procedures and limitations of the FEM inside acoustical simulations can be found in [243–246]. The acoustic sound pressure at the distinct microphone positions can either be approximated from analytical methods or, as employed in this thesis, be considered in an average sense by means of the total sound power. Therefore, not the local acoustic sound pressure level at the microphone positions were compared to the measurements but the total sound power at free-field conditions. From the mean sound pressure of all five microphone positions and the corresponding sphere surface, the total sound power of the given drive train can be approximated. The procedure is schematically illustrated in Figure 4.28.

4.4.2. Electromagnetic Forces

In Figure 4.29 the configuration of the investigated internal permanent magnet machine (IPM) is schematically illustrated. It is based on 12 poles with stepwise shifted permanent magnets inside the rotor as it was introduced in Section 2.1.1. The number of teeth of the stator is 72. Based on the configuration, the electromagnetic field of each pole pair of the of the IPM is rotationally symmetric.

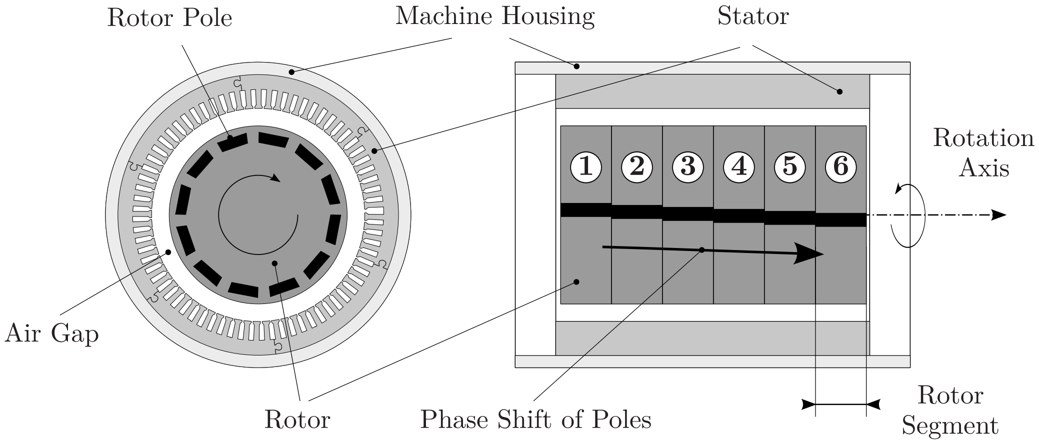

(a) Front view

(a) Side view

Figure 4.29.: Schematic front and side view of the investigated IPM with an electromagnetic design based on twelve poles and a stepwize shifted rotor configuration.

Due to the quadratic terms of the magnetic flux density b in Equation 2.1, the resulting magnetic force field is equal for each pole. Thus, assuming the local magnetic forces on each stator tooth in a certain axial segment of the machine to act as a resultant force vector including a radial and tangential component (see Section 2.1.2.2), the overall magnetic force excitation of the axial stator segment at a particular operation point can be calculated from the force excitation of the first six stator teeth. In Figure 4.30 the magnetic forces that radially and tangentially act on the first six stator teeth are given as a function of the mechanical rotation angle of the rotor for an exemplary operation point. The absolute values are normalized with respect to the tangential force value that corresponds to the absolute machine torque at that particular operation point.

Performing a FOURIER transform in both dimensions, the temporal and spatial dimension, the magnetic excitation of the stator can be expressed by engine orders (frequency orders) that correspond to the rotational speed of the electric motor and spatial orders that correspond to the spatial distribution of the forces around the circumference of the stator (see Section 2.1.1.1). In Figure 4.31 the two-dimensional radial and tangential magnetic excitation field is illustrated. The force magnitude is given as a logarithmic value referenced to the tangential force value that corresponds to the absolute machine torque at the exemplarily chosen operation point.

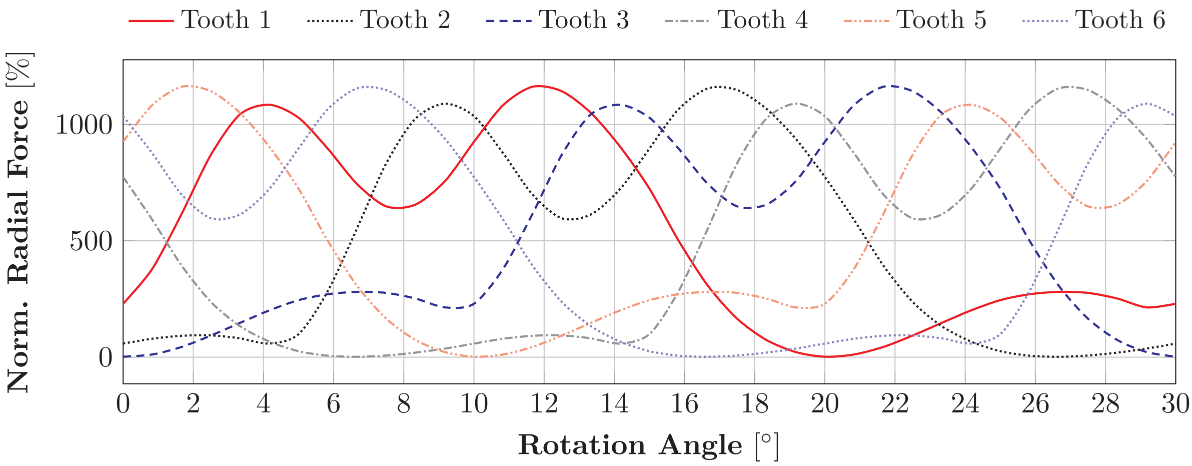

(a) Radial Tooth forces.

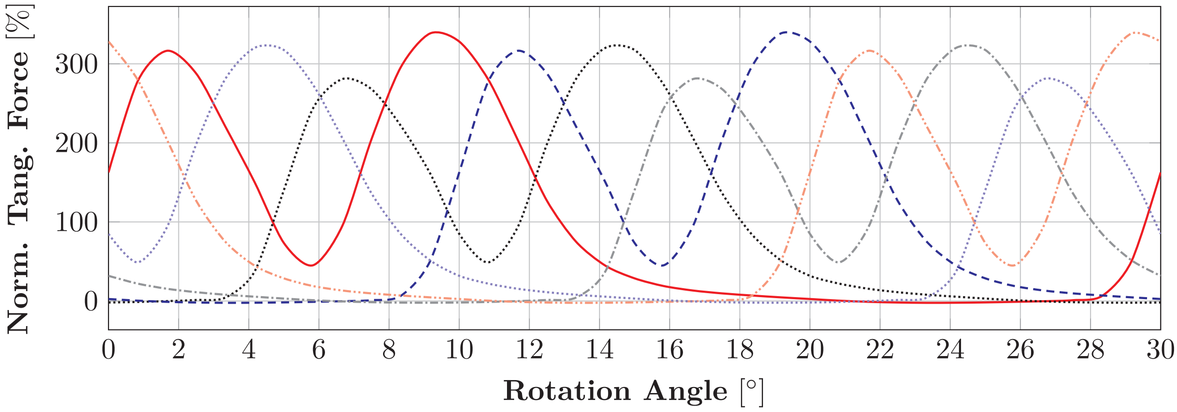

(b) Tangential Tooth forces.

Figure 4.30.: Radial and tangential resultant tooth forces of axial stator segment as a function of the rotor rotation.

Figure 4.31 shows that the spatial electromagnetic forces can be decomposed into six different rotating force waves where positive values denote forward-rotating force waves and negative values denote backward-rotating force waves. Based on the symmetric configuration of the IPM, the engine orders that occur are multiples of the number of poles $n_p = 12$ (see Section 2.1.1.1).

In this particular case, each engine order predominantly corresponds to two independent rotating force waves. During acoustic measurements of the electric machine, the highest acoustic sound pressure levels were generated inside the 72^{nd} and 60^{th} engine orders. The 72^{nd} engine order involves the spatial order zero and and a low magnitude of the spatial order 36 while the 60^{th} engine order corresponds to the spatial order minus twelve and a low magnitude of the 24^{th} spatial order. The magnitude and phase of the force excitations vary for each operation point and for each axial segment of the machine. However, the spatial orders that correspond to the different engine orders remain the same.

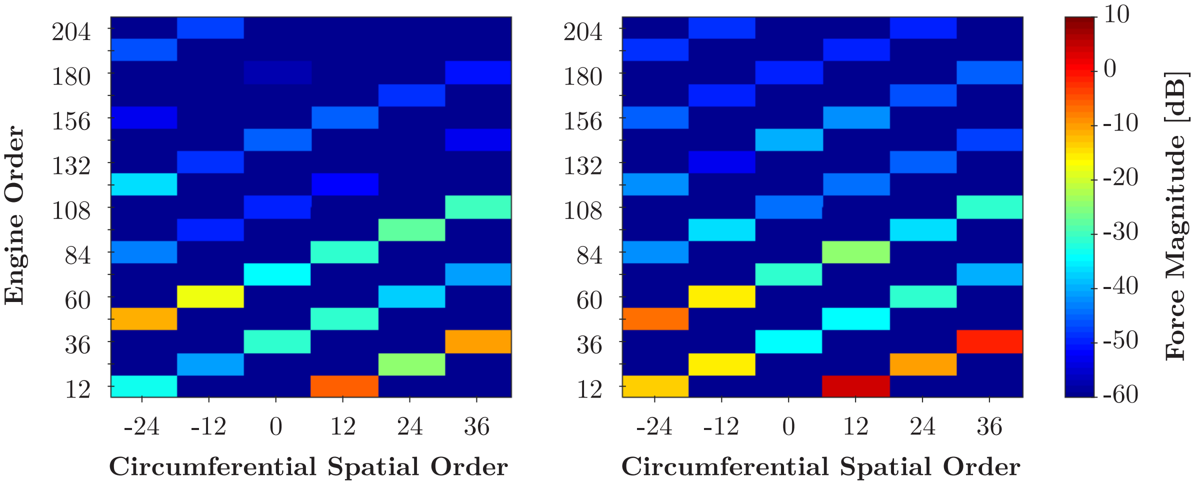

(a) Tangential Forces.

(b) Radial Forces.

Figure 4.31.: Two-dimensional decomposition of the transient magnetic force excitation field into engine orders and corresponding circumferential spatial orders.

4.4.3. Validation of the Acoustic Simulation Model

In Figure 4.32 the measured sound power of the two engine orders is compared to the simulated sound power at the outer surface of the acoustic volume and the equivalent radiated power (ERP) emitted by the drive train surface. The simulation model of the stator was based on the consideration of the laminations by using the advanced MOC including viscoelasticity and the directional stiffness behavior for both, the laminated stator iron core as well as the copper windings inside the slot and the end windings (see Sections 4.1, 4.2 and 4.3). The housing structure was represented as aluminum parts. WANG experimentally found the rotor of electric machines to hardly influence the eigenfrequencies of the system [54]. Thus, neither the rotor structure nor the rotor excitation were considered inside the simulation model. The structural damping of the entire structure was set to 3% since the influence of the gear box structure on the damping was unknown. The stator teeth of the structure were radially and tangentially excited by internal electromagnetic forces which were quantified based on a 2-dimensional electromagnetic finite element simulation for each of the six axial rotor segments at steps of 1000 rpm. Due to confidential reasons the electromagnetic simulation model can not be specified in this thesis. Figure 4.32 shows the comparison between the numerical and experimental results for both critical engine orders, the 72^{nd} EO and the 60^{th} EO. The simulations are in good accordance with the measurements for both engine orders. The sound power level of the 72^{nd} EO shows a distinct resonance at about 6.7 kHz and thus can be divided into a low-frequency increasing and a high-frequency decreasing area. In contrast, the sound power level of the 60^{th} EO almost monotonously increases over the entire frequency range. In Section 2.1.2.2 the relation between rotating spatial force waves and the correspondingly excited eigenmode shapes of electric machines was explained. The eigenfrequency of the 72^{nd} EO corresponds to the zeroth circumferential spatial order of the electric machine which was successfully predicted by the simulation (6713 Hz). In contrast, the first eigenfrequency which corresponds to the 60^{th} EO is is not located inside the investigated frequency range but was found to be about 18 kHz which is why the sound pressure level almost monotonously increases.

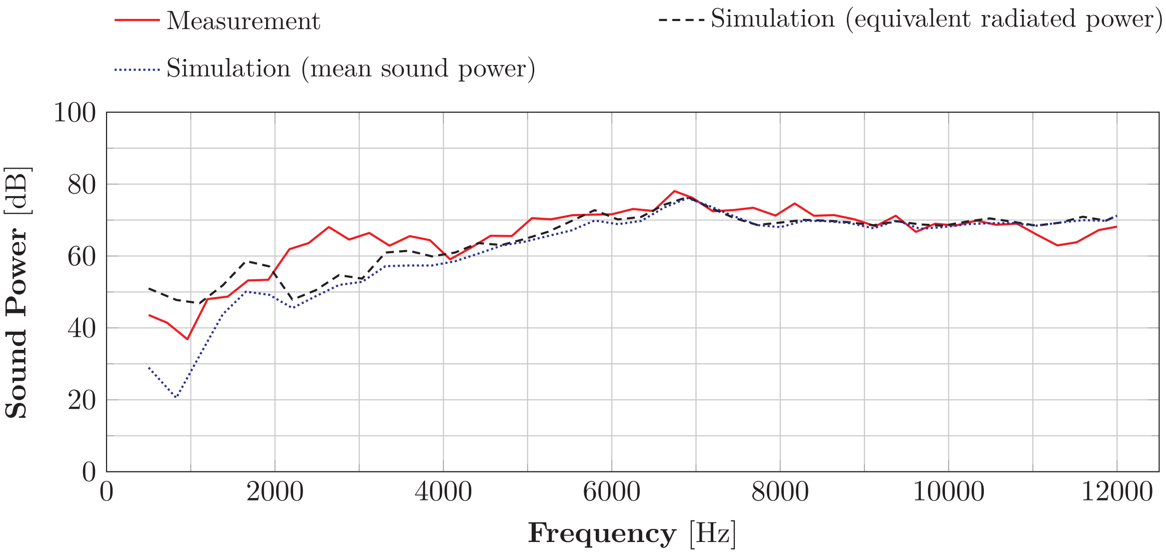

(a) 72^{nd} engine order.

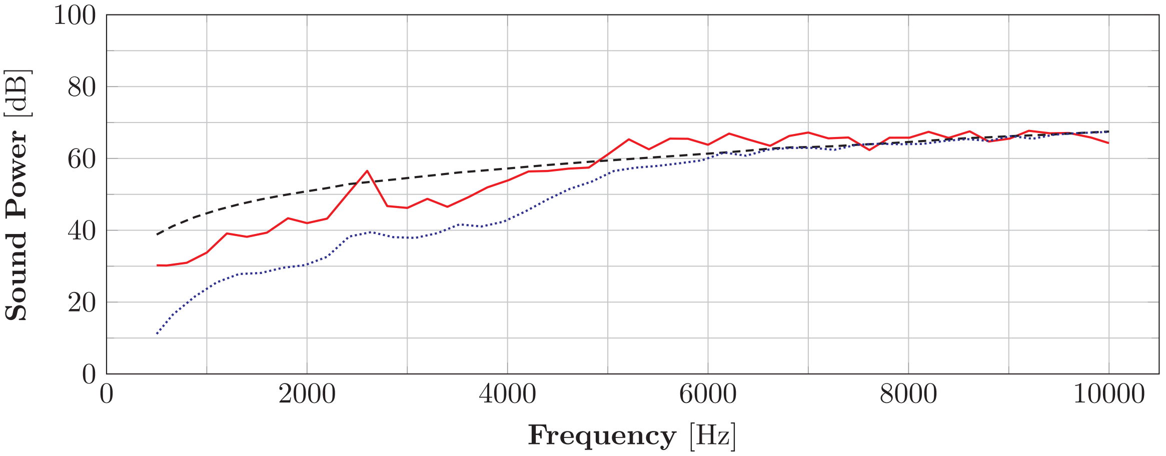

(b) 60^{th} engine order.

Figure 4.32.: Comparison of measured and simulated sound power level for two different engine orders.

Both basic curve trends of the two independent engine orders which were observed inside the measurements were successfully predicted by the simulation model. However, the deviation between the measurement and the simulation is significant at some areas especially at low frequencies. As will be shown later in this thesis, the modeling of the peripheral structure of the machine including gear box and bearers becomes less relevant to the dynamic behavior of the electric motor as the frequency increases. Thus, the accurate prediction of the absolute sound pressure values at high frequencies is a strong indication for a good overall representation of the vibrational character of the electric machine inside the simulation model.

5. Model Order Reduction Techniques

In Chapter 3 various modeling approaches that yield the accurate prognosis of the structural dynamic behavior of electric motors were introduced. In Chapter 4 these approaches were successively validated regarding the use in electric machines. In order to efficiently calculate the broadband sound emission of the electric motor at different operation points, the use of model order reduction methods can be advantageous. Depending on the type of coordinates of the reduced order system, model order reduction techniques can be divided into three basic categories: physical coordinate reduction, generalized coordinate reduction, and hybrid coordinate reduction [104]. While the coordinates of the physically reduced model represent a subset of the physical coordinates of the full model, generalized coordinate reduction yields a coordinate transformation into a reduced order subspace. The shape of the vectors that span the reduced order subspace strongly depends on the particular algorithm which is employed to generate them. In the following chapter different generalized and hybrid model order reduction techniques will be introduced and evaluated regarding their applicability for structural dynamic simulations of electric motors.

All following investigations involve the drive train structure that was introduced in Section 4.4 and illustrated in Figure 4.26. It consists of an electric motor which is attached to a gear box. The whole drive train is mounted to the chassis of the car.

5.1. Component Mode Synthesis

5.1.1. Influence of Machine Environment

It was shown that the vibrational behavior of electric motors is influenced by the mechanical properties of the circumferential parts (see [247]). In order to evaluate the effect of the peripheral components on the frequency response of the electric motor different ways of mounting the machine can numerically be compared. In the following, the vibrational behavior of the electric machine is analyzed virtually employing three different mounting configurations:

1. Elastic mounting by connection to the actual gear box model

2. Fixed mounting by fixed boundary conditions

3. Free mounting by free boundary conditions

All three mounting methods are applied to the degrees-of-freedom (DOF) that are located inside the contact area between the electric motor and the gearbox. The influence of the mounting models on the sound radiation of the electric motor is illustrated in Figure 5.1. The equivalent radiated sound power (ERP) is exemplarily given for the 72^{nd} engine order, since the dynamic transfer function that corresponds to the 72^{nd} involves the excitation of multiple different mode shapes including low-frequency, global eigenmode shapes (see Section 4.4).

The simulation results show that the mounting configuration affects the frequency response of the electric machine and hence the acoustic behavior especially at lower frequencies. However, the deviation between the three dynamic response functions decrease with an increasing frequency. As shown by SCHWARZER, the vibration of the electric machine surface changes from rather global oscillations at lower frequencies to rather local oscillations at higher frequencies [247]. Hence, the vibrational behavior at higher frequencies is less influenced by the circumferential parts than the vibrational behavior at lower frequencies.

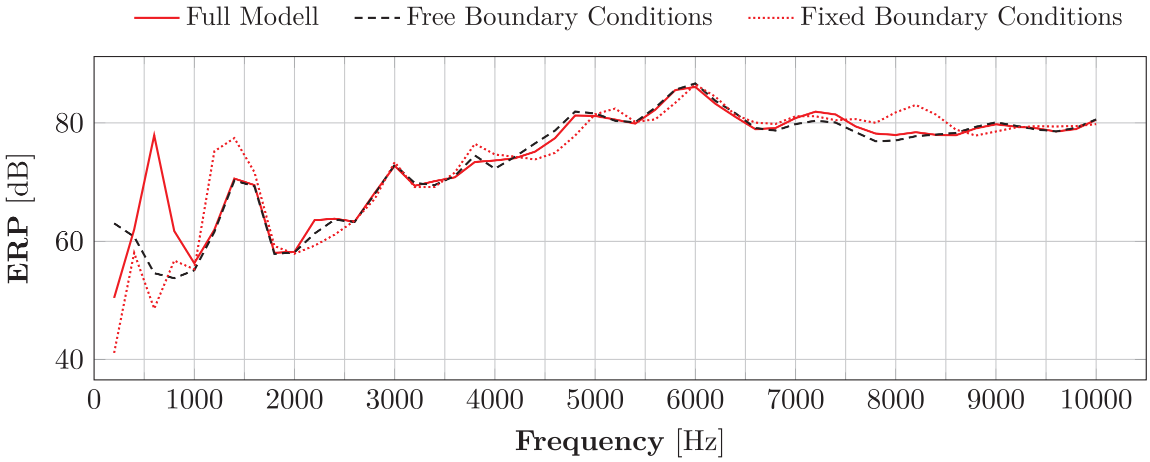

Figure 5.1.: Influence of different mounting models on the sound radiation of electric motors.

5.1.2. Linear Dynamic Simulations Using the Component Mode Synthesis

In order to accurately predict the vibrational behavior of the electric motor at lower frequencies, the stiffness, intertia and damping effects of the mounting structure as well as further components that are attached to the motor structure need to appropriately be represented inside the structural dynamic simulation model. An efficient way to consider the ambient structure of the electric motor is the component mode synthesis method (CMS). It yields the dynamic properties of structural components by only a few master DOFs that are coupled to the remaining DOFs. The basic principle of the CMS method was introduced in Section 2.3.3. In order to investigate the potential and applicability of the CMS method for vibrational simulations of electric drive trains, the gearbox structure given in Figure 4.26 was reduced, based on the standard CRAIG-BAMPTON procedure (see Section 2.3.3).

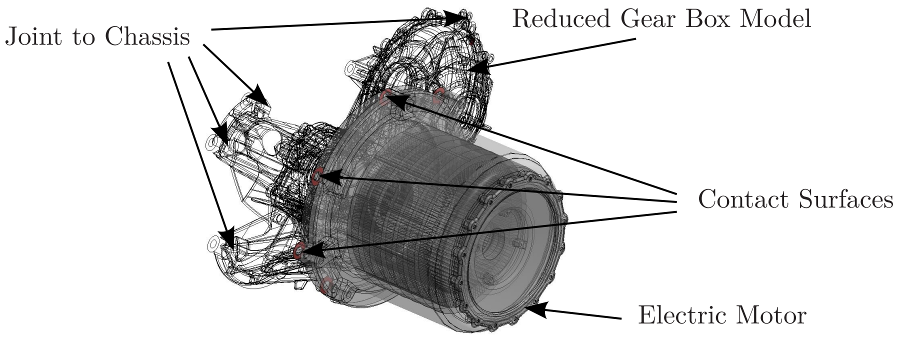

Figure 5.2.: Schematic view of electric drive train including the reduced gear box.

All DOFs that were located inside the contact area between the electric motor and the gearbox were defined as master nodes. The supporting DOFs of the four connection points from the gear box to the car chassis were assumed to be fixed. All 45 eigenmodes that were identified for the full gear box model within the frequency range between 0 Hz and 15 kHz were considered inside the model reduction. The resultant reduced structure is schematically given in Figure 5.2.

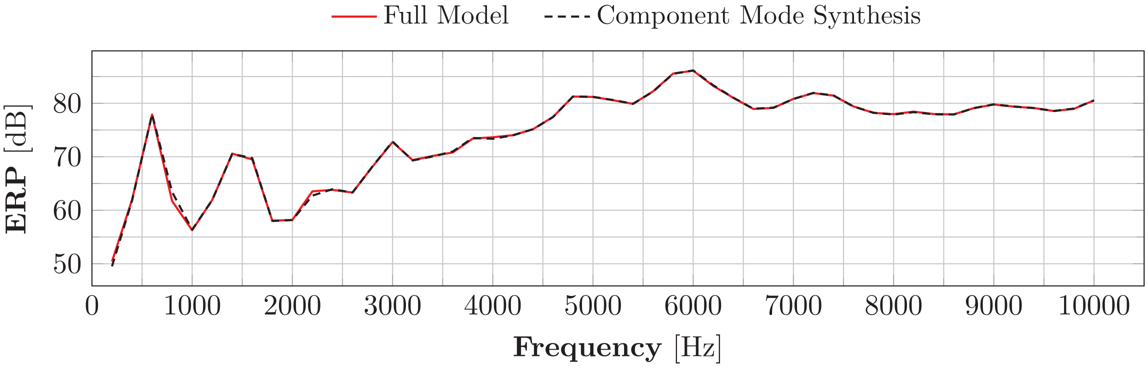

(a) 72^{nd} engine order.

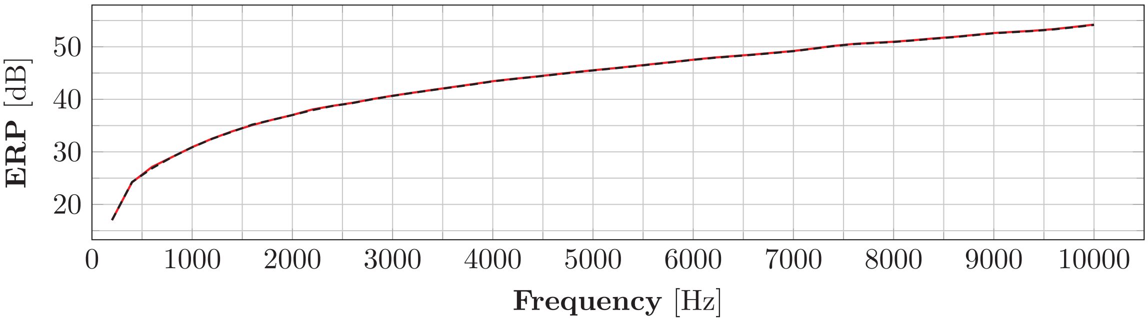

(b) 60^{th} engine order.

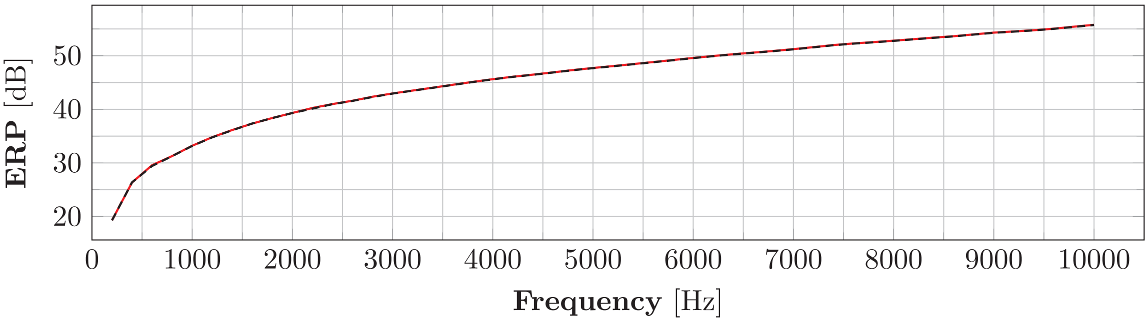

(c) 48^{th} engine order.

Figure 5.3.: Equivalent radiated power (ERP) of the electric motor using the full and the reduced environment model.

In Figure 5.3, the equivalent radiated power that is emitted from the surface of the electric motor is given for two individual models of the drive train and three different engine orders, namely the 48^{th}, 60^{th}, and 72^{nd} engine order. These three engine orders represent all different circumferential spatial orders that occur inside the given IPM configuration (see Figure 4.31). In Section 2.1.2.2 the relation between rotating spatial force waves, which are referred to as engine orders, and the correspondingly excited eigenmode shapes, which are referred to as spatial orders, was explained. The three different engine orders correspond to three different load cases that contain different circumferential spatial order force waves. The chosen engine order thus provide a very general validation. The first model given in Figure 5.3, referred to as the reference model, involves the consideration of the full gear box model as it was shown in Figure 4.26. The second model consists of the detailed finite element model of the electric motor and the reduced gear box model. The reference model contains 3.0 Mio DOFs while the reduced model consists of 1.49 Mio DOFs and 144 additional master DOFs. The results show that the CMS method provides accurate results for all given engine orders throughout the entire operation range. Due to the more local oscillation behavior of the system at higher frequencies, the model accuracy increases with an increasing frequency.

In Figure 5.4, the computational effort for the generation of the reduced model as well as the solution of the subsequent harmonic analysis is given. Employing the CMS method the computational effort can significantly be reduced. Furthermore, the CMS model of the gear box can be used in further simulation without having to be generated again. The CMS method can be applied preliminary to further generalized model order reduction techniques like the mode superposition or the KRYLOV subspace method which will both be discussed in the following sections.

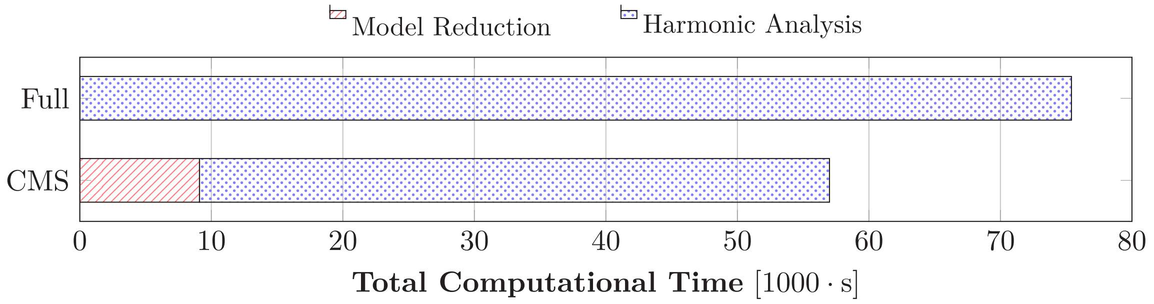

Figure 5.4.: Reduction of computational time for the harmonic analysis using the CMS method.

5.2. Mode Superposition

One of the most frequently used model order reduction techniques in linear dynamic analyses is the mode superposition. It has been employed in multiple publications that yield the prediction of the vibrational dynamic behavior of electric motors [26, 33, 57–63]. Its basic principle was introduced in Section 2.3.1. The mode superposition is based on a coordinate transformation of the system into the so-called modal subspace which is given by the mass-normalized mode shape vectors of the linear system. The solution of the generalized eigenvalue problem can be very time-consuming which needs to be considered when evaluating the overall computational benefit of the mode superposition. However, the solution of the resultant reduced order system is very efficient. In order to reduce the computational effort that is needed for the calculation of the modal subspace, modal truncation can be applied (see Section 2.3.1.1). However, truncating modes can cause a significant decrease of accuracy. In the following section the applicability of the mode superposition for the simulation of the vibrational behavior of an electric motor will be discussed.

5.2.1. The Modal Truncation Method for Electric Motors

The following investigations are based on the exemplary electric machine which was introduced in Section 4.4. In Section 5.1, the application of the CMS method for the representation of ambient components of the electric motor was found to provide results that are in good accordance with the full order system. Therefore, in the following investigations, the gear box stiffness and intertia will be represented by the previously developed reduced order component. Typically, the modal subspace is generated based on the maximum frequency that is considered within a subsequent harmonic analysis which was set to 10 kHz for the given system. However, due to the large modal density of the system for higher frequencies, all eigenmode shapes above 15 kHz were truncated. Still, about 3500 modal vectors were retained inside the modal subspace.

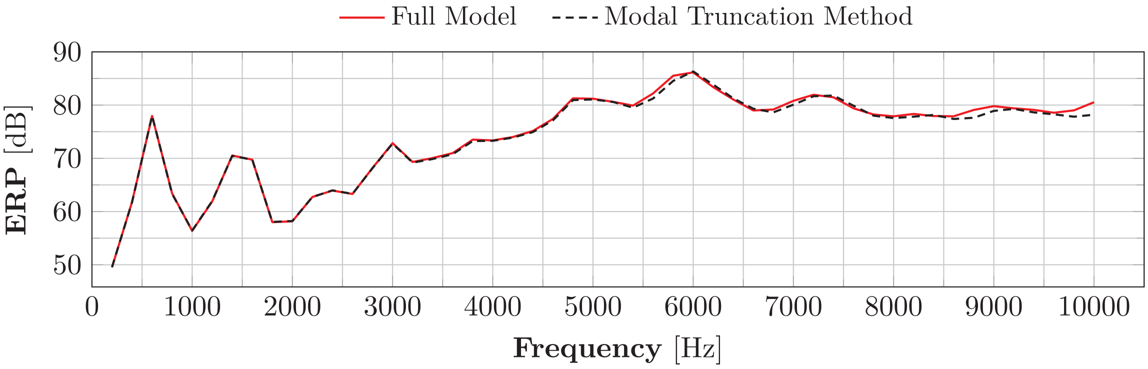

(a) 72^{nd} engine order.

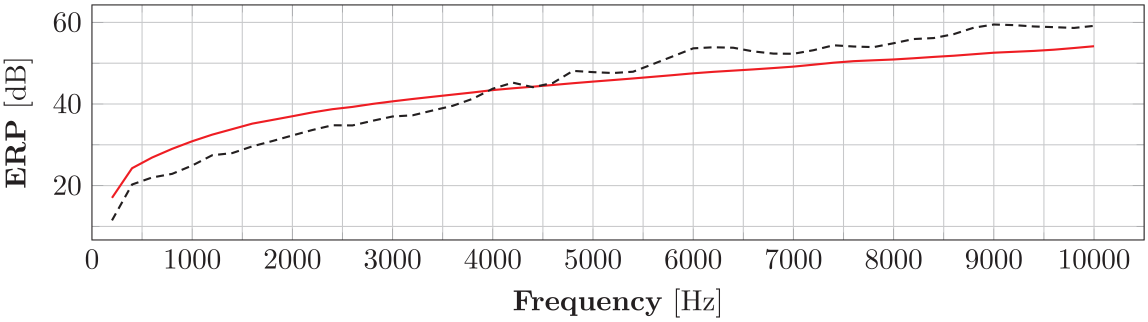

(b) 60^{th} engine order.

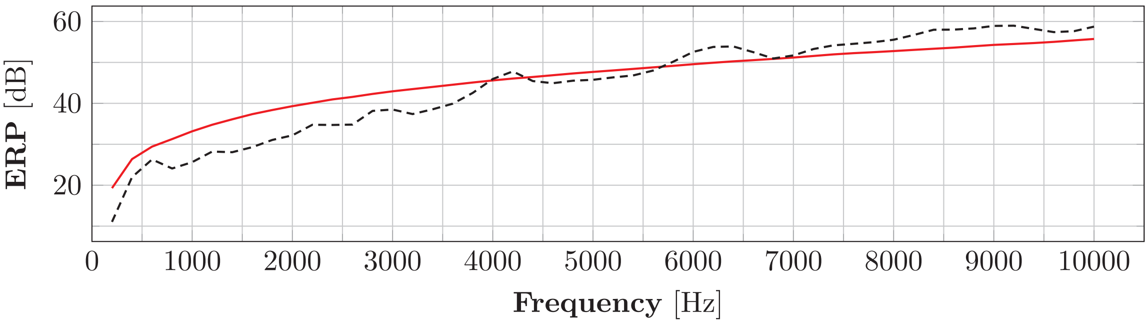

(c) 48^{th} engine order.

Figure 5.5.: Equivalent radiated power (ERP) of electric machine using the mode superposition method.

In Figure 5.5, the numerically obtained ERP values of the 48^{th}, 60^{th}, and 72^{nd} engine orders are shown for both system, the full order system as well as the modal reduced system. The error that is caused by the mode superposition is negligible for the 72^{nd} EO. However, it is significant for the 48^{th} and 60^{th} EO. The results show that the modal subspace sufficiently represents the spatial load case that correspond to the 72^{nd} EO but does not cover the spatial load cases that correspond to the 48^{th} and 60^{th} EO. Since the system matrices of the full system need to be independent of the frequency in order to perform a numerical modal analysis (see Section 2.2.2), viscoelastic effects of the impregnation resin were neglected inside both systems, the full and the reduced system. However, the insufficient representation of the spatial load case inside the modal subspace is independent of frequency-dependent stiffness and damping effects. It thus occurs in either case, with and without the consideration of the viscoelastic resin behavior inside the simulation models.

The limitations of the mode superposition have widely been discussed [64, 65]. Schwarzer et al. showed that the complex spatial load cases which occur in electric machines are mostly insufficiently represented by the corresponding modal subspace [107]. The effect can best be explained, considering only a thin rotationally symmetrical stator segment of the given stator. Assuming the stator to be elastically and homogeneously mounted around the circumference and excited by an electromagnetic force configuration that corresponds to the number poles $p = 12$. Based on the Nyquist criterion and the assumption that the force density distribution on each stator tooth tip surface can be approximated as a resultant force acting on the center of each stator tooth tip surface, only a few particular eigenmode shapes are excited by the rotating electromagnetic force waves. This phenomenon was described in Section 2.1.2.2. For the given thin annular stator segment, all eigenmode shapes as well as the corresponding eigenfrequencies that are excited by the electromagnetic forces based on the number of poles $p = 12$ are illustrated in Figure 5.6. Now, if all eigenmode shapes that correspond to eigenfrequencies above 15 kHz were truncated in a mode superposition analysis, higher spatial order force waves, as they e.g. occur inside the 48^{th} and 60^{th} EO, would not be sufficiently represented by the modal subspace.

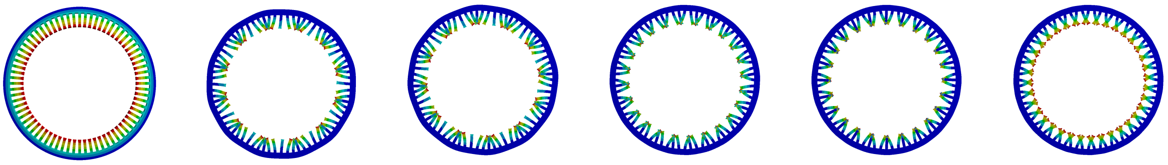

Mode 0_r,0	Mode 12_{t1},0	Mode 12_{t2},0	Mode 24_{t1},0	Mode 24_{t2},0	Mode 36_t,0
3428.3 Hz	5821.4 Hz	5822.8 Hz	6365.9 Hz	6375. Hz	6410.7 Hz

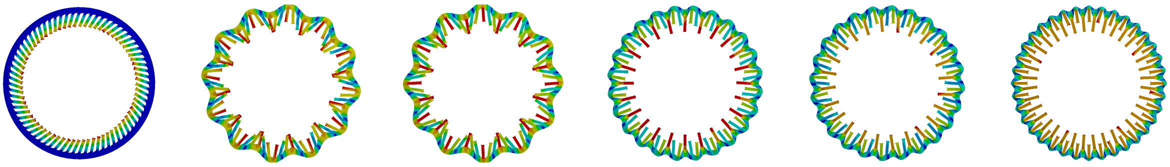

Mode 0_t,0	Mode 12_{r1},0	Mode 12_{r2},0	Mode 24_{r1},0	Mode 24_{r2},0	Mode 36_r,0
6725.9 Hz	18170 Hz	18182 Hz	44094 Hz	44140 Hz	50101 Hz

Figure 5.6.: Comparison of the different circumferential mode shapes and natural frequencies of an axially thin stator segment.

In contrast to perfectly symmetric stator structures, actual electric machine structures are not perfectly rotationally symmetric. Therefore, not only a few distinct but many eigenmode shapes are excited by the load cases, even if the load cases contain higher spatial order fractions. However, it was shown that specifically higher frequency force excitations cause local vibrations which are almost independent of the circumferential structure oscillations (see Section 5.1.1).

Thus, higher order eigenmode shapes are almost perfectly rotational symmetric due to their commonly high eigenfrequency values, which is why the error that is caused by using the ordinary modal truncation method on a full electric motor is particularly high for higher spatial order excitations. In order to evaluate the degree to which each eigenmode is excited by a particular load case, so-called participation factors can be quantified (see [25]). The sufficiency of the corresponding modal subspace can be approximated based on Equation 2.31.

5.2.2. The Modal Truncation Augmentation Method for Electric Motors

5.2.2.1. Load Case Decomposition

In order to improve the results of the ordinary mode superposition method as it was employed in the previous section different correction methods exist (see Section 2.3.1). One of them is the modal truncation augmentation method. Its main idea is to extend the initial modal subspace by so-called pseudo-modes (see Section 2.3.1.2). The pseudo-modes are also referred to as residual vectors since they are displacement vectors that correspond to a residual load vector which is the part of the original load vector that is not represented by the initial modal subspace. In contrast to the ordinary eigenmode vectors, residual vectors are based on specific load cases. In Section 2.1.1.1, the decomposition of the total electromagnetic force into spatial harmonic orders was introduced. In Section 2.1.2.2 it was shown that all engine orders can be expressed by a few particular axial and circumferential force vectors.

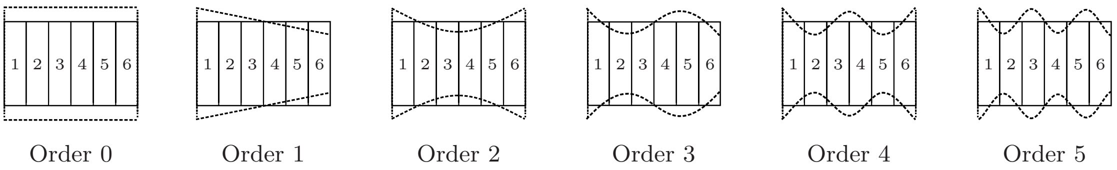

Axial Orders

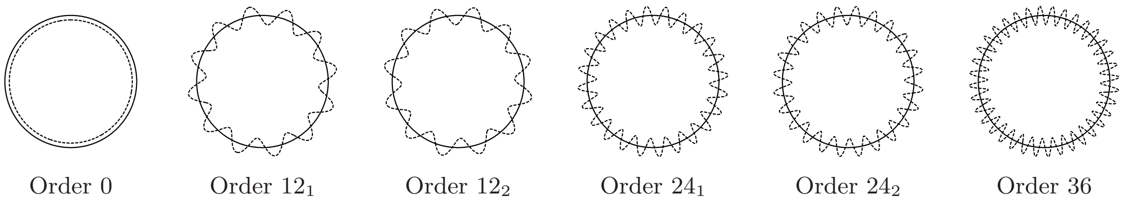

Circumferential Orders

Figure 5.7.: Schematic view of axial and circumferential spatial force vectors.

In the present example, apart from the zeroth circumferential spatial order, the 12^{th}, 24^{th}, and 36^{th} spatial order are of interest. All spatial orders have a radial and tangential component as well as a real and imaginary part. Based on the number of teeth $s = 72$ the real and imaginary part of the zeroth and 36^{th} spatial order are identical due to aliasing. Therefore, twelve different circumferential spatial orders exist for the given system (see Figure 5.6). The decomposition of the axial load spectrum depends on the discretization of the axial skewing scheme of the electric motor (see Section 2.1.1.1). In the present case, the step shift of the magnets was divided into six discrete steps (see Figure 4.29). Thus, in axial direction the total spectrum needs to at least be decomposed into six independent fundamental orders. Hence, the minimum number of different generic load cases that represent the variety of occurring electromagnetic load cases in the given electric motor is given by all permutations of the independent axial and circumferential spatial force vectors in Figure 5.7, once for the tangential and once for the axial direction yielding $6 \times 6 \times 2 = 72$ load cases. Thus, in order sufficiently represent all possible load cases 72 independent mode shape vectors are necessary.

5.2.2.2. The Modal Truncation Augmentation Method Using Generic Load Cases

In [107], it was shown that the use of the modal truncation augmentation method leads to a significantly reduced error for each stator. In Figure 5.8, the ERP values of the electric motor are given for the 48^{th}, 60^{th} and 72^{nd} EOs by using the modal truncation augmentation method and the full order model. The additional residual vectors that were used inside the modal truncation augmentation method are based on the 72 independent generic load cases that were introduced in Section 5.2.2.1.

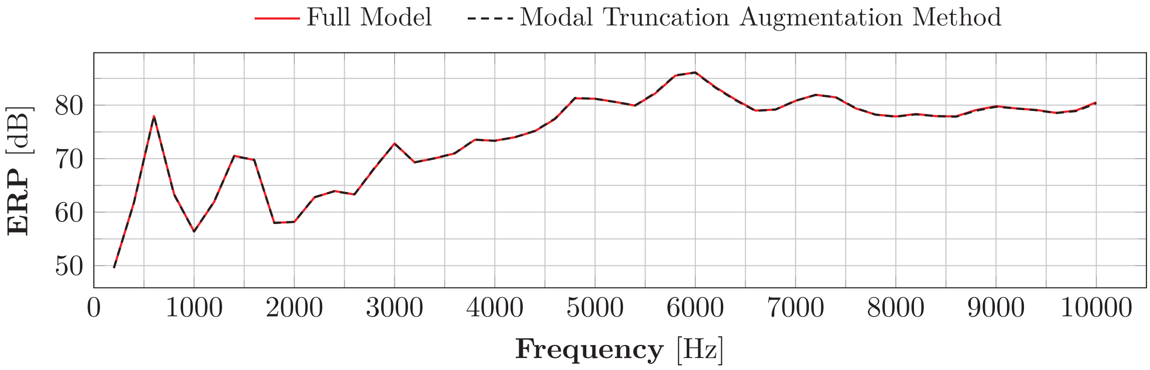

(a) 72^{nd} engine order.

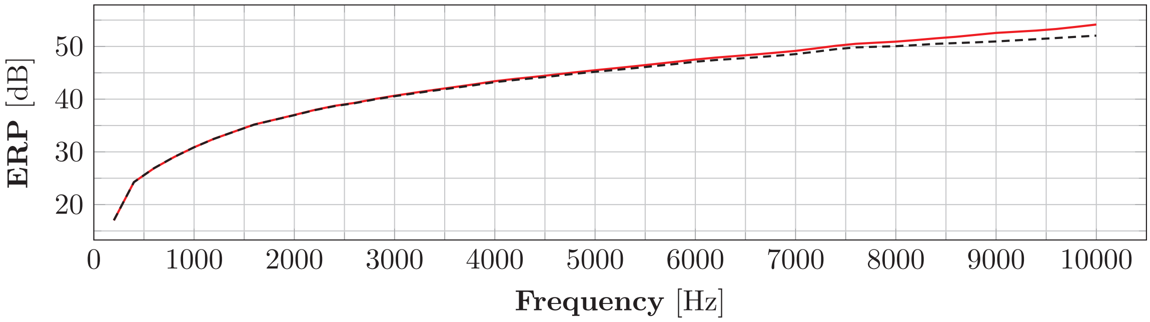

(b) 60^{th} engine order.

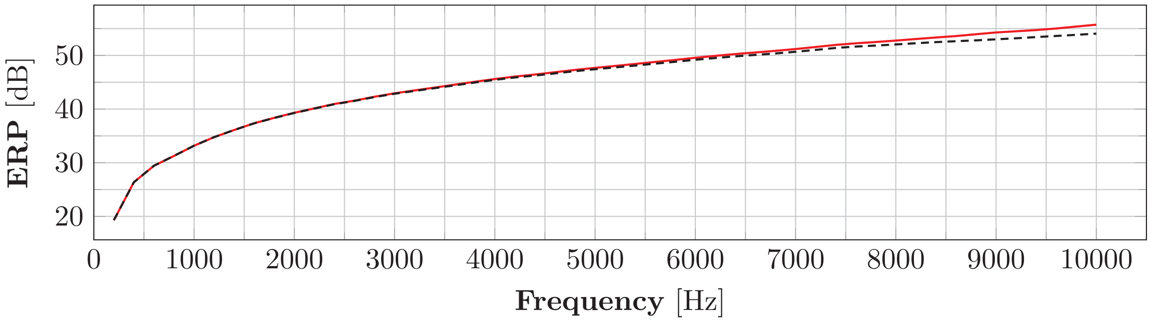

(c) 48^{th} engine order.

Figure 5.8.: Equivalent radiated power (ERP) of a single stator structure using the mode superposition method.

In the previous section it was shown that the ordinary modal truncation method causes considerable errors for the 48^{th} and 60^{th} EOs. Figure 5.8 shows that the consideration of residual vectors inside the mode superposition leads to significantly reduced errors for both engine orders. However, the use of residual vectors is connected to an increased computational effort due to the solution of the additional static load cases. Furthermore, the modal subspace is extended by the number of residual vectors. The overall computational efforts for all three cases, the full harmonic analysis, the ordinary modal truncation method (OMTM) and the modal truncation augmentation method (MTAM) are given in Figure 5.9. In this particular example, 50 different frequency steps in the range from 200 Hz to 10 kHz were calculated. The computational effort of the harmonic analysis scales linearly with the frequency steps while the effort for the model reduction is a one-time expense. Since the residual vectors are based on a generic concept even different model orders can be calculated based on the same modal subspace.

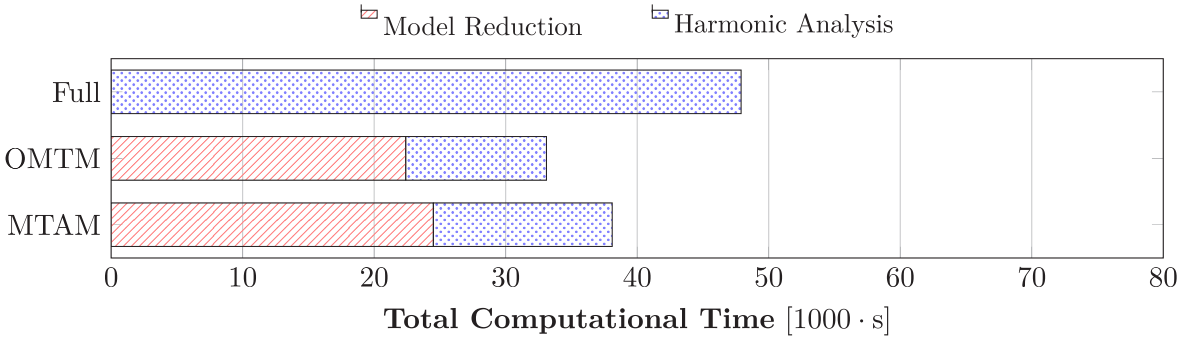

Figure 5.9.: Reduction of computational time for the harmonic analysis using the ordinary modal truncation method (OMTM) and the modal truncation augmentation method (MTAM).

For more complex housing topologies especially for housings with a complex surface structure like air cooled electric motors the modal truncation augmentation method is limited regarding model accuracy. Since the residual vector generation is based on the static deformation of the structure the pseudo-mode shapes differ from the actual corresponding dynamic mode shape which might include a significant oscillation of the outer fins. Thus, the modal truncation augmentation method is limited to conventional electric motors with rather cylindrical housing structures.

5.3. Krylov Subspace Method

In the previous section, the mode superposition as a generalized model order reduction technique was applied to the structural dynamic simulations of an exemplary electric motor. It was shown that the ordinary modal truncation method is limited towards more complex load cases with higher spatial orders. Meanwhile, the modal truncation augmentation method leads to an improved accuracy but increases the computational effort. In Section 2.3.2, a second generalized model order reduction technique, the KRYLOV subspace method, was introduced. The basic idea of the reduction method is to transform the full order system into a reduced order subspace that, for a particular load case, leads to the same frequency response function (FRF) as the original system. In this section, the use of the KRYLOV subspace method for structural dynamic simulations of electric motors will be investigated. All investigations correspond to the same exemplary electric machine that was already used in the previous sections and is illustrated in Figure 4.26.

5.3.1. Influence of the Model Order

In Section 2.3.2 the Arnoldi process was introduced. It yields the generation of Krylov subspaces based on a particular load vector $\underline{v}$ and the explicit system matrix $\underline{A}$.

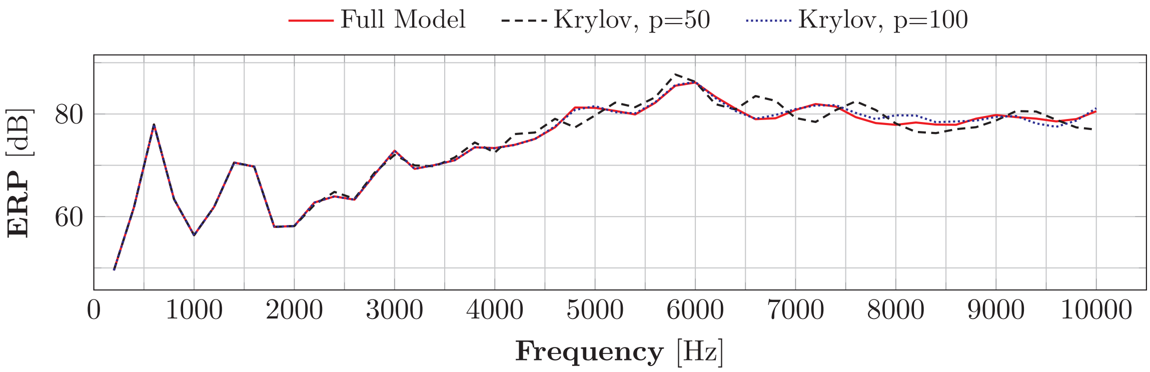

(a) 72^{nd} engine order.

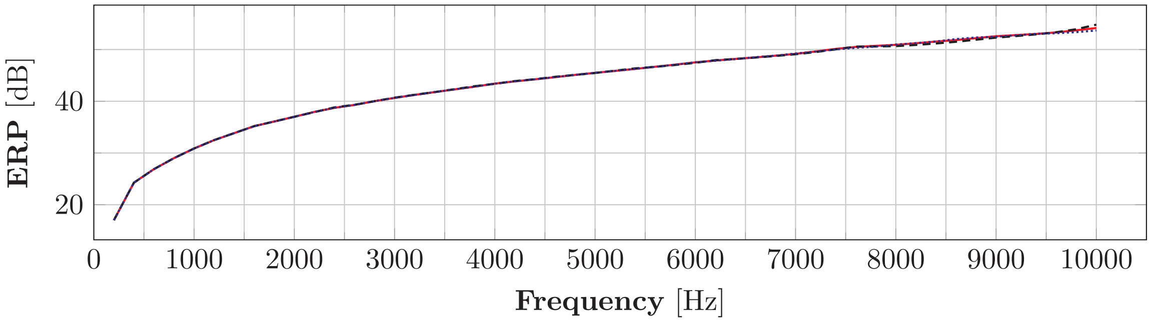

(b) 60^{th} engine order.

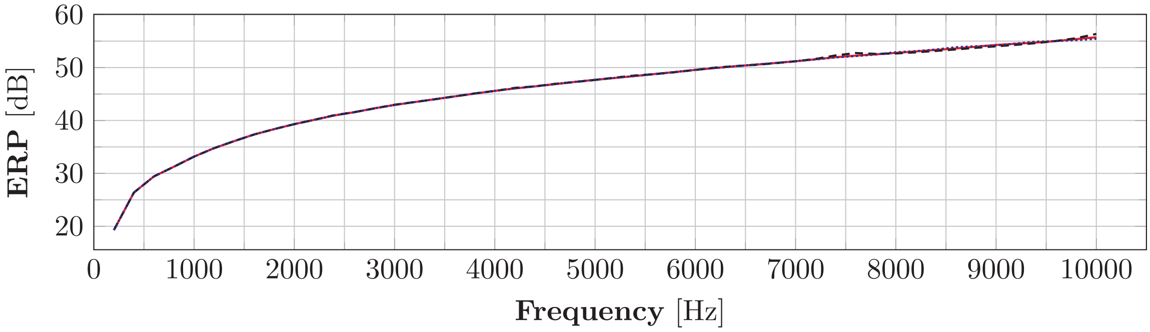

(c) 48^{th} engine order.

Figure 5.10.: Comparions of the equivalent radiated power (ERP) of an electric motor for different numbers of Krylov vectors.

In order to apply the Arnoldi process and obtain appropriate Krylov subspaces, the electromagnetic load case needs to be divided into the tangential and radial as well as the real and imaginary part. Hence, the electromagnetic load that corresponds to each engine order (EO) is represented by four independent load cases. The number of Krylov vectors and hence the order of the reduced system depends on the complexity of the system as well as the frequency range that is examined. However, no guideline for a reasonable number of Krylov vectors exists. Thus, an appropriate number of Krylov vectors that lead to a good model accuracy of the reduced order system needs to iteratively be identified for each system by evaluating the correspondent errors of the reduced system. In the following the number of Krylov vectors for each independent load case is set 50 and 100, leading to model orders of 200 and 400. In Figure 5.10, the FRF of the two reduced systems are compared to the response functions of the full system for three independent EOs. Both reduced order systems show a very good accordance with the full order system for the 60^{th} and 48^{th} EO which both correspond to higher spatial order electromagnetic load cases (see Section 2.1.2.2). The largest error occurs for the 72^{nd} EO which corresponds to the zeroth spatial order load case. Naturally, at 0 Hz, reduced systems based on Krylov subspaces that were expanded around the frequency of 0 Hz show excellent accordance with the dynamic response of the full order reference. This matches the theoretical background that was given in Section 2.3.2.3. However, as the frequency increases the error increases, especially for the 72^{nd} EO. The FRF of the 72^{nd} EO seems to be more complex than the other transfer functions in the given frequency range. Thus a higher number of Krylov vectors is necessary for the dynamic response of the 72^{nd} EO to be well predicted also for higher frequencies. Consequently, employing 100 instead of 50 Krylov vectors for each load case leads to a significantly reduced error.

5.3.2. Influence of the Expansion Point

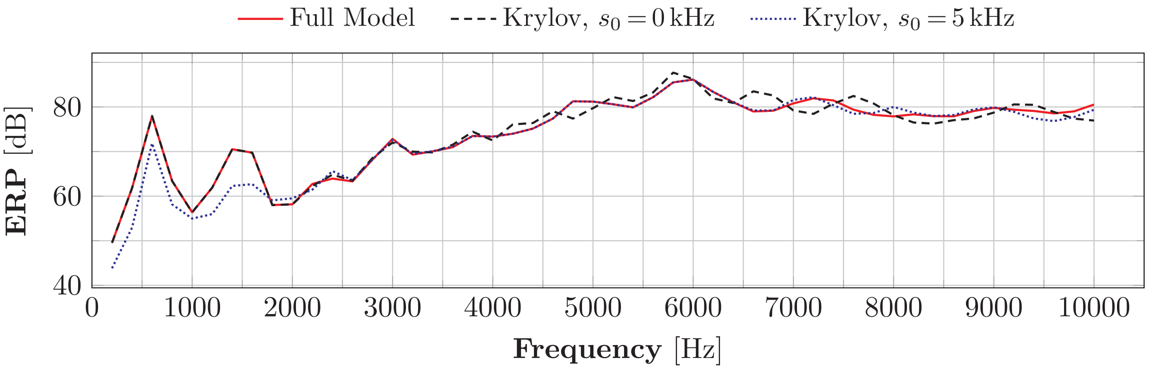

(a) Absolute results for 72^{nd} engine order.

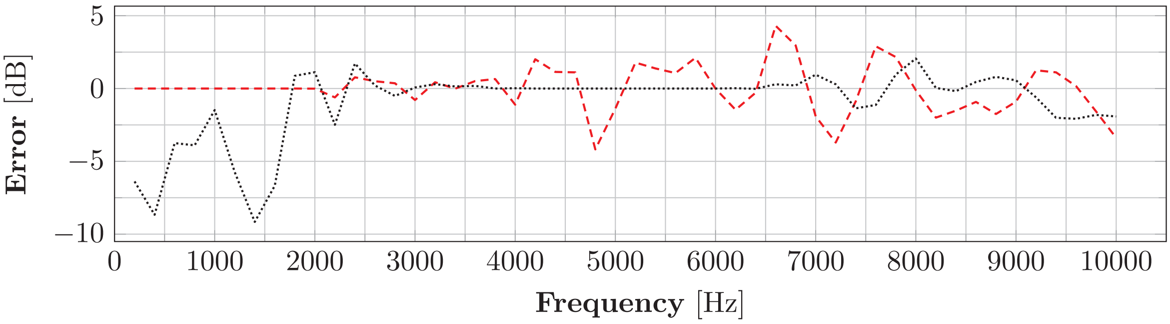

(b) Relative error.

Figure 5.11.: Comparison of the equivalent radiated power (ERP) of an electric motor for different expansion points of Krylov subspaces.

In Section 2.3.2.4, the so-called expansion point was introduced. Each Krylov subspace is expanded around a certain frequency at which the reduced system transfer function perfectly matches the transfer function of the full order system.

The variation of the expansion point can hence be a proper technique to improve of the overall reduced model accuracy without increasing the computational effort. In Figure 5.11(a), the ERP-results of the reduced order system are given for an expansion frequency of 5 kHz and 50 KRYLOV vectors. The dynamic response of the reduced system at a frequency of 5 kHz perfectly matches the response of the full system at 5 kHz. Analogue to the system which was expanded around the frequency of 0 Hz, the error increases with an increasing distance to the expansion frequency of 5 kHz.

The errors of the two expansion frequencies are given in Figure 5.11(b). The magnitudes of the relative error are comparable for both expansion frequencies. Nevertheless, the shift of the expansion point to higher frequencies leads to an increased error at low frequencies.

5.4. Evaluation of Model Reduction Techniques

5.4.1. Computational Effort

In the previous sections, the applicability of different model reduction methods for the dynamic structural simulation of electric motors was discussed. The component mode synthesis method is a hybrid coordinate transformation method that was used to reduce the order of the gearbox of the electric drive train (see Section 5.1). The ordinary modal truncation method (OMTM), the modal truncation augmentation method (MTAM) as well as the KRYLOV subspace method denote examples of generalized model order reduction techniques (see Sections 5.2 and 5.3). For the KRYLOV subspace method, the influence of the number of subspace vectors as well as different expansion frequencies were investigated.

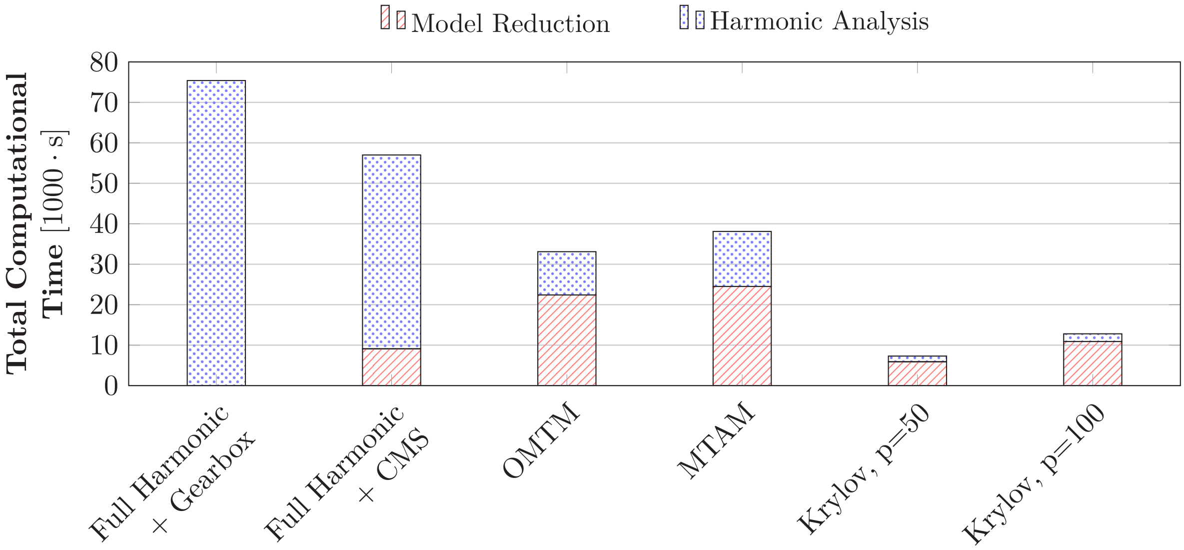

Figure 5.12.: Overview of computational times for the harmonic analysis and the model reduction using different model order reduction techniques.

All different model reduction techniques yield the reduction of the model order and hence a decrease of the computational effort. In Figure 5.12, the computational efforts of the different reduction methods are compared. The data correspond to the simulation of one engine order (EO) including 50 frequency steps. The total computational time is divided into the time that is used for the reduction of the model and the time for the actual solution of the linear system. The reduced system based on the CMS as well as the OMTM can be recycled for all EOs and thus only need to be reduced once. Based on the assumption of a set of fundamental load cases that can be linearly combined to form any occurring load case (see Section 5.2.1), the residual vectors based on the fundamental load cases can also be reused. In contrast, the Krylov subspaces are dependent on a particular load case and thus need to be generated for each EO individually. Thus, evaluating the overall benefits of each single model order reduction technique, not only the number of frequency steps but also the number of different EOs needs to additionally be taken into account.

5.4.2. Model Accuracy

In Figure 5.13, the maximum error of each of the applied model order reduction techniques is illustrated for the first six EOs of the analyzed electric motor. Depending on the original full system that was reduced two different reference models were employed for the calculation of the maximum error. The CMS method was compared to the full order model of the drive train including the FE-model of the gear box. In contrast, all further reduction methods were based on the system that already included the reduced gear box model and were thus compared to the corresponding CMS-reduced model of the drive train.

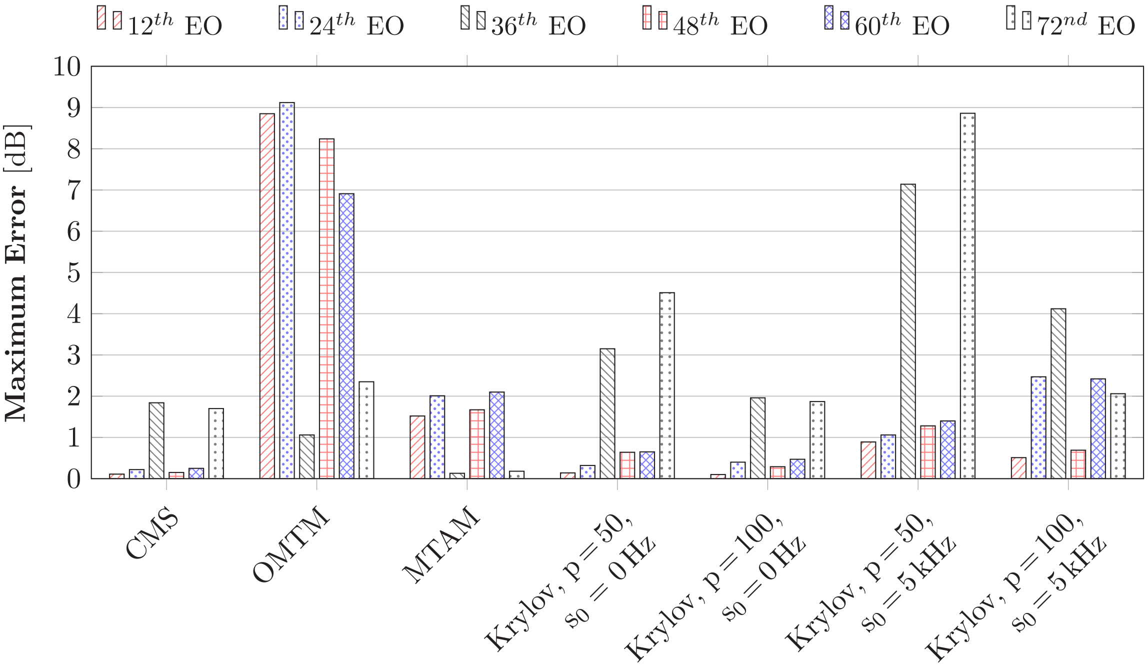

Figure 5.13.: Maximum error of the model order reduction techniques in relation to the full model for different engine orders.

As discussed in Section 5.1.2, the CMS methods provides a good approximation of the dynamic behavior of the peripheral structural components. The maximum error is lower than 2 dB for each EO. Apparently, the EOs that excite the zeroth spatial order, namely the 36^{th} and 72^{nd} EO, lead to a slightly increased maximum error compared to the other four EOs. Due to asymmetries inside the structure, the spatial force wave zero leads to an excitation of multiple eigenmode shapes which are partly low-frequented and thus involve oscillations of the peripheral components while all higher harmonic force waves excite distinct high-frequency eigenmodes (see Section 5.1.2).

Figure 5.13 shows that the OMTM is limited to the representation of lower spatial order excitations. The maximum error which is caused for higher spatial order excitation, in this case the 12^{th}, 24^{nd} and 36^{th} circumferential spatial order which occur in the 12^{th}, 24^{nd}, 48^{th} and 60^{th} EO, is significant. The modal truncation augmentation method yields the extension of the modal subspace by residual vectors. The use of residual vectors leads to a significant reduction of the maximum error for higher spatial order excitations.

The KRYLOV subspace method takes into account the complexity of the response function. In the investigated system, the transfer function of the circumferential spatial order zero (36^{th} and 72^{nd} EO) was found to be more complex than the transfer functions that correspond to higher order excitations. Thus, the maximum error that is caused by the KRYLOV subspace method is higher for the 36^{th} and 72^{nd} EO than for the other EOs. Hence, in order to accurately predict the 36^{th} and 72^{nd} EO transfer function by the reduced system, the reduced system order needs to be increased. In contrast, if only a few distinct eigenmodes contribute to the overall dynamic response of the system, as it is the case for the 12^{th}, 24^{nd}, 48^{th} and 60^{th} EO, the model order and thus the computational effort can significantly be reduced. The variation of the expansion frequency which was described in Section 5.3.2 leads to no significant reduction of the maximum error. It was shown that by an alternate expansion frequency the maximum error that is caused by the reduced order system is not reduced but just shifted to frequency ranges which are at a certain distance of the expansion frequency.

6. Conclusion and Outlook

6.1. Conclusion

The acoustics of electric motors inside electric cars significantly contribute to the overall noise emission of the car. Even though the absolute sound pressure level of the noise which is radiated from the electric motor structure might not be very high, the high frequency electromagnetic forces that occur inside the motor lead to highly tonal acoustic effects and thus considerably influence the overall sound profile of the vehicle.

However, the acoustic character of an electric car is often firstly fully assessable in later design phases in which large design changes are often connected to compromises and large financial efforts. In order to earlier gain information about the acoustic behavior of the car numerical simulations methods can be employed.

Nevertheless, the simulation of the structural dynamic behavior which determines the acoustic behavior of electric motors is very complex. The electric motor consists of strongly inhomogeneous components whose representation in dynamic simulations is connected to elaborate methods. In common structural simulation processes the internal structural parts of the machine are either totally neglected, strongly simplified or are characterized based on the experience of previous machine configurations. This reverse approach leads to the problem that certain design parameters, like the prestress of the stator iron core or the viscoelastic material properties of the stator impregnation resin which evidentially influence the overall structural response of the motor, are not accessible to early phase optimization yielding the improvement of the acoustic machine performance.

6.1.1. Structural Mechanical Modeling Techniques

In this thesis, different methods and procedures that yield the prediction of the acoustic behavior of electric motors, were developed and validated. The methods are all based on the original micromechanical structure of each underlying structural component.

Therefore, in the first step in Chapter 3, recurrent inhomogeneous elements of the structure, namely copper windings (Section 3.2) as well as non-impregnated and impregnated laminated steel stacks (Section 3.3.2 and 3.3.3), were separately investigated and their mechanical behavior modeled. In order to characterize the macroscopic mechanical behavior of an inhomogeneous composite structure, so-called homogenization techniques can be applied. Homogenization yields the quantification of so-called effective material properties that represent the macroscopic behavior of the underlying inhomogeneous composite (see Section 2.5). The different homogenization techniques were validated regarding the accurate representation of the stiffness and damping characteristics by comparing numerically to experimentally obtained eigenfrequencies and modal damping ratios.

Copper Windings The investigations of the copper windings in Section 3.2 showed that the actual effective material properties of the structure are not transversely isotropic, as propagated by most scientific papers but orthotropic due to the random distribution of the copper fibers inside the composite. However, the error caused by the assumption of a transversely isotropic material model was found to be small which is why the transversely isotropic material model can be proposed for homogenization purposes.

Based on the comparison between the numerically and experimentally obtained eigenfrequencies and modal damping ratios of different copper windings specimens it was shown that the homogenized material properties obtained from a micromechanical model sufficiently represent the actual stiffness and damping behavior of the copper windings. All different homogenization techniques, namely the RVE, standard analytical approaches as well as the MOC, provided good results. Due to the significantly reduced computational effort, analytical methods are advantageous for the quantification of effective stiffness properties of copper windings.

Laminated Steel In order to reduce eddy current losses, inside the electric motor the stator as well as the rotor iron core are assembled by multiple single steel sheets forming laminated steel packages. It is known that the mechanical properties of laminated steel packages differ from the mechanical properties of the underlying monolithic material. The effective material properties of laminated steel were assumed to be transversely isotropic. For production and vibrational reasons, the laminated steel stack is exposed to normal prestress. The influence of the prestress on the effective material properties of the laminated steel was investigated in multiple scientific works (see Section 3.3). However, the majority of corresponding publications yields the quantification of effective material properties as a function of the prestress, neglecting further parameters like e.g. the sheet thickness. In this thesis, the actual relation between the normal contact stiffness between two single coated iron sheets was carried out by analyzing the vibrational behavior of a prismatic impregnated laminated steel specimen (see Section 3.3.4). The contact stiffness was found to be significantly influenced by the normal prestress but less by the frequency of the oscillation. Thus, the effective material properties of the laminated steel stack depend on the normal prestress. The impregnation process to which the stator is exposed during its manufacturing process leads to a considerably increased stiffness of the laminated steel stack. It was shown, that the impregnation resin penetrates the small capillaries between the steel sheets (see Figure 3.1) and thus needs to be considered inside the quantification of homogenized effective stiffness and damping properties of the impregnated laminated stator iron core.

In order to validate the applicability of the modeling approaches of recurrent inhomogeneous elements inside electric machines, namely copper windings and laminated steel, which were developed in Chapter 3, different simulation models of an exemplary stator structure were investigated in Chapter 4. Therefore, the exemplary stator was divided into three independent structural parts which were successively analyzed inside experimental modal analyses. In the first modal analysis, the laminated stator iron core was analyzed. In order to provide stiffness and damping properties of the laminated steel close to its later application inside an electric motor the laminated stator iron core was impregnated before the measurements. In the second measurement, the the slot filling was added to the stator structure. In the third analysis, the entire stator including the end windings was measured.

Segmented Laminated Stator Iron Core Based on the developed relation between the normal contact stiffness of two coated steel sheets and the imposed axial prestress of the stator iron core (see Equation 3.6), the effective material properties of the exemplary stator iron core were quantified by using the MOC as an appropriate homogenization technique. Due to production reasons, the yoke of the exemplary stator structure was tangentially segmented. Thus, apart from the axial laminations, the occurring segmentation gap needed to be considered during the homogenization process. In Section 4.1, it was shown that both homogenization techniques, the RVE as well as the MOC, provide effective material properties of the laminated and segmented stator structure that are in very good accordance with the actual stiffness and damping of the stator. In contrast, assuming the stator iron core to isotropically consist of the underlying monolithic material, this leads to significantly erroneous eigenfrequencies and modal damping ratios. The consideration of the axial laminations as well as the tangential segmentation inside the model is mandatory in order to achieve accurate results.

Segmented Laminated Stator Iron Core Including Copper Windings The active copper windings which are located inside the stator slots are electrically insulated from the stator iron core by a thin slot insulation paper. In Section 4.2, it was shown that the compliant slot insulation significantly influences the vibrational behavior of the stator structure. The reduction of the contact stiffness between the stator iron core and the slot filling was found to be the most accurate and beneficial modeling approach of the slot insulation in terms of computational effort. The values of the corresponding contact stiffness factors were obtained from the results of an experimental modal analysis.

Segmented Laminated Stator Iron Core Including End Windings In order to electrically connect the active copper windings inside the stator slots, the copper wires are typically redirected at both ends of the stator iron core representing the so-called end windings. Each of the electrical phases inside the end windings needs to be insulated from the other phases by a phase insulation. In the exemplary stator which was analyzed in this thesis the phase insulation was provided by the same thin insulation paper that was already employed for the slot insulation. In Section 4.3, different stator simulation models that aim to the correct representation of the end windings were analyzed and validated. It was shown that modeling the end windings as a tangentially oriented transversely isotropic structure analogue to the active copper windings inside the stator slots provides results which are in good accordance with structural dynamic measurements. However, due to the insulation paper between two electrical phases, each single copper coil that corresponds to a particular phase inside the end windings vibrates almost independently of its neighboring structure. Thus, the end windings can not simply be modeled as a ring of tangentially oriented copper windings but should be modeled as multiple individual ring segments that partly overlap (see Section 4.3.2).

Temperature-Dependent Behavior Electric traction motors as used in vehicle applications are usually operated in a wide temperature range from about -40°C to 150°C. Thermosetting impregnation resins commonly show a distinct viscoelastic behavior which is characterized by a frequency- and temperature-dependent stiffness and damping behavior. It was shown that during the impregnation process the low-viscous impregnation resin tends to penetrate all capillaries inside the electric machine stator and thus covers not only the copper winding surfaces but also the laminated steel sheets inside the stator iron core. In order to evaluate the influence of the viscoelastic impregnation resin on the overall structural dynamic behavior of the electric motor, experimental modal analyses were performed on a full stator at different temperatures. The eigenfrequencies of the stator were found to decreased with an increasing temperature, thus indicating a decreasing stiffness. It was shown, that the temperature-dependent behavior of the structure can only be predicted accurately if the viscoelasticity of the impregnation resin is considered inside the micromechanical models (see Section 4.2.4).

6.1.2. Model Order Reduction Techniques

In order to evaluate and optimize the mechanical design of electric traction motors towards their acoustic behavior, the entire operation range of the particular motor, including all engine speeds, loads and temperatures, must be considered. The variety of different design parameter configurations and operations points of the system leads to a large number of simulations. Thus, the reduction of the computation effort of each simulation can be advantageous. In Chapter 5 different model order reduction techniques were investigated. They all yield the efficient transformation of the original system to a system of reduced order.

Component Mode Synthesis It was shown that the peripheral components significantly influence the structural dynamic and hence the acoustic behavior of the electric motor especially for lower frequencies. Thus, in order to accurately predict the sound emissions of the electric motor, peripheral components need to be considered inside the simulation model. The component mode synthesis method is a so-called hybrid model order reduction technique since it is based on the combination of selected physical DOFs of the original system and additional generalized modal DOFs. It is commonly used to reduce the total simulation model by substituting certain structural parts by so-called superelements of a lower order. It was shown that the CMS method provides simulation results which are in very good accordance to the results of the original system. It can furthermore be combined with additional model order reduction techniques like the mode superposition. Depending on the DOFs of the peripheral system the computational effort of the overall solution process can be significantly reduced. The resultant superelement can also be recycled in further analyses, provided that the frequency range remains unchanged. However, the computational effort for the reduction of the peripheral components can be considerably large. Furthermore, if the sound that is directly emitted from the surface of the peripheral structure is of interest the displacement results of the retained DOFs need to be transformed back into the original system which can also cause a significant additional computational effort.

Ordinary Modal Truncation Method The mode superposition is one of the most common model order reduction techniques. Its physical interpretation is trivial and the implementation is a standard procedure in all common finite-element software tools. Depending on the number of considered modal vectors, the ordinary modal truncation method which is based on the idea of truncating modal vectors whose eigenfrequencies are far out of the considered frequency range leads to significantly reduced computational efforts. However, the solution of the generalized eigenvalue problem and thus the quantification of the modal vectors can be very time-consuming. Since the modal subspace is independent of the load case, it can be used for different load cases. However, the ordinary modal subspace was shown to be insufficient for the spatial representation of complex load cases as they occur in electric motors (see Section 5.2). Particularly for engine orders that contain higher spatial order excitations, the error that is caused by the modal truncation is significant. Hence, the mode superposition based on the ordinary modal truncation is disadvantageous for dynamic simulations of electric motors.

Modal Truncation Augmentation Method The modal truncation augmentation method yields the extension of the modal subspace by so-called residual vectors. Residual vectors correspond to particular load cases and denote a static response of the system. Hence, residual vectors are not transferable to different load cases like the original modal subspace. Nevertheless, it was shown that residual vectors improve the system accuracy significantly.

Particularly for higher spatial order excitations, the use of residual vectors is strongly necessary. However, the generation of residual vectors is coupled to an additional computational effort that must be taken into account when evaluating the overall computational benefits. In Section 5.2.2, the use of so-called generic load cases for the generation of residual vectors was introduced. It was shown that each load case that corresponds to a particular engine order can be expressed by a linear combination of recurrent generic load cases. Thus, generating residual vectors based on the generic load cases the extended modal subspace only needs to be quantified once for all different different engine orders. Since the mode superposition in both forms, the ordinary modal truncation and the modal truncation augmentation method, are based on a linear frequency-independent system no viscoelasticity can be considered. Hence, if the system shows a strong frequency-dependent stiffness or damping behavior, neither the ordinary modal truncation nor the modal truncation augmentation method is recommendable. Furthermore, for more complex housing topologies, especially for housings with a complex surface structure like in air-cooled electric motors the static deflection that is used for the generation of the residual vectors, tends to differ from the actual dynamic eigenmode shapes of the system. Thus, despite the sufficient representation of the spatial load case, the modal truncation augmentation may cause errors for more complex systems.

Krylov Subspace Method A promising model order reduction technique, based on a generalized coordinate transformation, is the Krylov subspace method. It was investigated in Section 5.3. The Krylov subspace method is independent of the number of eigenfrequencies that occur within the considered frequency range but takes into account the complexity of the response function. If only a few distinct eigenmodes contribute to the overall dynamic response of the system, the model order and thus the computational effort can be reduced significantly. However, if the transfer function of the system is found to be complex, the reduction using the Krylov subspace method is limited. If only specific frequency ranges are of interest, a modified expansion point can be applied. Nevertheless, no guideline for an appropriate number of Krylov vectors exists. The Krylov subspace always corresponds to one particular load case and hence is not transferable to different load cases, e.g. in case of different engine orders or operational points of the electric motor.

6.2. Outlook

Model Accuracy In this thesis, different approaches regarding the efficient simulation of electric machine components were introduced. The applied homogenization methods consider both, the effective stiffness of the corresponding composite material as well as its directional damping properties. The representation of both properties, the stiffness and the damping, inside the homogenized materials were successfully validated by comparison to experimental results. However, the total damping that occurs in larger systems contains material-inherent damping, but also frictional damping at joints and component interfaces. Depending on the system, either type of damping can be dominant. In order to entirely predict the system acoustic behavior including housing and peripheral parts, the joint damping needs to be investigated more intensively.

Multiple literature studies have identified the significant influence of the axial prestress on the elastic behavior of laminated steel. In this thesis, an analytical relation between the prestress and the normal contact stiffness of coated steel sheets was developed. However, the normal contact stiffness of rough surfaces is dependent on multiple parameters like the surface roughness or the material combination. In order to obtain a more generic modeling approach, the analytical relation that was developed needs to be extended to further material combinations and sheet topologies. Furthermore, the tangential contact stiffness needs to be considered inside the investigation in order to quantify homogenized material properties also for non-impregnated laminated steel.

System Simulation In the thesis it was shown that the frequency-dependent behavior of the impregnation resin affects the system eigenfrequencies and thus the acoustic behavior of the electric motor. However, the introduced model order reduction techniques naturally are not applicable for the representation of viscoelastic material behavior. A way to overcome these problems is to divide the total frequency band into several frequency intervals. In case of the ordinary modal truncation method, the eigenfrequencies as well as the modal damping ratios of the system that are located inside the given frequency band can then be calculated based on the stiffness and damping properties that correspond to the given frequency band. In case of the modal truncation augmentation method, the pseudo-eigenfrequencies of the residual vectors can iteratively be identified by repetitively adapting the system stiffness and damping properties to the pseudo-eigenfrequencies that are the outcome of the reduced eigenvalue problem (see Equation 2.41). In case of the KRYLOV subspace method, an individual KRYLOV subspace can be expanded around the mean frequency of each of the frequency intervals. Since the frequency range of each interval is small compared to the overall frequency range, the number of KRYLOV can be reduced. Nevertheless, the factorization of the frequency-dependent system matrices is time-consuming and hence the overall computational effort might be increased compared to the ordinary KRYLOV subspace method. The principle of multiple expansion frequencies was successfully applied for various systems as published in multiple scientific publications (see Section 2.3.2.4).

In common electric vehicle applications a transmission of the torque and rotational speed of the electric traction motor is needed in order to provide an appropriate power to the car wheel. In most cases, the gear box which contains the corresponding gear wheels is directly attached to the electric motor. Thus, the vibration of the two components is mechanically coupled which can lead to further phenomena inside the system. The tangential electromagnetic forces acting on the rotor produce a torque ripple which leads to torsional vibrations of the rotating parts inside the drive train. Depending on the transmission topology, these torsional vibrations can cause radial excitations of the bearings seats and thus vibration of the housing structure. Thus, in order to get a full overview of the vibrational and acoustical behavior of the electric drive train, the rotor transfer path, meaning the rotor excitation as well as the rotating components, needs to be included inside the structural dynamic analysis.

A. Method of Cells

A.1. Directional Stiffness Properties

The methode of cells is a quasi-analytical homogenization technique. Its basic idea is to express a the effective stiffness matrix of a composite material by a set of algebraic equations which can be deduced from a discrete micromechanical model.
In order to do so, the MOC involves the following steps:

1. Extract a representative volume element (RVE) from a composite material .
2. Divide the RVE into subcells and extract the strain-displacement relations for each subcell based on a linear displacement field.
3. Apply the continuity of displacements at the RVE boundaries in an average sense.
4. Apply the continuity of tractions at the subcell interfaces.
5. Solve of the system for the normal stress relations.
6. Solve of the system for the shear stress relations.

In the following the MOC will exemplarily be demonstrated on a micromechanical model that consists of two subcells, $\beta = 1$ and $\beta = 2$, as shown in Figure A.1. The given procedure can be transferred to any complexity of micromechanical model with periodic boundary conditions. The full deduction of the set of algebraic equations for a micromechanical model with four subcells can be found in [151].

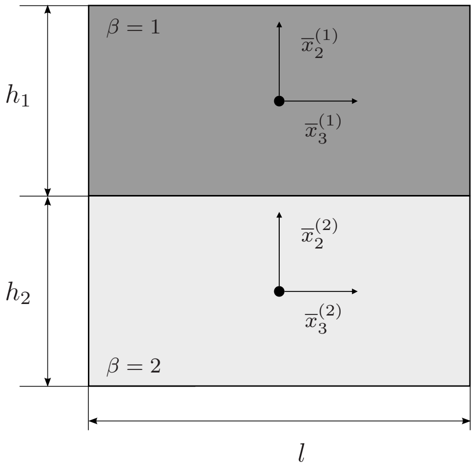

Figure A.1.: Micromechanical model with two subcells as it is employed by the method of cells (MOC).

A.1.1. Constitutive Equation of Composite

The constitutive equation of a composite material inside a RVE is given as

$$\overline{\sigma}_{ij} = K_{ijkl}\overline{\varepsilon}_{kl} \tag{A.1}$$

with $\overline{\sigma}_{ij}$ as the average stress, $\overline{\varepsilon}_{kl}$ as the average strain and the K_{ijkl} as the effective stiffness matrix of the composite.

For the MOC, the average strain $\overline{\varepsilon}_{ij}$ and the average stress $\overline{\sigma}_{ij}$ can simply be written as the sum of the subcells individual average strain and stress, respectively, weighted by their volume fraction

$$\overline{\varepsilon}_{ij} = \frac{1}{h}\sum_{\beta=1}^{2} h_\beta \overline{\varepsilon}_{ij}^{(\beta)} = \frac{h_1\overline{\varepsilon}_{ij}^{(1)} + h_2\overline{\varepsilon}_{ij}^{(2)}}{h}. \tag{A.2}$$

$$\overline{\sigma}_{ij} = \frac{1}{h}\sum_{\beta=1}^{2} h_\beta \overline{\sigma}_{ij}^{(\beta)} = \frac{h_1\overline{\sigma}_{ij}^{(1)} + h_2\overline{\sigma}_{ij}^{(2)}}{h}. \tag{A.3}$$

The displacement field in each subcell is obtained from a first order TAYLOR-expansion providing

$$u_i^{(\beta)} = w_i^{(\beta)} + \xi_i^{(\beta)}\overline{x}_1 + \phi_i^{(\beta)}\overline{x}_2^{(\beta)} + \psi_i^{(\beta)}\overline{x}_3 \tag{A.4}$$

in which ξ_i, ϕ_i, and ψ_i denote so-called microvariables that remain constant inside each subcell yielding a linear displacement field. Employing the generic strain-displacement relation

$$\varepsilon_{ij}^{(\beta)} = \frac{1}{2}\left[\frac{\partial u_i^{(\beta)}}{\partial \overline{x}_j^{(\beta)}} + \frac{\partial u_j^{(\beta)}}{\partial \overline{x}_i^{(\beta)}}\right], \tag{A.5}$$

the strain-displacement relation of each subcell can be written as

$$\begin{aligned}
\varepsilon_{11}^{(\beta)} &= \xi_1^{(\beta)} \\
\varepsilon_{22}^{(\beta)} &= \phi_2^{(\beta)} \\
\varepsilon_{33}^{(\beta)} &= \psi_3^{(\beta)} \\
2\varepsilon_{12}^{(\beta)} &= \xi_2^{(\beta)} + \phi_1^{(\beta)} \\
2\varepsilon_{13}^{(\beta)} &= \xi_3^{(\beta)} + \psi_1^{(\beta)} \\
2\varepsilon_{23}^{(\beta)} &= \phi_3^{(\beta)} + \psi_2^{(\beta)}.
\end{aligned} \tag{A.6}$$

A.1.2. Continuity of Displacements at Boundaries

In Figure A.2 the RVE from Figure A.1 is given in its three-dimensional environment.

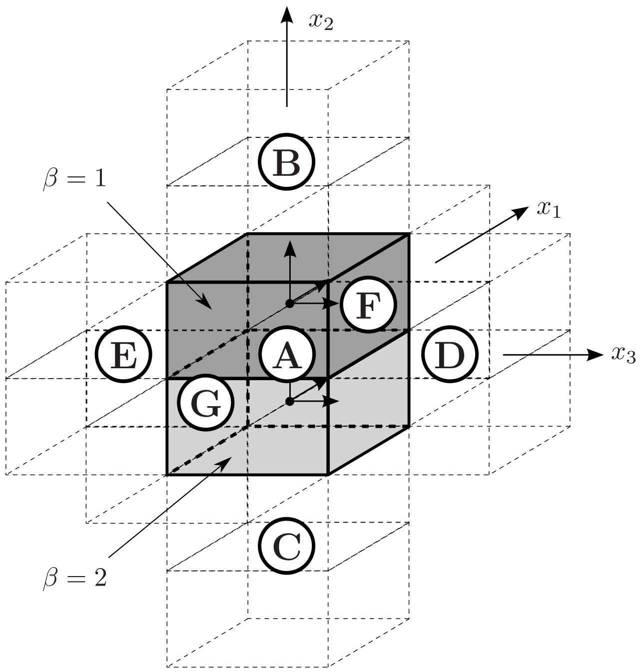

Figure A.2.: Schematic view of adjoining subcell systems and corresponding boundary conditions.

The RVE adjoins six further volume elements at all six boundary surfaces. Due to the assumption of periodicity each of the volume elements shows the same distortion and thus the microvariables are identical for each volume element

$$\xi_{i,X}^{(\beta)} = \xi i^{(\beta)} \tag{A.7}$$

$$\phi_{i,X}^{(\beta)} = \phi i^{(\beta)} \tag{A.8}$$

$$\psi_{i,X}^{(\beta)} = \psi_i^{(\beta)} \tag{A.9}$$

where X stands for the different RVEs from Figure A.2, namely A, B, C, D, E, F, and G. Applying the continuity of displacements in an average sense on each boundary condition yields:

$$\int\limits_d \int\limits_l \left(u_{i,A}^{(1)}\Big|_{\bar{x}_2=\frac{h_1}{2}} - u_{i,B}^{(2)}\Big|_{\bar{x}_3=\frac{-h_2}{2}} \right) d\bar{x}_2 d\bar{x}_1 = 0 \tag{A.10}$$

and

$$\int\limits_d \int\limits_l \left(u_{i,A}^{(2)}\Big|_{\bar{x}_2=\frac{-h_2}{2}} - u_{i,C}^{(1)}\Big|_{\bar{x}_2=\frac{h_1}{2}} \right) d\bar{x}_3 d\bar{x}_1 = 0 \tag{A.11}$$

which can be written as

$$w_{i,A}^{2} + \phi_i^{(2)} \frac{l_2}{2} = w_{i,B}^{(1)} - \phi_i^{(1)} \frac{l_1}{2} \tag{A.12}$$

and

$$w^1_{i,A} - \phi_i^{(1)} \frac{l_1}{2} = w_{i,C}^{(2)} + \phi_i^{(2)} \frac{l_2}{2}. \tag{A.13}$$

Expanding $w_i^{(\beta)}$ as a function of $\overline{x}_2$ with a first order TAYLOR series yields

$$w_i^{(\beta)} = w_{i,A}^{(\beta)} + \underbrace{\frac{\partial w_i}{\partial \overline{x}_2}}_{\text{const.}} \overline{x}_2^{(\beta)} \tag{A.14}$$

which can be inserted into Equations A.12 and A.13. By additionally considering Equation A.5,

$$\frac{\partial w_i^{(1)}}{\partial \overline{x}_2} = \frac{\partial w_i^{(1)}}{\partial \overline{x}_2} = \frac{\partial w_i}{\partial \overline{x}_2} = \overline{\varepsilon}_{2i} \tag{A.15}$$

and

$$\frac{\partial w_i}{\partial \overline{x}_2} = \frac{h_1 \phi_i^{(1)} + h_2 \phi_i^{(2)}}{h} \tag{A.16}$$

arise, which can be transformed into

$$\phi_i^{(2)} = \frac{h}{h_2} \overline{\varepsilon}_{2i} - \frac{h_1}{h_2} \phi_i^{(1)}. \tag{A.17}$$

Analogue to the boundary surfaces A-B and A-C the continuity of displacements can be performed on the other four boundary surfaces A-D, A-E, A-F, and A-G providing similar relations, namely

$$\frac{\partial w_i^{(\beta)}}{\partial \overline{x}_1} = \frac{\partial w_i}{\partial \overline{x}_1} = \xi_i^{(\beta)} = \xi_i = \varepsilon_{1i} = \overline{\varepsilon}_{1i} \tag{A.18}$$

and

$$\frac{\partial w_i^{(\beta)}}{\partial \overline{x}_3} = \frac{\partial w_i}{\partial \overline{x}_3} = \psi_i^{(\beta)} = \psi_i = \varepsilon_{3i} = \overline{\varepsilon}_{3i}. \tag{A.19}$$

The consideration of the boundary displacements shows that the strain field of each subcell is independent of $\overline{x}_1$, $\overline{x}_2$, and $\overline{x}_3$ which yields that the average strain and stress of each subcell are identical to the local strain and stress field of each subcell, respectively, meaning

$$\overline{\varepsilon}_{ij}^{(\alpha,\beta,\gamma)} = \varepsilon_{ij}^{(\alpha,\beta,\gamma)}, \quad \text{and } \overline{\sigma}_{ij}^{(\alpha,\beta,\gamma)} = \sigma_{ij}^{(\alpha,\beta,\gamma)}. \tag{A.20}$$

Thus, the strain-distortion relations from Equation A.6 can be inserted into Equation A.2 providing the stress-distortion relations for the composite.

A.1.3. Continuity of Tractions at Subcell Interfaces

Applying the continuity of tractions on the interface between the two subcells provides

$$\sigma_{2j}^{(1)} = \sigma_{2j}^{(2)} = \sigma_{2j} \tag{A.21}$$

For each subcell constitutive equation can be formulated

$$\sigma_{ij} = K_{ijkl}^{(\beta)} \varepsilon_{kl}^{(\beta)} \tag{A.22}$$

or

$$\begin{pmatrix} \sigma_{11}^{(\beta)} \\ \sigma_{22}^{(\beta)} \\ \sigma_{33}^{(\beta)} \\ \sigma_{12}^{(\beta)} \\ \sigma_{13}^{(\beta)} \\ \sigma_{23}^{(\beta)} \end{pmatrix} = \begin{pmatrix} K_{11}^{(\beta)} & K_{12}^{(\beta)} & K_{13}^{(\beta)} & 0 & 0 & 0 \\ K_{21}^{(\beta)} & K_{22}^{(\beta)} & K_{23}^{(\beta)} & 0 & 0 & 0 \\ K_{31}^{(\beta)} & K_{32}^{(\beta)} & K_{33}^{(\beta)} & 0 & 0 & 0 \\ 0 & 0 & 0 & K_{44}^{(\beta)} & 0 & 0 \\ 0 & 0 & 0 & 0 & K_{55}^{(\beta)} & 0 \\ 0 & 0 & 0 & 0 & 0 & K_{66}^{(\beta)} \end{pmatrix} \begin{pmatrix} \varepsilon_{11}^{(\beta)} \\ \varepsilon_{22}^{(\beta)} \\ \varepsilon_{33}^{(\beta)} \\ 2\varepsilon_{12}^{(\beta)} \\ 2\varepsilon_{13}^{(\beta)} \\ 2\varepsilon_{23}^{(\beta)} \end{pmatrix}. \tag{A.23}$$

A.1.4. Normal Stress-Strain Relations

The constitutive equation of the compositeA.1 in normal direction with $i = j$ can be expressed as

$$\begin{pmatrix} \overline{\sigma}_{11} \\ \overline{\sigma}_{22} \\ \overline{\sigma}_{33} \end{pmatrix} = \begin{pmatrix} K_{11} & K_{12} & K_{13} \\ K_{21} & K_{22} & K_{23} \\ K_{31} & K_{32} & K_{33} \end{pmatrix} \begin{pmatrix} \overline{\varepsilon}_{11} \\ \overline{\varepsilon}_{22} \\ \overline{\varepsilon}_{33} \end{pmatrix}. \tag{A.24}$$

By using Equation A.2 and the strain-displacement relations A.6, the average strains can be written as

$$\overline{\varepsilon}_{11} = \frac{h_1\varepsilon_{11}^{(1)} + h_2\varepsilon_{11}^{(2)}}{h} = \frac{h_1\xi_1^{(1)} + h_2\xi_1^{(2)}}{h} = \xi_1 = \varepsilon_{11}^{(1)} = \varepsilon_{11}^{(2)} = \varepsilon_{11} \tag{A.25}$$

$$\overline{\varepsilon}_{22} = \frac{h_1\varepsilon_{22}^{(1)} + h_2\varepsilon_{22}^{(2)}}{h} = \frac{h_1\phi_2^{(1)} + h_2\phi_2^{(2)}}{h} \tag{A.26}$$

$$\overline{\varepsilon}_{33} = \frac{h_1\varepsilon_{33}^{(1)} + h_2\varepsilon_{33}^{(2)}}{h} = \frac{h_1\psi_3^{(1)} + h_2\psi_3^{(2)}}{h} = \psi_3 = \varepsilon_{33}^{(1)} = \varepsilon_{33}^{(2)} = \varepsilon_{33}. \tag{A.27}$$

Proceeding from the continuity of tractions A.21 in normal direction with $j = 2$ and substituting for the constitutive equation A.23 as well as the microvariables from Equation A.6 yields

$$\sigma_{22}^{(1)} = \sigma_{22}^{(2)} \tag{A.28}$$

$$K_{12}^{(1)}\varepsilon_{11}^{(1)} + K_{22}^{(1)}\varepsilon_{22}^{(1)} + K_{23}^{(1)}\varepsilon_{33}^{(1)} = K_{21}^{(2)}\varepsilon_{11}^{(2)} + K_{22}^{(2)}\varepsilon_{22}^{(2)} + K_{23}^{(2)}\varepsilon_{33}^{(2)} \tag{A.29}$$

$$K_{21}^{(1)}\xi_1^{(1)} + K_{22}^{(1)}\phi_2^{(1)} + K_{23}^{(1)}\psi_3^{(1)} = K_{21}^{(2)}\xi_1^{(2)} + K_{22}^{(2)}\phi_2^{(2)} + K_{23}^{(2)}\psi_3^{(2)} \tag{A.30}$$

and thus with Equation A.25, A.26, and A.27

$$\phi_2^{(1)} = B_1\varepsilon_{11} + B_2\varepsilon_{22} + B_3\varepsilon_{33}. \tag{A.31}$$

with

$$B_1 = \frac{K^{(2)}_{21} - K^{(1)}_{21}}{K^{(2)}_{22}h_1 + K^{(1)}_{22}h_2}h_2 \tag{A.32}$$

$$B_2 = \frac{K^{(2)}_{22}\frac{h}{h_2}}{K^{(2)}_{22}h_1 + K^{(1)}_{22}h_2}h_2 \tag{A.33}$$

$$B_3 = \frac{K^{(2)}_{23} - K^{(1)}_{23}}{K^{(2)}_{22}h_1 + K^{(1)}_{22}h_2}h_2. \tag{A.34}$$

Employing Equation A.3 for the average stress and the constitutive equations of each of the two subcells A.22 provides

$$\overline{\sigma_{ij}} = \frac{h_1}{h}K^{(1)}_{ijkl}\varepsilon^{(1)}_{kl} + \frac{h_2}{h}K^{(2)}_{ijkl}\varepsilon^{(2)}_{kl} \tag{A.35}$$

and thus for $i = j$

$$\overline{\sigma}_{11} = \frac{h_1K^{(1)}_{11} + h_2K^{(2)}_{11}}{h}\varepsilon_{11} + \frac{h_1K^{(1)}_{12}}{h}\phi^{(1)}_2 + \frac{h_2K^{(2)}_{12}}{h}\phi^{(2)}_2 + \frac{h_1K^{(1)}_{13} + h_2K^{(2)}_{13}}{h}\varepsilon_{33} \tag{A.36}$$

$$\overline{\sigma}_{11} = \frac{h_1K^{(1)}_{12} + h_2K^{(2)}_{12}}{h}\varepsilon_{11} + \frac{h_1K^{(1)}_{22}}{h}\phi^{(1)}_2 + \frac{h_2K^{(2)}_{22}}{h}\phi^{(2)}_2 + \frac{h_1K^{(1)}_{23} + h_2K^{(2)}_{23}}{h}\varepsilon_{33} \tag{A.37}$$

$$\overline{\sigma}_{11} = \frac{h_1K^{(1)}_{13} + h_2K^{(2)}_{13}}{h}\varepsilon_{11} + \frac{h_1K^{(1)}_{23}}{h}\phi^{(1)}_2 + \frac{h_2K^{(2)}_{23}}{h}\phi^{(2)}_2 + \frac{h_1K^{(1)}_{33} + h_2K^{(2)}_{33}}{h}\varepsilon_{33} \tag{A.38}$$

which can be transformed using Equation A.17

$$\overline{\sigma}_{11} = K_{11,A}\varepsilon_{11} + K_1\phi^{(1)}_2 + K_{12,A}\varepsilon_{22} + K_{13,A}\varepsilon_{33} \tag{A.39}$$

$$\overline{\sigma}_{22} = K_{21,A}\varepsilon_{11} + K_2\phi^{(1)}_2 + K_{22,A}\varepsilon_{22} + K_{23,A}\varepsilon_{33} \tag{A.40}$$

$$\overline{\sigma}_{33} = K_{31,A}\varepsilon_{11} + K_3\phi^{(1)}_2 + K_{32,A}\varepsilon_{22} + K_{33,A}\varepsilon_{33} \tag{A.41}$$

with

$$
\begin{aligned}
K_{11,A} &= \frac{h_1 K_{11}^{(1)} + h_2 K_{11}^{(2)}}{h} && \text{(A.42)}\\
K_{12,A} &= \frac{h_2 K_{12}^{(2)}}{h_2}\\
K_{13,A} &= \frac{h_1 K_{13}^{(1)} + h_2 K_{13}^{(2)}}{h} && \text{(A.43)}\\
K_{21,A} &= \frac{h_1 K_{12}^{(1)} + h_2 K_{12}^{(2)}}{h} && \text{(A.44)}\\
K_{22,A} &= \frac{h_2 K_{22}^{(2)}}{h_2}\\
K_{23,A} &= \frac{h_1 K_{23}^{(1)} + h_2 K_{23}^{(2)}}{h} && \text{(A.45)}\\
K_{31,A} &= K_{13,A}\\
K_{32,A} &= \frac{h_2 K_{23}^{(2)}}{h_2}\\
K_{33,A} &= \frac{h_1 K_{33}^{(1)} + h_2 K_{33}^{(2)}}{h}. && \text{(A.46)}
\end{aligned}
$$

and

$$
\begin{aligned}
K_1 &= \frac{(K_{12}^{(1)} - K_{12}^{(2)}) h_1}{h} && \text{(A.47)}\\
K_2 &= \frac{(K_{22}^{(1)} - K_{22}^{(2)}) h_1}{h} && \text{(A.48)}\\
K_3 &= \frac{(K_{23}^{(1)} - K_{23}^{(2)}) h_1}{h} && \text{(A.49)}
\end{aligned}
$$

Finally, the normal stiffness coefficients inside the constitutive equation of the composite A.1 can be quantified by employing Equations A.39, A.40 and A.41 as well as Equation A.31

$$
\begin{aligned}
K_{11} &= K_{11,A} + K_1 B_1 && \text{(A.50)}\\
K_{12} &= K_{12,A} + K_1 B_2 && \text{(A.51)}\\
K_{13} &= K_{13,A} + K_1 B_3 && \text{(A.52)}\\
K_{22} &= K_{22,A} + K_2 B_2 && \text{(A.53)}\\
K_{23} &= K_{23,A} + K_2 B_3 && \text{(A.54)}\\
K_{33} &= K_{33,A} + K_3 B_3. && \text{(A.55)}
\end{aligned}
$$

A.1.5. Shear Stress-Strain Relations

The constitutive equation of the compositeA.1 in shear direction with $i \neq j$ can be expressed as

$$\begin{pmatrix}\overline{\sigma}_{12}\\ \overline{\sigma}_{13}\\ \overline{\sigma}_{23}\end{pmatrix} = \begin{pmatrix}K_{44} & 0 & 0\\ 0 & K_{55} & 0\\ 0 & 0 & K_{66}\end{pmatrix}\begin{pmatrix}2\overline{\varepsilon}_{12}\\ 2\overline{\varepsilon}_{13}\\ 2\overline{\varepsilon}_{23}\end{pmatrix}. \tag{A.56}$$

By using Equation A.2 and the strain-displacement relations A.6 as well as Equations A.18 and A.19, the average strains can be written as

$$\overline{\varepsilon}_{12} = \frac{h_1\varepsilon_{12}^{(1)} + h_2\varepsilon_{12}^{(2)}}{h} \Leftrightarrow \varepsilon_{12}^{(2)} = \frac{h}{h_2}\overline{\varepsilon}_{12} - \frac{h_1}{h_2}\varepsilon_{12}^{(1)} \tag{A.57}$$

$$\begin{aligned}\overline{\varepsilon}_{13} &= \frac{h_1\varepsilon_{13}^{(1)} + h_2\varepsilon_{13}^{(2)}}{h} = \frac{h_1(\xi_3^{(1)} + \psi_1^{(1)}) + h_2(\xi_3^{(2)} + \psi_1^{(2)})}{2h}\\ &= \frac{\xi_3 + \psi_1}{2} = \varepsilon_{13}^{(1)} = \varepsilon_{13}^{(2)} = \varepsilon_{13}\end{aligned} \tag{A.58}$$

$$\overline{\varepsilon}_{23} = \frac{h_1\varepsilon_{23}^{(1)} + h_2\varepsilon_{23}^{(2)}}{h} \Leftrightarrow \varepsilon_{23}^{(2)} = \frac{h}{h_2}\overline{\varepsilon}_{23} - \frac{h_1}{h_2}\varepsilon_{23}^{(1)}. \tag{A.59}$$

Employing the continuity of tractions A.21 at the interface between the two subcells in shear direction with $j = 1, 3$ and substituting for the constitutive equation A.23 as well as the microvariables from Equation A.6, yields

$$\begin{aligned}\sigma_{21}^{(1)} &= \sigma_{21}^{(2)}\\ K_{44}^{(1)}2\varepsilon_{12}^{(1)} &= K_{44}^{(2)}2\varepsilon_{12}^{(2)}\end{aligned} \tag{A.60}$$

and

$$\begin{aligned}\sigma_{23}^{(1)} &= \sigma_{23}^{(2)}\\ K_{55}^{(1)}2\varepsilon_{23}^{(1)} &= K_{55}^{(2)}2\varepsilon_{23}^{(2)}\end{aligned} \tag{A.61}$$

which can be transformed into

$$\varepsilon_{12}^{(2)} = \frac{K_{44}^{(1)}}{K_{44}^{(2)}}\varepsilon_{12}^{(1)} \tag{A.62}$$

and

$$\varepsilon_{23}^{(2)} = \frac{K_{55}^{(1)}}{K_{55}^{(2)}}\varepsilon_{23}^{(1)}. \tag{A.63}$$

Inserting Equation A.62 and A.63 into Equation A.57 and A.59, yields

$$\varepsilon_{12}^{(1)} = \frac{hK_{44}^{(2)}}{h_2K_{44}^{(1)} + h_1K_{44}^{(2)}}\overline{\varepsilon}_{12} \tag{A.64}$$

$$\varepsilon_{12}^{(2)} = \frac{hK_{44}^{(1)}}{h_2K_{44}^{(1)} + h_1K_{44}^{(2)}}\overline{\varepsilon}_{12} \tag{A.65}$$

$$\varepsilon_{23}^{(1)} = \frac{hK_{66}^{(2)}}{h_2K_{66}^{(1)} + h_1K_{66}^{(2)}}\overline{\varepsilon}_{23} \tag{A.66}$$

$$\varepsilon_{23}^{(2)} = \frac{hK_{66}^{(1)}}{h_2K_{66}^{(1)} + h_1K_{66}^{(2)}}\overline{\varepsilon}_{23}. \tag{A.67}$$

Employing Equation A.3 for the average stress and the constitutive equations of each of the two subcells A.22, provides

$$\overline{\sigma}_{ij} = \frac{h_1}{h}K_{ijkl}^{(1)}\varepsilon_{kl}^{(1)} + \frac{h_2}{h}K_{ijkl}^{(2)}\varepsilon_{kl}^{(2)} \tag{A.68}$$

and thus for $i \neq j$

$$\overline{\sigma}_{12} = \frac{h_1K_{44}^{(1)}2\varepsilon_{12}^{(1)} + h_2K_{44}^{(2)}2\varepsilon_{12}^{(2)}}{h} \tag{A.69}$$

$$\overline{\sigma}_{13} = \frac{h_1K_{55}^{(1)} + h_2K_{55}^{(2)}}{h}2\varepsilon_{13} \tag{A.70}$$

$$\overline{\sigma}_{23} = \frac{h_1K_{66}^{(1)}2\varepsilon_{23}^{(1)} + h_2K_{66}^{(2)}2\varepsilon_{23}^{(2)}}{h} \tag{A.71}$$

$$\tag{A.72}$$

which can be transformed using Equations A.64, A.65, A.66, and A.67

$$\overline{\sigma}_{12} = \frac{hK_{44}^{(1)}K_{44}^{(2)}}{h_2K_{44}^{(1)} + h_1K_{44}^{(2)}}2\overline{\varepsilon}_{12} \tag{A.73}$$

$$\overline{\sigma}_{13} = \frac{h_1K_{55}^{(1)} + h_2K_{55}^{(2)}}{h}2\overline{\varepsilon}_{13} \tag{A.74}$$

$$\overline{\sigma}_{23} = \frac{hK_{66}^{(1)}K_{66}^{(2)}}{h_2K_{66}^{(1)} + h_1K_{66}^{(2)}}2\overline{\varepsilon}_{23}. \tag{A.75}$$

Thus the shear stiffness coefficients inside the constitutive equation of the composite A.1 can be obtained from

$$K_{44} = \frac{hK_{44}^{(1)}K_{44}^{(2)}}{h_2K_{44}^{(1)} + h_1K_{44}^{(2)}} \tag{A.76}$$

$$K_{55} = \frac{h_1K_{55}^{(1)} + h_2K_{55}^{(2)}}{h} \tag{A.77}$$

$$K_{66} = \frac{hK_{66}^{(1)}K_{66}^{(2)}}{h_2K_{66}^{(1)} + h_1K_{66}^{(2)}}. \tag{A.78}$$

Thus, all entries of the stiffness matrix were quantified by algebraic equations. The elastic constants can now be extracted from the compliance matrix $\underline{B}$, which is the inverse of the stiffness matrix $\underline{K}$

$$\underline{B} = \underline{K}^{-1} = K_{ijkl}^{-1}. \tag{A.79}$$

The effective elastic constants of the composite material can be extracted from the entries of the compliance matrix $\underline{B}$ as follows:

Young's moduli:

$$E_{11} = \frac{1}{B_{11}}, \quad E_{22} = \frac{1}{B_{22}}, \quad E_{33} = \frac{1}{B_{33}} \tag{A.80}$$

Poisson ratios:

$$\nu_{12} = B_{12}E_{11}, \quad \nu_{13} = B_{13}E_{11}, \quad \nu_{23} = B_{23}E_{22} \tag{A.81}$$

Shear moduli:

$$G_{11} = \frac{1}{B_{44}}, \quad G_{22} = \frac{1}{B_{55}}, \quad G_{33} = \frac{1}{B_{66}}. \tag{A.82}$$

A.2. Directional Damping Properties

The effective damping of the composite material can be expressed in terms of directional loss factors η_{ii} which can be obtained from the effective elastic constants of the composite following Alfrey's so-called correspondence principle

$$\eta_{ii} = \frac{\Im(E_{ii})}{\Re(E_{ii})} \quad \text{and} \quad \eta_{ij} = \frac{\Im(G_{ij})}{\Re(G_{ij})}. \tag{A.83}$$

In order to enable the MOC towards the quantification of effective directional damping properties, the stiffness matrix of each subcell needs to be manipulated to represent the material inherent damping of each constituent. The material inherent damping of each constituent is typically expressed by the material's characteristic damping ratio ξ which can be transformed into the material's loss factor η by employing $tan(\delta) = \eta = \xi/2$ (see Section 2.4.1.2). Assuming the Poisson ratio to be real and thus ξ to be constant for each material the complex elastic values E^* and G^* of each subcell can be obtained from the elastic Young's and shear moduli, E and G, respectively, of the underlying material with

$$E^* = E(1 + i \cdot \frac{\xi}{2}) \quad \text{and} \quad G^* = G(1 + i \cdot \frac{\xi}{2}). \tag{A.84}$$

B. Representative Volume Element

B.1. Numerical Solution of RVE

In order to retrieve effective directional stiffness and damping properties of a composite material a micromechanical model of the underlying representative volume element can numerically be solved. The basic principles of the RVE were introduced in Section 2.5.1. In the following the numerical homogenization process using a representative volume element (RVE) will be demonstrated for an unidirectional fiber-reinforced structure with a hexagonal packing pattern and periodic boundary conditions as shown in Figure B.1.

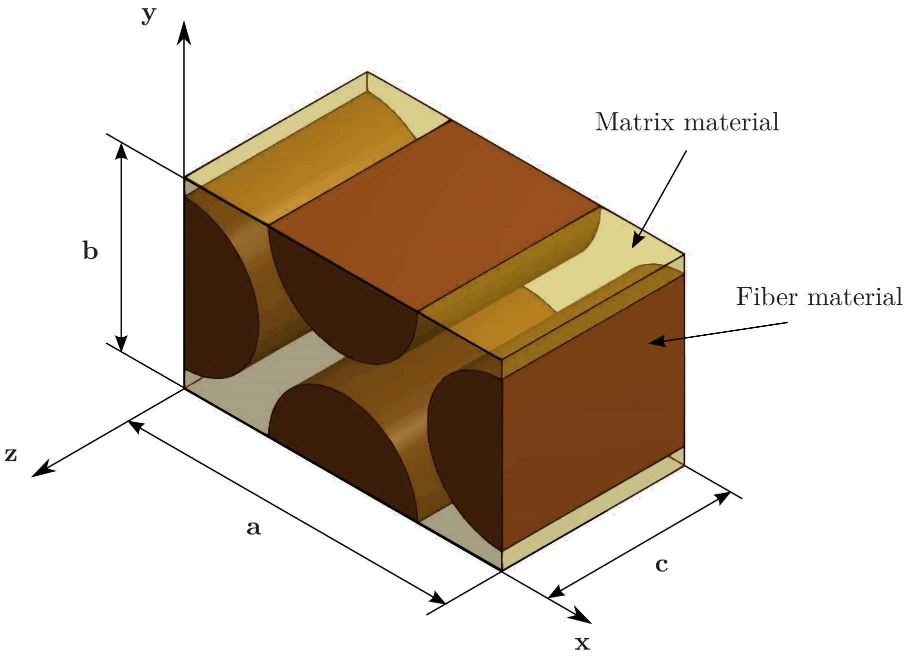

Figure B.1.: Exemplary RVE of unidirectional fiber-reinforced structure with a hexagonal packing pattern and periodic boundary conditions.

The composite consists of two constituents, a fiber material and a matrix material. The character of hexagonal packing patterns was illustrated in Figure 2.11. The dimensions of the RVE are

$$a = 17.32 \text{ mm}, \quad b = 10 \text{ mm}, \quad \text{and} \quad c = 10 \text{ mm}.$$

In this thesis the software Ansys and the corresponding modeling language APDL were used. However, the basic procedure is transferable to any other simulation software.

B.1.1. Implementation of Periodic Boundary Conditions

In Figure B.2 the 2D-cross section of an exemplary three-dimensional RVE is shown. It shows the RVE before and after the application of an external load.

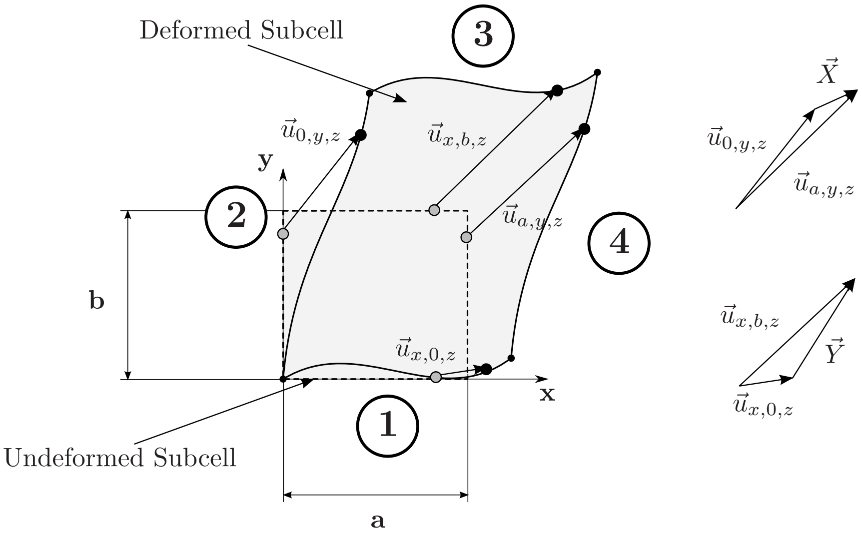

Figure B.2.: Schematic illustration of RVE with periodic boundary conditions.

In order to provide the continuity of displacements at the RVE boundary interfaces, periodic boundary conditions have to be implemented on the RVE surfaces. Therefore, the distortion of the interfaces 1 and 3 as well as the distortion of the interfaces 2 and 4 have to be equal which can be expressed by

$$u_i(a, y, z) = u_i(0, y, z) + X_i \tag{B.1}$$

and

$$u_i(x, b, z) = u_i(x, 0, z) + Y_i \tag{B.2}$$

where $u_i(x, y, z)$ are the displacements of each the surface at the coordinates (x, y) and X_i and Y_i are the constant deformation vectors with the index i denoting the spatial direction. Consequently, this also applies in z-direction

$$u_i(x, y, c) = u_i(x, y, 0) + Z_i \tag{B.3}$$

with c as the length of the RVE in z-direction and Z_i as the constant deformation vector.

In order to implement the above relations for the surface displacements inside the Ansys model, so-called constraint equations can be used with

$$\delta = \sum_{i=1}^{N} (k_i \cdot u_i) \tag{B.4}$$

where the sum of the degree-of-freedom u_i of one or more mesh nodes scaled by individual coefficients k_i must be equal to a constant value δ.

In order to avoid an overly constraint simulation model, the node sets of the diagonal edges and diagonal vertices are individually coupled with

$$u_i(a, b, z) = u_i(0, 0, z) + X_i + Y_i \tag{B.5}$$

$$u_i(x, b, c) = u_i(x, 0, 0) + Y_i + Z_i, \tag{B.6}$$

$$u_i(a,y,c) = u_i(0,y,0) + X_i + Z_i, \tag{B.7}$$

and finally

$$u_i(a,b,c) = u_i(0,0,0) + X_i + Y_i + Z_i \tag{B.8}$$

B.1.2. Load Application

The identification of directional stiffness and damping properties using the RVE requires the impose of an external load on the surfaces of the RVE (see Section 2.5.1). This can efficiently be provided by either using a homogeneous strain load or a homogeneous stress load. Employing a homogeneous strain load the corresponding state of internal stresses inside the RVE an thus the average stress $\overline{\sigma}_{ij}$ (see Equation 2.66) can directly be quantified from the reaction surface stresses yielding the solution of

$$\overline{\sigma}_{ij} = K_{ijkl}\overline{\varepsilon}_{kl} \tag{B.9}$$

In order to sufficiently quantify the effective stiffness matrix K_{ijkl} six independent strain loads need to be applied. Therefore, an additional node n_m with six degrees-of-freedom, three translational and three rotational, was inserted into the Ansys model. Each of the nodal DOFs was coupled to the surface DOFs of the RVE in order to impose homogeneous displacements an thus homogeneous strain boundary conditions.

The normal displacements of the RVE surfaces in each spatial direction were imposed by the translational displacement of the node external n_m yielding

$$0 = u_i(a,y,z) - u_i(0,y,z) - k_x \cdot \begin{pmatrix} u_x \\ 0 \\ 0 \end{pmatrix} \tag{B.10}$$

for the x-direction,

$$0 = u_i(x,b,z) - u_i(x,0,z) - k_y \begin{pmatrix} 0 \\ u_y \\ 0 \end{pmatrix} \tag{B.11}$$

for the y-direction,

$$0 = u_i(x,y,c) - u_i(x,y,0) - k_z \begin{pmatrix} 0 \\ 0 \\ u_z \end{pmatrix} \tag{B.12}$$

for the z-direction with k_x, k_y, and k_z as the coefficients of the translational DOFs u_x, u_y, and u_z, respectively, of n_m. The shear displacements of the RVE were coupled to the rotational DOFs of node n_m yielding

$$0 = u_i(a,y,z) - u_i(0,y,z) - k_{xy} \begin{pmatrix} 0 \\ u_{xy} \\ 0 \end{pmatrix} \tag{B.13}$$

for the rotation around the z-axis,

$$0 = u_i(x, b, z) - u_i(x, 0, y) - k_{yz} \begin{pmatrix} 0 \\ 0 \\ u_{yz} \end{pmatrix} \tag{B.14}$$

for the rotation around the x-axis, and

$$0 = u_i(x, y, c) - u_i(x, y, 0) - k_{xz} \begin{pmatrix} u_{xz} \\ 0 \\ 0 \end{pmatrix} \tag{B.15}$$

for the rotation around the y-axis, with k_{xy}, k_{yz}, and k_{xz} as the coefficients of the rotational DOFs u_{xy}, u_{yz}, and u_{xz}, respectively.

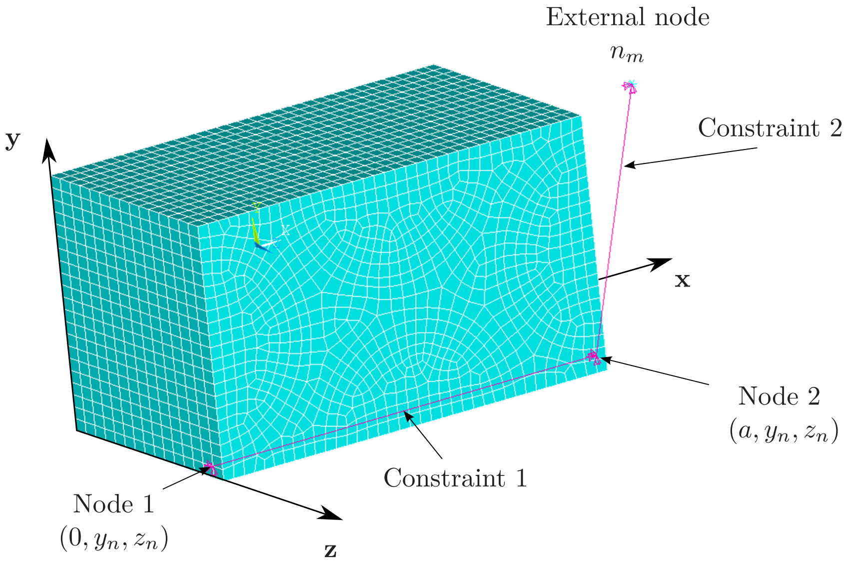

Figure B.3.: Constraint equation coupling two mesh nodes of the RVE to the external node n_m.

Figure B.3 shows exemplarily shows the constraint equations as applied to two nodes on opposite surfaces of the RVE in x-direction and the external node n_m. The corresponding constrain equations are given as

$$0 = u_x(a, y_n, z_n) - u_x(0, y_n, z_n) - k_x \cdot u_x \tag{B.16}$$

$$0 = u_x(a, y_n, z_n) - u_x(0, y_n, z_n) - k_{xy} \cdot u_{xy} \tag{B.17}$$

$$0 = u_x(a, y_n, z_n) - u_x(0, y_n, z_n) \tag{B.18}$$

with n indicating the coordinates of the particular node pair. Thus, applying a displacement to the external node n_m imposes a homogeneous strain on the RVE surfaces. The fixation of all DOFs of the central node inside the RVE provides a symmetrical deformation of the RVE.

B.2. Extraction of Directional Stiffness Properties

In order to obtain the directional stiffness matrix K_{ijkl} from the deformed RVE the internal stresses of the structure have to be analyzed following Equation B.9.

The internal strain energy is in equilibrium with the externally imposed energy

$$0 = \frac{1}{2} \int_V \sigma_{ij} \varepsilon ij dV + \int_u R_{ij} \cdot du_{ij} \tag{B.19}$$

with R_i as the reaction forces and u_i the DOF of the external node n_m and σ_{ij} and εij as the local stress and strain field inside the RVE. Following Equation 2.65 the total internal strain energy can be be calculated from the average stress and strain inside the RVE which are coupled by the constitutive equation of the composite B.9.

Thus Equation B.19 can be written as

$$0 = K_{ijkl} \cdot \overline{\varepsilon}_{ij}^2 \cdot V + R_{ij} \cdot u_{ij} \tag{B.20}$$

The homogeneous displacements imposed on the boundary surfaces of the RVE yield a homogeneous strain ε_{ij}^0 which is equal to the average strain inside the RVE (see Equation 2.69) and can be written as

$$\overline{\varepsilon}_{ij} = \varepsilon_{ij}^0 = \begin{pmatrix} \frac{u_x(a,y,z) - u_x(0,y,z)}{a} \\ \frac{u_y(x,b,z) - u_y(x,b,z)}{b} \\ \frac{u_z(x,y,c) - u_z(x,y,0)}{c} \\ \frac{u_y(a,y,z) - u_y(0,y,z)}{a} \\ \frac{u_z(x,b,z) - u_z(x,0,z)}{b} \\ \frac{u_x(x,y,c) - u_x(x,y,0)}{c} \end{pmatrix} = \begin{pmatrix} \frac{k_x \cdot u_x}{a} \\ \frac{k_y \cdot u_y}{b} \\ \frac{k_z \cdot u_z}{c} \\ \frac{k_{xy} \cdot u_{xy}}{a} \\ \frac{k_{yz} \cdot u_{yz}}{b} \\ \frac{k_{xz} \cdot u_{xz}}{c} \end{pmatrix}. \tag{B.21}$$

Thus, choosing the coefficients k_j as

$$k_{ij} = \begin{pmatrix} a \\ b \\ c \\ a \\ b \\ c \end{pmatrix} \tag{B.22}$$

provides $\overline{\varepsilon}_{ij} = 1$ for unity displacements $u_{ij} = 1$.

In Figure B.4 the deformation of the RVE as a reaction to the six independent homogeneous strain boundary conditions are illustrated.

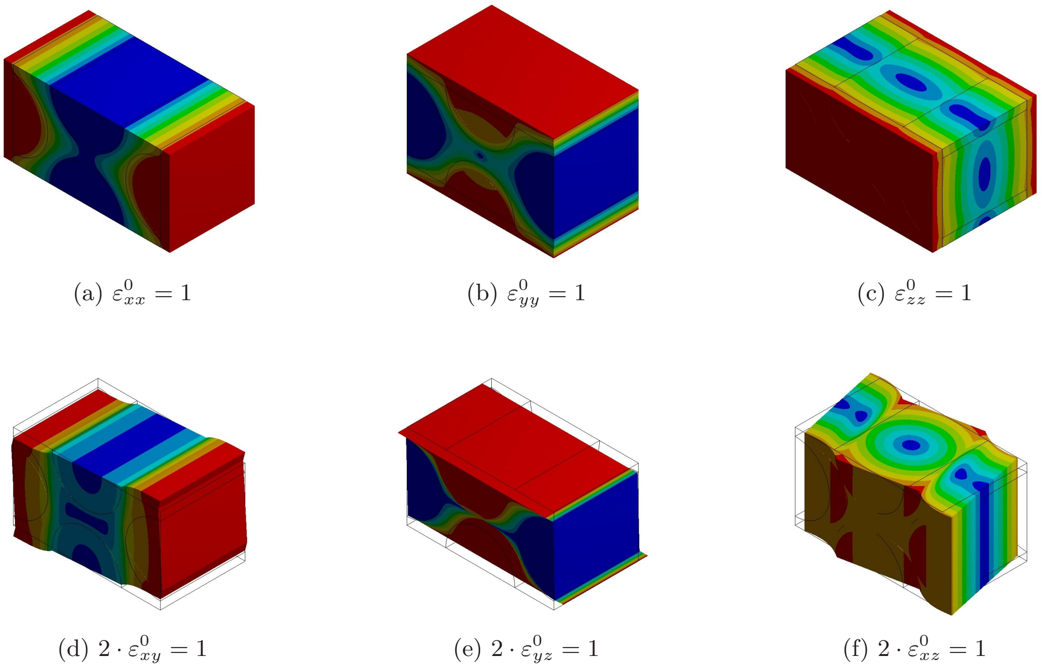
(a) $\varepsilon_{xx}^0 = 1$ (b) $\varepsilon_{yy}^0 = 1$ (c) $\varepsilon_{zz}^0 = 1$

(d) $2 \cdot \varepsilon_{xy}^0 = 1$ (e) $2 \cdot \varepsilon_{yz}^0 = 1$ (f) $2 \cdot \varepsilon_{xz}^0 = 1$

Figure B.4.: Deformation of the RVE as a reaction to the six independent homogeneous strain boundary conditions.

Employing Equation B.20 the columns of the effective stiffness matrix K_{ijkl} can directly be extracted from the reaction forces R_{ij} of each load case with

$$K_{ijkl} = \frac{R_{ij}}{V} \tag{B.23}$$

with V as the total volume of the RVE given as $V = a \cdot b \cdot c$.

Analogue to the procedure of the MOC the directional elastic constants can then be obtained from the compliance matrix $\underline{B}$, which is the inverse of the stiffness matrix $\underline{K} = K_{ijkl}$

$$\underline{B} = \underline{K}^{-1} = K_{ijkl}^{-1}. \tag{B.24}$$

The relations between the entries of the compliance matrix $\underline{B}$ and the effective elastic constants of the composite material are given as follows

YOUNG's modulus:

$$E_{11} = \frac{1}{B_{11}}, \quad E_{22} = \frac{1}{B_{22}}, \quad E_{33} = \frac{1}{B_{33}} \tag{B.25}$$

POISSON ratio:

$$\nu_{12} = -B_{12}E_{11}, \quad \nu_{13} = -B_{13}E_{11}, \quad \nu_{23} = -B_{23}E_{22} \tag{B.26}$$

Shear modulus:

$$G_{11} = \frac{1}{B_{44}}, \quad G_{22} = \frac{1}{B_{55}}, \quad G_{33} = \frac{1}{B_{66}}. \tag{B.27}$$

B.3. Extraction of Directional Damping Properties

In the previous section the identification of directional stiffness properties from the representative volume element (RVE) was shown. In order to retrieve the effective directional damping properties from the RVE the strain energy method will be applied. The strain energy method was briefly introduced in Section 2.5.4.1. Its basic idea is that the total loss factor of a particular deformation can be obtained from the sum of isotropic loss factors of all constituents weighted by the constituent's contribution to the global strain energy stored inside the structure (see Equation B.29).

The internal strain energy U^p of a particular volume element can be expressed by

$$U^p = \frac{1}{2} \int_{V^p} \sigma_{ij} \varepsilon_{ij} dV \tag{B.28}$$

as given in Equation 2.106. The effective directional loss factor η_{ij} can be obtained from the evaluation of strain energies as the reaction to the particular externally imposed homogeneous strain condition ε_{ij}^0

$$\eta_{ij} = \frac{\sum_{p=1}^{n} \eta^p U^p|_{ij}}{\sum_{k=1}^{n} U^p|_{ij}} \tag{B.29}$$

with $U^p|_{ij}$ as the total strain energy of a particular constituent p that arises from the externally imposed load in ij-direction. η^p denotes the material loss factor of the particular constituent. The total strain energy of each constituent can directly be obtained from the numerical simulation results as the sum of the constituent's element strain energies

$$U^p|_{ij} = \frac{1}{2} V^{p,e} \sum_{i=1}^{n} \sigma_{kl}^{p,e} \varepsilon_{kl}^{p,e} \tag{B.30}$$

with n denoting the number of elements, $V^{p,e}$ denoting the element volume and with $\sigma_{kl}^{p,e}$ and $\varepsilon_{kl}^{p,e}$ as the direction element stress and strain, respectively.

C. Resin Material Characterization

C.1. Generation of Master Curves

C.1.1. Dynamic-Mechanical-Analysis

The Dynamic-Mechanical-Analysis (DMA) is the standard measurement procedure for the identification of viscoelastic material properties. Its basic principles and applications are extensively discussed in [131].The basic measurement procedure is specified inside the international standard ISO 6721-1 [248].

In Section 2.4.1.1 the complex modulus E^* was introduced. It defined as the ratio between the dynamic stress $\sigma(t)$ and the dynamic strain $\varepsilon(t)$ (see Equation 2.56). Assuming a viscoelastic material subjected to a harmonic load, both values, the strain and the stress, are complex values as shown in the left part of Figure C.1.

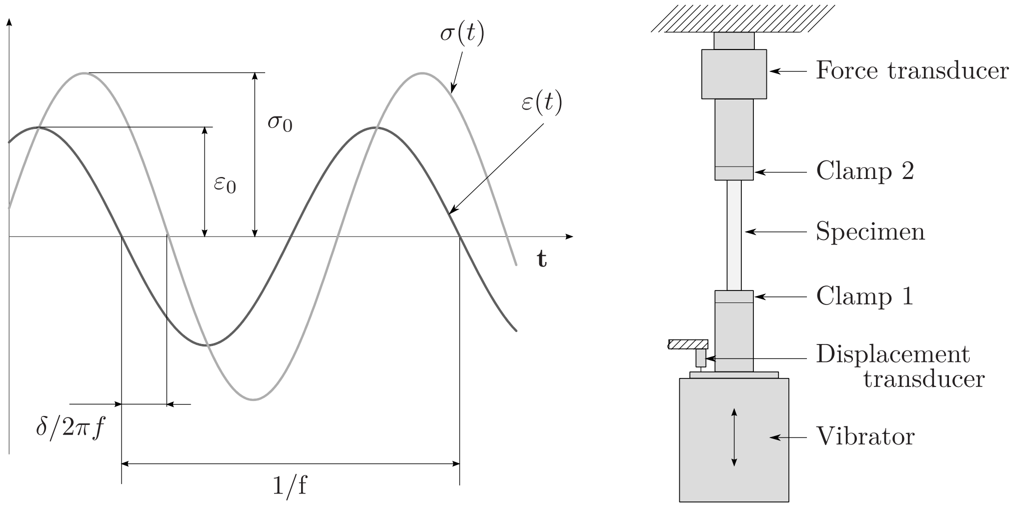

(a) Time-dependent stress and strain values.

(b) Tensional DMA testing device.

Figure C.1.: Time-dependent stress and strain values of viscoelastic materials (left) and schematic illustration of DMA testing device (right).

The complex modulus can thus be identified applying a harmonic load on a viscoelastic material specimen and measuring the magnitude and phase shift of the reaction. The load can either be a harmonic deformation of the specimen or a harmonic force. This is achieved by the Dynamic-Mechanical-Analysis (DMA). Two types of DMA testings were performed during this research work, the tensional DMA and the torsional DMA, providing the complex YOUNG's modulus and the complex shear modulus, respectively.

Tensional Dynamic-Mechanical-Analysis The tensional DMA yields the complex YOUNG's modulus of a material specimen. The basic measurement procedure is specified inside part 4 of the international standard ISO 6721-4 [249].

The principle of the test device is illustrated in the right part of Figure C.1. The material specimen is fixated between two clamps, Clamp 1 and Clamp 2, providing a homogeneous tensional stress and strain field inside the specimen. Clamp 1 is connected to a vibrator while Clamp 2 is fixed to the ground. The harmonic tensional load is generated by the vibrator. It is applied to one end of the specimen by means of Clamp 1. A displacement transducer continuously measures the harmonic load induced by the vibrator. The corresponding reaction force is measured by a force transducer which is located between Clamp 2 and the ground. In order to provide constant measurement temperatures other than the ambient temperature the test device is commonly enclosed by a temperature-controlled chamber.

The material specimen typically has a rectangular cross section. The width of the probe is supposed to be less than a sixth of the probe length. The probe thickness depends on the material stiffness. It should be chosen reasonably small so that the induced deformation of the probe can be measured with a sufficient accuracy.

Torsional Dynamic-Mechanical-Analysis The torsional DMA yields the complex shear modulus of a viscoelastic material. The basic measurement procedure is specified inside part 7 of the international standard ISO 6721-1 [250]. The test configuration is similar to the configuration of the tensional DMA illustrated in Figure C.1. However, the specimen is subjected to a harmonic rotation instead of a harmonic displacement. The force transducer is thus replaced by a torque transducer measuring the reaction torque between Clamp 2 and the ground. The specimens can either be bars with a rectangular cross section or be cylindrical in shape.

In Section 3.1 two different impregnation resin types, namely Resin 1 and Resin 2, were introduced. The viscoelastic properties of both resin types were identified using the tensional and torsional DMA as above described.

In Figure C.2 the specimen geometry of Resin 1 as it was used inside the DMA testings in this thesis is shown. The basic dimensions of the specimen are

length l : 80 mm
width h : 10 mm
thickness d : 2 mm.

The same dimensions were also used for the specimens of Resin 2.

Figure C.2.: Exemplary flat resin specimen for DMA testings.

C.1.2. Extracting Master Curves from DMA Data

The imposed load of both DMA testing types, the tensional DMA and the torsional DMA, can typically be varied in a range from 0.01 Hz to 100 Hz. In order to obtain properties for higher or lower frequencies the time-temperature superposition principle (TTSP) can be employed. The TTSP was briefly introduced in Section 2.4.2.3. Its basic idea is that viscoelastic materials show an equal mechanical behavior with time and temperature (see Section 2.4.2.3). The relation between the time and the temperature of an equal mechanical behavior can be expressed by shift-factors (see Equation 2.61).

Figure C.3 schematically shows the results that arise from multiple DMA testings at different temperatures. The curves are plotted as functions of the logarithm of frequency. The stiffness typically increases with a decreasing temperature and vice versa. Following Equation 2.61 the master curve that corresponds to a particular temperature $T = T_0$ can be extracted from the individual measurement curves by simply shifting the curves by a constant shift factor as schematically illustrated in Figure C.3.

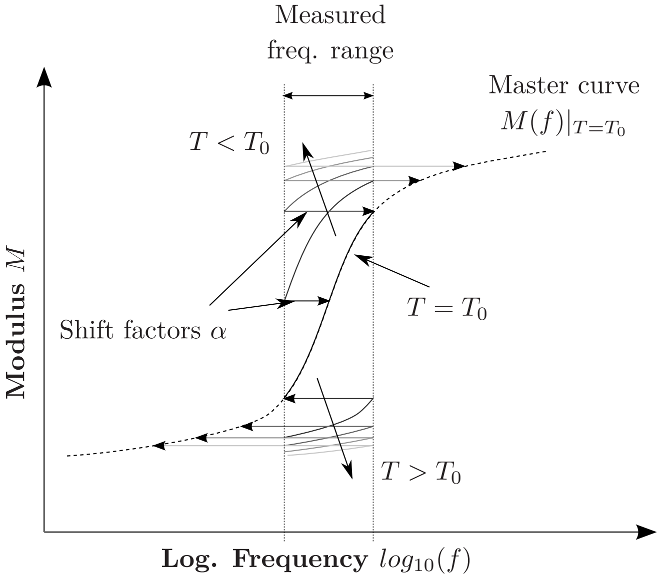

Figure C.3.: Schematic illustration of the generation of master curves from DMA testings at different temperatures [251].

Thus, in order to retrieve the mechanical properties of viscoelastic materials in a large frequency range the DMA testings have to be performed at different temperatures. The procedure of shifting the measurement curves and extracting the corresponding master curve as well as the discrete shift factors is usually performed by special software programs. In this thesis the software GABO Eplexor was used.

C.2. Prony Series

Assuming the stiffness and damping behavior of a material to be expressed by the complex modulus E^* and the frequency-dependency of the material properties to be represented by a generalized Maxwell model as given in Figure 2.9, the storage and loss modulus E' and E'' can be expressed by a Prony series as

$$E'(\omega) = E_\infty + \sum_j E_j \cdot \frac{(\omega\tau_j)^2}{1 + (\omega\tau_j)^2} \tag{C.1}$$

and

$$E''(\omega) = \sum_j E_j \cdot \frac{\omega\tau_j}{1+(\omega\tau_j)^2}, \tag{C.2}$$

respectively. Each of the single elements inside the PRONY series depends on two independent parameters, namely the relaxation time τ_j and the characteristic stiffness E_j. Using a curve fitting algorithm, the PRONY parameters τ_j and E_j can iteratively be quantified.

C.2.1. Identification of Prony Parameters

In this thesis the LSQNONLIN function which is an integrated MATLAB function was used to identify PRONY parameters that provide an optimal approximation of the measured data. The LSQNONLIN function is frequently applied for curve fitting problems with nonlinear regression. It is based on the least-squares method with

$$\min_x \|f(x)\|_2^2 = \min_x \left(f_1(x)^2 + f_2(x)^2 + \ldots + f_n(x)^2\right). \tag{C.3}$$

Thus, an objective function has to be formulated that can be minimized by the given MATLAB function. The number of relaxation times is typically chosen between 1 and 2 per frequency decade citebrinson2008. Due to the large frequency range of the measurement data, especially for Resin 1, the number of relaxation times will be set to 1 per frequency decade in this thesis. Thus for Resin 1 32 and for Resin 2 13 relaxation times were considered. Since each PRONY parameter influences both, the storage modulus and the loss modulus, both moduli have to be taken into account finding the optimal PRONY parameters. If the absolute errors of both moduli were equally weighted inside the objective function the relative error of the loss modulus would be much higher than the error of the storage modulus since the loss modulus is typically much smaller. This would significantly influence the damping value of the material which is proportional to the quotient of loss and storage modulus. However, if the relative error of each modulus were considered in the objective function the absolute error of the storage modulus and hence the stiffness of the material would significantly increase. Thus, numerous variations of objective functions are conceivable. The problem of formulating an appropriate objective function which satisfies both, the damping and the stiffness properties, has been addressed in multiple publications [124].

In this thesis, the curve fitting was divided into two steps with two individual objective functions. Both steps intended to provide optimal values of the PRONY parameters E_j and τ_j for the corresponding PRONY series to ideally approximate the experimental master curves of Resin 1 and Resin 2.

C.2.2. Objective Function for the Stiffness Representation

The first objective function exclusively took into account the absolute difference between the measured storage modulus $E'_m(\omega)$ and the approximated storage modulus obtained from the PRONY series (see Equation C.1)

$$f(\omega) = E'_m(\omega) - \underbrace{\left(E_\infty + \sum_j E_j \cdot \frac{(\omega\tau_j)^2}{1+(\omega\tau_j)^2}\right)}_{\text{Analytical storage modulus}}. \tag{C.4}$$

As starting values of the curve fitting process the relaxation times τ_j were set to multiples of 10 yielding one relaxation time per decade and the characteristic stiffness values E_j were set to 1.

C.2.3. Objective Function for the Damping Representation

In contrast to the first objective function, the one involved the absolute difference between the measured loss modulus $E'_m(\omega)$ and the approximated loss modulus obtained from the Prony series (see Equation C.2).

$$f(\omega) = E''_m(\omega) - \underbrace{\left(\sum_j E_j \cdot \frac{\omega\tau_j}{1 + (\omega\tau_j)^2} \right)}_{\text{Analytical loss modulus}} . \tag{C.5}$$

As starting values the outcome values of E_j and τ_j of the first optimization were employed. The second optimization intended to provide improved values of the Prony parameters in order to not only match the frequency-dependent stiffness but also the loss factor of the given resin type.

C.2.4. Analytical Approximations for Resin 1 and 2

In Figure C.4 and C.5 the results of the curve fitting are shown for Resin 1 and Resin 2. In either figure two analytical curves are compared to the measured Young's storage modulus in the upper part and the loss factor in the lower part. The first analytical curve corresponds to the values of the Prony parameters after the first optimization routine. Consequently, the second curve corresponds to the values of the Prony parameters after the second optimization routine. The results show, that the first optimization routine yields parameters that provide a good approximation for the storage modulus but more or less neglect the damping while the second optimization routine generates parameters that lead to a better approximation of the damping but increase the error for the storage modulus. Depending on which material property is more important for the structural behavior one can choose one or the other. For Resin 1 the second optimization routine significantly increases the error regarding the storage modulus while the increase of accuracy of the damping is negligible. Thus, for Resin 1 the set of Prony parameters that correspond to the first optimization were employed. In contrast, for Resin 2 the second optimization increases the accuracy of the damping especially for lower frequencies while the storage modulus only slightly changes. Thus, for Resin 2 the second set of Prony parameters was employed throughout this thesis.

C.3. Analytical Poisson Ratio

The complex Poisson ratio of viscoelastic materials can be derived from the complex Young's modulus E^* and the complex shear modulus G^* following Equation 3.1. However, the determination of the Poisson ratio based on the complex shear and Young's modulus is very sensitive towards errors of the Dynamic-Mechanical-Analysis (DMA) (see Section 2.4.3). In order to avoid numerical instabilities caused by erroneous values of the Poisson ratio, Göhler proposed a procedure which deduces a synthetic, numerically stable Poisson ratio from the originally measured Poisson ratio [141]. The ansatz function is given in Equation 2.63. Assuming the complex Poisson ratio ν^* to be purely real Göhler expressed the frequency-dependent Poisson ratio by a sigmoid function involving two independent variables b and m as well as the rubbery and glassy Poisson ratio, ν_0 and ν_∞, respectively.

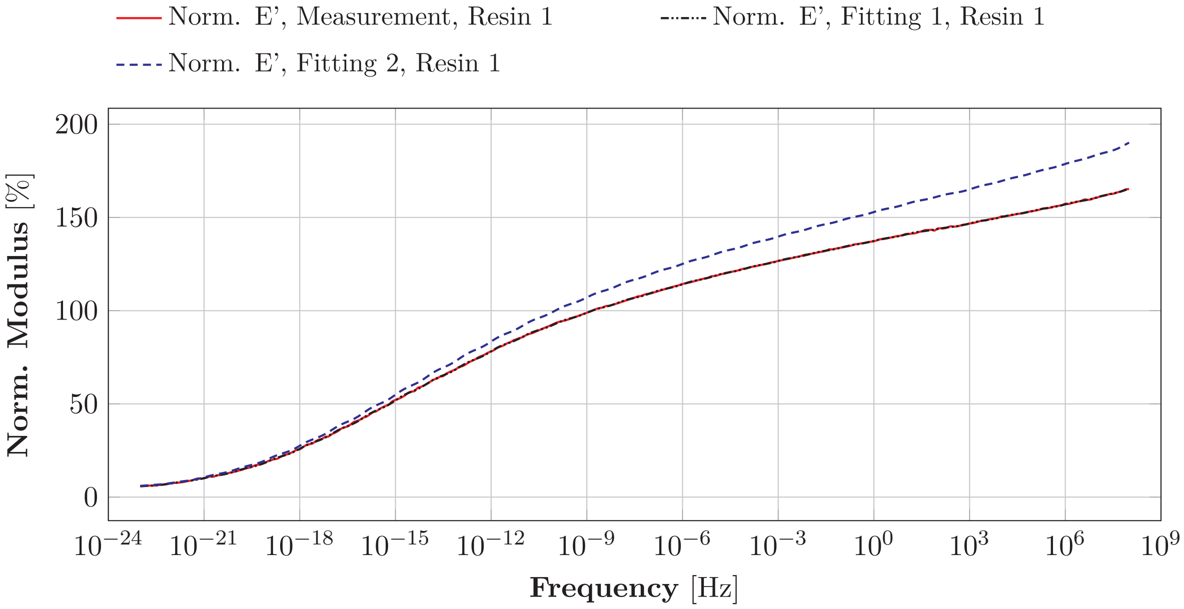

(a) Young's modulus.

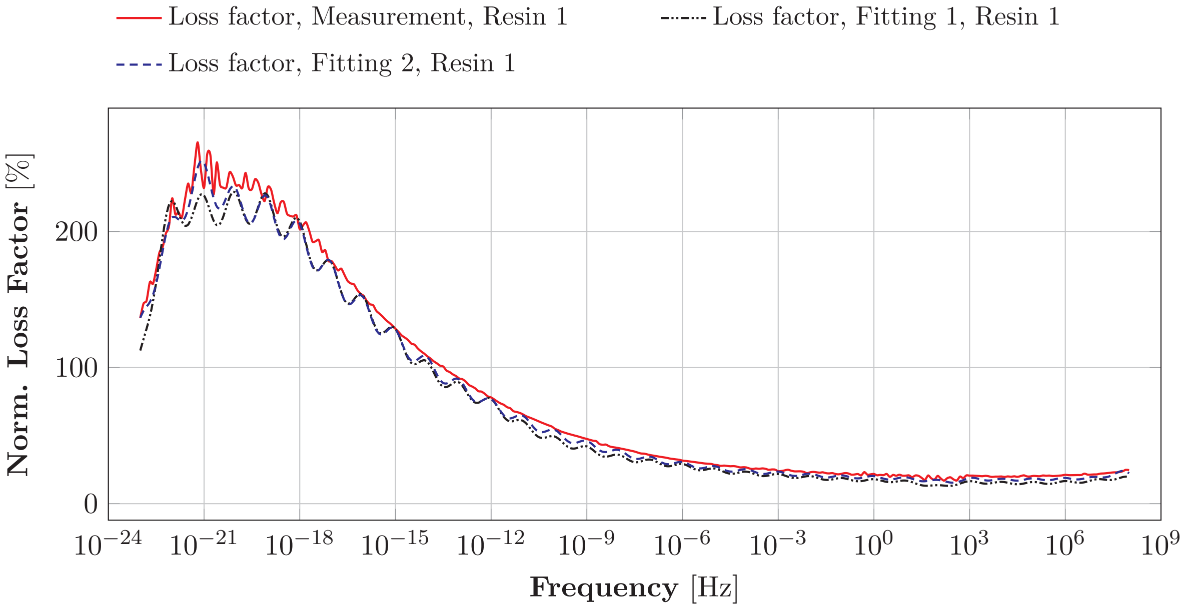

(b) Loss factor.

Figure C.4.: Comparison between the measured and analytically approximated normalized Young's storage modulus and loss factor of Resin 1 at $T_0 = 0°\text{C}$.

Presuming the rubbery and glassy Poisson ratio of the two different impregnation resins, Resin 1 and Resin 2 from Section 3.1 to be known the two variables b and m can be obtained from curve fitting with the experimental data of each resin.

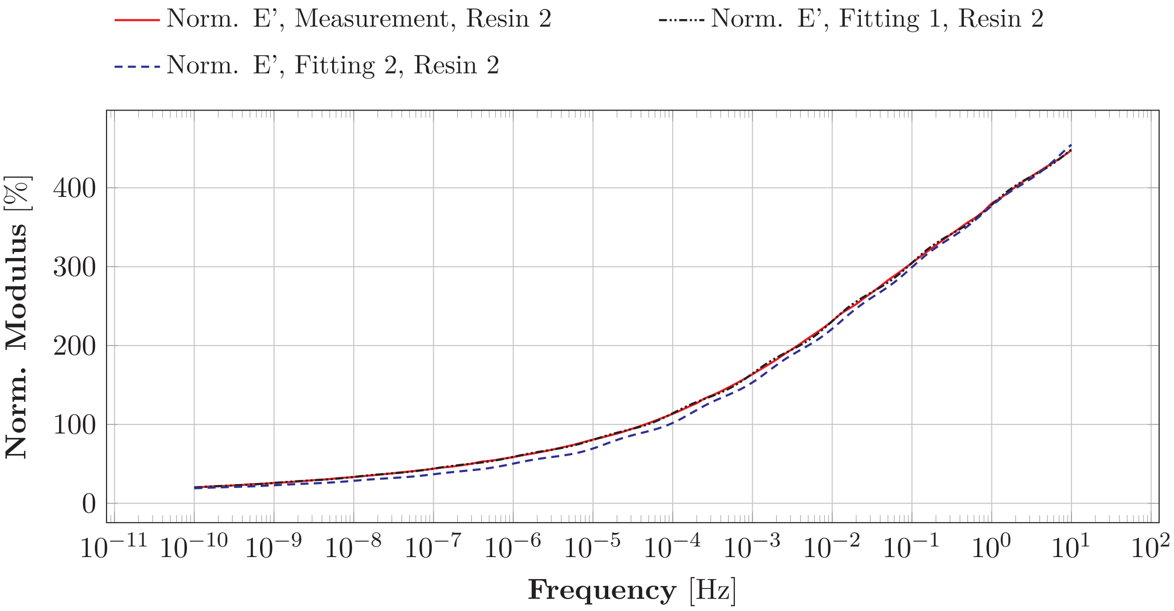

(a) Young's modulus.

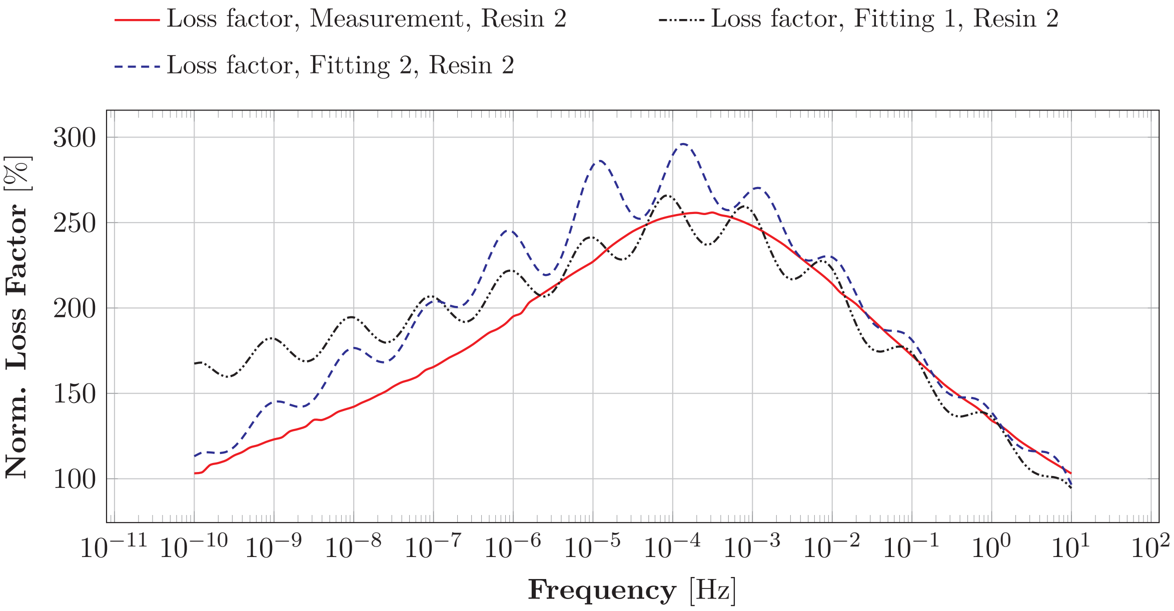

(b) Loss factor.

Figure C.5.: Comparison between the measured and analytically approximated normalized Young's storage modulus and loss factor of Resin 1 at $T_0 = 0°\mathrm{C}$.

The corresponding objective function was given as

$$f(\omega) = \nu'_m(\omega) - \underbrace{\left(\nu_\infty + \frac{\nu_0 - \nu_\infty}{1 + exp\left(10 \cdot \frac{log_{10}(\omega) - b}{m}\right)} \right)}_{\text{Sigmoid ansatz function}} . \tag{C.6}$$

with $\nu'_m(\omega)$ as the storage Poisson ratio obtained from the measured Young's and shear storage moduli E^* and G^*, respectively (see Figure 3.3).

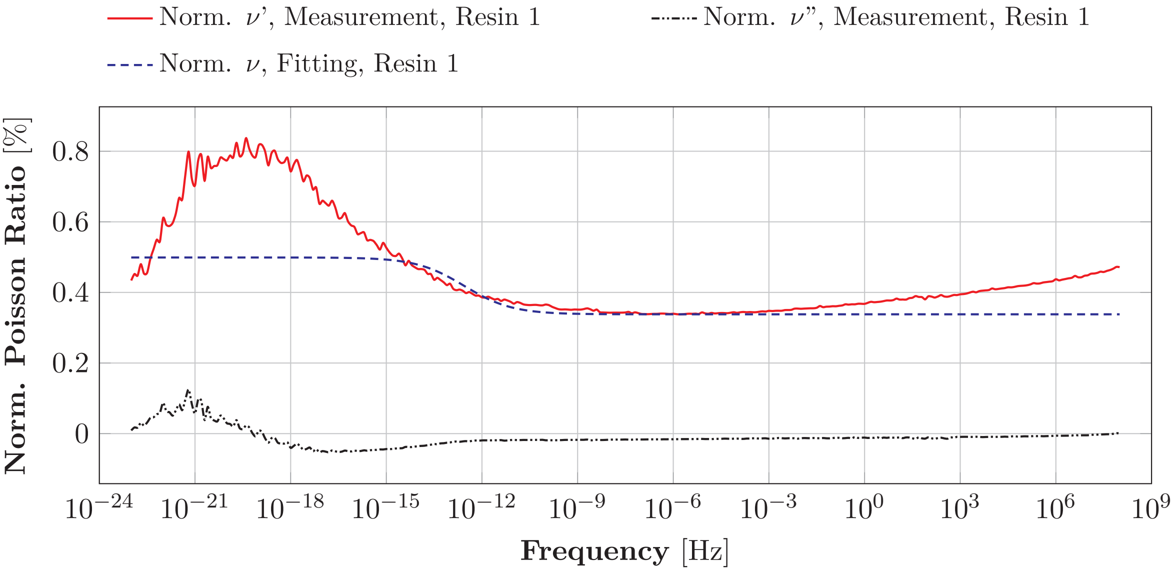

(a) Resin 1.

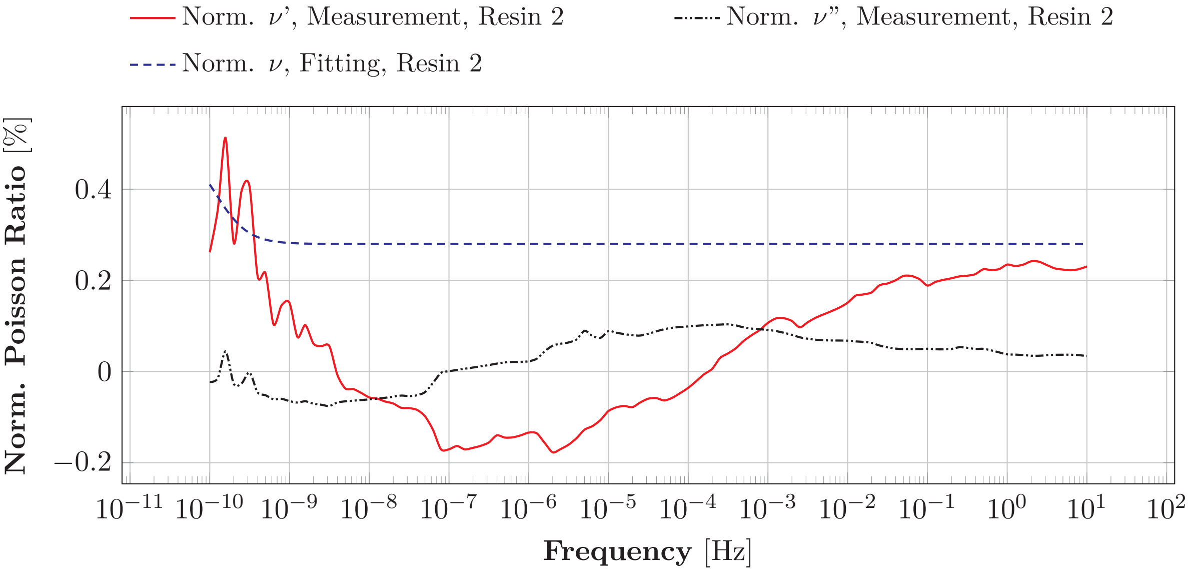

(b) Resin 2.

Figure C.6.: Comparison between the measured and analytically approximated Poisson ratio of Resin 1 and Resin 2 at $T_0 = 0$°C.

In Figure C.6 the curves of the analytical POISSON ratio are compared to the curves of the measured POISSON ratio for both resin type. The difference between the measured and the analytical POISSON ratios is significant for both resin types. However, the measured POISSON ratio curves of both resin types show physical implausibilities and thus were substituted by the analytical approximations throughout this thesis.

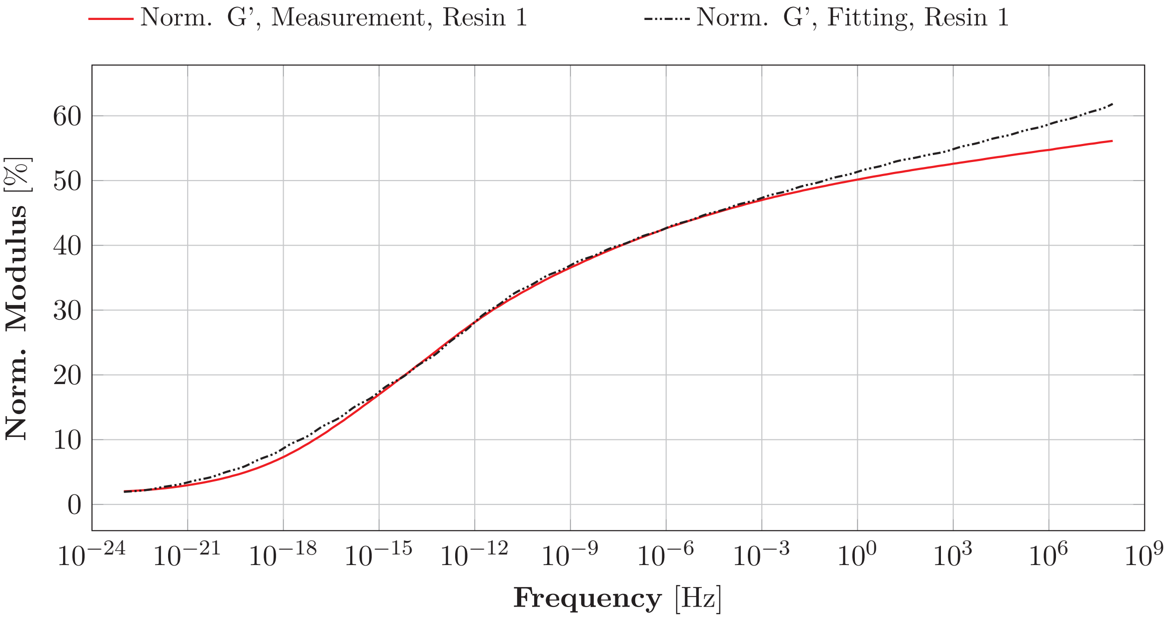

(a) Shear modulus.

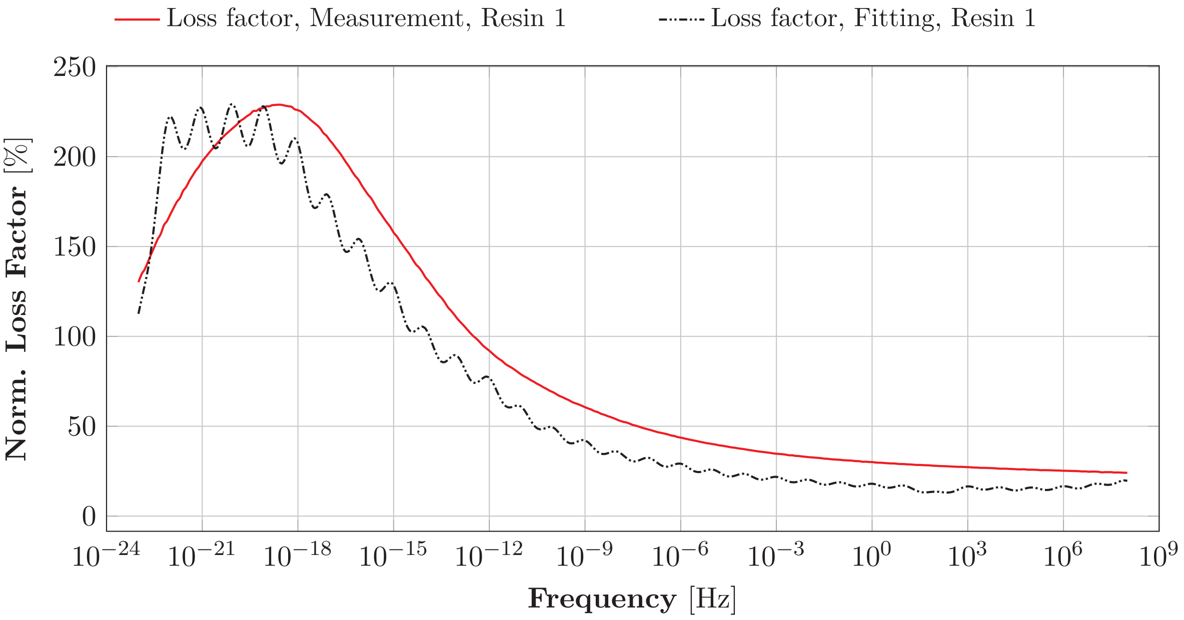

(b) Loss factor.

Figure C.7.: Comparison between the measured and analytically approximated normalized shear storage modulus and loss factor of Resin 1 at $T_0 = 0°\text{C}$.

The corresponding shear moduli and shear damping ratios which arise from the analytical Poisson ratios and the Prony approximations of the Young's moduli given in Figure C.4 and C.5 are illustrated and compared to the measured shear moduli from the DMA in Figure C.7 and C.8.

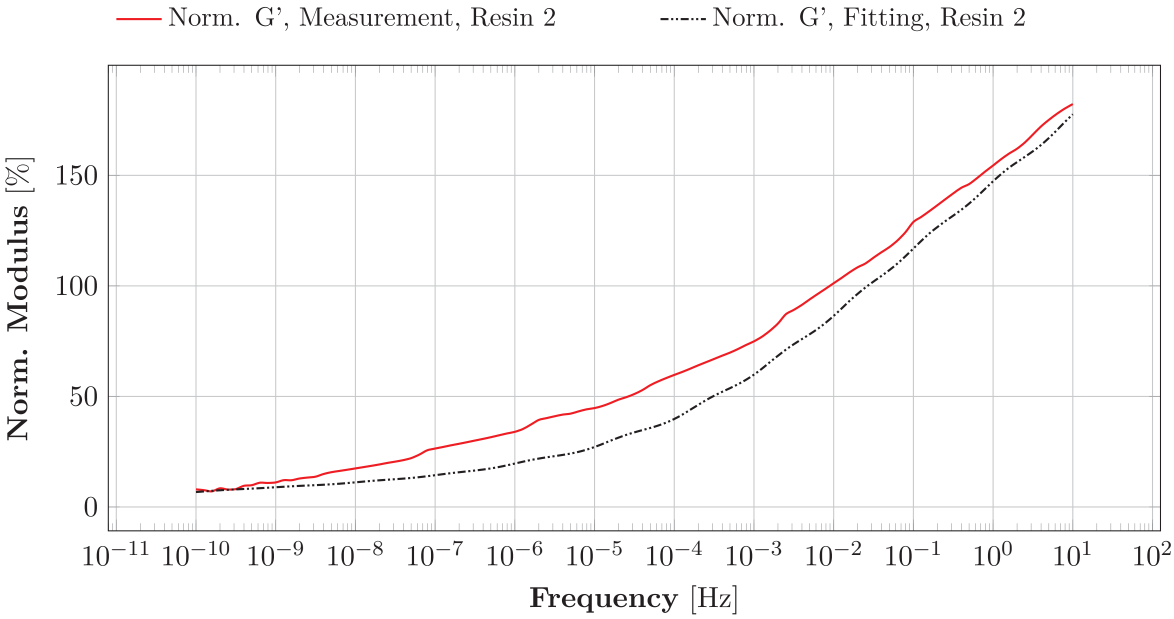

(a) Shear modulus.

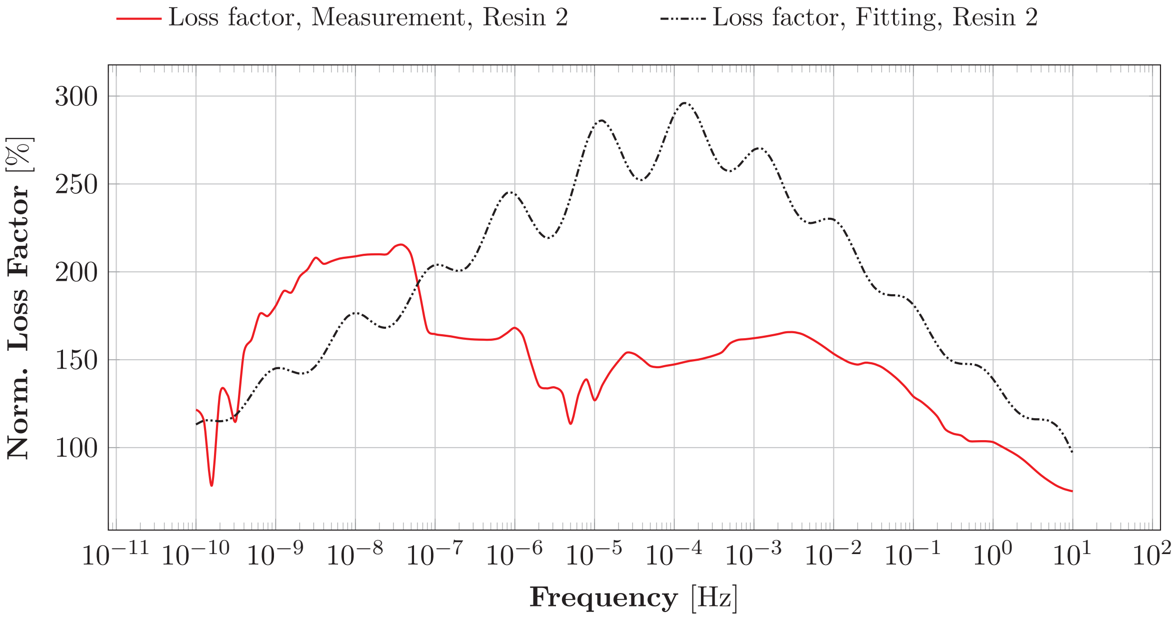

(b) Loss factor.

Figure C.8.: Comparison between the measured and analytically approximated normalized shear storage modulus and loss factor of Resin 2 at $T_0 = 0$°C.

D. Reproducibility of Laminated Steel Specimen

In Section 3.3.1 a generic laminated steel specimen was introduced. Three kinds of steel specimens were build for two different steel sheet thicknesses, 0.2 mm and 0.3 mm. All specimens were subjected to a normal prestress of 3.6 MPa. In order to validate the reproducibility of the dynamic behavior of the laminated steel specimen an experimental modal analysis was performed on all three given specimens of both kinds of sheet thicknesses.

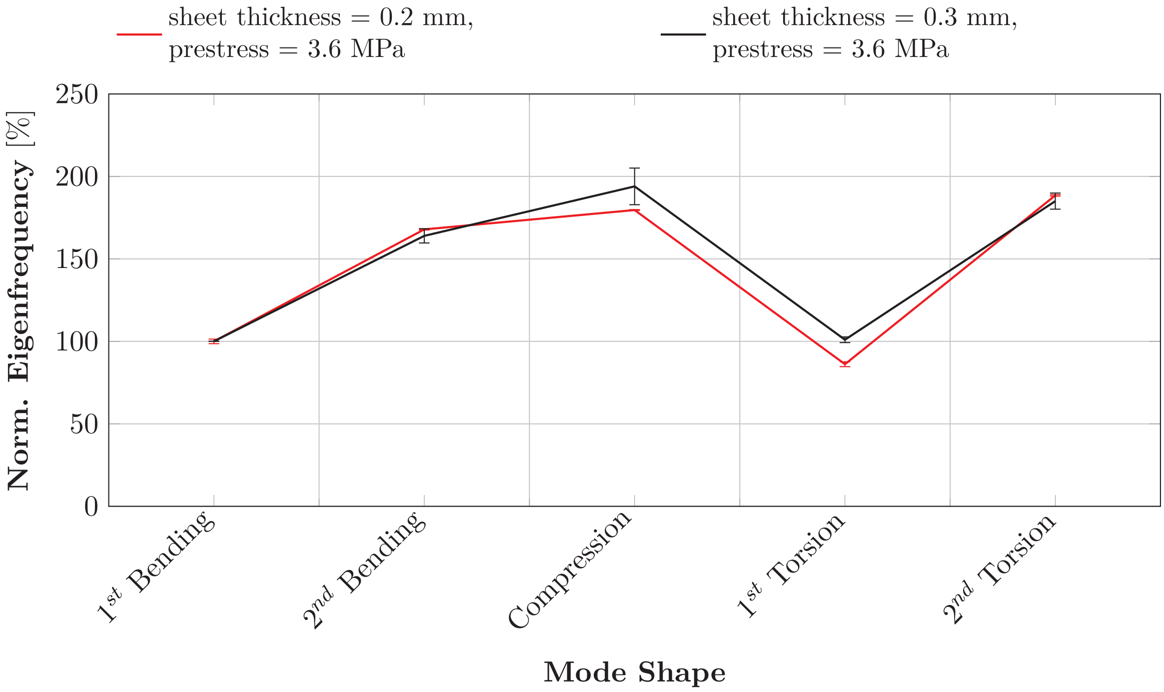

Figure D.1.: Normalized eigenfrequencies and standard deviations of the 0.2 mm and the 0.3 mm laminated steel specimens.

In Figure D.1 the measured eigenfrequencies of the 0.2 mm and the 0.3 mm lamination stack as well as the standard deviation are given. Table D.1 gives an overview of the normalized results of the different measurements. While the 0.2 mm-stacks show a small standard deviation and thus good reproducibility, the standard deviation of the 0.3 mm-stacks is large. Some mode shapes could not even be identified (see Table D.1). The reproducibility of the 0.3 mm-stack is thus limited. The large deviation might be due to undulations that were also identified during the assembly of the 0.3 mm-specimens. Due to the low reproducibility the 0.3 mm-stack was not further investigated during this research work.

Table D.1.: Normalized eigenfrequency results and corresponding mode shapes of laminated specimens.

Specimen	**Steel Sheet Thickness** [mm]	**Bend. 1** [%]	**Bend. 2** [%]	**Compr.** [%]	**Tors. 1** [%]	**Tors. 2** [%]
1	0.2	101.7	164.7	184.4	91.7	185.5
2	0.2	99.9	165.3	184.6	94.6	185.8
3	0.2	98.4	165.6	185.0	n.i.	186.5
4	0.3	100.0	169.9	205.0	99.2	191.8
5	0.3	n.i.	161.1	n.i.	102.7	181.5
6	0.3	n.i.	160.6	182.9	n.i.	181.7

Nomenclature

Greek Characters

Character	Denotation	Unit
α_r	Rayleigh coefficient of mass	1/s
α_T	Shift factor of TTSP	
β_r	Rayleigh coefficient of stiffness	s
β	Vertical subcell coordinate	
γ	Horizontal subcell coordinate	
χ	Filling/Stacking factor	
δ_{ij}	Kronecker-Delta	
ϵ	Relative Error	
ε	Mechanical strain	
ε^0	Homogeneous mechanical strain	
ϕ	Modal vector	
φ	Phase shift	$^\circ$
η	Loss factor	
λ	Eigen value	
μ	Permeability	$\mathrm{V \cdot s / A \cdot m}$
μ_0	Vacuum permeability	$\mathrm{V \cdot s / A \cdot m}$
ν	POISSON ratio	
π	Circular number	
θ	Tangential coordinate	rad
ρ	Density	$\mathrm{kg/m^3}$
ρ_a	Density of air	$\mathrm{kg/m^3}$
σ	Mechanical stress	Pa
σ^0	Homogeneous mechanical stress	Pa
σ_A	Acoustic radiation loss factor	

Character	**Denotation**	**Unit**
ς	Empirical parameter (Halpin-Tsai)	
τ	Time constant of Prony element	s
ω	Angular velocity	1/s
ω_i	Eigen angular frequency	1/s
ω_r	Pseudo-eigen-angular-frequency	1/s
ξ_i	Modal damping ratio	
ζ	Damping ratio	
Π	Sound power	W
Π_0	Sound power at machine surface	W
Φ	Modal subspace	
Ω	Eigen angular frequency matrix	1/s

Latin Characters

Character	**Denotation**	**Unit**
A	Surface area	m^2
B, b	Magnetic flux density	T
C, c	Damping coefficient	Ns/m
C_1	WLF constant	
C_2	WLF constant	K
c_a	Sound velocity of air	m/s
E	Young's modulus	Pa
F, f	Excitation force	N
$F_{c,h}$	Hysteretic damping force	N
$F_{c,v}$	Viscous damping force	N
G	Shear modulus	Pa
H	Structural transfer function	
h, l	Measures of subcell	m
h_t	Structural transfer admittance	m/s N
I	Identity matrix	

Character	**Denotation**	**Unit**
i	Imaginary unit	
K, k	Stiffness coefficient	N/m
M, m	Mass coefficient	kg
n	Number of DOFs	
n_p	Number of poles	
P	Sound power	W
p_i	Pole of transfer function	
p	Order of reduced system	
r	Circumferential space harmonic	
x, y, z	Cartesian coordinates	m
x_a	Arc length of rot. symmetry	m
x_m	Master DOF	m
x_s	Slave DOF	
s	Laplace parameter	
s_0	Expansion point	
t	Time	s
u	Displacement	m
v	Surface velocity	m/s
v_{eff}	RMS value of surface velocity	m/s
T	Temperature	K
T_0	Reference temperature	K
V	Volume	m^3
W_k	Stain energy	J
X	Transformation/Projection matrix	
z_i	Zero of transfer function	
$\Re$	Real part	
$\Im$	Imaginary part	

Matrix, Vector and Scalar Denotations

Subscript	Denotation
$\underline{\underline{\mathrm{K}}}$	Matrices
$\underline{\mathrm{k}}$	Vectors
k	Scalars

Cylindrical Mode Shape Denotations

X.Y	Mode Shape
X	Circumferential Spatial Order
Y	Axial Spatial Order

Complex Stiffness Values

Superscript	Denotation
M	Real modulus
$M*$	Complex modulus
M'	Storage modulus
M''	Loss modulus

Coordinate Systems

Coord.	Fib.-reinf. Mat.	Laminations	Cylindrical Systems
x	Perp. to dir. of fiber	Perp. to staple dir.	Radial direction
y	Perp. to dir. of fiber	Perp. to staple dir.	Tangential direction
z	Fiber direction	Staple direction	Axial direction

List of Abbreviations

Abbriviation	**Denotation**
BEM	Boundary element method
CMS	Component mode synthesis
DMA	Dynamic mechanical analysis
DOF	Degree-of-freedom
e.g.	For example
EO	Engine order
ERP	Equivalent radiated power
FEM	Finite element method
FRF	Frequency response function
IPM	Internal permanent magnet machine
LSV	Laser scanning vibrometer
MOC	Method of cells
MTAM	Modal truncation augmentation method
Norm.	Normalized
ODE	Ordinary differential equation
OEM	Original equipment manufacturer
OMTM	Ordinary modal truncation method
RMS	Root mean square
RUC	Repeating unit cell
RVE	Representative volume element
TTSP	Time-temperature superposition principle
WLF	WILLIAMS-LANDEL-FERRY

Bibliography

[1] A. Semuels. The future will be quiet. *The Atlantic*, 04/2016.

[2] T. Gara. The silence of electric cars: our national nightmare is almost over. *The Wall Street Journal*, 01/07/2013.

[3] T. Zeller. The silence of hybrids causes some alarm. *The New York Times*, 07/12/2009.

[4] P. Whoriskey. The deadly silence of the electric car. *Washington Post*, 09/23/2009.

[5] H. Jordan. Approximate calculation of the noise produced by squirrel cage motors. *Engineers: Digest*, 10:222, 1949.

[6] J. F. Gieras, C. H. Wang, and J. Cho Lai. *Noise of polyphase electric machines*. CRS Press Taylor & Francis Group USA, 2006.

[7] P. L. Timár, A. Fazekas, J. Kiss, A. Miklós, and S. J. Yang. *Noise and vibration of electrical machines*, volume 34. North Holland, 1989.

[8] S. J. Yang. Low noise electric motors. *IEEE Monographs in Electrical and Electronic Engineering*, pages 4–5, 1981.

[9] F. G. Kollmann. *Maschinenakustik: Grundlagen, Meßtechnik, Berechnung, Beeinflussung*. Springer-Verlag, 2011.

[10] S. P. Verma. Vibration behaviour of short laminated stators of electrical machines and validity of simplified frequency equation. In *4th International Conference on Electrical Machines and Drives*, pages 220–225. IET, 1989.

[11] S. P. Verma, K. Williams, and R. K. Singal. Vibrations of long and short laminated stators of electrical machines Part I: Theory, experimental models, procedure and set-up. *Journal of Sound and Vibration*, 129(1):1–13, 1989.

[12] K. Williams, R. K. Singal, and S. P. Verma. Vibrations of long and short laminated stators of electrical machines Part II: Results for long stators. *Journal of Sound and Vibration*, 129(1):15–29, 1989.

[13] R. K. Singal, S. P. Verma, and K. Williams. Vibrations of long and short laminated stators of electrical machines Part III: Results for short stators and validity of simplified frequency equation. *Journal of Sound and Vibration*, 129(1):31–44, 1989.

[14] R. K. Singal, K. Williams, and S. P. Verma. Theoretical and experimental study of vibrational behaviour of laminated stators of electrical machines. *Mechanical Systems and Signal Processing*, 6(6):535–549, 1992.

[15] C. Grabner and I. Hajdarevic. Analytical and numerical approaches for the prediction of resonance frequencies of a switched reluctance machine. In *Second International Conference on Power Electronics, Machines and Drives(PEMD 2004)*, volume 1, pages 392–397. IET, 2004.

[16] C. Yongxiao, W. Jianhua, and H. Jun. Analytical calculation of natural frequencies of stator of switched reluctance motor. In *IEEE conference publication*, pages 81–85. Institution of Electrical Engineers, 1997.

[17] S. Vivier, A. Ait-Hammouda, M. Hecquet, B. Napame, P. Brochet, and A. Randria. Vibro-acoustic optimization of a permanent magnet synchronous machine using the experimental design method. In *Recent Developments of Electrical Drives*, pages 101–114. Springer, 2006.

[18] R. Islam and I. Husain. Analytical model for predicting noise and vibration in permanent-magnet synchronous motors. *IEEE Transactions on Industry Applications*, 46(6):2346–2354, 2010.

[19] D. Braunisch, B. Ponick, and G. Bramerdorfer. Combined analytical-numerical noise calculation of electrical machines considering nonsinusoidal mode shapes. *IEEE Transactions on Magnetics*, 49(4):1407–1415, 2013.

[20] D. Franck, M. van der Giet, and K. Hameyer. Towards low audible noise drives for FEV applications. In *14th International Conference of Power Electronics and Motion Control Conference (EPE/PEMC)*, pages 11–25. IEEE.

[21] M. van der Giet and K. Hameyer. Identification of homogenized equivalent materials for the modal analysis of composite structures in electrical machines. *IMechE*, 1:437–448, 2008.

[22] M. Boesing, T. Schoenen, K. A. Kasper, and R. W. De Doncker. Vibration synthesis for electrical machines based on force response superposition. *IEEE Transactions on Magnetics*, 46(8):2986–2989, 2010.

[23] M. Boesing and R. W. De Doncker. Exploring a vibration synthesis process for the acoustic characterization of electric drives. *IEEE Transactions on Industry Applications*, 48(1):70–78, 2012.

[24] M. Boesing, A. Hofmann, and R. W. De Doncker. Universal acoustic modeling framework for electrical drives. In *7th IET International Conference on Power Electronics, Machines and Drives (PEMD 2014)*, pages 1–6. IET, 2014.

[25] K Delaere, A. P. Tenhunen, W. Heylen, K. Hameyer, and R. Belmans. Predicting the stator vibration spectrum of induction machines under normal operation. In *INTER-NOISE*, volume 3, pages 1719–1724. New Zealand Acoustical Society; 1998, 1999.

[26] C. G. C. Neves, R. Carlson, N. Sadowski, J. P. A. Bastos, and N. S. Soeiro. Forced vibrations calculation in a switched reluctance motor taking into account the viscous damping. In *International Conference on Electric Machines and Drives (IEMD'99)*, pages 110–112. IEEE, 1999.

[27] Z. Yang, M. Krishnamurthy, and I. P. Brown. Electromagnetic and vibrational characteristic of IPM over full torque-speed range. In *IEEE International Conference of Electric Machines & Drives Conference (IEMDC)*, pages 295–302. IEEE, 2013.

[28] C. K. Maliti. *Modelling and analysis of magnetic noise in squirrel-cage induction motors.* PhD thesis, KTH, Department of Electrical Power Engineering, School of Electrical Engineering, 2000.

[29] K. Hameyer, F. Henrotte, and K. Delaere. Electromagnetically excited audible noise in electrical machines. *IEEE Transactions on Magnetics*, 13:109–118, 2003.

[30] R Lach. *Magnetische Geräuschemission umrichtergespeister Käfigläufer-Asynchronmaschinen.* PhD thesis, Universität Dortmund, 2005.

[31] J. Le Besnerais, V. Lanfranchi, M. Hecquet, P. Brochet, and G. Friedrich. Prediction of audible magnetic noise radiated by adjustable-speed drive induction machines. *IEEE Transactions on Industry Applications*, 46(4):1367–1373, 2010.

[32] S. A. Long, Z. Q. Zhu, and D. Howe. Vibration behaviour of stators of switched reluctance motors. In *IEEE Proceedings - Electric Power Applications*, volume 148, pages 257–264. IET, 2001.

[33] X. Li, S. Huang, Q. Zhang, and Y. Dai. Electromagnetic noise assessment for EV's PM driving machines. In *17th International Conference on Electrical Machines and Systems (ICEMS)*, pages 1552–1555. IEEE, 2014.

[34] I. Ramesohl, G. Henneberger, S. Küppers, and W. Hadrys. Three dimensional calculation of magnetic forces and displacements of a claw-pole generator. *IEEE Transactions on Magnetics*, 32(3):1685–1688, 1996.

[35] I. Ramesohl, C. Kaehler, and G. Henneberger. Influencing factors on acoustical simulations including manufacturing tolerances and numerical strategies. In *9th International Conference on Electrical Machines and Drives*, pages 142–146. IET, 1999.

[36] S. Sakamoto, T. Hirata, T. Kobayashi, and K. Kajiwara. Vibration analysis considering higher harmonics of electromagnetic forces for rotating electric machines. *IEEE Transactions on Magnetics*, 35(3):1662–1665, 1999.

[37] J.-B. Dupont, P. Bouvet, and L. Humbert. Vibroacoustic simulation of an electric motor: Methodology and focus on the structural FEM representativity. In *20th International Conference on Electrical Machines (ICEM)*, pages 3027–3033. IEEE, 2012.

[38] M. Mair, B. Weilharter, S. Rainer, K. Ellermann, and O. Bíró. Numerical and experimental investigation of the structural characteristics of stator core stacks. *COMPEL: The International Journal for Computation and Mathematics in Electrical and Electronic Engineering*, 32(5):1643–1664, 2013.

[39] R. S. Colby, F. M. Mottier, and T. J. E. Miller. Vibration modes and acoustic noise in a four-phase switched reluctance motor. *IEEE Transactions on Industry Applications*, 32(6):1357–1364, 1996.

[40] Y. Tang. Characterization, numerical analysis and design of switched reluctance motor for improved material productivity and reduced noise. In *Industry Applications Conference*, volume 2, pages 715–722. IEEE, 1996.

[41] J. Mahn, D. Williams, P. Wung, G. Horst, J. Lloyd, and S. Randall. A systematic approach toward studying noise and vibration in switched reluctance machines: Preliminary results. In *Industry Applications Conference*, volume 2, pages 779–785. IEEE, 1996.

[42] E. Erdelyi and G. Horvay. Vibration modes of stators of induction motors. *ASME Transactions*, 24:30–45, 1957.

[43] C. Picod, M. Besbes, M. Gabs, and E. Pelle. Study of the vibratory behaviour of synchronous motors. In *International Conference on Electric Machines and Drives (IEMD'99)*, pages 153–155. IEEE, 1999.

[44] M. Boesing, K. A. Kasper, and R. W. De Doncker. Vibration excitation in an electric traction motor for a hybrid electric vehicle. In *INTER-NOISE and NOISE-CON Congress and Conference Proceedings*, volume 2008, pages 2451–2562. Institute of Noise Control Engineering, 2008.

[45] P. Sunghyuk, K. Wonho, and K. Sung-Il. A numerical prediction model for vibration and noise of axial flux motors. *IEEE Transactions on Industrial Electronics*, 61(10):5757–5762, 2014.

[46] F. L. M. Dos Santos, J. Anthonis, F. Naclerio, J. J. C. Gyselinck, H. Van der Auweraer, and L. Goes. Multiphysics NVH modeling: Simulation of a switched reluctance motor for an electric vehicle. *IEEE Transactions on Industrial Electronics*, 61(1):469–476, 2014.

[47] W. Cai, P. Pillay, and Z. Tang. Impact of stator windings and end-bells on resonant frequencies and mode shapes of switched reluctance motors. *IEEE Transactions on Industry Applications*, 38(4):1027–1036, 2002.

[48] T. Ishikawa. *Analysis of natural frequency, radial force and vibration of induction motors fed by PWM inverter*. INTECH Open Access Publisher, 2012.

[49] S. P. Verma and R. S. Girgis. Experimental verification of resonant frequencies and vibration behaviour of stators of electrical machines. Part 1: Models, experimental procedure and apparatus. *IEEE Proceedings B: Electric Power Applications*, 128(1):12–21, 1981.

[50] S. Watanabe, S. Kenjo, K. Ide, F. Sato, and M. Yamamoto. Natural frequencies and vibration behaviour of motor stators. *IEEE Transactions on Power Apparatus and Systems*, (4):949–956, 1983.

[51] B. Weilharter, M. Mair, H. Lang, K. Ellermann, and O. Bíró. Experimental investigation of the vibration behaviour of a laminated stack with winding. In *39th Annual Conference of the IEEE Industrial Electronics Society (IECON)*, pages 2816–2820. IEEE, 2013.

[52] Z. Fengge, T. Ningze, and W. Fengxiang. Analysis of vibration modes for large induction motor. In *Proceedings of the 8th International Conference on Electrical Machines and Systems (ICEMS 2005)*, volume 1, pages 64–67. IEEE, 2005.

[53] R Nitzsche. *Elektromagnetisch erzwungene und Eigenschwingungen des Statorgehäuses eines zweipoligen Turbogenerators*. PhD thesis, Fachbereich Elektrotechnik und Informationstechnik der Universität Hannover, 1998.

[54] C. Wang and J. C. S. Lai. Vibration analysis of an induction motor. *Journal of Sound and Vibration*, 224(4):733–756, 1999.

[55] R. K. Singal, K. Williams, and S. P. Verma. The effect of windings, frame and impregnation upon the resonant frequencies and vibrational behavior of an electrical machine stator. *Experimental Mechanics*, 30(3):270–280, 1990.

[56] M. van der Giet. *Analysis of electromagnetic acoustic noise excitations: A contribution to low-noise design and to the auralization of electrical machines*. Shaker, 2011.

[57] J. Le Besnerais. *Reduction of magnetic noise in PWM-supplied induction machines-low-noise design rules and multi-objective optimisation*. PhD thesis, Ecole Centrale de Lille, 2008.

[58] K. H. Yim, J. W. Jang, G. H. Jang, M. G. Kim, and K. N. Kim. Forced vibration analysis of an IPM motor for electrical vehicles due to magnetic force. *IEEE Transactions on Magnetics*, 48(11):2981–2984, 2012.

[59] C. G. C. Neves, R. Carlson, N. Sadowski, J. P. A. Bastos, N. S. Soeiro, and S. N. Y. Gerges. Experimental and numerical analysis of induction motor vibrations. *IEEE Transactions on Magnetics*, 35(3):1314–1317, 1999.

[60] H. Zhang, R. Gao, J. Zhang, and L. Wang. Vibration analysis for switched reluctance motor system based on finite element and FFT. In *International Conference on Mechatronics and Automation (ICMA 2009)*, pages 4257–4261. IEEE, 2009.

[61] D. Torregrossa, F. Peyraut, B. Fahimi, J. M'Boua, and A. Miraoui. Multiphysics finite-element modeling for vibration and acoustic analysis of permanent magnet synchronous machine. *IEEE Transactions on Energy Conversion*, 26(2):490–500, 2011.

[62] M. van der Giet, M. Müller-Trapet, P. Dietrich, M. Pollow, J. Blum, K. Hameyer, and M. Vorländer. Comparison of acoustic single-value parameters for the design process of electrical machines. In *39th International Congress on Noise Control Engineering INTER-NOISE*, pages 1–7, 2010.

[63] K. A. Kasper. *Analysis and control of the acoustic behavior of switched reluctance drives*. Shaker, 2010.

[64] D.-C. Liu, H.-L. Chung, and W.-M. Chang. Errors caused by modal truncation in structure dynamic analysis. In *Proceedings of the International Modal Analysis Conference (IMAC)*, volume 2, pages 1455–1460, 2000.

[65] J. M. Dickens, J. M. Nakagawa, and M. J. Wittbrodt. A critique of mode acceleration and modal truncation augmentation methods for modal response analysis. *Computers & Structures*, 62(6):985–998, 1997.

[66] A. Kampker, D. Vallée, and A. Schnettler. *Elektromobilität: Grundlagen einer Zukunftstechnologie*. Springer-Verlag, 2013.

[67] H.-H. Braess and U. Seiffert. *Vieweg Handbuch Kraftfahrzeugtechnik*. Springer-Verlag, 2011.

[68] J. F. Gieras. *Permanent magnet motor technology: design and applications*. CRC press, 2002.

[69] S. Huang, M. Aydin, and T. A. Lipo. Electromagnetic vibration and noise assessment for surface mounted PM machines. In *Power Engineering Society Summer Meeting*, volume 3, pages 1417–1426. IEEE, 2001.

[70] G. C. Stone, E. A. Boulter, I. Culbert, and H. Dhirani. *Electrical insulation for rotating machines: Design, evaluation, aging, testing, and repair*, volume 21. John Wiley & Sons, 2004.

[71] Z. Q. Zhu and D. Howe. Electrical machines and drives for electric, hybrid, and fuel cell vehicles. *Proceedings of the IEEE*, 95(4):746–765, 2007.

[72] S. Lakshmikanth, K. R. Natraj, and K. R. Rekha. Noise and vibration reduction in permanent magnet synchronous motors - a review. *International Journal of Electrical & Computer Engineering*, 2(3), 2012.

[73] S.-H. Lee, J.-P. Hong, S.-M. Hwang, W.-T. Lee, J.-Y. Lee, and Y.-K. Kim. Optimal design for noise reduction in interior permanent-magnet motor. *IEEE Transactions on Industry Applications*, 45(6):1954–1960, 2009.

[74] J. Li, X. G. Song, D. Choi, and Y. H. Cho. Research on reduction of vibration and acoustic noise in switched reluctance motors. In *8th International Symposium on Advanced Electromechanical Motion Systems & Electric Drives Joint Symposium (ELECTROMOTION 2009)*, pages 1–6. IEEE, 2009.

[75] K. N. Srinivas and R. Arumugam. Static and dynamic vibration analyses of switched reluctance motors including bearings, housing, rotor dynamics, and applied loads. *IEEE Transactions on Magnetics*, 40(4):1911–1919, 2004.

[76] T. H. Patel and A. K. Darpe. Vibration response of a cracked rotor in presence of rotor-stator rub. *Journal of Sound and Vibration*, 317(3):841–865, 2008.

[77] T. H. Patel and A. K. Darpe. Experimental investigations on vibration response of misaligned rotors. *Mechanical Systems and Signal Processing*, 23(7):2236–2252, 2009.

[78] P. Pellerey, V. Lanfranchi, and G. Friedrich. Numerical simulations of rotor dynamic eccentricity effects on synchronous machine vibrations for full run up. In *20th International Conference on Electrical Machines (ICEM)*, pages 3008–3014. IEEE, 2012.

[79] K. N. Srinivas and R. Arumugam. Analysis and characterization of switched reluctance motors: Part II. Flow, thermal, and vibration analyses. *IEEE Transactions on Magnetics*, 41(4):1321–1332, 2005.

[80] S. L. Nau. The influence of the skewed rotor slots on the magnetic noise of three-phase induction motors. In *8th International Conference on Electrical Machines and Drives*, pages 396–399. IET, 1997.

[81] H. Y. Kanaan, K. Al-Haddad, and G. Roy. Analysis of the electromechanical vibrations in induction motor drives due to the imperfections of the mechanical transmission system. *Mathematics and Computers in Simulation*, 63(3):421–433, 2003.

[82] I. Chindurza, D. G. Dorrell, and C. Cossar. Vibration analysis of a switched-reluctance machine with eccentric rotor. In *Second International Conference on Power Electronics, Machines and Drives (PEMD 2004)*, volume 2, pages 481–486. IET, 2004.

[83] D. Gerling. Comparison of different methods for calculating the air-gap field of induction motors. *Archiv für Elektrotechnik*, 77(2):101–106, 1994.

[84] R. J. Belmans, D. Verdyck, W. Geysen, and R. D. Findlay. Electro-mechanical analysis of the audible noise of an inverter-fed squirrel-cage induction motor. *IEEE Transactions on Industry Applications*, 27(3):539–544, 1991.

[85] W. Cai, P. Pillay, Z. Tang, and A. M. Omekanda. Low-vibration design of switched reluctance motors for automotive applications using modal analysis. *IEEE Transactions on Industry Applications*, 39(4):971–977, 2003.

[86] K. A. Kasper, M. Bösing, R. W. De Doncker, S. Fingerhuth, and M. Vorländer. Noise radiation of switched reluctance drives. In *7th International Conference on Power Electronics and Drive Systems (PEDS07)*, pages 967–973. IEEE, 2007.

[87] J. Li and Y. Cho. Investigation into reduction of vibration and acoustic noise in switched reluctance motors in radial force excitation and frame transfer function aspects. *IEEE Transactions on Magnetics*, 45(10):4664–4667, 2009.

[88] P. Vijayraghavan and R. Krishnan. Noise in electric machines: a review. In *Industry Applications Conference*, volume 1, pages 251–258. IEEE, 1998.

[89] S. D. Garvey, J. E. Penny, M. I. Friswell, and C. N. Glew. Modelling the vibrational behaviour of stator cores of electrical machines with a view to successfully predicting machine noise. In *IEEE Colloquium on Modeling the Performance of Electrical Machines*, pages 3–1. IET, 1997.

[90] S. D. Garvey and G. D. Le Flem. Tangential forces matter. In *9th International Conference on Electrical Machines and Drives*, pages 174–178. IET, 1999.

[91] F. Taegen and J. Kolbe. Elektromagnetisches Geräusch umrichtergespeister permanenterregter Synchronmaschinen. *Archiv für Elektrotechnik*, 74(4):289–295, 1991.

[92] J. J. C. Gyselinck, L. Vandevelde, and J. A. A. Melkebeek. Multi-slice FE modeling of electrical machines with skewed slots - the skew discretization error. *IEEE Transactions on Magnetics*, 37(5):3233–3237, 2001.

[93] G. Müller, K. Vogt, and B. Ponick. *Berechnung Elektrischer Maschinen*. John Wiley & Sons, 2012.

[94] P. Zeller. Handbuch Fahrzeugakustik. *Vieweg+ Teubner, GWV Fachverlage GmbH, Wiesbaden*, 2009.

[95] P. L. Alger. *The nature of induction machines*. Gordon and Breach, 1965.

[96] E. G. Williams. *Fourier acoustics: sound radiation and nearfield acoustical holography*. Academic press, 1999.

[97] Z. Q. Zhu and D. Howe. Improved methods for prediction of electromagnetic noise radiated by electrical machines. In *IEEE Proceedings - Electric Power Applications*, volume 141, pages 109–120. IET, 1994.

[98] H. Lee and R. Singh. Comparison of two analytical methods used to calculate sound radiation from radial vibration modes of a thick annular disk. *Journal of Sound and Vibration*, 285(4):1210–1216, 2005.

[99] C. Wang and J. C. S. Lai. The sound radiation efficiency of finite length acoustically thick circular cylindrical shells under mechanical excitation I: theoretical analysis. *Journal of Sound and Vibration*, 232(2):431–447, 2000.

[100] K.-J. Bathe. *Finite element procedures*. Klaus-Jurgen Bathe, 2006.

[101] A. Jeffrey. *Advanced engineering mathematics.* Academic Press, 2001.

[102] C. Beards. *Engineering vibration analysis with application to control systems.* Butterworth-Heinemann, 1995.

[103] L. Cremer and M. Heckl. *Körperschall: Physikalische Grundlagen und technische Anwendungen.* Springer-Verlag, 2013.

[104] Z.-Q. Qu. *Model order reduction techniques with applications in finite element analysis.* Springer Science & Business Media, 2013.

[105] J. W. Tedesco, W. G. McDougal, and C. A. Ross. *Structural dynamics: theory and applications.* Addison Wesley Longman, 1999.

[106] E. B. Rudnyi and J. G. Korvink. Review: Automatic model reduction for transient simulation of MEMS-based devices. *Sensors Update*, 11(1):3–33, 2002.

[107] M. Schwarzer, E. Barti, and T. Bein. Model order reduction of dynamical structural simulation models of electric motors using Krylov subspaces. In *International Conference on Noise and Vibration Engineering (ISMA)*, pages 1473–1486, 2014.

[108] W. E. Arnoldi. The principle of minimized iterations in the solution of the matrix eigenvalue problem. *Quarterly of Applied Mathematics*, 9(1):17–29, 1951.

[109] A. N. Krylov. On the numerical solution of the equation by which in technical questions frequencies of small oscillations of material systems are determined. *News of Academy of Sciences of the USSR*, 7(4):491–539, 1931.

[110] O. Nevanlinna. *Convergence of iterations for linear equations.* Birkhäuser, 2012.

[111] Y. Saad. *Iterative methods for sparse linear systems.* Siam, 2003.

[112] G. A. Baker and P. Graves-Morris. Pade approximants. Part 2: Extensions and applications. *Encyclopedia of Mathematics and its Applications*, 1, 1981.

[113] C. Brezinski. *Padé-type approximation and general orthogonal polynomials.* Springer, 1980.

[114] R. Eid, B. Salimbahrami, B. Lohmann, E. B. Rudnyi, and J. G. Korvink. Parametric order reduction of proportionally damped second-order systems. *Sensors and Materials*, 19(3):149–164, 2007.

[115] R. Eid, H. Panzer, and B. Lohmann. How to choose a single expansion point in Krylov-based model reduction. In *Technical Reports on Automatic Control (TRAC), Vol. 4, Lehrstuhl für Regelungstechnik.* Technische Universität München Germany, 2009.

[116] S. Gugercin, A. C. Antoulas, and C. Beattie. H_2 model reduction for large-scale linear dynamical systems. *Journal on Matrix Analysis and Applications*, 30(2):609–638, 2008.

[117] D. Kubalinska. Optimal interpolation-based model reduction. 2008.

[118] C. Lein, M. Beitelschmidt, and D. Bernstein. Improvement of Krylov-subspace-reduced models by iterative mode-truncation. *IFAC - PapersOnLine*, 48(1):178–183, 2015.

[119] B. Salimbahrami, R. Eid, and B. Lohmann. Model reduction by second order Krylov subspaces: Extensions, stability and proportional damping. In *IEEE International Conference on Control Applications*, pages 2997–3002. IEEE, 2006.

[120] T. Bonin, H. Faßbender, A. Soppa, and M. Zaeh. A fully adaptive rational global Arnoldi method for the model-order reduction of second-order MIMO systems with proportional damping. *Mathematics and Computers in Simulation*, 122:1–19, 2016.

[121] R. R. Craig and A. J. Kurdila. *Fundamentals of structural dynamics.* John Wiley & Sons, 2006.

[122] R. J. Guyan. Reduction of stiffness and mass matrices. *AIAA Journal*, 3(2):380–380, 1965.

[123] M. Pröbster. *Elastisch Kleben.* Springer, 2013.

[124] H. F. Brinson and L. C. Brinson. *Polymer engineering science and viscoelasticity.* Springer, 2008.

[125] W. G. Knauss, I. Emri, and H. Lu. *Mechanics of polymers: viscoelasticity.* Springer, 2008.

[126] P. Haupt. *Continuum mechanics and theory of materials.* Springer Science & Business Media, 2013.

[127] Z. V. I. Hashin. Complex moduli of viscoelastic composites - I. General theory and application to particulate composites. *International Journal of Solids and Structures*, 6(5):539–552, 1970.

[128] M. L. Williams, R. F. Landel, and J. D. Ferry. The temperature dependence of relaxation mechanisms in amorphous polymers and other glass-forming liquids. *Journal of the American Chemical Society*, 77(14):3701–3707, 1955.

[129] R. S. Lakes. Viscoelastic measurement techniques. *Review of Scientific Instruments*, 75(4):797–810, 2004.

[130] B. E. Read and G. D. Dean. *The determination of dynamic properties of polymers and composites.* Halsted Press, 1978.

[131] K. P. Menard. *Dynamic mechanical analysis: a practical introduction.* CRC press, 2008.

[132] N. W. Tschoegl, W. G. Knauss, and I. Emri. Poisson's ratio in linear viscoelasticity - a critical review. *Mechanics of Time-Dependent Materials*, 6(1):3–51, 2002.

[133] R. S. Lakes and A Wineman. On Poisson's ratio in linearly viscoelastic solids. *Journal of Elasticity*, 85(1):45–63, 2006.

[134] P. H. Mott, J. R. Dorgan, and C. M. Roland. The bulk modulus and Poisson's ratio of "incompressible" materials. *Journal of Sound and Vibration*, 312(4):572–575, 2008.

[135] W. G. Knauss and I. J. Emri. Non-linear viscoelasticity based on free volume consideration. *Computers and Structures*, 13(1):123–128, 1981.

[136] S. Tingfang. An analyses of viscoelastic Poisson's ratio and elastic Poisson's ratio. *Journal of Beijing Institute of Technology*, 6:004, 1999.

[137] L. Grassia, A. D'Amore, and S. L. Simon. On the viscoelastic Poisson's ratio in amorphous polymers. *Journal of Rheology*, 54(5):1009–1022, 2010.

[138] Q. Chen and K. Worden. A decomposition method for the analysis of viscoelastic structural dynamics with time-dependent Poisson's ratio. *Strain*, 47(s1), 2011.

[139] M. Ashrafi, H.and Shariyat. A mathematical approach for describing the time-dependent Poisson's ratio of viscoelastic ligaments mechanical characteristics of biological tissues. In *17th Iranian Conference of Biomedical Engineering (ICBME)*, pages 1–5. IEEE, 2010.

[140] L. Dong and R. S. Lakes. Frequency dependence of poisson's ratio of viscoelastic elastomer foam. *Cellular Polymers*, 30(6):277, 2011.

[141] J. Göhler. Das dreidimensionale Stoffverhalten im großen Temperatur-und Zeitbereich am Beispiel eines in der automobilen Klebtechnik verwendeten Epoxidharzklebstoffs. 2010.

[142] T. Pritz. Frequency dependences of complex moduli and complex Poisson's ratio of real solid materials. *Journal of Sound and Vibration*, 214(1):83–104, 1998.

[143] N. S. Bakhvalov and G. Panasenko. *Homogenisation: averaging processes in periodic media: mathematical problems in the mechanics of composite materials*, volume 36. Springer Science & Business Media, 2012.

[144] M. M. Kaminski. *Computational mechanics of composite materials: sensitivity, randomness and multiscale behaviour*. Springer Science & Business Media, 2006.

[145] G. Dal Maso and G. F. Dell' Antonio. Composite media and homogenization theory. In *Proceedings of the workshop held at the International Centre for Theoretical Physics*, 1991.

[146] B. Harris. *Engineering composite materials*. IoM, 1999.

[147] M.-J. Pindera, H. Khatam, A. S. Drago, and Y. Bansal. Micromechanics of spatially uniform heterogeneous media: A critical review and emerging approaches. *Composites Part B: Engineering*, 40(5):349–378, 2009.

[148] A. Drago and M.-J. Pindera. Micro-macromechanical analysis of heterogeneous materials: Macroscopically homogeneous vs periodic microstructures. *Composites Science and Technology*, 67(6):1243–1263, 2007.

[149] C. T. Sun and R. S. Vaidya. Prediction of composite properties from a representative volume element. *Composites Science and Technology*, 56(2):171–179, 1996.

[150] R. Hill. Elastic properties of reinforced solids: some theoretical principles. *Journal of the Mechanics and Physics of Solids*, 11(5):357–372, 1963.

[151] J. Aboudi, S. M. Arnold, and B. A. Bednarcyk. *Micromechanics of composite materials: a generalized multiscale analysis approach*. Butterworth-Heinemann, 2012.

[152] S. Li. Boundary conditions for unit cells from periodic microstructures and their implications. *Composites Science and Technology*, 68(9):1962–1974, 2008.

[153] S. Li. On the unit cell for micromechanical analysis of fibre-reinforced composites. In *Proceedings of the Royal Society of London A: Mathematical, Physical and Engineering Sciences*, volume 455, pages 815–838. The Royal Society, 1999.

[154] H. Altenbach. *Kontinuumsmechanik*. Springer, Berlin, 2012.

[155] J. C. Halpin and L. Nicolais. Composite materials - relation between property and structure. *Quaderni Dell Ingegnere Chimico Italiano*, 7(12):173, 1971.

[156] J. C. Halpin and J. L. Kardos. Moduli of crystalline polymers employing composite theory. *Journal of Applied Physics*, 43(5):2235–2241, 1972.

[157] J. L. Kardos. Structure property relations in short-fiber reinforced plastics. *Critical Reviews in Solid State and Material Sciences*, 3(4):419–450, 1973.

[158] J. C. Halpin. Some critical issues in advanced polymer science. *Polymer Engineering and Science*, 15(3):132–136, 1975.

[159] L. Nicolais. Mechanics of composites. *Polymer Engineering & Science*, 15(3):137–149, 1975.

[160] J. C. Affdl and J. L. Kardos. The Halpin-Tsai equations: A review. *Polymer Engineering and Science*, 16(5):344–352, 1976.

[161] G. W. Postma. Wave propagation in a stratified medium. *Geophysics*, 20(4):780–806, 1955.

[162] J. Aboudi and M.-J. Pindera. Micromechanics of metal matrix composites using the generalized method of cells model (GMC) user's guide. 1992.

[163] C. T. Sun, J. K. Wu, and R. F. Gibson. Prediction of material damping of laminated polymer matrix composites. *Journal of Materials Science*, 22(3):1006–1012, 1987.

[164] R. Chandra, S. P. Singh, and K. Gupta. Damping studies in fiber-reinforced composites - a review. *Composite Structures*, 46(1):41–51, 1999.

[165] R. Chandra, S. P. Singh, and K. Gupta. Micromechanical damping models for fiber-reinforced composites: a comparative study. *Composites Part A: Applied Science and Manufacturing*, 33(6):787–796, 2002.

[166] A. Treviso, B. Van Genechten, D. Mundo, and M. Tournour. Damping in composite materials: Properties and models. *Composites Part B: Engineering*, 78:144–152, 2015.

[167] R. Chandra, S. P. Singh, and K. Gupta. A study of damping in fiber-reinforced composites. *Journal of Sound and Vibration*, 262(3):475–496, 2003.

[168] J.-L. Tsai and Y.-K. Chi. Effect of fiber array on damping behaviors of fiber composites. *Composites Part B: Engineering*, 39(7):1196–1204, 2008.

[169] J.-M. Berthelot, M. Assarar, Y. Sefrani, and A. El Mahi. Damping analysis of composite materials and structures. *Composite Structures*, 85(3):189–204, 2008.

[170] F. Curà, A. Mura, and F. Scarpa. Modal strain energy based methods for the analysis of complex patterned free layer damped plates. *Journal of Vibration and Control*, 18(9):1291–1302, 2012.

[171] A. El Mahi, M. Assarar, Y. Sefrani, and J.-M. Berthelot. Damping analysis of orthotropic composite materials and laminates. *Composites Part B: Engineering*, 39(7):1069–1076, 2008.

[172] M. Kaliske and H. Rothert. Damping characterization of unidirectional fibre reinforced polymer composites. *Composites Engineering*, 5(5):551–567, 1995.

[173] J. D. D. Melo and D. W. Radford. Viscoelastic characterization of transversely isotropic composite laminae. *Journal of Composite Materials*, 37(2):129–145, 2003.

[174] R. S. Lakes. High damping composite materials: effect of structural hierarchy. *Journal of Composite Materials*, 36(3):287–297, 2002.

[175] C. T. Sun, R. F. Gibson, and S. K. Chaturvedi. Internal material damping of polymer matrix composites under off-axis loading. *Journal of Materials Science*, 20(7):2575–2585, 1985.

[176] J. P. Talbot and J. Woodhouse. The vibration damping of laminated plates. *Composites Part A: Applied Science and Manufacturing*, 28(12):1007–1012, 1997.

[177] Plastics - Determination of tensile properties - Part 1: General principles (ISO 527-1:2012). Technical Report ISO 527-1:2012, International Organization for Standardization, 2012.

[178] R. D. Widdle, C. M. Krousgrill, and S. D. Sudhoff. An induction motor model for high-frequency torsional vibration analysis. *Journal of Sound and Vibration*, 290(3):865–881, 2006.

[179] D. Görke. *Experimentelle und numerische Untersuchung des Normal-und Tangentialkontaktverhaltens rauer metallischer Oberflächen.* PhD thesis, Univ. Erlangen-Nürnberg, Lehrstuhl für Techn. Mechanik, 2010.

[180] C. Öztürk and A. Bahadir. Significance of the electromagnetic forces on the mechanical resonances of stator laminations. *Mechanical Systems and Signal Processing*, 10(5):501–515, 1996.

[181] S. Singhal, K. V. Singh, and A. Hyder. Effect of laminated core on rotor mode shape of large high speed induction motor. In *IEEE International Conference of Electric Machines & Drives Conference (IEMDC)*, pages 1557–1562. IEEE, 2011.

[182] J. D. Ede, Z. Q. Zhu, and D. Howe. Rotor resonances of high-speed permanent-magnet brushless machines. *IEEE Transactions on Industry Applications*, 38(6):1542–1548, 2002.

[183] S. D. Garvey. *The prediction of vibration in large electric machines.* PhD thesis, Aston University, 1988.

[184] S. D. Garvey. The vibrational behaviour of laminated components in electrical machines. In *4th International Conference on Electrical Machines and Drives*, pages 226–231. IET, 1989.

[185] M. van der Giet, K. Kasper, R. W. De Doncker, and K. Hameyer. Material parameters for the structural dynamic simulation of electrical machines. In *20th International Conference on Electrical Machines (ICEM)*, pages 2994–3000. IEEE, 2012.

[186] Z. Tang, P. Pillay, A. M. Omekanda, C. Li, and C. Cetinkaya. Young's modulus for laminated machine structures with particular reference to switched reluctance motor vibrations. *IEEE Transactions on Industry Applications*, 40(3):748–754, 2004.

[187] P. Millithaler, É. Sadoulet-Reboul, M. Ouisse, J.-B. Dupont, and N. Bouhaddi. Structural dynamics of electric machine stators: Modelling guidelines and identification of three-dimensional equivalent material properties for multi-layered orthotropic laminates. *Journal of Sound and Vibration*, 348:185–205, 2015.

[188] H.-J. Wang, Y.-R. Chen, and L.-W. Chen. Finite element dynamic analysis of rotating orthotropic sandwich annular plates. *Composite Structures*, 62(2):205–212, 2003.

[189] H. Wang and K. Williams. Effects of laminations on the vibrational behaviour of electrical machine stators. *Journal of Sound and Vibration*, 202(5):703–715, 1997.

[190] K. Williams and H. Wang. The effect of laminations on the vibrational modes of circular annular plates. *Experimental Mechanics*, 36(2):180–186, 1996.

[191] P. Millithaler, É. Sadoulet-Reboul, M. Ouisse, J.-B. Dupont, and N. Bouhaddi. 3D homogenization: Identification of equivalent anisotropic material properties of heterogeneous structures and dynamic applications on preloaded finite element models and superelements. 2014.

[192] J. H. Walker, G. J. Rogers, and R. L. Jackson. Pressing and clamping laminated cores. *Proceedings of the Institution of Electrical Engineers*, 111(3):565–577, 1964.

[193] G. Čepon, M. Pirnat, and M. Boltežar. An experimental and numerical identification of laminated structure dynamics. 2012.

[194] M. Pirnat, G. Čepon, and M. Boltežar. Introduction of the linear contact model in the dynamic model of laminated structure dynamics: an experimental and numerical identification. *Mechanism and Machine Theory*, 64:144–154, 2013.

[195] V. Luchscheider, K. Willner, and M. Maidorn. Development of a model to describe the stiffness of an electric motor lamination stack. In *2nd International Conference of Electric Drives Production Conference (EDPC)*, pages 1–5. IEEE, 2012.

[196] V. Luchscheider, K. Willner, and M. Maidorn. Development of a contact and a material model of laminated stacks. In *3rd International Conference of Electric Drives Production Conference (EDPC)*, pages 1–5. IEEE, 2013.

[197] V. Luchscheider, M. Maidorn, and K. Willner. Computation of the effective lamination stack's behavior considering the contact simulation with a multi-scale homogenization. In *11th World Congress on Computational Mechanics*, 2014.

[198] V. Luchscheider, M. Maidorn, and K. Willner. Identification of the lamination stack's behavior simulated with a multi-scale homogenization using a progressive contact formulation. *PAMM*, 14(1):253–254, 2014.

[199] K. L. Johnson. *Contact mechanics.* Cambridge university press, 1987.

[200] F.-S. Liao and T.-C. J. Hsu. Prediction of vibration damping properties of polymer-laminated steel sheet using time-temperature superposition principle. *Journal of Applied Polymer Science*, 45(5):893–900, 1992.

[201] S. Ghinet and N. Atalla. Modeling of general laminate composite structures with viscoelastic layer. *Canadian Acoustics*, 35(3):202–203, 2007.

[202] M. A. Biot. Simplified dynamics of multilayered orthotropic viscoelastic plates. *International Journal of Solids and Structures*, 8(4):491–509, 1972.

[203] M. D. Rao, R. Echempati, and S. Nadella. Dynamic analysis and damping of composite structures embedded with viscoelastic layers. *Composites Part B: Engineering*, 28(5):547–554, 1997.

[204] S. H. Zhang and H. L. Chen. A study on the damping characteristics of laminated composites with integral viscoelastic layers. *Composite Structures*, 74(1):63–69, 2006.

[205] Y.-C. Hu and S.-C. Huang. The frequency response and damping effect of three-layer thin shell with viscoelastic core. *Computers & Structures*, 76(5):577–591, 2000.

[206] H.-J. Wang and L.-W. Chen. Finite element dynamic analysis of orthotropic cylindrical shells with a constrained damping layer. *Finite Elements in Analysis and Design*, 40(7):737–755, 2004.

[207] J. De Visscher, H. Sol, W. P. De Wilde, and J. Vantomme. Identification of the damping properties of orthotropic composite materials using a mixed numerical experimental method. *Applied Composite Materials*, 4(1):13–33, 1997.

[208] L. Pan and B. Zhang. A new method for the determination of damping in cocured composite laminates with embedded viscoelastic layer. *Journal of Sound and Vibration*, 319(3):822–831, 2009.

[209] S. Nadella and M. D. Rao. Damping of composite structures using embedded viscoelastic layers. In *SPIE - The International Society for Optical Engineering*, pages 233–233. SPIE INTERNATIONAL SOCIETY FOR OPTICAL, 1995.

[210] C. D. Johnson and D. A. Kienholz. Finite element prediction of damping in structures with constrained viscoelastic layers. *AIAA Journal*, 20(9):1284–1290, 1982.

[211] Y. S Chen, T. J. Hsu, and S. I. Chen. Vibration damping characteristics of laminated steel sheet. *Metallurgical Transactions A*, 22(3):653–656, 1991.

[212] S. Akarapu, T. Sharp, and M. O. Robbins. Stiffness of contacts between rough surfaces. *Physical Review Letters*, 106(20):204301, 2011.

[213] X. Shi and A. A. Polycarpou. Measurement and modeling of normal contact stiffness and contact damping at the meso scale. *Journal of Vibration and Acoustics*, 127(1):52–60, 2005.

[214] S Stupkiewicz. *Micromechanics of contact and interphase layers*, volume 30. Springer Science & Business Media, 2007.

[215] M. V. Berry and T. M. Blackwell. Diffractal echoes. *Journal of Physics A: Mathematical and General*, 14(11):3101, 1981.

[216] S. P. Verma and R. S. Girgis. Resonance frequencies of electrical machine stators having encased construction, Part I: Derivation of the general frequency equation. *IEEE Transactions on Power Apparatus and Systems*, 5(PAS-92):1577–1585, 1973.

[217] S. P. Verma and R. S. Girgis. Resonance frequencies of electrical machine stators having encased construction, Part II: Numerical results and experimental verification. *IEEE Transactions on Power Apparatus and Systems*, 5(PAS-92):1586–1593, 1973.

[218] R. S. Girgis and S. P. Verma. Method for accurate determination of resonant frequencies and vibration behaviour of stators of electrical machines. *IEEE Proceedings B: Electric Power Applications*, 128(1):1, 1981.

[219] S. P. Verma, R. K. Singal, and K. Williams. Vibration behaviour of stators of electrical machines, Part I: Theoretical study. *Journal of Sound and Vibration*, 115(1):1–12, 1987.

[220] S. P. Verma. Vibration behaviour of stators of electrical machines. In *Vibrations and Audible Noise in Alternating Current Machines*, pages 499–513. Springer, 1988.

[221] G. Henneberger, P. K. Sattler, W. Hadrys, and D. Shen. Procedure for the numerical computation of mechanical vibrations in electrical machines. *IEEE Transactions on Magnetics*, 28(2):1351–1354, 1992.

[222] J. Roivainen. *Unit-wave response-based modeling of electromechanical noise and vibration of electrical machines*. PhD thesis, 2009.

[223] M. Schwarzer, C. Zimmerling, E. Barti, M. Dannemann, R. Bochynek, and T. Bein. Analytical prediction of the effective dynamic behavior and the damping characteristics of laminated steel stacks as used in electric machines. In *International Conference of Sound and Vibration (ICSV)*, 2015.

[224] P. Millithaler, É. Sadoulet-Reboul, M. Ouisse, J.-B. Dupont, and N. Bouhaddi. Equivalent orthotropic material properties for stators of electric cars. In *12th International Conference on Computational Structures Technology*, 2014.

[225] L. Durantay, F. Laurent, Y. Messin, and V. Kromer. Large-band reduction of magnetic vibrations of induction machines with “breaking-of-impedance“ interface. *IEEE Transactions on Industry Applications*, 36(4):1126–1131, 2000.

[226] S. P. Verma and A. Balan. Experimental investigations on the stators of electrical machines in relation to vibration and noise problems. In *IEEE Proceedings - Electric Power Applications*, volume 145, pages 455–461. IET, 1998.

[227] H. Wang and K. Williams. The vibrational analysis and experimental verification of a plane electrical machine stator model. *Mechanical Systems and Signal Processing*, 9(4):429–438, 1995.

[228] K. Niskanen. *Mechanics of paper products*. Walter de Gruyter, 2012.

[229] P. Pillay and W. Cai. An investigation into vibration in switched reluctance motors. *IEEE Transactions on Industry Applications*, 35(3):589–596, 1999.

[230] A. J. Ellison and S. J. Yang. Natural frequencies of stators of small electric machines. *Proceedings of the Institution of Electrical Engineers*, 118(1):185–190, 1971.

[231] H.-J. Shin and J.-Y. Choi. General vibration characteristics for stators of electric machines. In *International Conference on Electrical Machines and Systems (ICEMS)*, pages 1144–1147. IEEE, 2013.

[232] Z. Tang, P. Pillay, A. M. Omekanda, C. Li, and C. Cetinkaya. Measurement of Young's modulus for switched reluctance motor vibration determination. In *IEEE International Conference of Electric Machines and Drives Conference (IEMDC'03)*, volume 3, pages 1590–1595. IEEE, 2003.

[233] S. C. Chang and R. Yacamini. Experimental study of the vibrational behaviour of machine stators. In *IEEE Proceedings - Electric Power Applications*, volume 143, pages 242–250. IET, 1996.

[234] M. Benbouzid, M. Benbouzid, S. Derou, and A. Foggia. Finite element modeling of a synchronous machine: electromagnetic forces and mode shapes. *IEEE Transactions on Magnetics*, 29(2):2014–2018, 1993.

[235] S. Noda, S. Mori, F. Ishibashi, and K. Itomi. Effect of coils on natural frequencies of stator cores in small induction motors. *IEEE Transactions on Energy Conversion*, (1):93–99, 1987.

[236] R. Lin, A. N. Laiho, A. Haavisto, and A. Arkkio. End-winding vibrations caused by steady-state magnetic forces in an induction machine. *IEEE Transactions on Magnetics*, 46(7):2665–2674, 2010.

[237] B. Schlegl, F. Schönleitner, A. Marn, F. Neumayer, and F. Heitmeir. Analytical determination of the orthotropic material behavior of stator bars in the range of the end windings and determination of the material characteristics of the orthotropic composite space brackets via experimental modal analysis and FE-calculation. In *20th International Conference on Electrical Machines (ICEM)*, pages 1948–1956. IEEE, 2012.

[238] B. Schlegl, C. Scheinecker, A. Marn, F. Neumayer, M. Himmelreich, and F. Heitmeir. Development of a full parameterized FE-modeling tool for efficient vibration investigations on end windings of turbo-and hydro-generators. In *20th International Conference on Electrical Machines (ICEM)*, pages 2961–2968. IEEE, 2012.

[239] B. Schlegl, F. Schönleitner, A. Marn, F. Neumayer, and F. Heitmeir. Determination of the orthotropic material behavior of stator bars and of the material characteristics of the space brackets. *Journal of Energy and Power Engineering*, 7(7):1352, 2013.

[240] O. Drubel, S. Kulig, and K. Senske. End winding deformations in different turbo generators during 3-phase short circuit and full load operation. *Electrical Engineering*, 82(3-4):145–152, 2000.

[241] K. Senske, S. Kulig, J. Hauhoff, and D. Wünsch. Oscillation behaviour of the end winding region of a turbo generator during electrical failures. In *Conference Proceedings CIGRE, Yokohama*, 1997.

[242] S. Marburg. Discretization requirements: How many elements per wavelength are necessary? In *Computational Acoustics of Noise Propagation in Fluids-Finite and Boundary Element Methods*, pages 309–332. Springer, 2008.

[243] A. Oskooi and S. G. Johnson. Distinguishing correct from incorrect PML proposals and a corrected unsplit PML for anisotropic, dispersive media. *Journal of Computational Physics*, 230(7):2369–2377, 2011.

[244] W. Bangerth and R. Rannacher. Finite element approximation of the acoustic wave equation: Error control and mesh adaptation. *East West Journal of Numerical Mathematics*, 7(4):263–282, 1999.

[245] F. P. Mechel. *Formulas of acoustics.* Springer Science & Business Media, 2013.

[246] T. Łodygowski and W. Sumelka. Limitations in application of finite element method in acoustic numerical simulation. *Journal of theoretical and applied mechanics*, 44(4):849–865, 2006.

[247] M. Schwarzer, E. Barti, and T. Bein. Strukturdynamische Simulationen eines elektrischen Antriebsstrangs unter Verwendung der Component-Mode-Synthesis Methode. In *40. Jahrestagung für Akustik (DAGA)*, pages 1473–1486, 2013.

[248] Plastics - Determination of dynamic mechanical properties - Part 1: General principles (ISO 6721-1:2011(E)). Technical Report ISO 6721-1:2011(E), International Organization for Standardization, 2011.

[249] Plastics - Determination of dynamic mechanical properties - Part 4: Tensile vibration - Non-resonance method (ISO 6721-4:2008(E)). Technical Report ISO 6721-4:2008(E), International Organization for Standardization, 2008.

[250] Plastics - Determination of dynamic mechanical properties - Part 7: Torsional vibration - Non-resonance method (ISO 6721-7:1996/Amd.1:2007(E)). Technical Report ISO 6721-7:1996/Amd.1:2007(E), International Organization for Standardization, 1996.

[251] T. Naumann. *Beitrag zur Beschreibung des mechanischen Langzeitdeformationsverhaltens von thermoplastischen Kunststoffen.* PhD thesis, Universität des Saarlandes, 2013.

Lebenslauf

Michael Schwarzer

Geburtstag und -ort	:	28.12.1984 in Kleve
Nationalität	:	deutsch

Wissenschaftlicher Werdegang

seit 02/2012	:	**TU Darmstadt** Institut für Systemzuverlässigkeit und Maschinenakustik Maschinenbaustudium (Promotionsstudium) Akustik von Elektrischen Maschinen
10/2007 - 09/2011	:	**RWTH Aachen** Maschinenbaustudium (Haupstudium) Vertiefung in Richtung Energietechnik - Verbrennungsmotoren Diplom-Gesamtnote: Mit Auszeichnung bestanden
09/2008 - 07/2009	:	**UC Davis, CA, USA** Maschinenbaustudium (Auslandsstudium)
10/2005 - 09/2007	:	**RWTH Aachen** Maschinenbaustudium (Grundstudium) Vordiplom-Durschnittsnote: 1,7
06/2004	:	**St.-Georg-Gymnasium, Bocholt** Abitur, Durchschnittsnote: 1,8

München, 22. April 2017